2016

Studies of Rotationally and Vibrationally Inelastic Collisions of NaK with Atomic Perturbers

Kara Richter
Lehigh University

Studies of Rotationally and Vibrationally Inelastic Collisions of NaK with Atomic Perturbers

by

Kara M. Richter

A Dissertation
Presented to the Graduate Committee
of Lehigh University
in Candidacy for the Degree of
Doctor of Philosophy
in
Physics

Lehigh University
August 2016

Approved and recommended for acceptance as a dissertation in partial fulfillment of the requirements for the degree of Doctor of Philosophy.

Kara M Richter

Studies of Rotationally and Vibrationally Inelastic Collisions of NaK with Atomic Perturbers

---

Date

John Huennekens, Dissertation Director, Chair

Accepted Date

Committee Members

A. Peet Hickman

Ivan Biaggio

Gary DeLeo

Andrew Kortyna

Acknowledgments

First, I would like to begin by thanking my husband John ("Ria" as he was when we were introduced) for his unending support throughout our time together while I was in school. Anyone that knows me knows that I can be quite the literal bear to deal with on bad days, and Ria is the only person who can bring a smile to my face no matter my mood. He has been there through qualifiers and committee meetings, always with a hug and a snack to help ease the stress. No matter what happens in our future (near and far) I know we'll face it together.

To Professor Huennekens: You have been unyielding in your support of me in my time at Lehigh, from a timid REU student to an outspoken voice in the department in my last year. From Jackson to Herzberg, you had dedication to my education and expansion as a scientist, and you were always patient and respectful even when I had the knowledge but the words just wouldn't come. It will be a sad day for the department when your office door closes for the last time.

In support of my love of outreach, I want to thank Professor Gary DeLeo for allowing me to tag along on countless trips to local schools to bring the joy of science to inquiring young minds. It really takes a special type to gain the love and trust of the elementary students (and teachers) like he has. In my time here, he has not only been a great educational mentor but also a friend, supporting my quirky obsession with roller derby time and again by showing up to events.

I would also like to thank my other committee members Professor Hickman, Professor Biaggio and Dr. Andrew Kortyna for their help with the research process and insight in committee meetings. Special thanks go to Dr. Hickman, for his continued work and help with the theory side of NaK collisions, and to Andy, for his assistance in the lab with a myriad of things.

A brief thank you does not do justice to the experience of working with Drs. Amanda Ross, Patrick Crozet, and Heather Harker at Université Lyon-1 in Lyon, France. Not only would this dissertation not exist without their support and laboratory, but Amanda and Patrick opened up their home to allow me further time in France for research. They allowed me experiences (both scientific and travel based) that have continued to change me as a person, and I cannot thank them enough.

I would like to thank our families for being understanding during the last few years. Holidays spent with flash cards and text books came and went and yet you still all show your support and love. The largest thanks go to my parents, who despite not really understanding what any of this dissertation means, sent care packages and love, and have always supported me no matter how crazy or outrageous my dreams are. Our other family, the Lehigh Valley Rollergirls, is owed thanks as well, for giving me an outlet for life's stresses. I have gotten lifelong friendships out of my time with you all. You will always be my first home when it comes to roller derby.

Thanks on many levels go to my fellow (past and present) AMO group members. Seth Ashman, who was the graduate student whom I followed around as an REU dutifully, Chris Wolfe, who paved the way for this project, and Ruthie Malenda, who will forever be a friend and partner in crime covered in glitter. Thank you to Josh Jones for our matching black eyes that one DAMOP, and constant foodie conversations. To Carl Faust, the person most likely to nerd out with me in the office: I hope you find the internet someday. Teri Price, thank you for being willing to try new things like roller skating on random Wednesday nights.

I have been fortunate to have met some absolutely wonderful graduate students. Most thanks to some people from my year: Ben Sofka, Donovan Ruth, and Kebra Ward. Ben and Donovan, may Louie always watch over you and protect your work.

To Kebra, thank you for constantly being there with fresh veggies and libations when we all needed it most. I would also like to thank others not in my year: Vinnie Zoutenbier (hi Vinnie), Phil Weiser (my constant Star Wars buddy) and Massooma Pirbhai, who always had a hug and a chocolate bar for anyone having a bad day.

Contents

List of Tables

List of Figures

Abstract

This dissertation discusses investigations of vibrationally and rotationally inelastic collisions of NaK with argon, helium and potassium as collision partners. We have investigated collisions of NaK molecules in the $2(A)^1\Sigma^+$ state with argon and helium collision partners in a laser-induced fluorescence (LIF) experiment. The pump laser prepares the molecules in particular ro-vibrational (v, J) levels in the $2(A)^1\Sigma^+$ state. These excited molecules then emit fluorescence as they make transitions back to the ground [$1(X)^1\Sigma^+$] state, and this fluorescence is collected by a Bomem Fourier-transform spectrometer. Weak collisional satellite lines appear flanking strong, direct lines in the recorded spectra. These satellite lines are due to collisions of the NaK molecule in the $2(A)^1\Sigma^+$ state with noble gas and alkali atom perturbers, which carry population to nearby rotational levels [$(v,\ J) \rightarrow (v,\ J + \Delta J)$] or to various rotational levels of nearby vibrational levels, [$(v,\ J) \rightarrow (v + \Delta v,\ J + \Delta J)$]. Ratios of the intensity of each collisional line to the intensity of the direct line then yields information pertaining to the transfer of population in the collision. Our results show a propensity for ΔJ = even collisions of NaK with noble gas atoms, which is slightly more pronounced for collisions with helium than with argon. Such a ΔJ = even propensity was not observed in the vibrationally inelastic collisions. Although it would be desirable to operate in the single collision regime, practical considerations make that difficult to achieve. Therefore, we have developed a method to estimate the effects of multiple collisions on our measured rate coefficients and have obtained approximate corrected values.

Chapter 1

Introduction

1.1 Overview

In this dissertation, an analysis of population transfer that occurs in collisions of diatomic alkali molecules with neutral atoms will be presented. Each alkali atom in the diatomic molecule can be approximated as having a single loosely bound electron, so that the alkali diatomic is (to first order) effectively a two electron molecule. Consequently these molecules represent a fairly simple quantum mechanical system and these experiments can serve as tests of the fundamental ideas of quantum mechanics. The experimentally measured rate coefficients serve as benchmarks for theoretical calculations of these molecule-atom collisions. This chapter presents an introduction to laser induced fluorescence (the technique used in Lyon, France to record the data obtained for this work), alkali spectroscopy and collisions, and a brief discussion of optical-optical double resonance spectroscopy (used at Lehigh University). Previous collisional studies will also be discussed, including previous experimental and theoretical work carried out in our research group at

Lehigh University.

1.2 Laser Induced Fluorescence

Laser induced fluorescence (LIF), with its wide range of applications in spectroscopy, provides a variety of options to monitor the absorption and emission of photons with high sensitivity, and is well suited to obtain information on molecular states. In its most basic form, LIF uses a narrow band, stable laser to excite a molecule from a ground state to a higher electronic state by tuning the laser to the resonance frequency of a particular transition. In the work I present in this dissertation, NaK molecules in a particular rotational-vibrational (ro-vibrational) level of the ground state $[1(X)^1\Sigma^+]$ are excited to a particular ro-vibrational level of the first excited state $[2(A)^1\Sigma^+]$, from which they decay back to the ground state with the emission of fluorescence. LIF also offers a method to study collisional processes, where population from the directly populated excited state level can be transferred to a neighboring level via these collisions. Previous studies of this type of process are discussed in Sec. 1.4 and details of the experimental technique used in our work are provided in Chapter 4. Refs [1, 2, 3, 4] provide experimental details and a general introduction to LIF. Fourier transform spectroscopy, combined with LIF, allows the acquisition of spectra over wide ranges of frequency, containing thousands of spectral lines (due to the simultaneous collection of all fluorescence lines at one time), with relatively high signal-to-noise ratios. Molecules studied using this method include Rb_2 [5] and Cs_2 [6].

Of particular interest for this work are data which have been collected on a

plethora of vibrational and rotational levels in the electronic ground state $[1(X)^1\Sigma^+]$ by Ross *et al.* [7] and Russier-Antoine *et al.* [8] and in the first excited state $[2(A)^1\Sigma^+]$ of NaK by Ross *et al.* [9]. Further work leading to even more accurate potentials was carried out by Gerdes *et al.* [10] for the NaK ground state $[1(X)^1\Sigma^+]$ and by Harker *et al.* [11] for the $2(A)^1\Sigma^+$ state. Most of this work was done using Fourier transform spectroscopy (see Chapter 4), and the data collected in these works was used by the authors to produce accurate potential energy curves and determine spectroscopic constants for these electronic states.

1.3 Optical-Optical Double Resonance

The experimental technique used in the Lehigh experiments, which preceded the current work, is a two-step method called optical-optical double resonance (OODR). One laser (the pump laser) excites the molecule from the ground state to the first excited state, preparing the molecule in a particular ro-vibrational level of this intermediate state. A second (probe) laser is then used to excite the molecule to a higher electronic state. Fluorescence associated with downward transitions from both the intermediate state and the excited state are typically observed in order to monitor the populations of these particular ro-vibrational levels. Woerdman [12] used this method in early experiments to study the high lying $^1\Sigma_g^+$ electronic states of Na_2 molecules. A modified version of OODR, called perturbation facilitated OODR (PFOODR) [13] has been used to study high lying triplet states, utilizing intermediate levels that carry mixed singlet-triplet spin character due to localized spin-orbit coupling between specific rotational levels of neighboring singlet and triplet states.

These two techniques have been applied to both homo- and heteronuclear diatomic alkali molecules. In our research group at Lehigh, the $3^1\Pi$ [14], $3^3\Pi$ [15], $1^3\Delta$ [16, 17], $4^3\Pi$ [18] and $4^3\Sigma^+$ [19] electronic states of NaK have been mapped utilizing these methods. Experimental studies of the $11(0^+)(5^3\Pi_0)$ [20] and $12(0^+)(7^1\Sigma^+)$ [21] electronic states of NaCs have also been carried out.

1.4 Collisional Studies of Diatomic Molecules

Important to this work are previous studies of ro-vibrationally inelastic collisions, which have been carried out by many molecular physics research groups. Propensities for certain transitions due to collisions have been observed in several of these experiments. Ottinger *et al.* studied collisions of Li_2 $1(B)^1\Pi_u$ molecules with argon atoms, and observed a propensity for a positive or negative change in J based on the initial Λ-doubled component excited [22]. Collisional studies of Li_2 $1(A)^1\Sigma_u^+$ molecules with a range of collisional partners (xenon, argon, neon) showed a propensity for $\Delta J = -4\Delta v$ [23, 24, 25]. Pritchard and coworkers attributed this to an approximate energy resonance, since the vibrational energy gap in this electronic state is approximately equal to the energy gap between rotational levels J and $J + 4$ for the range of J's they studied.

Observing fluorescence following collisional transfer of population allows collisional rate coefficients to be determined. In most cases, as in the current work, these rate coefficients were determined by comparing fluorescence from the directly

populated level to the fluorescence of nearby collisionally populated vibrational or rotational levels. Pritchard and coworkers [23, 24, 25] also determined rate coefficients for rotationally and vibrationally inelastic collisions of Li_2 with various perturbers, and these studies were expanded in further experiments by Gao and Stewart [26] and Gao *et al.* [27]. Bergmann and Demtröder [28] examined collisional cross sections for collisions of Na_2 [in the $1(B)^1\Pi_u$ state] with helium.

Theoretical calculations of collision cross sections and rate coefficients have also been carried out for collisions of diatomic alkali molecules with atomic perturbers, which can be directly compared to experiment. Calculations for vibrationally inelastic collisions of Li_2 in the $1(A)^1\Sigma_u^+$ state were performed by McCaffery [29] and gave a kinematic interpretation for these collisions, while *ab initio* calculations for collisions of Li_2 molecules in this state with neon perturbers was completed by Alexander and Werner [30]. The theoretical results of [30] agree quite well with the experimental results of Scott *et al.* [23].

More recent work at Lehigh combines both experimental studies and theoretical calculations. Wolfe *et al.* [31] studied collisions of a heteronuclear molecule, NaK, in the $2(A)^1\Sigma^+$ electronic state, with argon and potassium perturbers. This work observed both ΔJ = even and ΔJ = odd collisional transitions (only ΔJ = even collisional transitions are observed in the homonuclear molecules due to symmetry considerations). However Wolfe *et al.* did observe a strong *propensity* for ΔJ = even in the experimentally determined argon rate coefficients, but they reported a monotonic fall off with increasing $|\Delta J|$ in the potassium rate coefficients. Data were

collected in this experiment using the OODR technique, and using polarization labeling spectroscopy. The polarization experiment gave information on the transfer of both population *and* orientation, with the latter representing the distribution of population over the magnetic sublevels of the NaK intermediate state, during inelastic collisions of the NaK molecules with atomic perturbers. Wolfe *et al.* also observed that collisions of the NaK molecules with potassium atoms were both more likely to transfer population, and more likely to destroy orientation, than collisions of the NaK molecules with argon atoms. In addition to experimentally determined collisional rate coefficients, Wolfe *et al.* also obtained line broadening rates and studied velocity-changing collisions using their data.

Early calculations by Malenda [32] of collisional cross sections for the NaK-He system showed no ΔJ = even propensity, in apparent disagreement with the experimental data collected by Wolfe *et al.* However the conditions used for these calculations differed from those of the experiments both in the buffer gas and in the initially populated $2(A)^1\Sigma^+$ ro-vibrational level. Specifically, the calculations were carried out for NaK-He, rather than for NaK-Ar since the latter would have required computer resources beyond those available at the time, and the $2(A)^1\Sigma^+$ (16, 30) level was initially populated in the experiment, while the calculations were performed for $2(A)^1\Sigma^+$ (0, 14) (again due to limitations on computer resources). Work carried out by REU student Ariel Fragale and graduate student Phil Weiser attempted to extend the calculations to $v = 16$ by averaging the potential over a range of internuclear separations, using the square of the wavefunction. This average was then used for the scattering calculations (rather than fixing this parameter at the v=0 equilibrium separation). In this early calculation, a weak propensity for

ΔJ = even was displayed, leading us to believe that the vibrational state might play an important role in this effect (see Ruth Malenda's thesis, [32] p. 143). However, improvements in the basis sets used in the calculations of Malenda *et al.* [33] led to higher quality potential surfaces, and the ΔJ = even propensity was observed in the theoretical results for $v = 0$. In addition, a strong dependence of the rate coefficients on initial J was also predicted.

The observed early discrepancies between theory and experiment, and the predicted J dependence of rate coefficients also led to plans to expand the experiment to use helium as a collision partner, as well as to move to lower initial rotational and vibrational levels within the $2(A)^1\Sigma^+$ state. The experiments described by Wolfe *et al.* [31] were extended by Jones [34] to include NaK collisions with helium perturbers, which also showed this ΔJ = even propensity. The ΔJ = even propensity observed by Jones for NaK-He collisions is more pronounced than that for NaK-Ar collisions, and Jones found that collisions of NaK with helium are less likely to destroy orientation than collisions of NaK with argon. Jones also experimentally looked at collisions of NaCs with argon and helium perturbers, where a monotonic fall off of rate coefficients for increasing $|\Delta J|$ was observed for NaCs-Ar collisions, but a weak ΔJ = even propensity was observed for NaCs-He collisions. This result seemed to be consistent with the intuitive idea that the ΔJ = even propensity observed in NaK is due to the fact that NaK is "almost homonuclear" (i.e. Na and K are both alkali atoms with similar electronic structure and not too different masses). Conversely, the ΔJ = even propensity is much reduced in NaCs since NaCs is "more heteronuclear". However other experimental facts, such as that the different perturbers produce different degrees of ΔJ = even propensity, seem to contradict this

naive idea. The most recent theory now indicates that the origin of the ΔJ = even propensity is much more subtle, depending on the details of the potential surfaces at long-range.

The theoretical calculations are now also being extended by Price *et al.* [35]. Further improvements in the basis sets have been made, leading to improved collisional cross sections for both NaK-He and NaK-Ar collisions. Price *et al.* also expanded the range of initial J (and ΔJ) used in the calculations. Combined with the current set of experimental results, we can now make direct and detailed comparisons between experiment and theory for NaK-He and NaK-Ar collisions, with initially populated levels ($v = 0$, $J = 14$) and ($v = 0$, $J = 30$), over a wide range of ΔJ.

1.5 Summary of Content

It is the aim of this work to investigate the transfer of population during collisions of NaK molecules with argon, helium, or potassium collision partners using LIF spectroscopy. We have measured rate coefficients of population transfer for both rotation and vibration-rotation changing collisions, and we compare the effects of different buffer gas perturbers. We excite low lying vibrational levels ($v = 0$, 1, 2) so that we can directly compare our experimental results with theoretical calculations of Malenda *et al.* [33] and Price *et al.* [35].

The collection of data for this work was completed during the collaboration

with Drs. A. J. Ross and Patrick Crozet at Université Lyon-1, during two separate visits of the author to Lyon in November 2013 and November 2014. The Fourier Transform Spectrometer (FTS) allowed a wider range of ΔJ collisional lines to be investigated rapidly in comparison to previous experiments at Lehigh. In addition $\Delta v, \Delta J$ collisional spectra could also be collected with the Lyon setup. Unfortunately, the higher densities needed to observe v-changing collisions also meant that the approximation of being in the single collision regime was no longer always satisfied. Therefore considerable effort was needed to analyze the effects of multiple collisions on our measured rate coefficients.

Chapter 2 outlines some background information pertaining to diatomic molecules, including solutions of the Schrödinger equation for vibrational and rotational motion, and the most common Hund's cases. Chapter 3 describes the experimental setup used in our experiment in Lyon, France, as well as the experimental setup at Lehigh University. The experimental techniques used in this work are discussed in Chapter 4, which includes discussions concerning the determination of the alkali vapor pressures and densities, and of laser-induced fluorescence (LIF), which is the primary experimental method used in this work. An extensive discussion of the empirical model used to analyze our data is outlined in Chapter 5, along with a description of the error analysis. Chapter 6 includes a presentation of the results of the experiment for both rotation (J)-changing and vibration, rotation(v, J)-changing collisions of NaK with Ar, He, and K perturbers. This chapter also discusses how the breakdown of several assumptions and approximations used in our analysis can be taken into account after the fact. Chapter 7 then summarizes these results and presents possible future work.

Chapter 2

Molecular Physics Background

2.1 Overview

In this chapter, I give a summary of how the diatomic molecule is treated quantum mechanically. This treatment begins with the time-independent Schrödinger equation (TISE). We begin in Sec. 2.2 by separating the TISE into electronic and nuclear portions utilizing the Born-Oppenheimer approximation. This allows for a simplification, based on the relative speeds of the nuclei and electrons, such that the electrons move in the field of the nuclei, which are considered frozen at fixed separations. In Section 2.3 I discuss the nuclear vibrational and rotational motion, as well as higher order effects due to these motions that must also be included in the calculations. I then briefly discuss the most common Hund's cases in Sec. 2.4, which provide a vector representation of the relative strengths of the electric and magnetic interactions within the molecule. I close the chapter with a discussion of electronic transitions and selection rules in Sec. 2.5.

2.2 The Born-Oppenheimer Approximation

When we look at the diatomic molecule, we know two things about the molecular system: the molecule vibrates, changing the distance between the two nuclei, and the molecule also rotates about the center of mass of the system. Even though the diatomic molecule is the simplest molecular form there is, the quantum mechanical treatment of the diatomic molecule is already quite complicated. We begin our solution of the time-independent Schrödinger equation (TISE) by defining the position vectors of the electrons and nuclei, as seen in Fig. 2.1. Here A and B are the two nuclei, and $\vec{R}_A$ and $\vec{R}_B$ describe the location of these nuclei with respect to their center of mass (CoM). The $\vec{r}_1$, $\vec{r}_2$,..., $\vec{r}_n$ represent the locations of electrons 1, 2, ..., n with respect to the CoM.

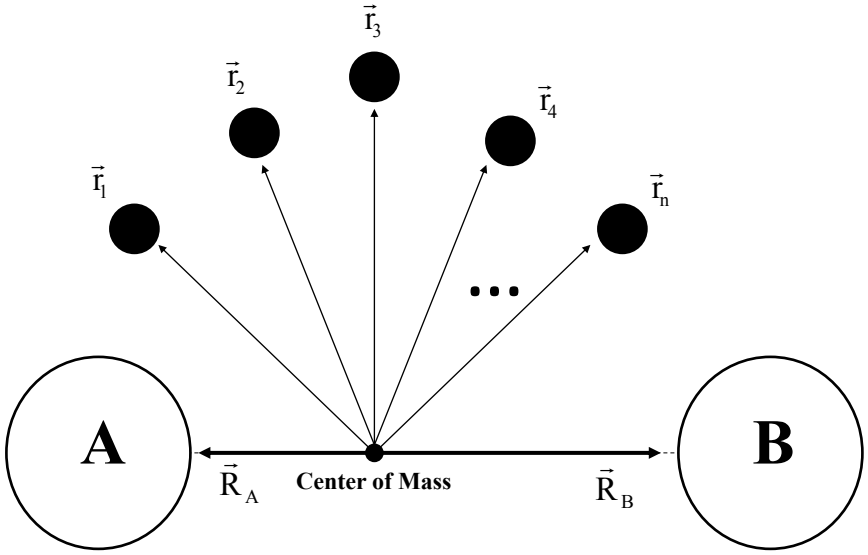

Figure 2.1: The coordinate system used in treating the diatomic molecule.

We begin consideration of the molecular TISE

$$\hat{H}\Psi = E\Psi, \tag{2.1}$$

where the Hamiltonian contains both nuclear ($\hat{T}_N$) and electronic ($\hat{T}_E$) kinetic energy terms, as well as Coulomb interaction potential energy terms (V):

$$(\hat{T}_N + \hat{T}_E + V)\Psi(\vec{R}, \vec{r}_1, \vec{r}_2, ..., \vec{r}_n) = E\Psi(\vec{R}, \vec{r}_1, \vec{r}_2, ..., \vec{r}_n). \tag{2.2}$$

Here $\vec{R} \equiv \vec{R}_A - \vec{R}_B$ is the internuclear separation vector. The term describing the motion of the two nuclei, $\hat{T}_N$, can be translated into the CoM reference frame as

$$\hat{T}_N = \frac{-\hbar^2}{2\mu}\nabla_R^2, \tag{2.3}$$

where μ is the reduced nuclear mass $\frac{M_A M_B}{M_A + M_B}$. We also include the kinetic energy for all electrons in the system $\hat{T}_E$ (m_e is the electron mass), as

$$\hat{T}_E = \sum_{i=1}^{n} \left(\frac{-\hbar^2}{2m_e} \nabla_{r_i}^2 \right). \tag{2.4}$$

Since the electrons and nuclei all carry charges, the potential energy term V includes electron-electron and nucleus-nucleus repulsion terms, as well as nucleus-electron attraction terms:

$$\begin{aligned} V &= V_{\mathrm{N-N}} + V_{\mathrm{e-e}} + V_{\mathrm{N-e}} \\ &= \frac{Z_A Z_B e^2}{4\pi\epsilon_0 R} + \sum_{i>j}^{n} \frac{e^2}{4\pi\epsilon_0} \frac{1}{|\vec{r}_i - \vec{r}_j|} - \sum_{i=1}^{n} \frac{Z_A e^2}{4\pi\epsilon_0 |\vec{r}_i - \vec{R}_A|} - \sum_{i=1}^{n} \frac{Z_B e^2}{4\pi\epsilon_0 |\vec{r}_i - \vec{R}_B|}. \end{aligned} \tag{2.5}$$

The solution of the time-independent Schrödinger equation, with a Hamiltonian consisting of all the kinetic and potential energy terms, would be quite complicated. To simplify this, we can exploit the fact that the nuclei are significantly heavier than the electrons, and therefore the electrons move much faster than the nuclei. This means, if the distance $R = |\vec{R}|$ between the two nuclei does change, the electrons readjust to this change almost instantaneously. We can fix the internuclear separation R at a given value and first solve the electronic portion of the TISE:

$$[T_E + V]\,\phi_q(\vec{R}, \vec{r}_1, \vec{r}_2, ..., \vec{r}_n) = E_q \phi_q(\vec{R}, \vec{r}_1, ..., \vec{r}_n). \tag{2.6}$$

The total wavefunction $\Psi(\vec{R}, \vec{r}_1, \vec{r}_2, ..., \vec{r}_n)$ can be expanded in terms of these electronic wavefunctions $\phi_q(\vec{R}, \vec{r}_1, \vec{r}_2, ..., \vec{r}_n)$ which form a complete set of functions over the electronic coordinates. Since the potential energy terms depend on $\vec{R}$, the electronic wavefunctions $\phi_q(\vec{R}, \vec{r}_1, \vec{r}_2, ..., \vec{r}_n)$ depend on $\vec{R}$ parametrically and the expansion coefficients depend on $\vec{R}$; i.e.,

$$\Psi(\vec{R}, \vec{r}_1, \vec{r}_2, ..., \vec{r}_n) = \sum_q F_q(\vec{R}) \phi_q(\vec{R}, \vec{r}_1 ... \vec{r}_n). \tag{2.7}$$

The electronic wavefunctions ϕ_q are ortho-normal

$$\int \mathrm{d}r_1 ... \mathrm{d}r_n \phi_p^*(\vec{R}, \vec{r}_1 ... \vec{r}_n) \phi_q(\vec{R}, \vec{r}_1 ... \vec{r}_n) = \delta_{pq}. \tag{2.8}$$

If we substitute Eq. 2.7 into Eq. 2.2 and rearrange slightly, we find

$$\left[\hat{T}_N + \hat{T}_E + V - E\right] \left(\sum_q F_q(\vec{R}) \phi_q(\vec{R}, \vec{r}_1 ... \vec{r}_n) \right) = 0. \tag{2.9}$$

We can then multiply this expression on the left by $\phi_p^*(\vec{R}, \vec{r}_1 ... \vec{r}_n)$, integrate over electron coordinates, and use

$$\left[\hat{T}_E + V\right] \left(\sum_q F_q(\vec{R}) \phi_q(\vec{R}, \vec{r}_1 ... \vec{r}_n) \right) = \sum_q E_q F_q(\vec{R}) \phi_q(\vec{R}, \vec{r}_1 ... \vec{r}_n) \tag{2.10}$$

to write

$$\int \mathrm{d}r_1 ... \mathrm{d}r_n \phi_p^*(\vec{R}, \vec{r}_1 ... \vec{r}_n) \hat{T}_N \sum_q F_q(\vec{R}) \phi_q(\vec{R}, \vec{r}_1 ... \vec{r}_n)$$
$$= \left[E - E_p(\vec{R})\right] F_p(\vec{R}). \tag{2.11}$$

Since both $F_q(\vec{R})$ and $\phi_q(\vec{R}, \vec{r}_1, \vec{r}_2, ..., \vec{r}_n)$ depend on $\vec{R}$, the nuclear kinetic energy term $\hat{T}_N \sum_q F_q(\vec{R}) \phi_q(\vec{R}, \vec{r}_1 ... \vec{r}_n)$ is fairly complicated. The identity

$$\nabla^2(fg) = f\nabla^2 g + 2\nabla f \cdot \nabla g + g\nabla^2 f \tag{2.12}$$

allows us to write

$$\begin{aligned} \hat{T}_N \sum_q F_q \phi_q &= \frac{-\hbar^2}{2\mu} \nabla_R^2 \left(\sum_q F_q \phi_q \right) \\ &= \frac{-\hbar^2}{2\mu} \sum_q \left[F_q \nabla_R^2 \phi_q + 2\nabla_R F_q \cdot \nabla_R \phi_q + \phi_q \nabla_R^2 F_q \right]. \end{aligned} \tag{2.13}$$

It is common at this point to invoke the Born-Oppenheimer approximation. This approximation assumes that the electron wavefunctions depend only weakly on $\vec{R}$, and therefore

$$|\nabla_R F_q(\vec{R})| \gg |\nabla_R \phi_q(\vec{R}; \vec{r}_1 ... \vec{r}_n)|. \tag{2.14}$$

This allows us to neglect the $F_q\nabla_R^2\phi_q + 2\nabla_R F_q \cdot \nabla_R\phi_q$ terms in Eq. 2.13, leaving a simplified version of Eq. 2.11:

$$\sum_q \int \mathrm{d}r_1 ... \mathrm{d}r_n \phi_p^* \left[\frac{-\hbar^2}{2\mu}\nabla_R^2 F_q\right]\phi_q = \frac{-\hbar^2}{2\mu}\nabla_R^2 F_p(\vec{R}). \tag{2.15}$$

Here, the orthonormality of the electronic wavefunctions ϕ_q collapses the sum to a single term, and Eq. 2.15 reduces to

$$\frac{-\hbar^2}{2\mu}\nabla_R^2 F_p(\vec{R}) + \left[E_p(\vec{R}) - E\right] F_p(\vec{R}) = 0, \tag{2.16}$$

which is a Schrödinger equation for the nuclei moving in a "potential" $E_p(\vec{R})$. Note that this potential energy in the nuclear equation is the energy eigenvalue from the electronic Schrödinger equation. Further separation of the nuclear equation into radial and angular terms is now possible, as shown in Sec. 2.3.

2.3 Motion of Nuclei

2.3.1 Vibration and Rotation

In addition to the motion of the electrons, the diatomic molecule also can vibrate and rotate about it's center of mass. As previously mentioned in the Born-Oppenheimer approximation, the electronic eigenvalues act as potential energy terms in the nuclear equation. The solution of the nuclear equation (Eq. 2.16) with this electronic potential determines the energies of the many vibrational and rotational levels allowed for a given electronic potential.

The nuclear wavefunction, $F_p(\vec{R})$, introduced in Sec. 2.2, can be split into a radial (vibrational) term $\chi(R)$ and an angular (rotational) term $\psi(\theta, \phi)$ using the technique of separation of variables:

$$F_p(\vec{R}) = \frac{1}{R}\chi_{p,v}(R)\psi_{p,J}(\theta, \phi). \tag{2.17}$$

To carry out this procedure, we expand the nuclear kinetic energy term in Eq. 2.16 in spherical coordinates as

$$\begin{aligned}\nabla_R^2\left[\frac{1}{R}\chi_{p,v}(R)\psi_{p,J}(\theta,\phi)\right] = {} & \frac{\psi_{p,J}(\theta,\phi)}{R}\frac{d^2}{dR^2}\chi_{p,v}(R) \\ & + \frac{\chi_{p,v}(R)}{R^3}\left[\frac{1}{\sin\theta}\frac{\partial}{\partial\theta}\left(\sin\theta\frac{\partial\psi_{p,J}(\theta,\phi)}{\partial\theta}\right)\right. \\ & \left. + \frac{1}{\sin^2\theta}\frac{\partial^2\psi_{p,J}(\theta,\phi)}{\partial\phi^2}\right]. \end{aligned} \tag{2.18}$$

At this point, we consider $E_p(\vec{R}) \approx E_p(R)$. Inserting Eq. 2.18 into the nuclear Schrödinger equation (2.16), and multiplying through by $\frac{-2\mu}{\hbar^2}\frac{R^3}{\chi\psi}$, we obtain

$$\frac{R^2}{\chi}\frac{d^2\chi}{dR^2} - \frac{2\mu R^2}{\hbar^2}[E_p(R) - E] = \frac{-1}{\psi}\left[\frac{1}{\sin\theta}\frac{\partial}{\partial\theta}\left(\sin\theta\frac{\partial\psi}{\partial\theta}\right) + \frac{1}{\sin^2\theta}\frac{\partial^2\psi}{\partial\phi^2}\right]. \tag{2.19}$$

The equation is now separated. The left hand side only depends on R and the right hand side only on θ and ϕ, so both sides must be a constant which we call $J(J+1)$. Setting the right hand side equal to this constant yields

$$\frac{1}{\sin\theta}\frac{\partial}{\partial\theta}\left[\left(\sin\theta\frac{\partial\psi}{\partial\theta}\right) + \frac{1}{\sin^2\theta}\frac{\partial^2\psi}{\partial\phi^2}\right] + J(J+1)\psi = 0. \tag{2.20}$$

The eigenfunction solutions of this last equation are the spherical harmonics $\psi =$

$Y_{JM_J}(\theta, \phi)$.

If we return to Eq. 2.19 and set the left hand side equal to $J(J+1)$, we find

$$\frac{-\hbar^2}{2\mu}\frac{d^2}{dR^2}\chi_{p,v}(R) + \left[E_p(R) + \frac{J(J+1)\hbar^2}{2\mu R^2} - E_{p,v,J}\right]\chi_{p,v} = 0, \tag{2.21}$$

which is just the one-dimensional Schrödinger equation for a particle of mass μ, moving in an effective potential

$$V_{\text{eff}}(R) = E_p(R) + \frac{J(J+1)\hbar^2}{2\mu R^2}. \tag{2.22}$$

The first term in Eq. 2.22 represents the electronic potential $E_p(R) = V(R)$, while the second is the centrifugal potential term. Equation 2.21 can be solved numerically for any potential of the form (2.22). The various radial solutions $\chi_{p,v}(R)$ are labeled by the quantum number v (for vibration), which represents the number of nodes in the radial wavefunction $\chi_{p,v}(R)$.

2.3.2 The Rigid Rotor Approximation

In general, we can write the total energy of the molecule as the sum of three energy terms: electronic, vibrational, and rotational.

$$E = E_{el} + E_{vib} + E_{rot}. \tag{2.23}$$

Since the molecule vibrates about an equilibrium separation R_0, a good first order approximation to the rotational energy is given by

$$E_r = \frac{\hbar^2}{2\mu R_0^2}J(J+1) \equiv B_e J(J+1) \tag{2.24}$$

where B_e is the rotational constant $B_e = \frac{\hbar^2}{2I}$, and I is the moment of inertia $I = \mu R_0^2$ of a mass μ rotating about a fixed center at orbital radius R_0. This is the rigid rotor approximation.

2.3.3 The Harmonic Oscillator Approximation

If we consider a molecule in a bound state, near the minimum of the effective potential (i.e. a low lying vibrational level), the the average position of the nuclei is close to the equilibrium separation R_0. The potential energy curve near the minimum can be expanded in a Taylor expansion about $R = R_0$ as

$$V(R) = V(R_0) + (R - R_0)\left.\frac{dV(R)}{dR}\right|_{R=R_0} + \frac{(R-R_0)^2}{2!}\left.\frac{d^2V(R)}{dR^2}\right|_{R=R_0} + ... \quad (2.25)$$

The first term, $V(R_0)$, signifies the minimum of the potential well, and is a constant energy offset, while the first derivative, when evaluated at the minimum, is equal to zero. If we then ignore the terms beyond the second derivative, we find a simple harmonic oscillator potential,

$$V(R) \approx V(R_0) + \frac{1}{2}k(R - R_0)^2, \quad (2.26)$$

with a spring constant $k = \left.\frac{d^2V(R)}{dR^2}\right|_{R=R_0}$. The vibrational energy levels associated with this first order approximation are given by

$$E_v = V(R_0) + \hbar\omega_0(v + \frac{1}{2}), \quad (2.27)$$

where each vibrational level is characterized by the quantum number $v = 0, 1, 2,...$, with the oscillation frequency $\omega_0 = \sqrt{\frac{k}{\mu}}$. The rigid rotor and harmonic oscillator solutions are good as first approximations, but higher order effects need to be considered to accurately describe the energy levels of the molecule.

2.3.4 Higher Order Effects

As the energy of the system increases, the range of radial motion increases to the point where the harmonic oscillator approximation breaks down. A typical electronic potential is shown in Fig. 2.2 where it can be seen that it is more repulsive than a harmonic oscillator at small R and less repulsive at large R (where it must asymptotically approach the molecular dissociation limit). Thus the potential becomes progressively more anharmonic as energy increases.

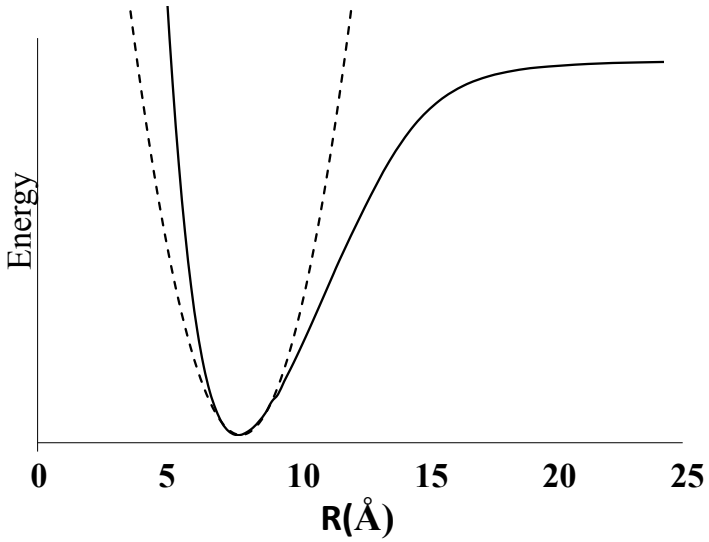

Figure 2.2: Comparison of a harmonic oscillator (dashed line) and the $2(A)^1\Sigma^+$ electronic potential for NaK (solid line), where a relative shift has been made so that the two potentials have the same equalibrium separation R_0 and minimum T_e.

A better approximation to a real potential is the Morse potential,

$$V(R) = D_e \left[1 - e^{\alpha(R-R_0)}\right]^2, \tag{2.28}$$

where α and D_e are constants. D_e represents the well depth $E_p(\infty) - E_p(R_0)$. When the Morse potential is substituted into Eq. 2.21 with $J = 0$, the vibrational energies are given exactly by

$$E_v = \omega_e(v + \frac{1}{2}) - \omega_e x_e (v + \frac{1}{2})^2. \tag{2.29}$$

Here the second term in Eq. 2.29 represents the anharmonicity, and $\omega_e x_e$ is the anharmonicity constant. In this expression, one can show [36] that

$$\omega_e = \sqrt{\frac{\hbar D_e}{\pi c \mu}}\beta \tag{2.30}$$

and

$$\omega_e x_e = \frac{\omega_e^2}{4D_e}, \tag{2.31}$$

for ω_e, $\omega_e x_e$ and D_e all measured in wavenumbers (cm^{-1}). Figure 2.3 shows a comparison of a Morse potential to a harmonic oscillator, both with minima at T_e. Figure 2.4 shows a comparison of the vibrational energies calculated using a Morse potential with those for a harmonic oscillator potential.

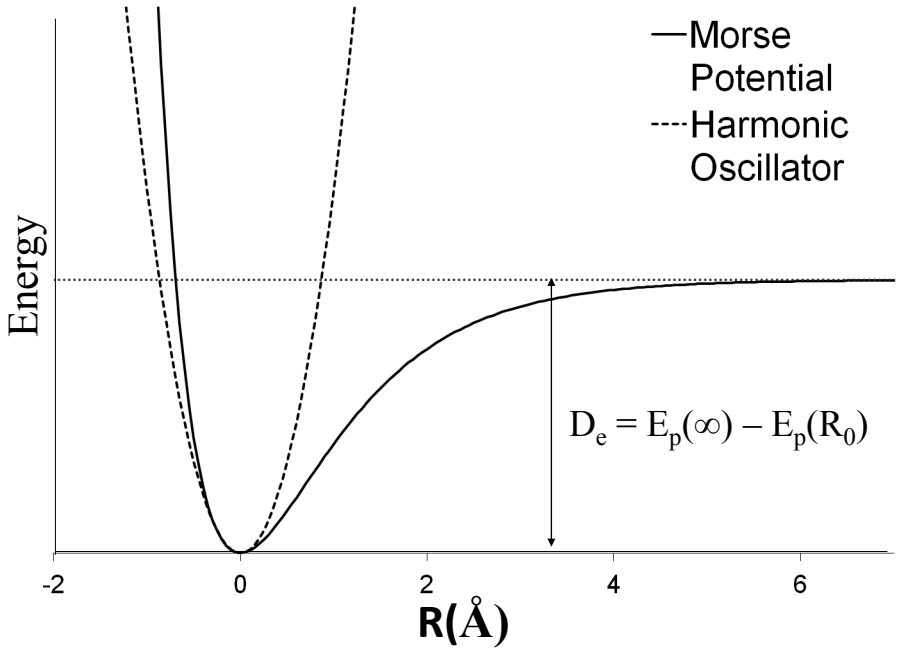

Figure 2.3: Comparison of a Morse potential with a harmonic oscillator potential. Note the similarity of the Morse potential to the actual $2(A)^1\Sigma^+$ state potential shown in Fig. 2.2. The well depth of the Morse potential, D_e, is also indicated.

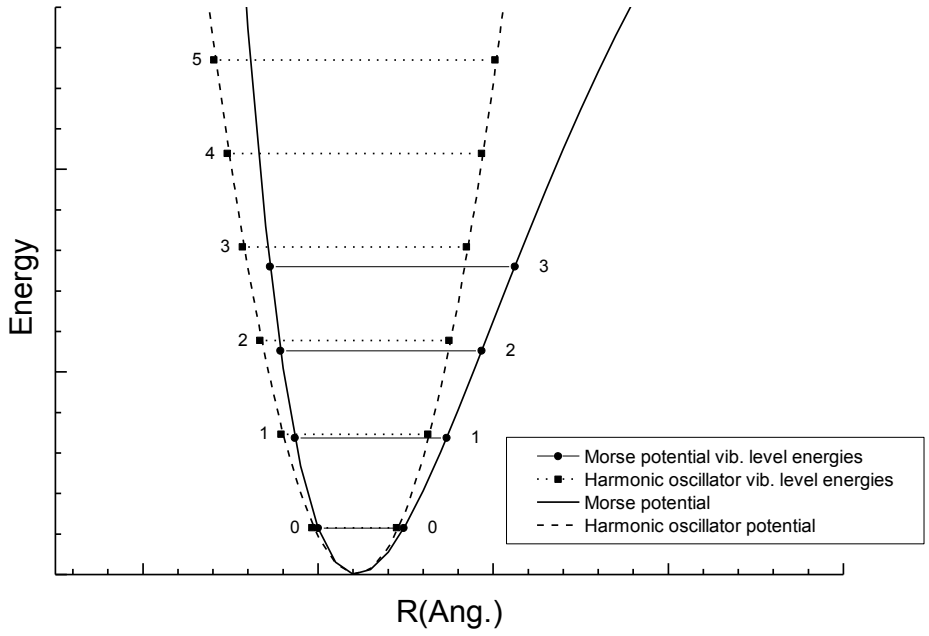

Figure 2.4: Comparison of the vibrational levels of a harmonic oscillator with those of a Morse potential for $\omega_e = \omega_0$. The separation between the vibrational level energies associated with the Morse potential, $\Delta E_v = \omega_e - 2\omega_e x_e(v + \frac{1}{2})$ are smaller than for the harmonic oscillator potential $\Delta E_v = \omega_0$. Consequently the energy discrepancies increase with v.

Although the Morse potential is a good approximation to real potentials, it's still an approximation. Thus we can include additional terms in the expansion of Eq. 2.29 to obtain an even more accurate representation of the energy levels of the molecule; i.e.,

$$E_v = G_v = \omega_e(v + \frac{1}{2}) - \omega_e x_e(v + \frac{1}{2})^2 + \omega_e y_e(v + \frac{1}{2})^3 + ..., \tag{2.32}$$

but when more terms are added it becomes harder to associate physical interpretations with these additional correction terms, and they are usually just considered

fitting parameters.

In addition to the anharmonicity in the potential, additional corrections are needed because rotation also causes the molecule to stretch due to the centrifugal force. Since the effective equilibrium separation (the minimum of the effective potential $V_{\text{eff}}(R)$ in Eq. 2.22) increases with increasing rotation, the rotational energy is reduced relative to Eq. 2.24. The first order correction to Eq. 2.24 is given by

$$E_r = B_e J(J+1) - D_v[J(J+1)]^2, \tag{2.33}$$

where D_v is called the centrifugal distortion constant. The last term in Eq. 2.33, is the centrifugal distortion term, which reduces the spacings between levels of large J relative to those of a rigid rotor.

Up to this point, we have been dealing with the vibrational and rotational motions separately. However, a more accurate model of a diatomic molecule is the vibrating rotor, which couples the vibrational and rotational motion. Specifically, the fact that the potential is slightly anharmonic means that the equilibrium internuclear separation (and therefore the moment of inertia) increases as the molecular vibration increases, and this, in turn, decreases the effective rotational constant. This is usually expressed as expansions of the rotational and centrifugal distortion constants in powers of $(v + \frac{1}{2})$. Thus we obtain slightly different rotational coefficients for each vibrational state:

$$B_v = B_e - \alpha_e \left(v + \frac{1}{2}\right) + \gamma_{e1} \left(v + \frac{1}{2}\right)^2 + \gamma_{e2} \left(v + \frac{1}{2}\right)^3 + ... \tag{2.34}$$

and

$$D_v = D_e + \beta_{e1}\left(v+\frac{1}{2}\right) + \beta_{e2}\left(v+\frac{1}{2}\right)^2 + \beta_{e3}\left(v+\frac{1}{2}\right)^3 + ... \tag{2.35}$$

Finally we combine the electronic, vibrational, and rotational energies (in descending order of contribution) in Eq. 2.23 to obtain

$$E(v,J) = E_{el} + E_v + E_r = T_e + G_v + F_v(J) \tag{2.36}$$

with

$$G_v = \omega_e(v+\frac{1}{2}) - \omega_e x_e(v+\frac{1}{2})^2 + \omega_e y_e(v+\frac{1}{2})^3 + ... \tag{2.37}$$

and

$$F_v(J) = B_v J(J+1) - D_v[J(J+1)]^2 + ... \tag{2.38}$$

Dunham [37] developed a concise way to represent Eq. 2.36, as

$$E_{p,v,J} = \sum_{i,k} Y_{i,k}\left(v+\frac{1}{2}\right)^i \left[J(J+1)-\Omega^2\right]^k \tag{2.39}$$

where the constant vector $\mathbf{\Omega} = \mathbf{\Lambda} + \mathbf{\Sigma}$, and will be discussed briefly in the next section. The constants associated with the Dunham expansion can be determined spectroscopically, and are used to reproduce ro-vibrational level energies. Table 2.1 lists the relationship between some of the lowest order Dunham coefficients $Y_{i,k}$ and the physical (spectroscopic) constants that are usually listed in older publications.

$Y_{ik} =$

$i \diagdown k$	0	1	2
0	T_e	B_e	$-D_e$
1	ω_e	$-\alpha_e$	$-\beta_{e1}$
2	$-\omega_e x_e$	γ_{e1}	$-\beta_{e2}$
3	$\omega_e y_e$	γ_{e2}	$-\beta_{e3}$

Table 2.1: The spectroscopic constants and the corresponding Dunham coefficients $Y_{i,k}$.

2.4 Hund's Cases

The Hund's cases consider the different ways the various internal molecular angular momenta vectors can couple due to the electric and magnetic interactions. In all cases, we must take into account four angular momentum vectors; the electron orbital angular momentum **L**, the electron spin angular momentum **S**, the nuclear orbital angular momentum **N**, and the nuclear spin angular momenta **I**, all of which can couple to each other as well as to the internuclear axis. While each angular momentum vector interacts with every other angular momentum vector via magnetic dipole interactions in the molecule, the Hund's cases allow for a simplified method of taking the various interactions into account based on the relative strengths of these interactions. Fortunately some interactions are sufficiently weak that they can be neglected entirely.

Equation 2.40 describes the molecular Hamiltonian including the most important of these interactions involving the angular momentum vectors [38],

$$\begin{aligned} \hat{H} &= \hat{H}_{\text{el}} + \hat{H}_{\text{vib}} + \hat{H}_{\text{rot}} + \hat{H}_{SO} + \hat{H}_{HFS} + \hat{H}_{SR} + ... \\ &\approx \hat{H}_0 + \hat{H}_{SO} + \hat{H}_{HFS} + \hat{H}_{SR} \end{aligned} \tag{2.40}$$

or

$$\hat{H} = \hat{H}_0 + A\mathrm{L} \bullet \mathrm{S} + \mathrm{bI} \bullet \mathrm{S} + \gamma \mathrm{N} \bullet \mathrm{S}. \tag{2.41}$$

Here the first term, $\hat{H}_0$, includes the previously discussed electronic, vibrational, and rotational energy terms, but typically neglects the parts of the kinetic energy that were dropped when the Born-Oppenheimer approximation was invoked. The second term ($A\mathbf{L}\bullet\mathbf{S}$) describes the spin-orbit interaction, while the third term (b$\mathbf{I}\bullet$ $\mathbf{S}$) describes the Fermi-contact portion of the hyperfine interaction (which is the dominant hyperfine interaction in all diatomic alkali molecules). The final interaction term here (spin-rotation) is significantly smaller than the other terms, but should ideally be included as well. As previously mentioned, there are several other terms that are even smaller (including the electron spin-spin interactions, but they are neglected here.

The various coupling schemes are described by the Hund's cases. Hund's cases (a), (b) and (c) are the most common and will be discussed in moderate detail here; further information can be found in [36] and [38].

The three main Hund's cases [(a), (b), and (c)] are distinguished first by the strengths of the interactions between $\mathbf{L}$, $\mathbf{S}$, and the internuclear axis. In case (a) and case (b), the electron orbital angular momentum $\mathbf{L}$ is strongly coupled to the electric field along the internuclear axis. Cases (a), (b) and (c) are further distinguished by the strength of the spin-orbit interaction relative to other interactions.

2.4.1 Hund's Case (a)

Case (a) is valid when the strongest of the angular momentum coupling terms is the interaction of **L** with the strong internuclear electric field. This causes the vector **L** to precess about the internuclear axis (dotted ellipse shown in Fig. 2.5) with a constant projection Λ along the axis. Although **L** does not correspond to a "good quantum number", its projection along the internuclear axis (Λ) can be taken to be a constant of the motion and is usually used to label the molecular states using Greek symbols as given in Table 2.2. Note that the Greek labels for Λ are chosen analogously to the Roman symbols for values of the quantum number L, used in atomic physics. In Hund's case (a), the next interaction that must be

L	Atomic State	Λ	Molecule State
0	S	0	Σ
1	P	1	Π
2	D	2	Δ
3	F	3	Φ

Table 2.2: Values of Λ and the corresponding molecular labels. The analogous atomic labels for the quantum number L are also given.

considered is the spin-orbit interaction. The precession of **L** around the internuclear axis is sufficiently fast that, on average, only the component Λ survives. Therefore, because of the **L•S** interaction, **S** also precesses rapidly about the internuclear axis, and we need only consider its component Σ along the axis. Note that the use of Σ as the component of **S** along the internuclear axis should not be confused with the label for states with $\Lambda = 0$. **L**, **S** and their components Λ and Σ are depicted in Fig. 2.5 where it can be seen that a vector $\mathbf{\Omega}$ of length $\Lambda + \Sigma$ can also be defined.

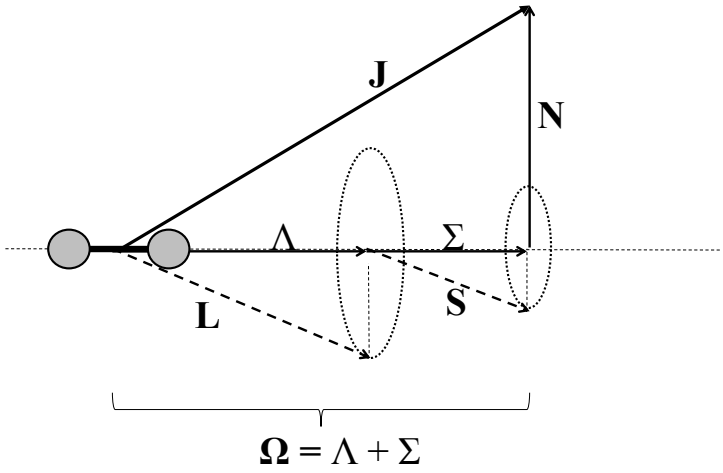

Figure 2.5: Vector diagram of Hund's case (a). The ellipses on the diagram show the precession of the vectors.

In case (a) the final interaction to consider is the coupling of $\mathbf{\Omega}$ with the nuclear orbital angular momentum $\mathbf{N}$ to create the total angular momentum $\mathbf{J}$ (i.e. $\mathbf{\Omega}$ and $\mathbf{N}$ both precess slowly about $\mathbf{J}$). Case (a) is more common in lower rotational levels and in heavier molecules. A good rule of thumb is obtained by calculating the ratio $\frac{A}{B_\upsilon J}$, where A is the spin-orbit constant and B_υ is the rotational constant. When this ratio is greater than 1, Hund's case (a) is usually a good approximation, unless the spin-orbit interaction is so strong that case (c) is valid (see Sec. 2.4.5). If $\frac{A}{B_\upsilon J}$ is much less than 1, the state is usually well described by case (b).

2.4.2 Hund's Case (b)

Hund's case (b) is used for cases where the electron spin is either weakly coupled to the internuclear axis or not coupled to it at all. Σ, the component of electron spin along the internuclear axis, is no longer a good quantum number, but this does

not necessarily mean that S=0. Since the spin-orbit interaction is very weak for molecules in states that can be described by Hund's case (b), Λ first couples to **N** to form the intermediate vector $\mathbf{K} = \Lambda + \mathbf{N}$. The electron spin **S** then couples to **K** to form **J** [$\mathbf{J} = \mathbf{S} + \mathbf{K}$]. Figure 2.6 shows the Hund's case (b) vector coupling diagram.

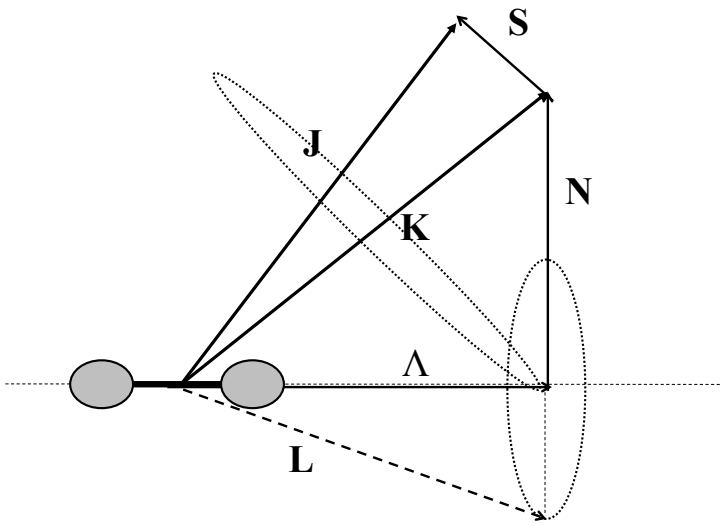

Figure 2.6: Vector diagram showing the Hund's case (b) coupling scheme, including the ellipse depicting the precession of **Λ** and **N** about **K**.

2.4.3 Notation

In both cases (a) and (b), Λ and S are good quantum numbers [Σ and Ω are also good quantum numbers for case (a)]. This is the basis for the most common notation used to describe molecular states, which is also the one that is used throughout this dissertation to describe the states of alkali diatomic molecules. States are labeled using the format $n^{2S+1}\Lambda_{\Omega}(v, J)$. Here n is the number corresponding to the ordering of states of a particular symmetry, with n=1 representing the lowest energy state

of that symmetry. In an alkali molecule, there are two free valence electrons, each with spin $s_1 = s_2 = \frac{1}{2}$. Thus the total electron spin is given by $\mathbf{S} = \sum_i \mathbf{s}_i$ and the corresponding quantum number S can only take on two values; either $S = 0$ for electron spins in an anti-parallel orientation, or $S = 1$ if the electron spins are parallel. These values correspond to spin multiplicities, $(2S + 1)$ of one (singlet states) or three (triplet states).

In addition to the Λ and multiplicity labels, case (a) and case (b) electronic states with $\Lambda = 0$ (Σ states) also carry a superscript $^-$ or $^+$ label (i.e. Σ^- or Σ^+), depending on whether the wavefunction changes sign or not when the electron coordinates are reflected through a plane running through the two nuclei. Finally, we also use the previously discussed vibration and rotation quantum numbers, v and J, to describe the ro-vibrational level within the electronic state $n^{2S+1}\Lambda$.

In case (a) and case (b) [as well as case (c)], the vector $\mathbf{J}$ represents the total angular momentum sans the nuclear spin. The corresponding quantum number is J, which is generally called the rotational quantum number. Note that this notation is used for all states of the NaK molecule, all of which typically follow case (a) or case (b) coupling (or something intermediate between the two).

2.4.4 Hyperfine Structure

When the nuclear spin vector is included, cases (a) and (b) are further broken down into sub cases α and β based on whether or not $\mathbf{I}$ couples strongly to the internuclear axis. In case a_α, $\mathbf{I}$ couples strongly to the internuclear axis, so $\Omega = \Lambda + \Sigma + I_z$ and $\mathbf{J} = \Omega + \mathbf{N}$ is still valid. In case a_β, $\mathbf{\Omega}$ and $\mathbf{J}$ are as shown in Fig.

2.5, then **I** couples to **J** to form the total angular momentum **F**, where $\mathbf{F} = \mathbf{J} + \mathbf{I}$.

In case (b) it turns out that case b_α doesn't occur because if **S** is not coupled to the internuclear axis then it is unlikely that **I** would couple to the axis. However, in case b_β there are two different coupling schemes, $b_{\beta J}$ and $b_{\beta S}$, that must be considered. In case $b_{\beta J}$, **S** first interacts with **K** to form **J**, and then **J** interacts with **I** to form **F**. This hyperfine coupling scheme is shown in Fig. 2.7 (A). In case $b_{\beta S}$, **S** interacts most strongly with **I**, creating the intermediate vector **G**, and then $\mathbf{F} = \mathbf{K} + \mathbf{G}$. The case $b_{\beta S}$ coupling scheme is shown in Fig. 2.7 (B). a_β, $b_{\beta J}$ and $b_{\beta S}$ hyperfine coupling schemes are common in the alkali diatomics, and have been observed in many laboratories for Li_2 [39, 40], Na_2 [41, 42, 43], K_2 [44, 45] and NaK [15, 16, 17, 19, 46].

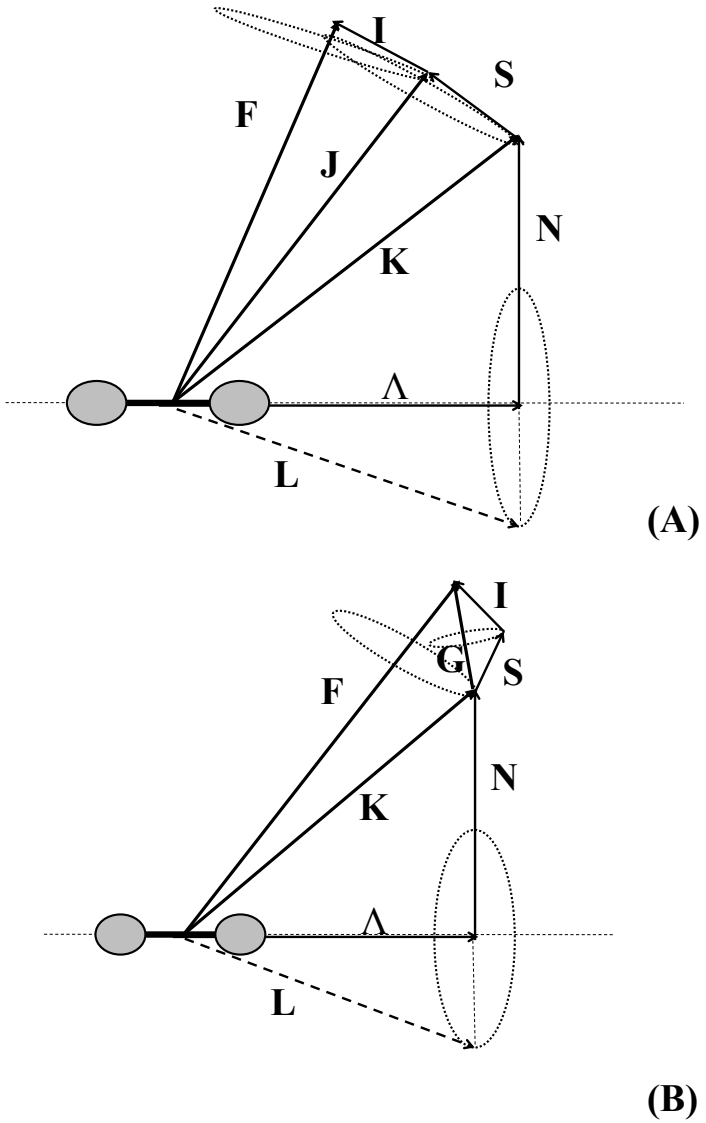

Figure 2.7: Vector coupling diagrams of the two most common hyperfine interaction schemes in Hund's case (b). The first diagram (panel A) shows case $b_{\beta J}$, while the second (panel B) shows case $b_{\beta S}$.

2.4.5 Hund's Case (c)

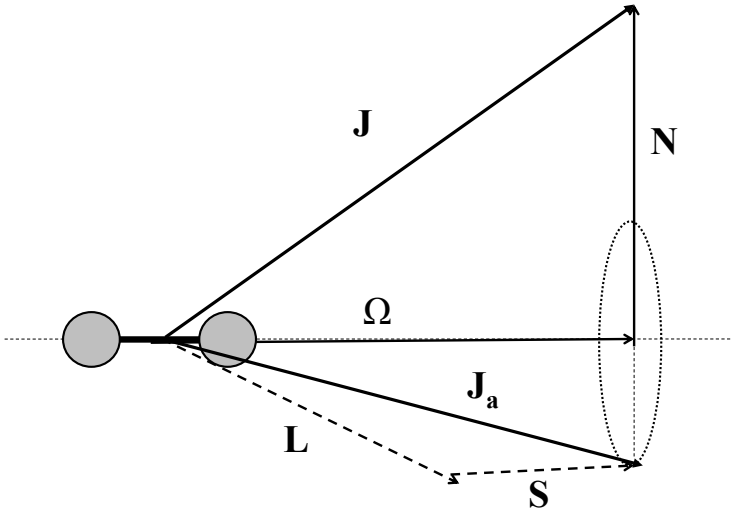

Figure 2.8: Vector diagram of Hund's case (c). Vectors **L** and **S** precess about $\mathbf{J}_a$, which has component Ω along the internuclear axis. Ω then interacts with **N** to create **J**.

In Hund's case (c), the interaction between **L** and **S** is stronger than the interaction of either one with the internuclear axis (see Fig. 2.8). Consequently, we first form the vector $\mathbf{J}_a$ [$\mathbf{J}_a = \mathbf{L} + \mathbf{S}$], and then $\mathbf{J}_a$ couples with the internuclear axis. Ω is the component of $\mathbf{J}_a$ along the axis. In states that follow case (c), Λ and Σ are not good quantum numbers while Ω is. Therefore the labeling convention of cases (a) and (b) is not really valid. Instead, we use the notation $n\Omega^{+/-}$, where again n denotes the ordering in energy of the electronic states of a given symmetry (1 being lowest), and the +/- symmetry of the wavefunction for $\Omega = 0$ states is denoted by a superscript (for these $\Omega = 0$ states only).

2.5 Electronic Transitions

Discrete energy differences occur between specific ro-vibrational levels of a lower electronic state and ro-vibrational levels of a higher electronic state. When a molecule in level v_m, J_m of the lower state is subjected to an electromagnetic wave, and a photon with energy equal to this energy difference ($\Delta E = h\nu_{nm}$) encounters the molecule, the photon may be absorbed. This absorption causes the molecule to make a transition to level v_n, J_n of the higher electronic state. In other instances, the excited molecule can emit a photon, making a downward transition instead. Following Refs. [36] and [38], the intensity of a spectral line in emission, in terms of the energy emitted per second by a source, is

$$I_{\text{em.}}^{nm} = N_n h\nu_{nm} A_{nm}, \tag{2.42}$$

where $h\nu_{nm}$ is the energy of a single photon being emitted at line center ν_{nm}. N_n is the number of atoms or molecules in the initial state, and A_{nm} represents the rate at which these excited atoms or molecules make radiative transitions from level n to level m. A_{nm} is called the Einstein coefficient of spontaneous emission, or the Einstein A coefficient, and is given by

$$A_{nm} = \frac{8\pi^2 \nu_{nm}^3}{3\varepsilon_0 \hbar c^3} |\mathbf{R}^{nm}|^2, \tag{2.43}$$

where $\mathbf{R}^{nm}$ is the transition dipole moment

$$\mathbf{R}^{nm} = \frac{S_{J_n,J_m}}{2J_n+1}\int \chi_n^{v*}(R)\chi_m^{v}(R)dR \times \int \phi_n^{el*}(\vec{R},\vec{r_1}...\vec{r_n})\hat{\mu_{el}}\phi_m^{el}(\vec{R},\vec{r_1}...\vec{r_n})d^3r_1...d^3r_n \quad (2.44)$$

and $\hat{\mu_{el}} = -\sum_i e\vec{r_i}$ is the electric dipole operator. In this last expression, we separated the total wavefunction into the electronic and nuclear wavefunctions as in Eq. 2.7, and further separated the nuclear wavefunctions into radial and angular terms according to Eq. 2.17. The Hönl-London factors, S_{J_n,J_m}, divided by $(2J_n + 1)$ are obtained from integrating the nuclear angular coordinates, thus eliminating the rotational wavefunctions. When we insert Eq. 2.44 into Eq. 2.43, we obtain

$$A_{nm} = \frac{8\pi^2\nu_{nm}^3 S_{J_n,J_m}}{3\varepsilon_0 c^3\hbar(2J_n+1)}\left|\int \chi_n^{v*}(R)\chi_m^{v}(R)dR \times \int \phi_n^{el*}(\vec{R},\vec{r_1}...\vec{r_n})\hat{\mu_{el}}\phi_m^{el}(\vec{R},\vec{r_1}...\vec{r_n})d^3r_1...d^3r_n\right|^2. \quad (2.45)$$

The Hönl-London factors are representative of the line strength of a particular rotational transition within a particular electronic-vibrational band, and they depend on several factors. The first is whether the transition is a P, Q, or R transition, $J_m = J_n + 1$, $J_m = J_n$ or $J_m = J_n - 1$, respectively. It also is dependent on the electron spin and the change in the quantum number Λ of the electronic transition. For a $\Delta\Lambda = 0$ transition between two $^1\Sigma$ states, relevant to the present work in which we observe NaK $2(A)^1\Sigma^+\,(v,\ J) \rightarrow 1(X)^1\Sigma^+\,(v_l, J_l)$ downward transitions,

the Hönl-London factors for P and R lines, [36, 38] respectively, are given by

$$S^P_{J,J_l} = S^P_{J,J+1} = \frac{(J_l + \Lambda_l)(J_l - \Lambda_l)}{J_l} = \frac{(J+1)(J+1)}{J+1} = (J+1) \tag{2.46}$$

for P transitions and

$$S^R_{J,J_l} = S^R_{J,J-1} = \frac{(J_l + 1 + \Lambda_l)(J_l + 1 - \Lambda_l)}{J_l + 1} = \frac{(J-1+1)(J-1+1)}{J-1+1} = J \tag{2.47}$$

for R transitions.

The contribution from the integral over the vibrational wavefunctions can be written as

$$\left| \int \chi_n^{v*}(R) \mu_{el}(R) \chi_m^v(R) dR \right|^2, \tag{2.48}$$

where

$$\mu_{el}(R) \equiv \int \phi_n^{el*}(\vec{R}, \vec{r_1} ... \vec{r_n}) \hat{\mu_{el}} \phi_m^{el}(\vec{R}, \vec{r_1} ... \vec{r_n}) d^3 r_1 ... d^3 r_n. \tag{2.49}$$

If $\mu_{el}(R)$ is approximately independent of R, we can write Eq. 2.48 as

$$\left| \int \chi_n^{v*}(R) \mu_{el}(R) \chi_m^v(R) dR \right|^2 \approx \bar{\mu_{el}^2} \left| \int \chi_n^{v*}(R) \chi_m^v(R) dR \right|^2 \tag{2.50}$$

where the square of the vibrational wavefunction overlap integral $\left| \int \chi_n^{v*}(R) \chi_m^v(R) dR \right|^2$ is called the Franck-Condon factor. This factor is largely responsible for the relative intensities of vibrational bands.

Transitions between electronic states must obey selection rules which can be derived from the consideration of the Hönl-London factors, as well as the matrix elements of the transition electric dipole moment operator. Some selection rules are generally valid, while other approximate selection rules are only valid in certain Hund's coupling limits. These selection rules for electronic transitions are listed in Table 2.3.

Quantum number	Selection rule	Hund's case validity
Λ	$\Delta\Lambda = 0, \pm 1$	(a), (b)
Σ	$\Delta\Sigma = 0$	(a)
Ω	$\Delta\Omega = 0, \pm 1$	(a), (c)
S	$\Delta S = 0$	(a), (b)
J	$\Delta J = 0, \pm 1$	(a), (b), (c)
v	Δv =anything	(a), (b), (c)

Table 2.3: The selection rules for dipole allowed electronic transitions, and the Hund's cases in which they are valid.

Chapter 3

Experimental Setup

3.1 Overview

In this chapter I discuss the experimental set up, which was used for the data collection in Lyon, France, and which is shown in Fig. 3.1. I made two separate visits to Lyon to collect data: one in November 2013 and one in November 2014. The main experimental setup used during both visits was the same, while some aspects of the data collection procedure were improved for the second visit. Section 3.2 discusses the heat pipe oven and its theory of operation, followed in Sec. 3.3 by a discussion of the laser system. The Fourier Transform Spectrometer (FTS) and optical systems are explained in Sec. 3.4. The chapter concludes with a brief explanation of the experimental set up and data acquisition procedure in the Lehigh University experiment (see Sec. 3.5).

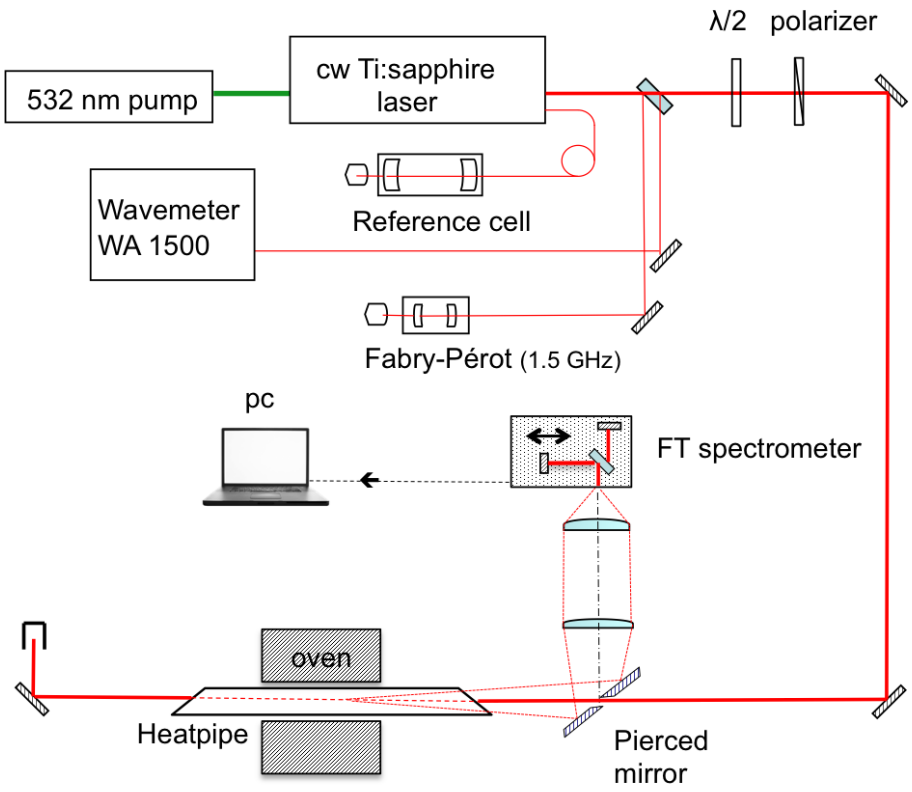

Figure 3.1: Experimental setup in Lyon including the linear heat pipe oven, laser system and Bomem Fourier Transform Spectrometer.

3.2 Heat Pipe Oven

The heat pipe oven is a linear pipe with the inner surface lined by a stainless steel mesh in the central region. BK-7 glass windows are affixed to flanges with epoxy and the flanges are bolted to either end of the heat pipe. The windows were either affixed at 90 degrees to the oven axis or at approximately Brewster's angle. Different combinations of the window orientations were used in 2013. In 2014 both

windows were oriented at Brewster's angle. Because the Lyon heat pipe does not have side arms for the collection of fluorescence, the use of Brewster windows reduces the laser scatter contaminating the signal.

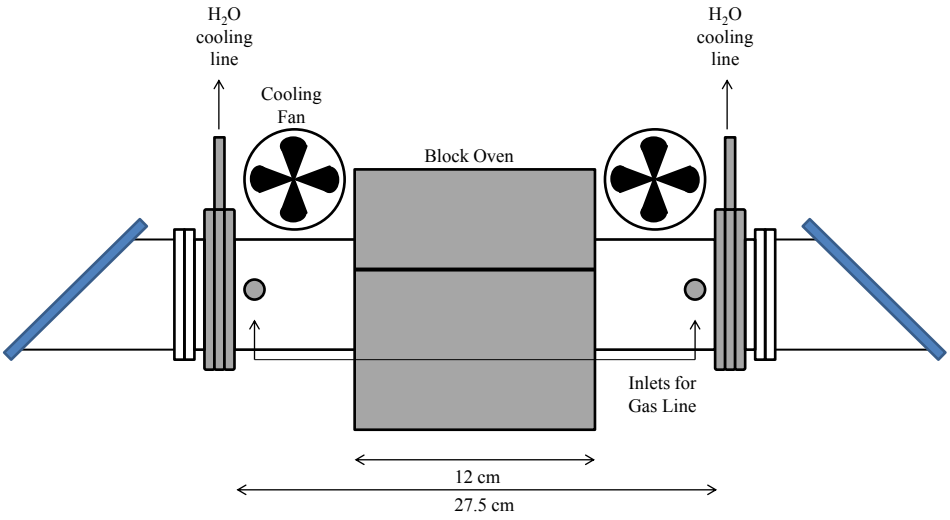

Figure 3.2: Linear heat pipe used in Lyon.

The first report of heat pipe oven construction and theory of operation was published by Vidal and Cooper [47]. The heat pipe sits within a block oven with a heater length of 12 cm. Sodium and potassium metals were loaded into the heat pipe oven and, when heated, creates a mixed vapor of sodium and potassium atoms as well as K_2, Na_2 and NaK molecules. The oven is also filled with argon or helium buffer gas. This buffer gas is necessary, not only for the collisional study, but also to prevent the alkali vapor from reaching (and coating) the windows. The outermost portion of each arm (outside the oven block) is cooled with external water coils and

cooling fans (see Fig. 3.2). This causes the alkali vapor to condense in this region. The liquid alkali metal is then wicked by the internal screen back into the central hot region of the oven.

The heat pipe oven has two possible modes of operation. The Lyon heat pipe was run in "oven" mode. In this regime, the buffer gas vapor pressure exceeds the alkali vapor pressure, usually by a large amount. The buffer gas fills the entire oven, becoming the dominant collision partner with the excited NaK molecules within the central zone. When the oven temperature is sufficiently high, the alkali vapor pressure becomes equal to the buffer gas pressure, and the so called "heat pipe" mode is attained. In this mode, the alkali vapor and buffer gas separate. The central zone of the heat pipe is void of buffer gas, the regions near the ends of the pipe contain only buffer gas, and there is a relatively short transition zone in between. In this mode, alkali atoms are the dominant collision partners with the excited NaK molecules.

Different methods were used to fill the heat pipe oven in 2013 and 2014. In 2013, the heat pipe itself was removed from the optical table and transported to a secondary location for filling. The oven was connected to a vacuum and gas handling system in this other room. It was first evacuated using the vacuum pump and then filled to the desired buffer gas pressure, all at room temperature. The heat pipe was then sealed and taken back into the lab where it was heated to the desired temperature. The same pressure and temperature conditions were maintained for the entire day.

Maintaining the same pressure for the course of the day limited the number of different temperature and buffer gas pressure combinations that could be completed in the course of our visit. In 2014, a new gas system was installed in the lab so that the pressure could be adjusted throughout the day. The new vacuum system includes a rough pump (a 2-stage Edwards rotary pump), an argon or helium gas tank, a pressure gauge and a series of valves allowing evacuation and filling of the oven (see Fig. 3.3). This allows the pressure to be changed while the oven is hot. When the heat pipe is used in the oven mode, the buffer gas pressure in the hot region is $P_{BG} = P_{tot} - P_{alk}$ where P_{alk} is the alkali vapor pressure and P_{tot} is the total fill pressure.

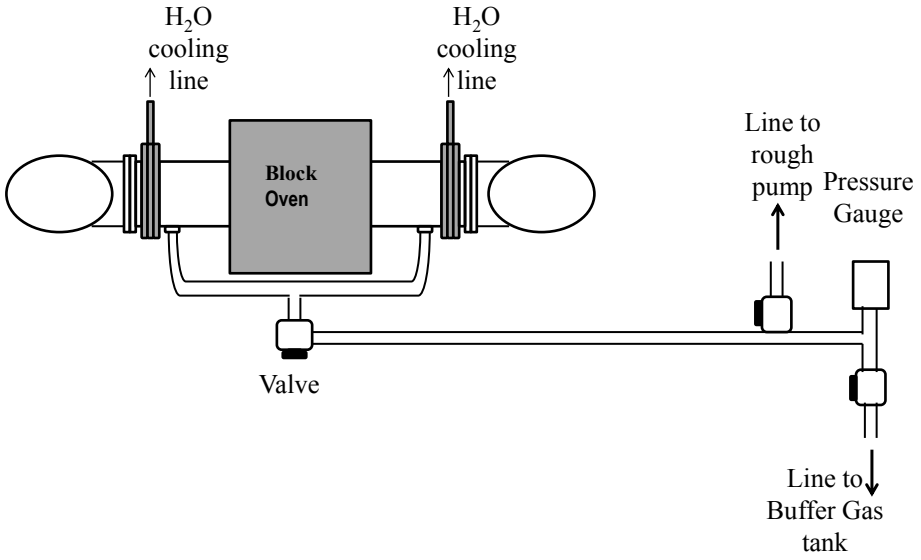

Figure 3.3: 2014 vacuum system in Lyon.

3.3 Laser System

The tunable laser used in the Lyon experiment is a Spectra Physics Sirah Matisse cw, single-mode, Titanium:Sapphire (Ti:S) laser, which is pumped by 7 W from a frequency doubled 532 nm YVO_4 laser (Spectra Physics Millennia) (see Fig. 3.1). The Matisse has an output power of 600-900 mW, a linewidth of approximately 1 MHz and can complete a 1-wavenumber continuous scan. In our experiments the laser frequency was typically set at a given value to pump a particular molecular transition. The laser beam exits the laser cavity and is split by a thick beam splitter. The secondary (reflected) beam is sent to an external wavemeter (Burleigh WA 1500) where the wavelength is measured to $3\text{x}10^{-3}$ cm^{-1} precision. The main beam passing through the splitter continues through a half-wave plate followed by a polarizer and then is sent to the heat pipe. The polarizer is set to minimize the reflection from the windows on the heat pipe, while the half-wave plate can be rotated to attenuate the power of the beam that is sent to the experiment. This can be reduced further with apertures and neutral density filters for the laser line absorption measurement.

The external wavemeter was used to monitor the Ti:S once it was set to the desired transition frequency for the duration of a scan of the Bomem Fourier Transform Spectrometer. The Ti:S laser uses a birefringent filter for coarse adjustments to the frequency and intracavity etalons for finer frequency adjustments.

Particular transition frequencies were calculated using the ground state $1(X)^1\Sigma^+$ ro-vibrational level energies of [10] and $2(A)^1\Sigma^+$ ro-vibrational level energies of [9, 11].

The Ti:S was then tuned to a particular transition frequency, which was verified by measuring the spacing between P and R lines of the fluorescence spectrum (see Fig. 3.4).

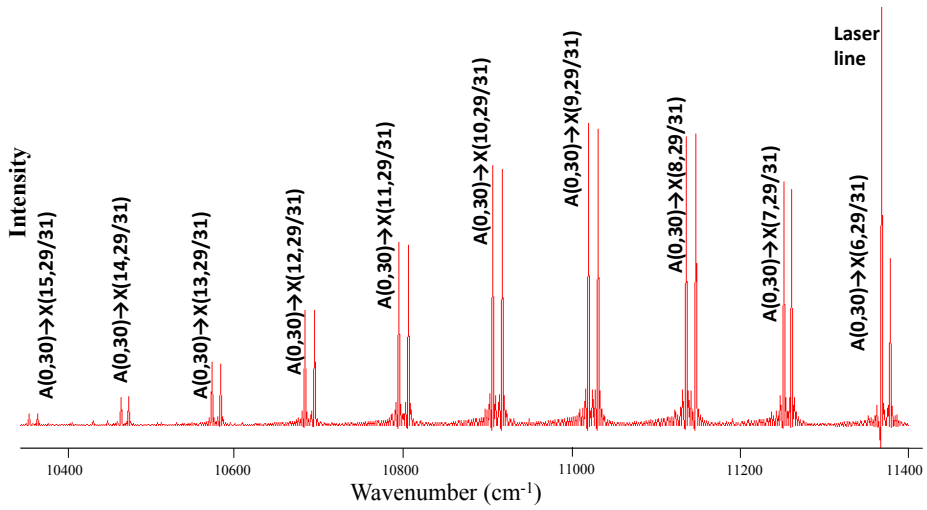

Figure 3.4: An example of a $2(A)^1\Sigma^+$ $(0, 30) \rightarrow 1(X)^1\Sigma^+$ (v'', J'') fluorescence spectrum. Transitions down to each ground state vibrational level give rise to strong P and R direct lines ($J'' = J_{upper} + 1$ and $J'' = J_{upper} - 1$, respectively) and to much weaker collisional line progressions. The anomalously large P line in the right-most band is the direct laser line, which is contaminated with scattered laser light.

3.4 Fourier Transform Spectrometer (FTS) and Light Detection System

The principal spectroscopic tool used in this work is the Bomem DA3 Fourier Transform Spectrometer (FTS). The FTS is basically a traveling Michelson interferometer (see Fig. 3.5). Light entering the FTS is collimated and sent through a 50/50 beam splitter. One half of the light is sent along one arm of the interferometer to a fixed mirror and then reflected back towards the beam splitter. The other half is sent along the second interferometer arm to a traveling mirror, where it is reflected back toward the beam splitter. The motorized mirror allows the length of the second beam path to be varied in the vertical arm. After the light traverses the two paths, the beams are recombined at the beam splitter, where, depending on the path difference, individual frequency components either add constructively or destructively. For example, when the beam paths are of equal lengths, there is zero path difference, and all the frequency components interfere constructively. Because the incoming light is usually made up of a number of different frequency components, as the position of the traveling mirror is scanned, the recombined beams create a complicated interference pattern, which is recorded by one of the light detectors installed in the detector compartments (see Fig. 3.5). A calibrated helium-neon (He-Ne) laser located inside the Bomem (FTS) is used as a frequency reference. This keeps track of the distance that the traveling mirror has traveled, while an internal white light allows the spectrometer to find the mirror location corresponding to zero path difference.

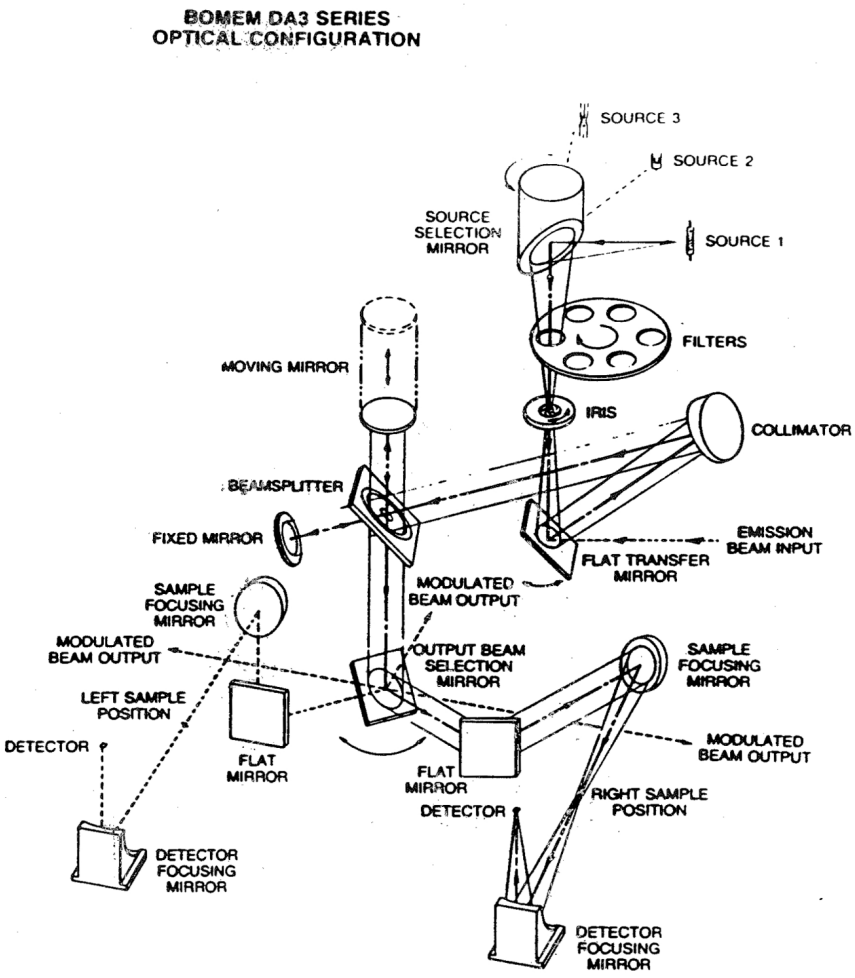

Figure 3.5: Fourier Transform Spectrometer optical schematic. [48]

A white light is mounted outside the main FTS compartment, which can be used to align the external optics guiding the fluorescence into the FTS with the aligned internal optical path. This white light is an equivalent distance from the beam splitter as are the detectors, and light from this source passes backwards through the Bomem's optics to exit through the fluorescence input port. As explained later, this is used to align the optics used to direct the fluorescence from the heat pipe oven to the FTS. The Bomem is also equipped with a vacuum pump to evacuate the entire housing, and various detectors can be cooled using liquid air or liquid nitrogen (as well as operate at room temperature). Both of these options are used to reduce the noise of the detectors.

The spectral resolution increases in proportion to the travel distance of the mirror in the vertical arm (i.e. to the total path length difference). However, increasing the travel distance also increases the scan time. The Bomem in Lyon is equipped with the extended vertical arm, which allows for greater resolution than a standard, shorter arm. In our experiments, the Bomem traveling mirror was scanned at a rate of 0.3 cm/s. The spectral resolution for all recorded fluorescence spectra was 0.025 cm^{-1}. An increase in exposure time (more total up and down scans of the traveling mirror) enables more light to be accumulated and increases signal-to-noise across the entire frequency range. Because all fluorescence in the collected spectral range (generally spanning roughly 2000 cm^{-1} in our experiments) is gathered at the same time, all line intensities in the spectrum scale together, creating consistent *relative* intensities even in the event of small laser frequency drifts.

The intensity measurements and spectral resolution of a Michelson interferometer (MI) can be estimated as follows [1]. Figure 3.6 shows the basic interferometer design. The distance the moving mirror travels during a given scan is the path difference Δy, which represents an optical path difference $\Delta s = 2n\Delta y$. Here n is the index of refraction for a particular frequency, for whatever medium occupies the volume between the beam splitter S and the mirrors. If the interferometer has been evacuated, $n = 1$.

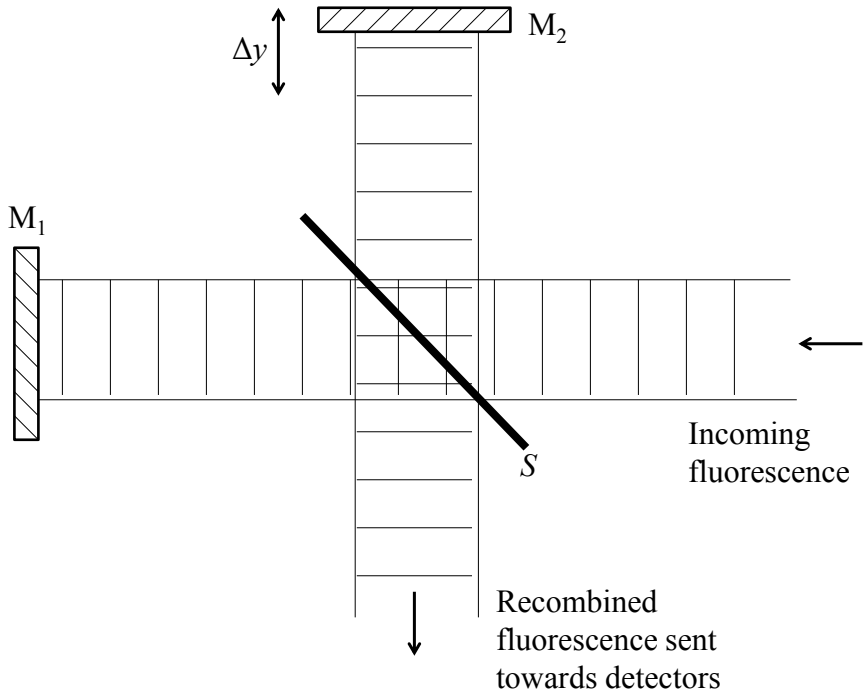

Figure 3.6: The incoming fluorescence enters from the right side and reaches beam splitter S where it is split into two waves, one traveling towards a stationary mirror (M_1) and the second moving towards a traveling mirror (M_2). Both beams are reflected and return to the beam splitter where they are recombined. The two beams interfere (either contructively, destructively, or something in between) depending on the accumulated phase difference.

Once the two beam components are reflected by their respective mirrors and interfere at the beam splitter, the number of interference maxima N_i counted by the detector for an incident wave with wavelength λ_i is

$$N_i = \frac{2\Delta y}{\lambda_i}. \tag{3.1}$$

Two wavelengths (λ_1 and λ_2, where $\lambda_1 > \lambda_2$) with a difference $\Delta\lambda = \lambda_1 - \lambda_2$, which is small compared to either wavelength, can be clearly distinguished when $N_2 \geq N_1 + 1$. Combining this criterion with Eq. 3.1 allows us to determine the spectral resolving power $\frac{\frac{1}{2}(\lambda_1+\lambda_2)}{\Delta\lambda}$ as

$$\frac{\frac{1}{2}(\lambda_1 + \lambda_2)}{\Delta\lambda} = \frac{2\Delta y}{\frac{1}{2}(\lambda_1 + \lambda_2)} = \frac{\Delta s}{\frac{1}{2}(\lambda_1 + \lambda_2)}, \tag{3.2}$$

which shows that the spectral resolving power of the instrument is proportional to the optical path difference, measured in units of wavelength.

Two detectors can be housed in the FTS at a given time, and a particular detector can be chosen by orienting the flat mirror (labeled "output beam selection mirror" in Fig. 3.5). Both the silicon avalanche (Si-Av) and the Indium-Gallium-Arsenide (InGaAs) detectors used in this experiment were cooled with liquid air to reduce the dark noise, or thermal background. The choice of detector depends on the wavelength range of interest: the Si-Av is used for wavelengths shorter than 1 μm, while the InGaAs is used for further into the infrared. Once the light from the recombined beams is collected by the detector, it is recorded as an interferogram (IGM) on the computer (see Fig. 3.7). The computer then calculates a Fourier transform of the IGM to obtain a high resolution spectrum as seen in Fig. 3.8.

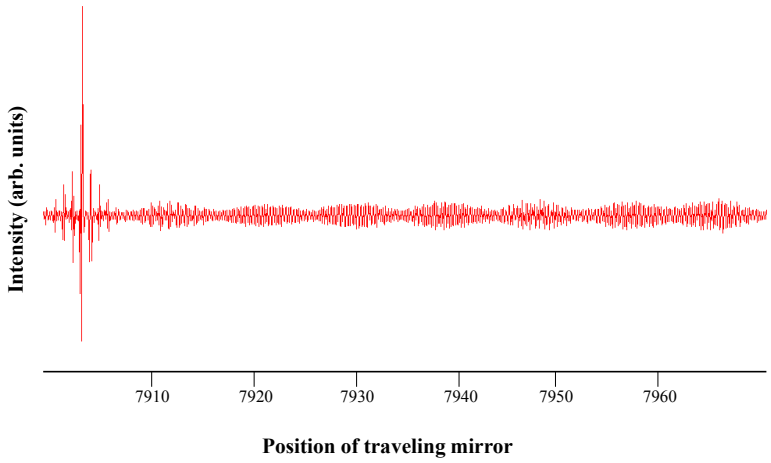

Figure 3.7: Pre-processed interferogram (IGM) of NaK fluorescence as collected by Bomem FTS before the Fourier transform is performed.

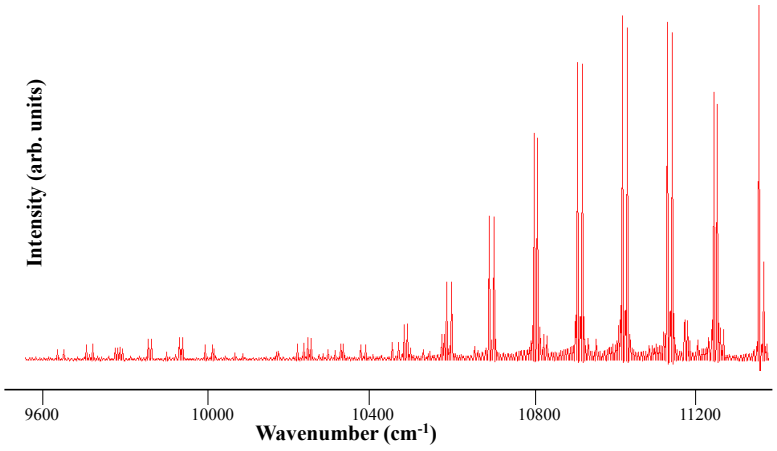

Figure 3.8: The Fourier transform of the NaK fluorescence interferogram in Fig. 3.7.

In our experiment, NaK molecules in the heat pipe oven are excited by the laser beam after it passes through a pierced mirror (see Fig. 3.9). Fluorescence emitted along the laser propagation axis in the backward direction is collected by the pierced mirror and is focused onto the input aperture of the FTS. Scattered laser light is blocked with long and short-pass filters, depending on the selected $2(A)^1\Sigma^+$ level to be excited. In 2013, a long-pass 900 nm filter was used for all $v = 0$ scans, and in 2014 a long-pass 750 nm filter was used for collection of all $v = 0$, 1 and 2 fluorescence. In both cases, the filter was placed inside of the detector housing.

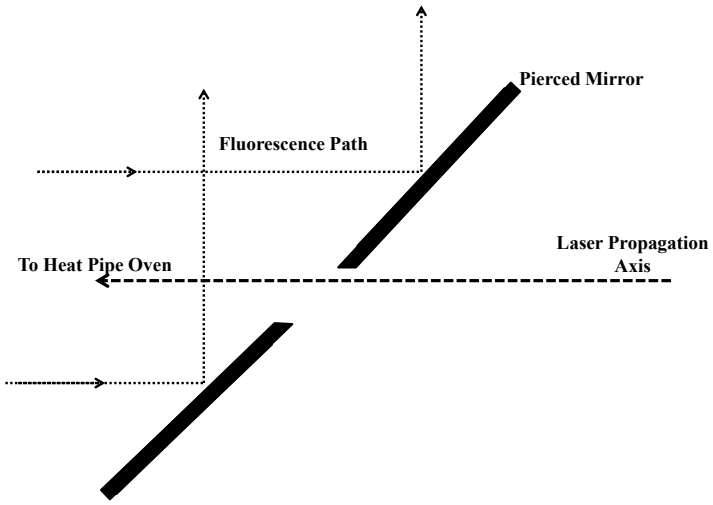

Figure 3.9: A representation of the laser and fluorescence paths near the pierced mirror.

An interferogram is recorded as the traveling mirror moves up and back a given number of times, where the actual number is chosen by the operator. We generally used between 4 and 15 repetitions of the mirror movement in a given scan. After processing, the different ro-vibrational transitions give rise to separate peaks in the Fourier transform spectrum. Although the signal-to-noise is usually quite good, the recorded spectral lines are sometimes asymmetric or broader than they should be.

For example, if the fluorescence path is misaligned with the interferometer axis, the spectral lines will appear to be asymmetric, non-Gaussian, in nature and can have an uneven baseline. While this can occur for all spectral lines, it is most easily seen in the direct lines, [see Fig. 3.10(b)]. A proper alignment of the fluorescence optical path with the Bomem optical axis can reduce these asymmetries. To align the external optics with the internal light path, the previously mentioned white light mounted external to the main Bomem chamber is sent through the FTS in the direction opposite to the fluorescence path. This light comes to a focus just outside the FTS. This focused white light is then sent through the heat pipe, again in the direction opposite to the fluorescence path. The fluorescence collection optics are then adjusted to focus this light to the approximate center of the heat pipe, thus aligning the optics between the Bomem and the heat pipe oven. In the event that, after proper alignment, a spectral line is still asymmetric, there are mathematical steps which can be taken to correct these errors in the IGM processing stage. It is important to mention that the correction of the IGM does not alter the relative heights of individual lines, and the majority of collisional lines are not noticeably asymmetrical. The effect is most noticible for large intensities, as seen in the direct lines, and has little effect on the relatively small intensities of the collisional spectral lines.

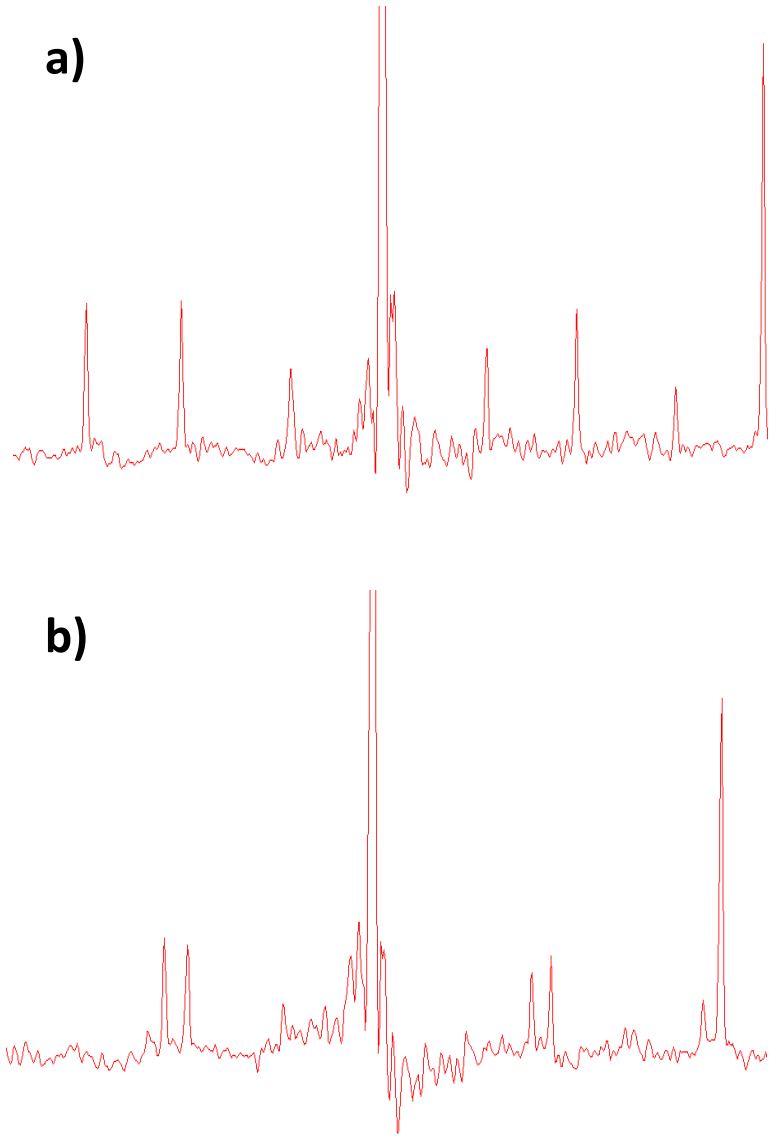

Figure 3.10: Bomem spectra showing a symmetrical (a) and an asymmetrical (b) direct line spectral baseline. The shorter peaks to either side are collisionally populated lines and do not visibly exibit the same asymmetry as the direct line due to the fact that they are much weaker lines.

3.5 Lehigh Experiment

A full discussion of the experimental setup at Lehigh can be found in [34], [49] or [50], but a basic outline of it will be laid out here. Figure 3.11 shows the Lehigh experimental setup. Two laser systems are used in these experiments; an argon ion laser pumped tunable, single-mode, cw Ti:S laser (Coherent 899-29) and an argon ion laser pumped tunable, single-mode, cw ring dye laser (Coherent 699-29). Beams from the two tunable lasers are counter-propagated through the heat pipe oven and create a two-step excitation. In the NaK experiment, the dye laser acts as the initial excitation laser (pump laser) and the Ti:S is the second step (probe) laser. The pump laser excites specific rovibrational levels of the NaK $2(A)^1\Sigma^+$ state [$2(A)^1\Sigma^+(v', J') \leftarrow 1(X)^1\Sigma^+(v'', J'' = J' \pm 1)$], while the probe laser further excites the molecule from the directly excited level $2(A)^1\Sigma^+(v', J')$ or from a collisionally excited level $2(A)^1\Sigma^+(v', J' + \Delta J)$ to levels of the $3^1\Pi$ state [$3^1\Pi(v, J = J' \text{ or } J = J' \pm 1) \leftarrow 2(A)^1\Sigma^+(v', J')$ or $3^1\Pi(v, J = J' + \Delta J$ or $J = J' \pm 1 + \Delta J) \leftarrow 2(A)^1\Sigma^+(v', J' + \Delta J)$, respectively.]

One large difference between the Lyon and Lehigh setups is the shape of the heat pipe oven. Lehigh's oven has four horizontal arms in a cross shape with a fifth vertical arm. This allows the collection of fluorescence through the windows of the arms perpendicular to the laser propagation axis. The vertical arm is used for loading metal into the oven. Violet $3^1\Pi \rightarrow 1(X)^1\Sigma^+$ fluorescence is detected with a free-standing photomultiplier tube ("Total Violet PMT" in Fig. 3.11) while red $2(A)^1\Sigma^+ \rightarrow 1(X)^1\Sigma^+$ fluorescence is detected with a second free-standing PMT ("Total Red PMT").

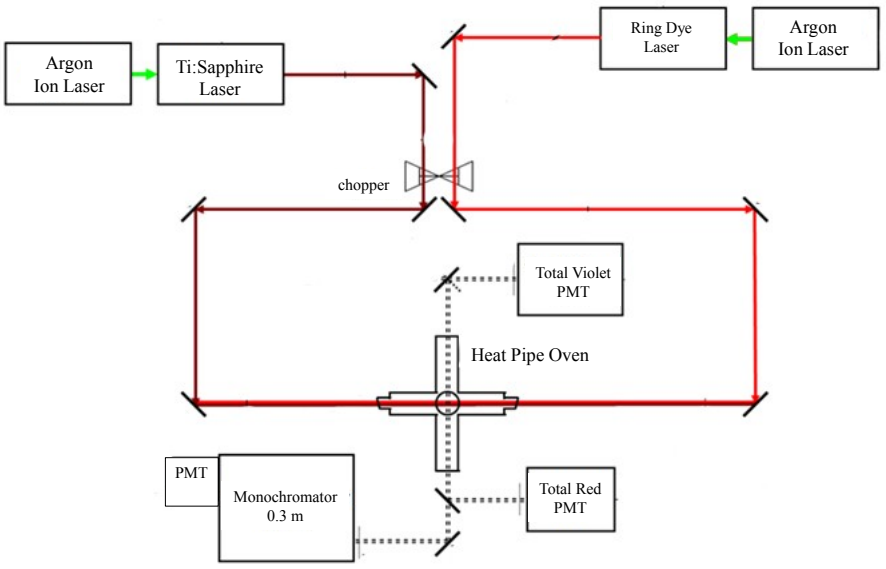

Figure 3.11: Experimental setup used at Lehigh University. The main differences between this setup and the Lyon setup are the cross-shaped heat pipe used at Lehigh and the use of double resonance excitation.

Chapter 4

Experimental Techniques

4.1 Overview

I begin this chapter with a discussion (Sec. 4.2) of how both buffer gas and alkali densities are experimentally determined. The discussion highlights the differences in the procedures used in the two different time periods that data were recorded in Lyon, France. In Sec. 4.2.1 I describe the buffer gas filling procedure and pressure measurements used in November 2013 and in November 2014. Section 4.2.2 discusses the vapor pressure formulas used to form initial estimates of the alkali densities. Section 4.2.3 then details the use of a white light source to determine alkali vapor densities (actually column densities) in both years, and the laser line absorption method used for the same purpose, but only in November 2013. In this discussion, the relationship between the absorption lineshape and atomic number density is presented.

Section 4.3 details the technique of Laser Induced Fluorescence (LIF) and how

it was used to collect data on the collisional transfer of population from one ro-vibrational molecular level to another. This is the experimental technique used for all of the data collected in Lyon. A brief description of the two-step excitation used in the Lehigh experiments is also included in this section.

4.2 Determining Vapor Densities

4.2.1 Buffer Gas Densities

In order to determine collisional rates from measured fluorescence intensities, we must have accurate determinations of both the alkali atom densities and buffer gas atom densities. The current section describes the determination of the buffer gas density.

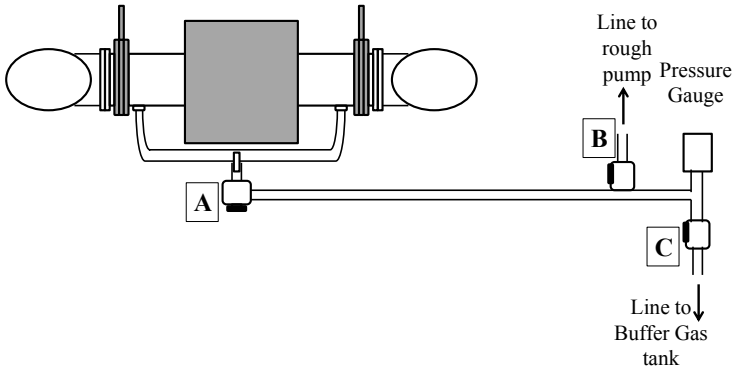

Figure 4.1: Vacuum system used in Lyon, 2014. There are three labeled valves in the system; valve A closes off the heat pipe oven from the outside environment, valve B controls the flow to the rough pump, and valve C connects to the buffer gas tank.

As seen in Fig. 4.1, we can close off the heat pipe from the outside environment by a valve (A) at its entrance. This valve allows the heat pipe to be evacuated by the vacuum system, consisting of a rough pump connected through valve B, or to be filled with buffer gas from attached gas bottles (through valve C). When valves A and C are open with valve B closed, the volume of the system is roughly double compared to when valve A is closed. The pressure gauge is near valves B and C, where it remains at room temperature, roughly 21° C. The vacuum systems used in 2013 and 2014 were constructed with essentially the same layout as shown in Figure 4.1, and in 2014 the system was located next to the optical table where the fluorescence measurements were made.

As previously stated, in 2013 the heat pipe was filled at room temperature in a separate location from the optical setup and then valve A was closed. In principle, after that point the number of buffer gas atoms in the heat pipe does not change, nor does the volume. Applying the ideal gas law, $PV = Nk_BT$

$$n = \frac{N}{V} = \frac{P}{k_BT}, \tag{4.1}$$

we see that the pressure P in the heat pipe oven will rise proportionally to the temperature, T. n is the atomic number density (atoms/cm^3) and k_B is Boltzmann's constant. Since there is no change in the atomic number density for the buffer gas throughout the course of the day (assuming no leaks), we use $n_{hot} = n_{cold} = \frac{P_{fill}}{k_BT_{room}} = \frac{P_{meas}}{k_BT_{room}}$ for the 2013 data.

In 2014, a new vacuum system was constructed so that the pressure could be adjusted during the course of the day. To fill the heat pipe, both valve A and the vacuum pump valve (B) were opened and the system evacuated. Valve B was then closed, valve C was opened, and the oven was refilled to the desired pressure. The measured pressure readings, P_{meas}, were carried out with valve A opened and the heat pipe oven hot. Periodically throughout the day, valve A could be opened to check the pressure or A and C could both be opened to adjust the pressure to a new value.

Since the oven was already at the operating temperature when these pressure readings were made, we need to take into account the fact that the vapor within the hot zone would also have contributions from the *alkali* vapor pressure. By adjusting the power sent to the heating elements, we can vary the alkali vapor density, which also changes the value of the buffer gas density in the central (hot) zone. Using the fact that the measured pressure has contributions from both the buffer gas and alkali vapor, we find the buffer gas pressure in the hot zone, P_{BG}, which is given by

$$\begin{aligned} P_{meas} &= P_{BG} + P_{alk} \\ P_{BG} &= P_{meas} - P_{alk} \\ &= P_{meas} - n_{alk} k_B T_{hot}. \end{aligned} \tag{4.2}$$

We use Eq. 4.2 to determine the buffer gas pressure in the hot oven. The buffer gas atom density in the hot oven is then found from Eq. 4.1, but with the hot oven temperature; i.e.

$$n_{BG} = \frac{P_{BG}}{k_B T_{\text{hot}}} = \frac{P_{\text{meas}}}{k_B T_{\text{hot}}} - n_{alk}. \tag{4.3}$$

4.2.2 Nesmeyanov Vapor Pressure Equation

Determining the alkali vapor densities can be done in several ways, starting with a simple estimate based on an equation (vapor pressure formula) relating the temperature of the oven to the pressure or density of the species being investigated. In 1963, Nesmeyanov published a critical compilation of pressure vs temperature data [51]. He used the available data to create a vapor pressure formula of the general form

$$\log_{10} P = A - \frac{B}{T} + CT + D \log_{10} T, \tag{4.4}$$

providing the best fit values for the coefficients A, B, C and D for each element. The values for sodium and potassium are listed in Table 4.1.

Species	A	B	C	D
Na	10.86423	5619.409	-3.45x10^{-6}	-1.04111
K	13.83624	4857.902	3.494x10^{-4}	-2.21542

Table 4.1: Nesmeyanov vapor pressure coefficients for species pertinent to this experiment. [51]

Vapor pressure formulas like Nesmeyanov's are based on the assumption that the vapor in question contains only a single pure atomic or molecular species. In our experiment, we heat a mixture of two different species of atoms, which creates a mixed vapor. This mixed vapor is better defined using a combination of Dalton's law [52] and Raoult's law [53] to describe the mixed vapor once the components have

reached equilibrium. The former states that the total pressure of a mixed system is the sum of the partial pressures of each species,

$$P_{total} = \sum_i P_i, \tag{4.5}$$

while the latter states that partial vapor pressure P_i of a species is related to the vapor pressure of the pure component P_i^* weighted by its mole fraction χ_i in the mixture

$$P_i = P_i^* \chi_i. \tag{4.6}$$

Combining Eq. 4.5 with Eq. 4.6 yields

$$P_{total} = \sum_i P_i^* \chi_i. \tag{4.7}$$

However, it is important to note that Eq. 4.7 has limited validity. In general, we have found that experimentally measured densities in the Lyon heatpipe are systematically significantly lower than those calculated directly from the Nesmeyanov formula, because the Lyon heat pipe is loaded with relatively small amounts of alkali metal. With the Lehigh heat pipe, which is loaded with much larger amounts of metal, the measured densities are typically between those calculated directly from the Nesmeyanov formula and those calculated from the Nesmeyanov formula modified by Raoult's Law [34].

4.2.3 White Light Absorption and Laser Line Absorption

The previously discussed equations for vapor pressure (or density) can be used to make a simple initial prediction of the alkali atomic densities. These calculations, however, do not replace an actual measurement of the vapor densities. In the 2013 experiments in Lyon, we used a combination of white light absorption spectra and laser line absorption measurements to accurately determine the alkali atom densities. In 2014, only white light absorption measurements were used to determine these vapor densities, since this method was easier to implement and generally more reproducible. In both the white light and laser absorption methods, the potassium vapor density was determined by comparing measured and calculated absorption in the wings of the potassium D2 line.

For white light absorption, we directed the light from a calibrated tungsten halogen lamp through the heat pipe along the path of fluorescence and into the Bomem FTS. A cold background scan was recorded with the oven heaters off to determine the baseline transmitted intensity with $n_K = 0$. The oven was then heated up to the desired temperature and a second scan was recorded. Such a scan is shown in Fig. 4.2. We determine the fraction of light absorbed as a function of frequency by dividing the hot scan by the background scan.

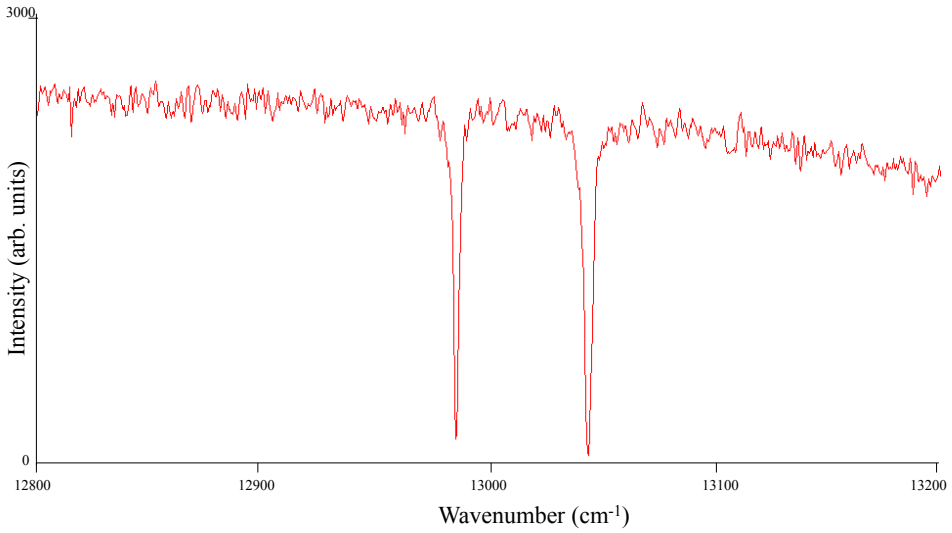

Figure 4.2: Example of a white light absorption scan recorded with the oven at 435°C.

Figure 4.3 shows the data of Fig. 4.2 after division by the background scan. For these density measurements we used the Bomem at a 1.0 cm^{-1} resolution in 2013 and at a 0.5 cm^{-1} resolution in 2014. Both of these resolutions are small compared to the absorption linewidths. The fraction of the white light transmitted as a function of frequency was then used to determine the potassium vapor densities. To maintain good signal-to-noise, we only used transmission values in the range of 20% to 80%. Every time we changed the buffer gas pressure or temperature, a new white light absorption scan was recorded.

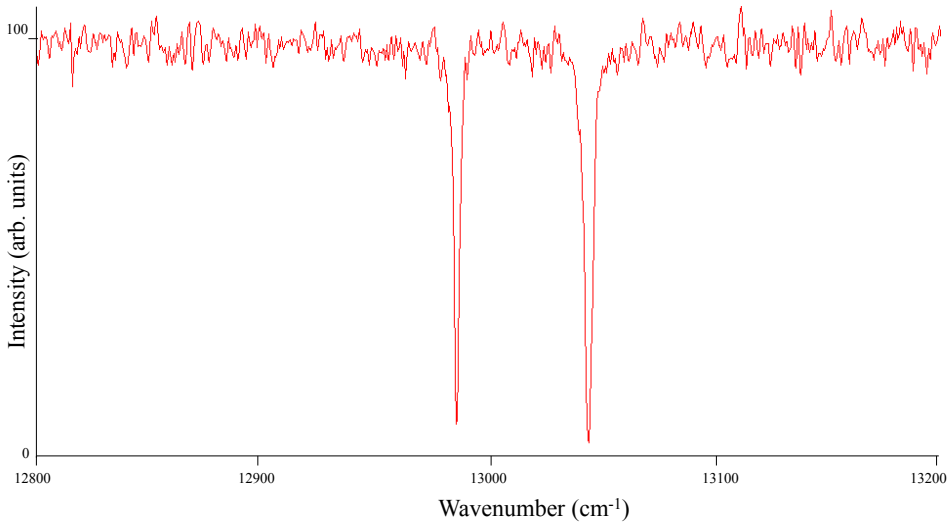

Figure 4.3: Transmission spectrum of the potassium D1 and D2 lines. The hot scan shown in Fig. 4.2 has been divided by the cold background white light scan, leaving a flat baseline of 100% transmission.

The laser line absorption method also uses the absorption in the line wings and determines the fraction of laser intensity absorbed at specific detunings from line center. The Ti:Sapphire laser has a very narrow linewidth (approximately 750 kHz) which provides very high resolution. However, the intensity is also very high. Therefore, to avoid saturation effects, the laser was sent through almost crossed polarizers to reduce the laser beam intensity to the order of microWatts. We set the laser to specific detunings from line center and recorded the laser intensity both before and after the heat pipe. Correcting for window losses (by recording the laser intensities before and after the heat pipe with the oven off), we determined the fraction of light transmitted through the vapor at these specific frequencies.

Under our experimental conditions, the absorption coefficient for the resonance lines of the alkali atoms can be described by a Voigt lineshape [54]:

$$k_\nu = \frac{\lambda_0^2 n A_{21}}{8\pi}\frac{g_2}{g_1}\int \mathcal{G}(\nu'-\nu_0)\mathcal{L}(\nu-\nu')\,\mathrm{d}\nu' \tag{4.8}$$

Equation 4.8 is the convolution of a normalized Gaussian $\mathcal{G}(\nu'-\nu_0)$, due to Doppler broadening and a normalized Lorentzian lineshape $\mathcal{L}(\nu-\nu')$, due to natural and collisional broadening, which are used to describe the total lineshape k_ν.

While the Voigt profile is an extremely good representation of the true line shape, if we concentrate on absorption well out in the line wings where the Gaussian function is very small, we can approximate the lineshape as a single Lorentzian function

$$\int \mathcal{G}(\nu'-\nu_0)\mathcal{L}(\nu-\nu')\,\mathrm{d}\nu' = \mathcal{L}(\nu-\nu_0) = \frac{\Gamma}{4\pi^2(\nu-\nu_0)^2+(\frac{\Gamma}{2})^2}. \tag{4.9}$$

Thus the absorption coefficient k_ν in the line wings can be written as

$$k_\nu = \frac{\lambda_0^2 n A_{21}}{8\pi}\frac{g_2}{g_1}\frac{\Gamma}{4\pi^2(\nu-\nu_0)^2+(\frac{\Gamma}{2})^2}. \tag{4.10}$$

Here Γ contains information about the homogenous broadening contributions including natural broadening and collisional broadening from both the alkali and buffer gas collision partners ($\Gamma = \Gamma_{nat} + k_{alk}^{br} n_{alk} + k_{BG}^{br} n_{BG}$).

The intensity of light of frequency ν that is transmitted through a length L of the vapor, $I_\nu(L)$, is related to the absorption coefficient through Beer's Law:

$$I_\nu(L) = I_\nu(0)\mathrm{e}^{-k_\nu L}. \tag{4.11}$$

In our experiment, L is the length of the central hot region (defined by the length of the housing containing the heating elements) within the heat pipe. Solving Eq. 4.11 for k_ν and comparing to Eq. 4.10 we find

$$k_\nu = \frac{1}{L}\ln\left(\frac{I_\nu(0)}{I_\nu(L)}\right) = \frac{\lambda_0^2 n A_{21}}{8\pi}\frac{g_2}{g_1}\frac{\Gamma}{4\pi^2(\nu-\nu_0)^2 + (\frac{\Gamma}{2})^2}. \tag{4.12}$$

Assuming the values of the detuning $(\nu - \nu_0)$, linewidth Γ (where $\Gamma = \Gamma_{\mathrm{nat}} + k^{br}_{\mathrm{self}} n_{\mathrm{alk}} + k^{br}_{BG} n_{BG}$), and Einstein A coefficients are known, the atomic density n can be determined via Eq. 4.12. Table 4.2 lists the self broadening rates and buffer gas broadening rates (Ar and He) for the D1 and D2 lines of sodium and potassium.

Alkali		k^{br}_{self} ($\mathrm{cm^3 s^{-1}}$)	k^{br}_{He} ($\mathrm{cm^3 s^{-1}}$)	k^{br}_{Ar} ($\mathrm{cm^3 s^{-1}}$)
Sodium	D1	3.07 x 10^{-7} [55]	1.90 x 10^{-9} [56]	2.77 x 10^{-9} [56]
	D2	4.67 x 10^{-7} [55]	2.19 x 10^{-9} [56]	2.27 x 10^{-9} [56]
Potassium	D1	3.91 x 10^{-7} [57]	1.55 x 10^{-9} [58]	2.45 x 10^{-9} [58]
	D2	6.36 x 10^{-7} [57]	2.06 x 10^{-9} [58]	1.98 x 10^{-9} [58]

Table 4.2: Broadening rate coefficients for the sodium and potassium atomic lines used in the calculation of Γ. The D1 and D2 line rate coefficients for sodium (the $3S_{\frac{1}{2}} \rightarrow 3P_{\frac{1}{2},\frac{3}{2}}$ transitions) and potassium (the $4S_{\frac{1}{2}} \rightarrow 4P_{\frac{1}{2},\frac{3}{2}}$ transitions) for broadening by collisions of each alkali with other alkali atoms of the same type and by collisions with helium and argon are listed.

Potassium densities were determined using measured transmissions $I_\nu(L)/I_\nu(0)$ at various points in the line wings and Eq. 4.12 for the D2 transition. As previously stated, atomic number densities were determines in both 2013 and 2014 by the white light absorption method. In 2013, laser line absorption measurements were also obtained as a secondary check to the white light method. However, all the alkali

density values used in the present analysis are those derived from the white light scans.

4.3 Laser Induced Fluorescence (LIF) Intensity Ratios

In Lyon we used laser excitation (the Matisse Ti:Sapphire) to induce transitions from a specific ro-vibrational level within the ground state, $1(X)^1\Sigma^+$, to a specific ro-vibrational level within the $2(A)^1\Sigma^+$ state. This upper $2(A)^1\Sigma^+\,(v', J')$ level then decays back to the ground state via spontaneous emission, which we observe as a progression of transitions to all ground state vibrational levels. These $1(X)^1\Sigma^+\,(v'', J'\pm1) \leftarrow 2(A)^1\Sigma^+\,(v', J')$ transitions, as previously discussed in Chapter 2, obey the standard selection rule $\Delta J = \pm1$ for a $^1\Sigma \rightarrow ^1\,\Sigma$ transition. Therefore, the spectrum consists of a series of P($J'' = J' + 1$) and R($J'' = J' - 1$) lines, as shown in Figure 4.4.

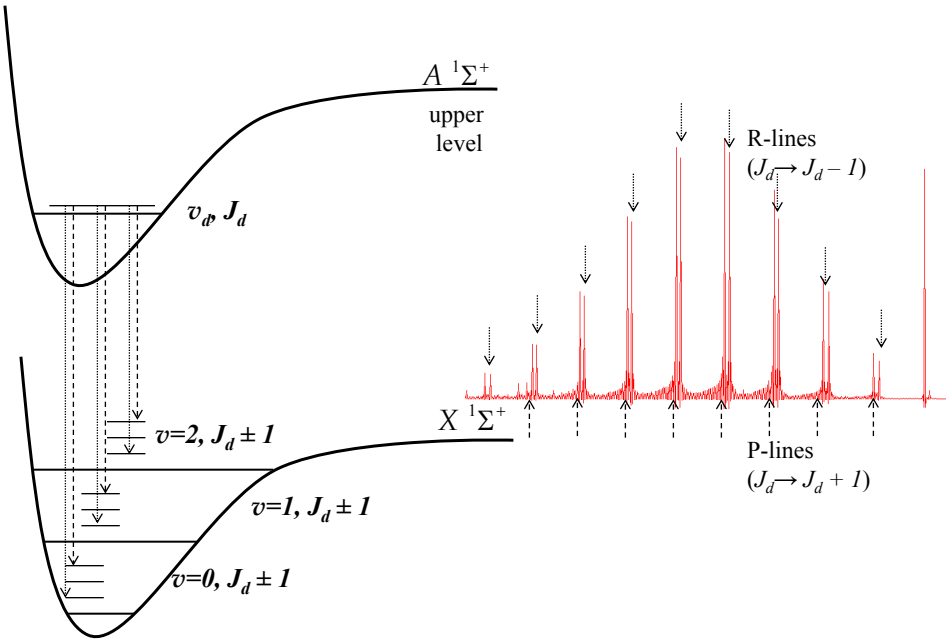

Figure 4.4: NaK molecules in a particular $2(A)^1\Sigma^+$ ro-vibrational level (v_d, J_d) decay by spontaneous emission on transitions to all ground state vibrational levels. The intensities of these transitions are proportional to the Einstein A coefficients of each transition. All transitions originate in the same upper level with population density n_{upper}. The schematic on the left is reflected in the FTS scan on the right as the strong transitions, marked with arrows.

Before decaying to the ground state, the excited molecules can collide with buffer gas atoms, alkali atoms, or other alkali molecules (NaK, Na_2, K_2) that are all present in the oven. These collisions can result in the transfer of population from the directly excited level $2(A)^1\Sigma^+ (v_d, J_d)$ to an adjacent J level $J = J_d + \Delta J$. Molecules in these collisionally populated ro-vibrational levels also radiate down to the $1(X)^1\Sigma^+$ state. The final ground state vibrational level v'' can have any value, with the fluorescence intensities of the various transitions being proportional to the Einstein A coefficients as discussed previously. In Fig. 4.5 we present a spectrum showing fluorescence from both directly and collisionally populated ro-vibrational levels decaying to the ground state via P and R transitions. It is also possible that a collision will not only change J, but will also change v. Evidence of such v-changing collisions can be seen in the spectra shown in Figure 4.6.

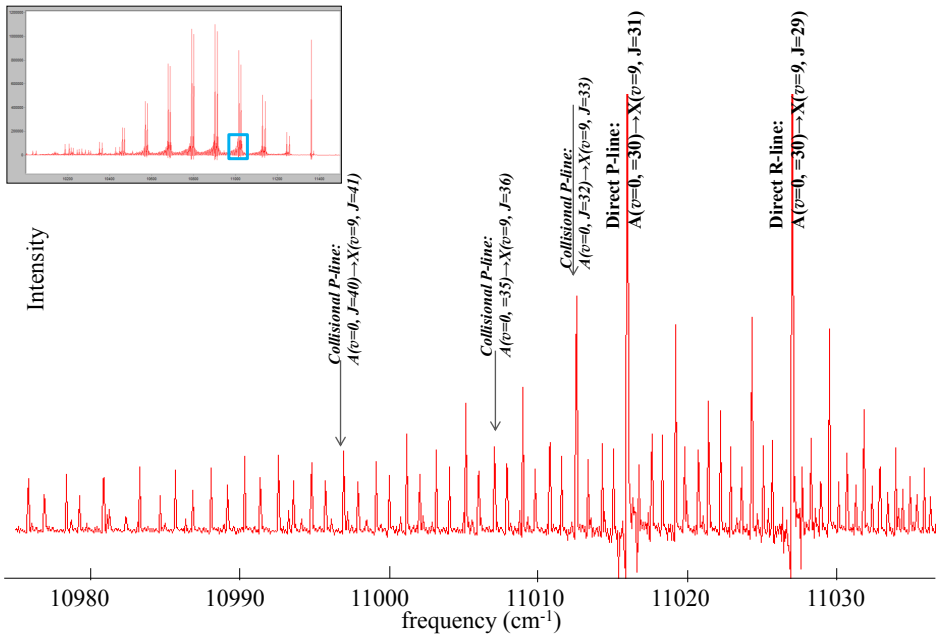

Figure 4.5: Fluorescence from directly populated and collisionally populated $2(A)^1\Sigma^+$ ro-vibrational levels making transitions to a particular vibrational level $v'' = 9$ of the ground state. This FTS scan shows that levels $J = J_d + \Delta J$ are collisionally populated out beyond $|\Delta J| = 10$. Note that the direct lines are much stronger than the collisional lines (the direct lines go far off scale).

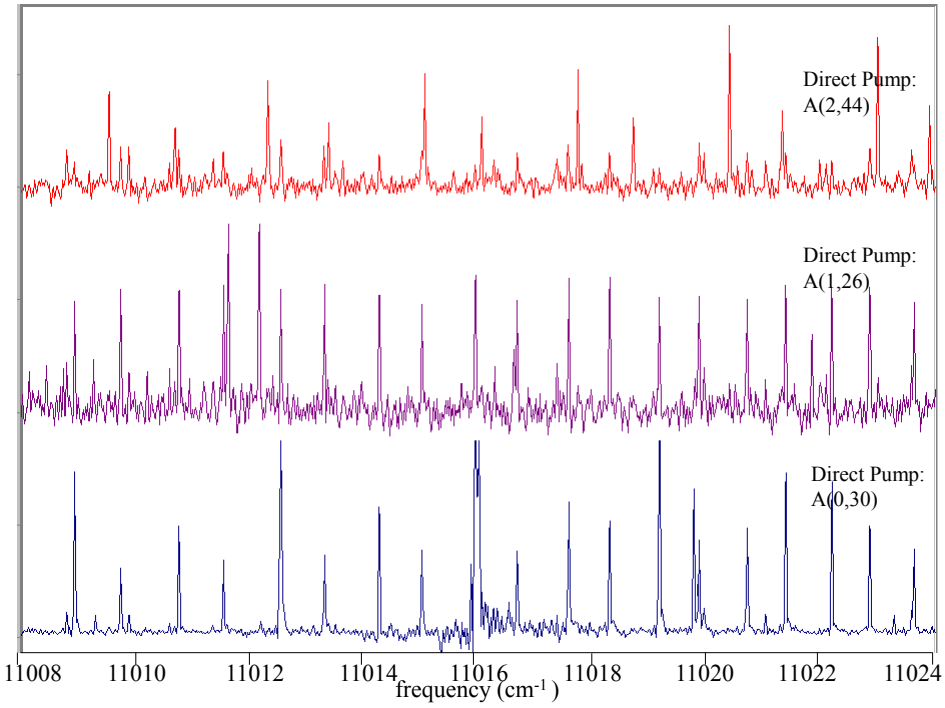

Figure 4.6: Three spectra recorded following excitation of three different $2(A)^1\Sigma^+$ levels: The top trace corresponds to direct pumping of $2(A)^1\Sigma^+$ (2,44), the middle trace corresponds to direct pumping of $2(A)^1\Sigma^+$ (1,26) and the bottom spectrum shows fluorescence following the direct pumping of $2(A)^1\Sigma^+$ (0,30). In all cases, the observed fluorescence in this spectral region corresponds to the $2(A)^1\Sigma^+$ ($v = 0$)$\rightarrow$1$(X)^1\Sigma^+$ ($v = 9$) transitions. The fact that emission from $v = 0$ is observed following excitation of $v = 1$ and $v = 2$ is evidence of v-changing collisions in the A state.

Figure 4.6 shows three separate recorded spectra, each highlighting fluorescence emitted by molecules in the $v = 0$ vibrational level of the $2(A)^1\Sigma^+$ electronic state. The difference between the three spectra is the level *directly* excited by the laser: $2(A)^1\Sigma^+ (v = 2, J = 44)$, $2(A)^1\Sigma^+ (v = 1, J = 26)$ and $2(A)^1\Sigma^+ (v = 0, J = 30)$ from top to bottom. The bottom spectrum obviously does not represent v-changing collisions. Rather, it is provided as a reference to easily discern the small v-changing collisional lines corresponding to $v = 0$ in the other spectra.

4.3.1 Optical-Optical Double Resonance Spectroscopy

As discussed in Section 3.5, the Lehigh experiment utilizes a two laser pump-probe scheme. This optical-optical double resonance (OODR) technique uses counter-propagating beams to first excite NaK molecules on a specific transition $1(X)^1\Sigma^+ (v'', J' \pm 1) \rightarrow 2(A)^1\Sigma^+ (v', J')$. Similar to the Lyon experiment, collisions of perturbers with molecules in the $2(A)^1\Sigma^+$ state can transfer population to neighboring rotational levels. The molecules in directly excited level $[2(A)^1\Sigma^+ (v', J')]$ and molecules in collisionally populated levels $[2(A)^1\Sigma^+ (v', J' + \Delta J)]$ are then excited by the probe laser to various ro-vibrational levels of a particular upper electronic state. As described in Refs. [31] and [34], the chosen upper electronic state used in the Lehigh experiment was the NaK $3^1\Pi$ state. In the experiment, the total red fluorescence signal, corresponding to transitions from the intermediate state to the ground state, was constantly monitored to insure that the pump laser frequency didn't drift. Fluorescence from the $3^1\Pi$ state was monitored by a second (violet filtered) PMT as the probe laser frequency was scanned over transitions involving the direct and collisionally populated levels. In general, the number of rotational lines flanking the direct line (the ΔJ progression) observed in this pump-probe experiment is much

smaller than the number observable with the FTS experiment in Lyon. This also limits the ability to record fluorescence from v-changing collisional lines at Lehigh as these lines are approximately an order of magnitude smaller than the $|\Delta J| \leq 4$ collisional lines. Thus, all of the data reported in this dissertation were recorded in Lyon.

Chapter 5

Empirical Model of Collisional Population Transfer

5.1 Overview

In this chapter, I discuss the theoretical basis of our collision experiment and the way we assign uncertainties to the measured quantities. Section 5.2 discusses the population transfer resulting from inelastic collisions. This begins with a general steady state rate equation analysis that can be applied to both rotation changing collisions and to vibration-rotation changing collisions. The results of the rate equation model are then inserted into expressions for the measured fluorescence intensity ratios, which must be treated in slightly different ways for the two types of collisions.

Section 5.3 contains a description of the major sources of uncertainty in our experiment and how we assign uncertainties to the measured intensity ratios.

5.2 Collisional Transfer of Population

The purpose of studying rotation and/or vibration changing collisions is to determine relative and absolute rate coefficients for the various processes. Thus we construct a rate equation model to describe the flow of population between molecular energy levels.

Figure 5.1 shows a schematic diagram of the various processes affecting the population in the excited $2(A)^1\Sigma^+(v', J')$ levels for the single laser experiment carried out in Lyon. The rate equation model provides an expression for the ratio of population in a given collisionally populated level relative to the population in the directly populated level. That population ratio is then related to the fluorescence intensity ratio which is the quantity we measure. The final equations show the dependence of the measured intensity ratios on the various rate coefficients we wish to determine.

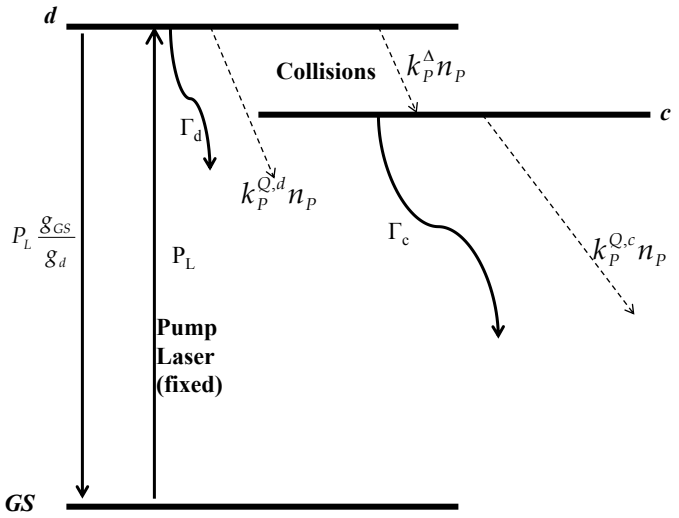

Figure 5.1: Schematic diagram of the collisional and radiative processes involved in the transfer of populations. The pump laser excites ground state (GS) molecules to the directly populated level d. Collisions transfer population from the directly populated level to a collisional level, c, and are designated by the rate constant $k_P^{\Delta J}$, relating. Both states decay by radiation to various lower levels at a total rate Γ_i ($i = c$ or d) and by collisional transfer to all final states (quenching collisions) at a rate $k_P^{Q,i} n_P$. The subscript P represents a particular type of perturber (collisional partner).

The directly excited level, d, is the upper level in the laser excitation $2(A)^1\Sigma^+$ $(v', J') \leftarrow 1(X)^1\Sigma^+$ (v'', J''). Level c is a neighboring level populated by collisions, and can be in the same vibrational level as the directly excited level or can be in a different vibrational state. Both levels d and c are affected by collisional and radiative processes. Figure 5.1 only includes the three previously mentioned levels (GS, d, c) but in reality there are many neighboring levels within the ground and excited states.

5.2.1 The Rate Equation Model

Based on the collisional and radiative population transfer mechanisms depicted in Fig. 5.1, we can write steady-state rate equations for the populations of the directly excited and collisionally populated levels.

$$\frac{dn_d}{dt} = P_L n_{GS} + \sum_P n_P \sum_i k_P^{i\to d} n_i - \left(P_L \frac{g_{GS}}{g_d} + \Gamma_d + \sum_P k_P^{Q,d} n_P \right) n_d = 0 \quad (5.1)$$

$$\frac{dn_c}{dt} = \sum_P k_P^{d\to c} n_P n_d + \sum_P n_P \sum_{i\neq d} k_P^{i\to c} n_i - \left(\Gamma_c + \sum_P k_P^{Q,c} n_P \right) n_c = 0 \quad (5.2)$$

where $n_{d,c}$ are the population number densities of molecules in the directly and collisionally populated levels, respectively, and n_P is the density of perturbing atoms or molecules of type P. P_L is the laser pumping rate, $P_L \frac{g_{GS}}{g_d}$ is the pump laser induced stimulated emission rate, $k_P^{i\to j}$ is the rate constant for transfer of population from level i to level j, $k_P^{Q,i}$ is the rate coefficient for transfer of population out of level i to all final states (quenching) due to the perturber P, and Γ_i is the total radiative rate out of a level i. The laser pump rate P_L is difficult to determine quantitatively due to variations of the laser beam intensity in both the radial and longitudinal directions. Consequently Eq. 5.1 is difficult to solve. However Eq. 5.2 provides the steady state solution

$$\frac{n_c}{n_d} = \frac{\sum_P n_P \left[k_P^{d\to c} + \sum_{i\neq d} k_P^{i\to c} \frac{n_i}{n_d} \right]}{\left[\Gamma + \sum_P k_P^{Q,c} n_P \right]} \quad (5.3)$$

If we now also assume that the experiment is in the "single collision" regime, where all the levels $i \neq d$ obey $\frac{n_i}{n_d} \ll 1$ and hence the second term in the numerator

of Eq. 5.3 is negligible compared to the first, Eq. 5.3 reduces to

$$\frac{n_c}{n_d} = \frac{\sum_P \left(\frac{k_P^{d\to c}}{\Gamma}\right) n_P}{1 + \sum_P \left(\frac{k_P^{Q,c}}{\Gamma}\right) n_P}. \tag{5.4}$$

Note that the single collision regime is a valid assumption if the probability of a collisional transition occurring within one radiative lifetime is small; i.e., if $\sum_P k_P^{d\to c} n_P \ll \Gamma$, since that means that it is very highly unlikely that two such collisions would take place before the excited molecule decays to the ground state.

Within the oven, we have several types of perturbers (possible collision partners). Our data are obtained with different combinations of potassium and either argon or helium buffer gas densities, and we include both types of perturbers in Eq. 5.4. Other species not included in our analysis are sodium atoms and K_2, Na_2 and NaK molecules. The number of molecules is very small (n_{K_2}, n_{Na_2}, $n_{NaK} \ll n_K$, n_{Na}), so we neglect them. In addition, $n_{Na} \ll n_K$, so we can also neglect collisions with sodium atoms. However, later we will show (in Chapter 6) how the sodium atom collisions can be taken into account (approximately) after the fact. Therefore, labeling terms with BG for buffer gas and K for potassium, we obtain

$$\frac{n_c}{n_d} = \frac{\frac{k_{BG}^{\Delta}}{\Gamma} n_{BG} + \frac{k_K^{\Delta}}{\Gamma} n_K}{1 + \frac{k_{BG}^{Q,c}}{\Gamma} n_{BG} + \frac{k_K^{Q,c}}{\Gamma} n_K}. \tag{5.5}$$

When fluorescence is emitted during a transition between upper level u and lower level l, the measured laser-induced fluorescence intensity ($I_{u\to l}$) is given by

$$I_{u\to l} = h\nu_{u\to l} n_u \Gamma_{u\to l} \varepsilon_{u\to l} V \frac{d\Omega}{4\pi} F. \tag{5.6}$$

Here $h\nu_{u\to l}$ represents the energy of a single fluorescence photon, n_u is the density of molecules in the upper level, and $\Gamma_{u\to l}$ is the radiative rate for the observed transition (Einstein A coefficient discussed in Chapter 2). V is the the observation volume within the oven, $\frac{\mathrm{d}\Omega}{4\pi}$ is the fraction of the total 4π sterradian emission solid angle that is focused on the detector, and F is an anisotropy factor, which is due to the fact that the fluorescence is polarized and hence the emission is not isotropic. $\varepsilon_{u\to l}$ represents the detector efficiency at the given transition energy. Because some of these factors are not well known absolutely, we always look at ratios of a collisional line intensity to a direct line intensity; i.e.,

$$\frac{I_{c\to l_c}}{I_{d\to l_d}} = \frac{h\nu_{c\to l_c} n_c \Gamma_{c\to l_c} \varepsilon_{c\to l_c} V \frac{d\Omega}{4\pi} F_{c\to l_c}}{h\nu_{d\to l_d} n_d \Gamma_{d\to l_d} \varepsilon_{d\to l_d} V \frac{d\Omega}{4\pi} F_{d\to l_d}}. \tag{5.7}$$

To simplify this expression, we make several reasonable assumptions. First, we assume that the detection solid angle and the observation volume within the oven do not change during the course of a measurement. We also only compare P collisional lines to P direct lines (and R lines to R lines), so that the anisotropy factor F also cancels (I will return to this point in Chapter 6). The ratio of the spectral efficiencies of the detector $\frac{\varepsilon_{c\to l_c}}{\varepsilon_{d\to l_d}}$ can be taken to be one when comparing closely spaced rotational lines. However, for the $2(A)^1\Sigma^+(v'=0,1,2) \to 1(X)^1\Sigma^+(v'')$ transitions we study, the fluorescence spans the frequency range from 10000 cm^{-1} to 12000 cm^{-1}. It is erroneous to assume that the detector efficiency is constant through this large frequency range. Therefore when comparing collisional and direct line intensities from within a single vibrational band, we assume the efficiency factors are identical. However, when comparing collisional and direct lines from different vibrational levels (v changing collisions), the different efficiency factors must be taken into account.

If we label $I_{c\to l_c}$ as the intensity of the $c \to l_c$ fluorescence corresponding to transitions from a particular collisionally populated level c to some lower level l_c and $I_{d\to l_d}$ as the intensity of fluorescence corresponding to transitions from directly populated level d to a lower level l_d, we find the ratio

$$R_F \equiv \frac{I_{c\to l_c}}{I_{d\to l_d}} = \frac{\nu_{c\to l_c}\Gamma_{c\to l_c}}{\nu_{d\to l_d}\Gamma_{d\to l_d}} \frac{\varepsilon_{c\to l_c}}{\varepsilon_{d\to l_d}} \frac{n_c}{n_d} \tag{5.8}$$

as the quantity that we determine experimentally. If we use Eq. 2.45 for the Einstein A coefficients (Γ factors) from our discussion in Chapter 2 on electronic transitions

$$\Gamma_{u\to l} \equiv A_{ul} = \frac{8\pi^2\nu^3_{u\to l}S_{J_u,J_l}}{3\varepsilon_0 c^3\hbar(2J_u+1)} \left| \int \chi_u^{v*}\chi_l^v dR \int \phi_u^{el*}\hat{\mu_{el}}\phi_l^{el} \right|^2 \tag{5.9}$$

and insert this into Eq. 5.8, the general expression for the intensity ratio becomes

$$R_F = \frac{I_{c\to l_c}}{I_{d\to l_d}} = \frac{\nu^4_{c\to l_c}}{\nu^4_{d\to l_d}} \frac{\varepsilon_{c\to l_c}}{\varepsilon_{d\to l_d}} \frac{n_c}{n_d} \frac{\frac{S_{J_c,J_{l_c}}}{(2J_c+1)}}{\frac{S_{J_d,J_{l_d}}}{(2J_d+1)}} \frac{|\int \chi_c^{v*}\chi_{l_c}^v dR \int \phi_c^{el*}\hat{\mu_{el}}\phi_{l_c}^{el}|^2}{|\int \chi_d^{v*}\chi_{l_d}^v dR \int \phi_d^{el*}\hat{\mu_{el}}\phi_{l_d}^{el}|^2}. \tag{5.10}$$

5.2.2 Rotation Changing Collisions

If we consider a collision that changes only the rotational level and compare intensities of P to P (or R to R) lines in the same vibrational band, the integrals over the vibrational and electronic wavefunctions are the same for the directly populated level d and the collisional level c. In addition, if we compare fluorescence lines that are part of the same vibrational band, the emission frequencies are sufficiently close

that we can take $\frac{\varepsilon_{c\to l_c}}{\varepsilon_{d\to l_d}} \approx 1$. Thus the intensity ratio R_F reduces to

$$R_F = \frac{I_{c\to l_c}}{I_{d\to l_d}} = \frac{\nu^4_{c\to l_c}}{\nu^4_{d\to l_d}} \frac{n_c}{n_d} \frac{\frac{S_{J_c,J_{l_c}}}{(2J_c+1)}}{\frac{S_{J_d,J_{l_d}}}{(2J_d+1)}}. \tag{5.11}$$

As mentioned in Chapter 2, the Hönl-London factors, $S_{J',J''}$, are determined by the rotational numbers of the levels involved in the specific transitions, the line type (P and R in this experiment), as well as the transition type ([36], p. 208). For transitions between two $^1\Sigma$ states, where $\Delta\Lambda = 0$, the Hönl-London factors are given by $S^R_{J,J-1} = J$ and $S^P_{J,J+1} = J + 1$. Therefore the intensity ratio can be written as

$$\left(\frac{I_{c\to l_c}}{I_{d\to l_d}}\right)_{\text{R-lines}} = \frac{\nu^4_{c\to l_c}}{\nu^4_{d\to l_d}} \frac{n_c}{n_d} \frac{\frac{J_c}{(2J_c+1)}}{\frac{J_d}{(2J_d+1)}} \tag{5.12}$$

and

$$\left(\frac{I_{c\to l_c}}{I_{d\to l_d}}\right)_{\text{P-lines}} = \frac{\nu^4_{c\to l_c}}{\nu^4_{d\to l_d}} \frac{n_c}{n_d} \frac{\frac{J_c+1}{(2J_c+1)}}{\frac{J_d+1}{(2J_d+1)}}. \tag{5.13}$$

It is apparent that the ratio of the J dependent factors is ~ 1 when J_d is large and ΔJ is small, but it is easy to include this factor regardless. Solving Eqs. 5.12 and 5.13 for $\frac{n_c}{n_d}$ allows us to combine them with the rate equation result 5.5 to yield

$$\frac{I_{c\to l_c}}{I_{d\to l_d}} \frac{\nu^4_{d\to l_d}}{\nu^4_{c\to l_c}} \frac{\frac{J_d}{(2J_d+1)}}{\frac{J_c}{(2J_c+1)}} = \left(\frac{n_c}{n_d}\right)_{\text{R-lines}} = \frac{\frac{k^\Delta_{BG}}{\Gamma} n_{BG} + \frac{k^\Delta_K}{\Gamma} n_K}{1 + \frac{k^{Q,c}_{BG}}{\Gamma} n_{BG} + \frac{k^{Q,c}_K}{\Gamma} n_K} \tag{5.14a}$$

$$\frac{I_{c\to l_c}}{I_{d\to l_d}} \frac{\nu^4_{d\to l_d}}{\nu^4_{c\to l_c}} \frac{\frac{J_d+1}{(2J_d+1)}}{\frac{J_c+1}{(2J_c+1)}} = \left(\frac{n_c}{n_d}\right)_{\text{P-lines}} = \frac{\frac{k^\Delta_{BG}}{\Gamma} n_{BG} + \frac{k^\Delta_K}{\Gamma} n_K}{1 + \frac{k^{Q,c}_{BG}}{\Gamma} n_{BG} + \frac{k^{Q,c}_K}{\Gamma} n_K}. \tag{5.14b}$$

These equations are valid for any value of ΔJ as long as there is no change in upper vibrational level and we compare fluorescence intensities of transitions to the same

ground state vibrational level.

5.2.3 Vibration-Rotation Changing Collisions

In a collision that changes *both* vibrational and rotational level, we return to Eq. 5.7

$$\frac{I_{c\to l_c}}{I_{d\to l_d}} = \frac{h\nu_{c\to l_c} n_c \Gamma_{c\to l_c} \varepsilon_{c\to l_c} V \frac{d\Omega}{4\pi} F_{c\to l_c}}{h\nu_{d\to l_d} n_d \Gamma_{d\to l_d} \varepsilon_{d\to l_d} V \frac{d\Omega}{4\pi} F_{d\to l_d}}. \tag{5.15}$$

As discussed previously in Sec. 5.2.1, we still assume that the detection solid angle and the observation volume within the oven do not change, and that the anisotropy factors cancel out. With these assumptions, we can solve Eq. 5.15 for the population ratio

$$\frac{n_c}{n_d} = \frac{n^{col}_{v_c,J_c}}{n^{dir}_{v_d,J_d}} = \frac{I_{v_c,J_c\to v_{lc},J_c\pm1}}{I_{v_d,J_d\to v_{ld},J_d\pm1}} \frac{\nu_{v_d,J_d\to v_{ld},J_d\pm1}}{\nu_{v_c,J_c\to v_{lc},J_c\pm1}} \frac{\varepsilon_{v_d,J_d\to v_{ld},J_d\pm1}}{\varepsilon_{v_c,J_c\to v_{lc},J_c\pm1}} \frac{\Gamma_{v_d,J_d\to v_{ld},J_d\pm1}}{\Gamma_{v_c,J_c\to v_{lc},J_c\pm1}}. \tag{5.16}$$

In this expression, we have been more explicit in indicating the vibrational and rotational quantum numbers of the levels involved in the observed transitions: v_{l_c} and v_{l_d} are the lower (ground) vibrational states of the observed transitions. Plus signs in the transition labels are used for P lines while minus signs are used for R lines. The ratios of radiative rates can be calculated fairly accurately using the program LEVEL 8.0 [59]. The relative efficiency factors are not known when we compare intensities of lines belonging to different vibrational bands that are separated in frequency. However, we can determine these factors by comparing the measured intensities of different lines to intensities of standard reference lines designated for each $2(A)^1\Sigma^+$ state vibrational level. In Table 5.1 we list the chosen reference transitions for each directly populated $2(A)^1\Sigma^+$ level studied in this work: (v_d, J_d) =(0, 14), (0, 30), (1, 26) and (2, 44). These reference transitions are used to normalize

the measured intensities when a collisionally populated level lies in a different vibrational state than the directly populated level, as will be shown below.

$2(A)^1\Sigma^+$ Directly Pop. Level and Reference Transition		Primary or Subsidiary
(v'_d, J'_d)	$(v'_d, J'_d) \rightarrow (v''_d, J'_d \pm 1)$	
(0,14)	$2(A)^1\Sigma^+$ (v'=0,J'=14)$\rightarrow$ $1(X)^1\Sigma^+$ (v'=9,J'=13,15)	Subsidiary
(0,14)	$2(A)^1\Sigma^+$ (v'=0,J'=14)$\rightarrow$ $1(X)^1\Sigma^+$ (v'=10,J'=13,15)	Primary
(0,30)	$2(A)^1\Sigma^+$ (v'=0,J'=30)$\rightarrow$ $1(X)^1\Sigma^+$ (v'=9,J'=29,31)	Subsidiary
(0,30)	$2(A)^1\Sigma^+$ (v'=0,J'=30)$\rightarrow$ $1(X)^1\Sigma^+$ (v'=10,J'=29,31)	Primary
(1,26)	$2(A)^1\Sigma^+$ (v'=1,J'=26)$\rightarrow$ $1(X)^1\Sigma^+$ (v'=11,J'=25,27)	Subsidiary
(1,26)	$2(A)^1\Sigma^+$ (v'=1,J'=26)$\rightarrow$ $1(X)^1\Sigma^+$ (v'=12,J'=25,27)	Primary
(2,44)	$2(A)^1\Sigma^+$ (v'=2,J'=44)$\rightarrow$ $1(X)^1\Sigma^+$ (v'=14,J'=43,45)	Subsidiary
(2,44)	$2(A)^1\Sigma^+$ (v'=2,J'=44)$\rightarrow$ $1(X)^1\Sigma^+$ (v'=15,J'=43,45)	Primary

Table 5.1: The reference transitions for each directly populated level. The reference bands were chosen based on stronger direct line intensities (Franck-Condon Factors) and signal to noise ratios within the spectra. The table includes both P and R lines, which only differ in the $1(X)^1\Sigma^+$ rotational level of the transitions.

For example, when we directly pump level $(v_d, J_d) = (0, 30)$ and wish to analyze $2(A)^1\Sigma^+ (v_c = 1, J_c = 15) \rightarrow 1(X)^1\Sigma^+ (v_{lc} = 12, J_{lc} = 16)$ fluorescence from the collisionally populated level $(v_c, J_c) = (1, 15)$, we would first determine the product of ratios

$$\left(\frac{I_{1,15\rightarrow 12,16}}{I_{1,26\rightarrow 12,27}}\right)\left(\frac{I_{1,26\rightarrow 12,27}}{I_{0,30\rightarrow 10,31}}\right). \tag{5.17}$$

If we wish to analyze the collisional P line in the $v_c = 1 \rightarrow v_{lc} = 11$ band, we instead use the "subsidiary" reference line $2(A)^1\Sigma^+ (v_c = 1, J_c = 26) \rightarrow 1(X)^1\Sigma^+ (v_{lc} = 11, J_{lc} = 27)$.

Next, we consider the ratio of a specific direct line (P or R) intensity to the total

intensity of all (P or R) transitions for that level. From Eq. 5.15 we find

$$\left(\frac{I^{dir}_{v_d,J_d\rightarrow v_{ld},J_d\pm1}}{\sum\limits_{v''} I^{dir}_{v_d,J_d\rightarrow v'',J_d\pm1}} \right) = \frac{\nu_{v_d,J_d\rightarrow v_{ld},J_d\pm1}\varepsilon_{v_d,J_d\rightarrow v_{ld},J_d\pm1}\Gamma_{v_d,J_d\rightarrow v_{ld},J_d\pm1}}{\sum\limits_{v''} \nu_{v_d,J_d\rightarrow v'',J_d\pm1}\varepsilon_{v_d,J_d\rightarrow v'',J_d\pm1}\Gamma_{v_d,J_d\rightarrow v'',J_d\pm1}}. \tag{5.18}$$

Note that since each line in both the numerator and denominator of 5.18 originates from the same upper level (v_d, J_d), the level densities cancel in the ratio. These ratios can be determined from the experimental spectra shown in Figs. 5.2, 5.3, 5.4, and 5.5. Table 5.2 includes the values used for analysis for a direct pump of (0, 14), Table 5.3 for (0, 30), Table 5.4 for (1, 26) and Table 5.5 for (2, 44). The specific values included are the observed intensity ratios (branching ratios) for these strong lines corresponding to transitions from the directly excited $2(A)^1\Sigma^+$ (v_d, J_d) level.

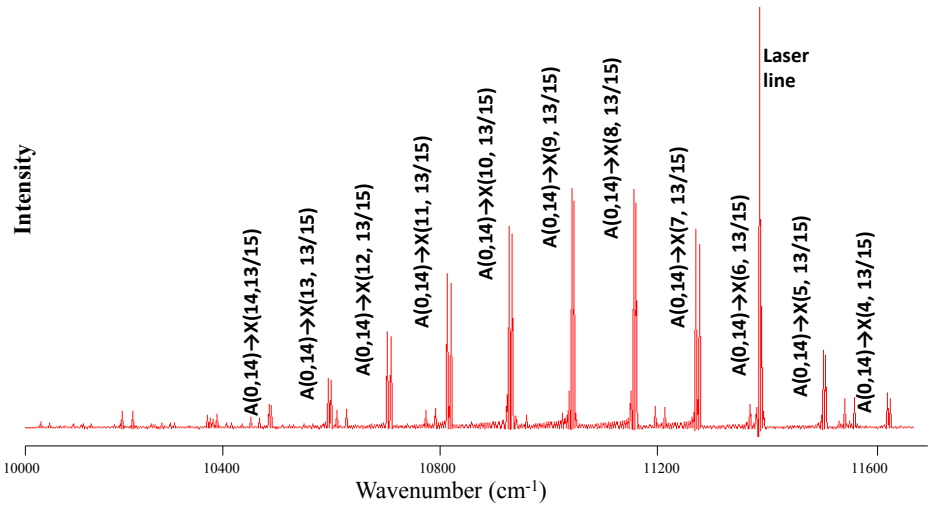

Figure 5.2: Fluorescence emission following direct population of $2(A)^1\Sigma^+$ (0, 14). The direct line branching ratios are independent of collisions, or variations in temperature or pressure.

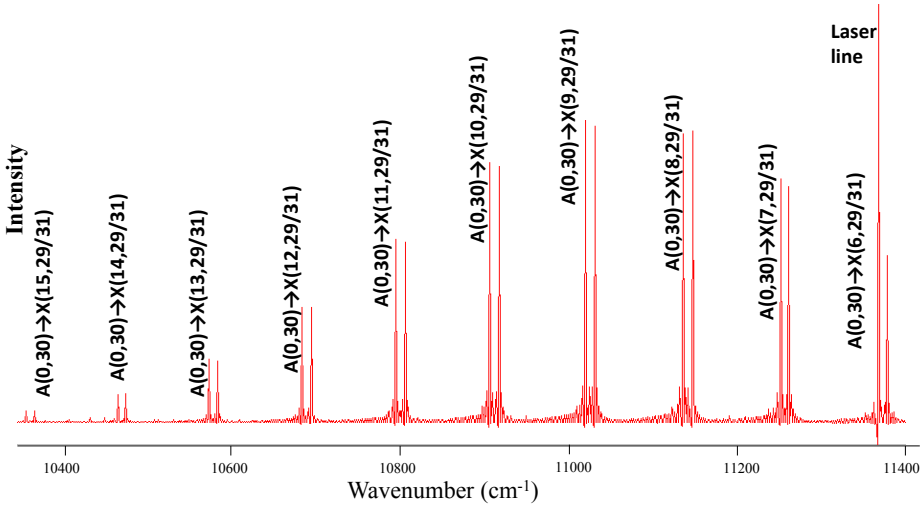

Figure 5.3: Fluorescence emission following direct population of $2(A)^1\Sigma^+$ (0, 30). The direct line branching ratios are independent of collisions, or variations in temperature or pressure.

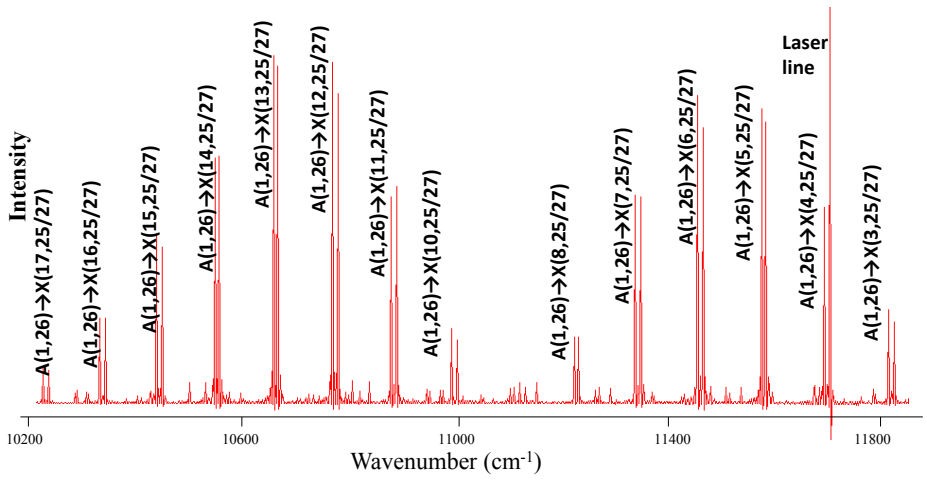

Figure 5.4: Fluorescence emission following direct population of $2(A)^1\Sigma^+$ (1, 26). The direct line branching ratios are independent of collisions, or variations in temperature or pressure.

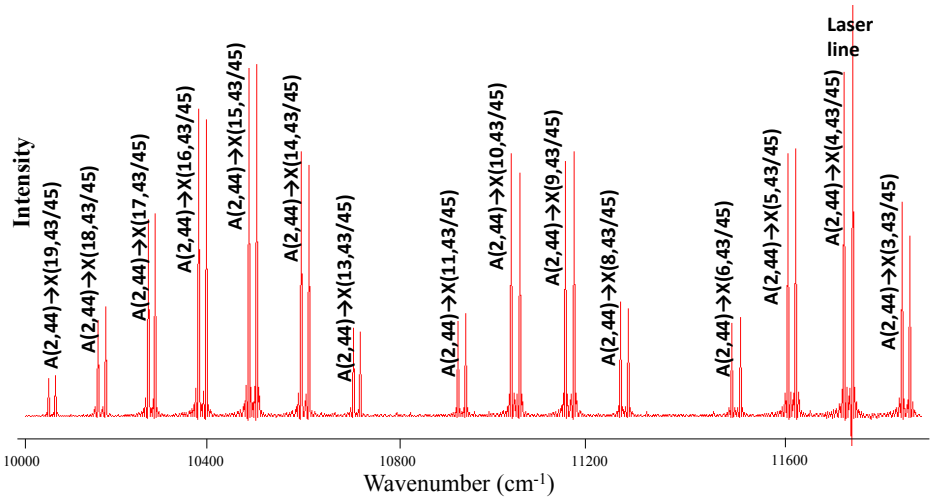

Figure 5.5: Fluorescence emission following direct population of $2(A)^1\Sigma^+$ (2, 44). The direct line branching ratios are independent of collisions, or variations in temperature or pressure.

We determine separate ratios for P and R transitions since our assumptions require that only P line intensities are compared to P line intensities (and the same for R lines). Note also that these ratios are constants for our experiments since they don't depend on experimental conditions that change over time. Thus, once they are determined, they can be set for all future work.

$2(A)^1\Sigma^+$ (0, 14) Branching Ratios					
	v_X	$\frac{I_{0,14\rightarrow v_X,J''}}{\sum_{v''} I_{0,14\rightarrow v'',J''}}$	$\frac{A_{0,14\rightarrow v_X,J''}}{\sum_{v''} A_{0,14\rightarrow v'',J''}}$	$\frac{I_{\rm ratio}}{A_{\rm ratio}}$	Franck-Condon Factors
P ($J''=15$)	14	0.0162	0.0192	0.8467	2.11E-02
	13	0.0340	0.0388	0.8757	4.17E-02
	12	0.0666	0.0685	0.9721	7.19E-02
	11	0.1066	0.1051	1.0142	1.08E-01
	10	0.1395	0.1399	0.9972	1.40E-01
	9	0.1657	0.1610	1.0296	1.58E-01
	8	0.1649	0.1590	1.0369	1.52E-01
	7	0.1373	0.1336	1.0277	1.25E-01
	6	0.0913	0.0943	0.9684	8.63E-02
	5	0.0536	0.0549	0.9755	4.92E-02
	4	0.0243	0.0257	0.9443	2.25E-02
R ($J''=13$)	14	0.0163	0.0194	0.8406	2.13E-02
	13	0.0350	0.0392	0.8927	4.21E-02
	12	0.0674	0.0690	0.9776	7.23E-02
	11	0.1064	0.1056	1.0077	1.08E-01
	10	0.1430	0.1402	1.0197	1.40E-01
	9	0.1671	0.1610	1.0376	1.58E-01
	8	0.1656	0.1587	1.0432	1.52E-01
	7	0.1347	0.1331	1.0116	1.25E-01
	6	0.0896	0.0938	0.9550	8.58E-02
	5	0.0533	0.0545	0.9778	4.88E-02
	4	0.0217	0.0255	0.8526	2.23E-02

Table 5.2: Observed branching ratios for both P and R lines originating in the level $2(A)^1\Sigma^+$ (0, 14). This list does not include ground state vibrational levels lower than $v''=4$ or higher than $v''=14$ since the lines associated with these levels are very weak due to the small Franck-Condon factors. The fourth column indicates the ratio of the Einstein A coefficient for the indicated tansition relative to the total for all the bands listed in the table. The fifth column gives the ratio of the third and fourth columns, which is a rough indication of the relative efficiency factors. The final column lists the calculated Franck-Condon factors from LEVEL 8.0 for the given band. The listed Franck-Condon factors sum to 0.975 for both P and R branches, indicating that about 97.5% of the total emission has been included in this table.

$2(A)^1\Sigma^+$ (0, 30) Branching Ratios					
	v_X	$\frac{I_{0,30\rightarrow v_X,J''}}{\sum_{v''} I_{0,30\rightarrow v'',J''}}$	$\frac{A_{0,30\rightarrow v_X,J''}}{\sum_{v''} A_{0,30\rightarrow v'',J''}}$	$\frac{I_{\text{ratio}}}{A_{\text{ratio}}}$	Franck-Condon Factors
P ($J''=31$)	15	0.0068	0.0088	0.7758	9.21E-03
	14	0.0166	0.0206	0.8066	2.10E-02
	13	0.0377	0.0418	0.9015	4.17E-02
	12	0.0688	0.0739	0.9306	7.20E-02
	11	0.1097	0.1135	0.9665	1.08E-01
	10	0.1561	0.1511	1.0334	1.40E-01
	9	0.1814	0.1737	1.0440	1.58E-01
	8	0.1734	0.1714	1.0118	1.52E-01
	7	0.1462	0.1438	1.0164	1.25E-01
	6	0.1033	0.1013	1.0191	8.61E-02
R ($J''=29$)	15	0.0068	0.0090	0.7558	9.48E-03
	14	0.0173	0.0211	0.8236	2.15E-02
	13	0.0375	0.0426	0.8812	4.25E-02
	12	0.0701	0.0748	0.9364	7.29E-02
	11	0.1098	0.1144	0.9604	1.09E-01
	10	0.1560	0.1516	1.0291	1.41E-01
	9	0.1802	0.1735	1.0385	1.58E-01
	8	0.1773	0.1705	1.0396	1.52E-01
	7	0.1436	0.1425	1.0072	1.24E-01
	6	0.1014	0.1000	1.0137	8.51E-02

Table 5.3: Observed branching ratios for both P and R lines originating in the level $2(A)^1\Sigma^+$ (0, 30). This list does not include ground state vibrational levels lower than $v''=6$ or higher than $v''=15$ since the lines associated with these levels are very weak due to the small Franck-Condon factors. The listed Franck-Condon factors sum to 0.913 for the P branch and 0.915 for the R branch, indicating that about 91.4% of the total emission has been included in this table.

$2(A)^1\Sigma^+$ (1, 26) Branching Ratios					
	v_X	$\frac{I_{1,26\rightarrow v_X,J''}}{\sum_{v''} I_{1,26\rightarrow v'',J''}}$	$\frac{A_{1,26\rightarrow v_X,J''}}{\sum_{v''} A_{1,26\rightarrow v'',J''}}$	$\frac{I_{\text{ratio}}}{A_{\text{ratio}}}$	Franck-Condon Factors
P ($J''=27$)	17	0.0131	0.0159	0.8266	1.84E-02
	16	0.0320	0.0351	0.9095	3.97E-02
	15	0.0635	0.0645	0.9845	7.11E-02
	14	0.0917	0.0974	0.9418	1.05E-01
	13	0.1302	0.1180	1.1032	1.24E-01
	12	0.1278	0.1092	1.1703	1.12E-01
	11	0.0773	0.0690	1.1204	6.91E-02
	10	0.0279	0.0204	1.3670	2.00E-02
	9	0.0000	0.0001	0.0000	8.92E-05
	8	0.0247	0.0268	0.9221	2.51E-02
	7	0.0778	0.0810	0.9604	7.42E-02
	6	0.1153	0.1206	0.9557	1.08E-01
	5	0.1104	0.1183	0.9327	1.04E-01
	4	0.0734	0.0825	0.8897	7.08E-02
	3	0.0349	0.0411	0.8495	3.46E-02
R ($J''=25$)	17	0.0131	0.0163	0.7998	1.89E-02
	16	0.0336	0.0358	0.9383	4.05E-02
	15	0.0618	0.0654	0.9450	7.20E-02
	14	0.0976	0.0981	0.9947	1.05E-01
	13	0.1333	0.1181	1.1294	1.24E-01
	12	0.1225	0.1084	1.1301	1.11E-01
	11	0.0857	0.0676	1.2674	6.77E-02
	10	0.0251	0.0194	1.2903	1.90E-02
	9	0.0000	0.0002	0.0000	1.70E-04
	8	0.0262	0.0278	0.9423	2.60E-02
	7	0.0814	0.0821	0.9923	7.51E-02
	6	0.1090	0.1208	0.9017	1.08E-01
	5	0.1112	0.1177	0.9439	1.03E-01
	4	0.0675	0.0816	0.8263	7.01E-02
	3	0.0321	0.0405	0.7924	3.41E-02

Table 5.4: Observed branching ratios for both P and R lines originating in the level $2(A)^1\Sigma^+$ (1, 26). This list does not include ground state vibrational levels lower than $v''=3$ or higher than $v''=17$ since the lines associated with these levels are very weak due to the small Franck-Condon factors. The listed Franck-Condon factors sum to 0.976 for the P branch and 0.975 for the R branch, indicating that about 97.5% of the total emission has been included in this table.

$2(A)^1\Sigma^+$ (2, 44) Branching Ratios					
	v_X	$\frac{I_{2,44\rightarrow v_X,J''}}{\sum_{v''} I_{2,44\rightarrow v'',J''}}$	$\frac{A_{2,44\rightarrow v_X,J''}}{\sum_{v''} A_{2,44\rightarrow v'',J''}}$	$\frac{I_{\text{ratio}}}{A_{\text{ratio}}}$	Franck-Condon Factors
P ($J''=45$)	19	0.0134	0.0194	0.6912	2.23E-02
	18	0.0366	0.0431	0.8479	4.84E-02
	17	0.0725	0.0766	0.9466	8.36E-02
	16	0.1110	0.1059	1.0473	1.13E-01
	15	0.1203	0.1085	1.1096	1.13E-01
	14	0.0838	0.0728	1.1505	7.39E-02
	13	0.0315	0.0213	1.4766	2.11E-02
	12	0.0000	0.0003	0.0000	3.27E-04
	11	0.0305	0.0314	0.9695	2.97E-02
	10	0.0839	0.0763	1.0991	7.05E-02
	9	0.0915	0.0761	1.2018	6.88E-02
	8	0.0359	0.0293	1.2279	2.59E-02
	7	0.0000	0.0000	0.0000	7.41E-06
	6	0.0275	0.0338	0.8127	2.86E-02
	5	0.0872	0.0960	0.9083	7.96E-02
	4	0.1111	0.1199	0.9270	9.73E-02
	3	0.0634	0.0892	0.7108	7.09E-02
R ($J''=43$)	19	0.0148	0.0203	0.7300	2.33E-02
	18	0.0363	0.0446	0.8138	5.00E-02
	17	0.0755	0.0782	0.9659	8.53E-02
	16	0.1133	0.1066	1.0632	1.13E-01
	15	0.1158	0.1073	1.0794	1.11E-01
	14	0.0835	0.0703	1.1880	7.13E-02
	13	0.0266	0.0193	1.3771	1.92E-02
	12	0.0000	0.0007	0.0000	6.41E-04
	11	0.0329	0.0334	0.9838	3.15E-02
	10	0.0888	0.0773	1.1496	7.14E-02
	9	0.0855	0.0747	1.1445	6.76E-02
	8	0.0327	0.0274	1.1931	2.42E-02
	7	0.0000	0.0001	0.0000	7.62E-05
	6	0.0321	0.0357	0.9008	3.02E-02
	5	0.0906	0.0972	0.9320	8.06E-02
	4	0.1155	0.1193	0.9681	9.69E-02
	3	0.0560	0.0877	0.6387	6.98E-02

Table 5.5: Observed branching ratios for both P and R lines originating in the level $2(A)^1\Sigma^+$ (2, 44). This list does not include ground state vibrational levels lower than $v''=3$ or higher than $v''=19$ since the lines associated with these levels are very weak due to the small Franck-Condon factors. The listed Franck-Condon factors sum to 0.947 for the P branch and 0.947 for the R branch, indicating that about 94.7% of the total emission has been included in this table.

Returning to Eq. 5.16

$$\frac{n^{col}_{v_c,J_c}}{n^{dir}_{v_d,J_d}} = \frac{I_{v_c,J_c\rightarrow v_{lc},J_c\pm1}}{I_{v_d,J_d\rightarrow v_{ld},J_d\pm1}} \frac{\nu_{v_d,J_d\rightarrow v_{ld},J_d\pm1}}{\nu_{v_c,J_c\rightarrow v_{lc},J_c\pm1}} \frac{\varepsilon_{v_d,J_d\rightarrow v_{ld},J_d\pm1}}{\varepsilon_{v_c,J_c\rightarrow v_{lc},J_c\pm1}} \frac{\Gamma_{v_d,J_d\rightarrow v_{ld},J_d\pm1}}{\Gamma_{v_c,J_c\rightarrow v_{lc},J_c\pm1}}, \tag{5.19}$$

we can write

$$\frac{n^{col}_{v_c,J_c}}{n^{dir}_{v_d,J_d}} = \frac{I_{v_c,J_c\rightarrow v_{lc},J_c\pm1}}{I_{v_d,J_d\rightarrow v_{ld},J_d\pm1}} \frac{\nu_{v_d,J_d\rightarrow v_{ld},J_d\pm1}}{\nu_{v_c,J_c\rightarrow v_{lc},J_c\pm1}} \frac{\varepsilon_{v_d,J_d\rightarrow v_{ld},J_d\pm1}}{\varepsilon_{v_c,J_c\rightarrow v_{lc},J_c\pm1}} \frac{\Gamma_{v_d,J_d\rightarrow v_{ld},J_d\pm1}}{\Gamma_{v_c,J_{cr}\rightarrow v_{lc},J_{cr}\pm1}} \left(\frac{\Gamma_{v_c,J_{cr}\rightarrow v_{lc},J_{cr}\pm1}}{\Gamma_{v_c,J_c\rightarrow v_{lc},J_c\pm1}}\right), \tag{5.20}$$

where we introduce the collisional reference transition $v_c, J_{cr} \rightarrow v_{lc}, J_{cr} \pm 1$. The relative ratio of Γ factors of two rotational lines A and B within the same band can be obtained from Eq. 5.9

$$\frac{\Gamma_{v,J_A\rightarrow v'',J_A\pm1}}{\Gamma_{v,J_B\rightarrow v'',J_B\pm1}} = \frac{\nu^3_{v,J_A\rightarrow v'',J_A\pm1}}{\nu^3_{v,J_B\rightarrow v'',J_B\pm1}} \frac{S_{J_A,J_A\pm1}}{S_{J_B,J_B\pm1}} \frac{(2J_B+1)}{(2J_A+1)} \tag{5.21}$$

since the vibrational and electronic terms cancel. Thus Eq. 5.20 becomes

$$\frac{n^{col}_{v_c,J_c}}{n^{dir}_{v_d,J_d}} = \frac{I_{v_c,J_c\rightarrow v_{lc},J_c\pm1}}{I_{v_d,J_d\rightarrow v_{ld},J_d\pm1}} \frac{\nu_{v_d,J_d\rightarrow v_{ld},J_d\pm1}}{\nu_{v_c,J_c\rightarrow v_{lc},J_c\pm1}} \frac{\varepsilon_{v_d,J_d\rightarrow v_{ld},J_d\pm1}}{\varepsilon_{v_c,J_c\rightarrow v_{lc},J_c\pm1}} \frac{\Gamma_{v_d,J_d\rightarrow v_{ld},J_d\pm1}}{\Gamma_{v_c,J_{cr}\rightarrow v_{lc},J_{cr}\pm1}} \frac{\nu^3_{v_c,J_{cr}\rightarrow v_{lc},J_{cr}\pm1} S_{J_{cr},J_{cr}\pm1}}{\nu^3_{v_c,J_c\rightarrow v_{lc},J_c\pm1} S_{J_c,J_c\pm1}} \frac{(2J_c+1)}{(2J_{cr}+1)} \tag{5.22}$$

Equation 5.22 now includes the Hönl-London factors for the reference and collisional lines. Figure 5.6 shows that both lines originate from the same upper vibrational level v_c within the $2(A)^1\Sigma^+$ state and radiate down to the same $1(X)^1\Sigma^+$ vibrational level, v_{lc}.

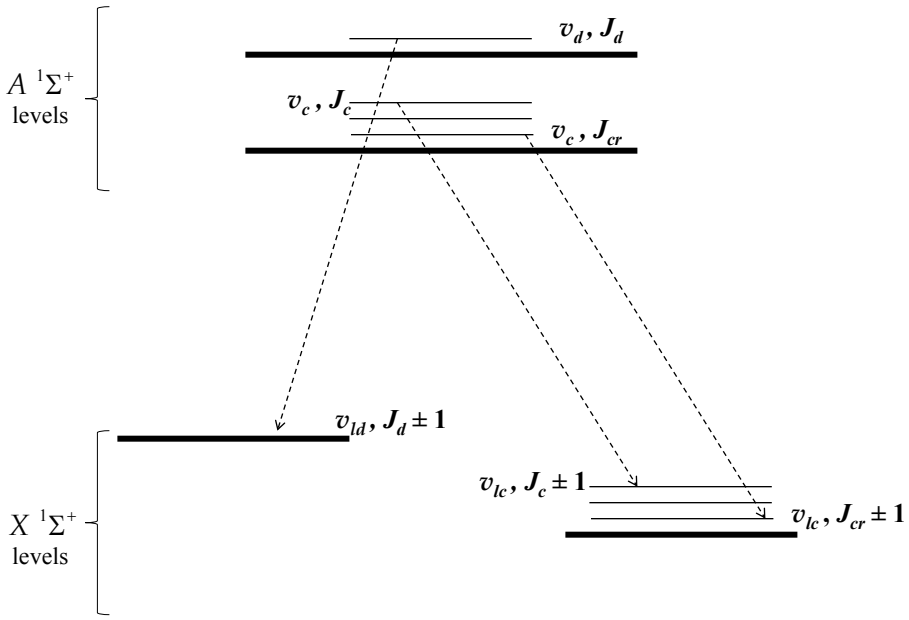

Figure 5.6: Schematic of the transitions and levels discussed in the derivation in this section. The $2(A)^1\Sigma^+$ levels fluoresce in transitions down to the various $1(X)^1\Sigma^+$ levels. It is important to note that the collisional and reference lines both begin and end in the same vibrational levels of the $2(A)^1\Sigma^+$ and $1(X)^1\Sigma^+$ states, respectively.

We now relate the relative efficiencies between the collisional and direct lines to the branching ratios of the direct and reference bands. We accomplish this by expanding the ε and Γ terms in Eq. 5.22. We begin by multiplying Eq. 5.22 on the right by $(\varepsilon_{v_c,J_{cr}\to v_{lc},J_{cr}\pm1}/\varepsilon_{v_c,J_{cr}\to v_{lc},J_{cr}\pm1}) = 1$. This yields

$$\frac{n^{col}_{v_c,J_c}}{n^{dir}_{v_d,J_d}} = \frac{I_{v_c,J_c\to v_{lc},J_c\pm1}}{I_{v_d,J_d\to v_{ld},J_d\pm1}} \frac{\nu_{v_d,J_d\to v_{ld},J_d\pm1}}{\nu_{v_c,J_c\to v_{lc},J_c\pm1}} \frac{\varepsilon_{v_d,J_d\to v_{ld},J_d\pm1}}{\varepsilon_{v_c,J_{cr}\to v_{lc},J_{cr}\pm1}} \frac{\varepsilon_{v_c,J_{cr}\to v_{lc},J_{cr}\pm1}}{\varepsilon_{v_c,J_c\to v_{lc},J_c\pm1}} \times \frac{\Gamma_{v_d,J_d\to v_{ld},J_d\pm1}}{\Gamma_{v_c,J_{cr}\to v_{lc},J_{cr}\pm1}} \frac{\nu^3_{v_c,J_{cr}\to v_{lc},J_{cr}\pm1} S_{J_{cr},J_{cr}\pm1}}{\nu^3_{v_c,J_c\to v_{lc},J_c\pm1} S_{J_c,J_c\pm1}} \frac{(2J_c+1)}{(2J_{cr}+1)}. \quad (5.23)$$

Next we substitute in Eq. 5.18 for the product $\nu_{v_d,J_d\to v_{ld},J_d\pm1}\varepsilon_{v_d,J_d\to v_{ld},J_d\pm1}\Gamma_{v_d,J_d\to v_{ld},J_d\pm1}$ and a similar expression for $\nu_{v_c,J_{cr}\to v_{lc},J_{cr}\pm1}\varepsilon_{v_c,J_{cr}\to v_{lc},J_{cr}\pm1}\Gamma_{v_c,J_{cr}\to v_{lc},J_{cr}\pm1}$.

$$\begin{aligned}\frac{n^{col}_{v_c,J_c}}{n^{dir}_{v_d,J_d}} = \frac{I_{v_c,J_c\to v_{lc},J_c\pm1}}{I_{v_d,J_d\to v_{ld},J_d\pm1}}\frac{\nu_{v_c,J_{cr}\to v_{lc},J_{cr}\pm1}}{\nu_{v_c,J_c\to v_{lc},J_c\pm1}}\frac{\varepsilon_{v_c,J_{cr}\to v_{lc},J_{cr}\pm1}}{\varepsilon_{v_c,J_c\to v_{lc},J_c\pm1}} \\ \times\left(\frac{I^{dir}_{v_d,J_d\to v_{ld},J_d\pm1}}{\sum\limits_{v''} I^{dir}_{v_d,J_d\to v'',J_d\pm1}}\right)\left(\frac{\sum\limits_{v''} I^{ref}_{v_c,J_{cr}\to v'',J_{cr}\pm1}}{I^{ref}_{v_c,J_{cr}\to v_{lc},J_{cr}\pm1}}\right) \\ \times\frac{\sum\limits_{v''}\nu_{v_d,J_d\to v'',J_d\pm1}\varepsilon_{v_d,J_d\to v'',J_d\pm1}\Gamma_{v_d,J_d\to v'',J_d\pm1}}{\sum\limits_{v''}\nu_{v_c,J_{cr}\to v'',J_{cr}\pm1}\varepsilon_{v_c,J_{cr}\to v'',J_{cr}\pm1}\Gamma_{v_c,J_{cr}\to v'',J_{cr}\pm1}} \\ \times\frac{\nu^3_{v_c,J_{cr}\to v_{lc},J_{cr}\pm1}S_{J_{cr},J_{cr}\pm1}}{\nu^3_{v_c,J_c\to v_{lc},J_c\pm1}S_{J_c,J_c\pm1}}\frac{(2J_c+1)}{(2J_{cr}+1)} \quad (5.24)\end{aligned}$$

As in the pure J-changing collision analysis, we assume that $\frac{\varepsilon_{v_c,J_{cr}\to v_{lc},J_{cr}\pm1}}{\varepsilon_{v_c,J_c\to v_{lc},J_c\pm1}}\approx 1$ since the two transitions lie in the same vibrational band.

Finally, since the $2(A)^1\Sigma^+(v')\to 1(X)^1\Sigma^+(v'')$ emission spans approximately the same spectral range for $v'=0$, 1 and 2, and since the efficiency factors don't change much over this range (see Tables 5.2, 5.3, 5.4 and 5.5), we replace $\varepsilon_{v_d,J_d\to v'',J_d\pm1}$ and $\varepsilon_{v_c,J_{cr}\to v'',J_{cr}\pm1}$ by average efficiencies $\bar{\varepsilon}$ over this spectral range. These factors then cancel leaving

$$\begin{aligned}\frac{n^{col}_{v_c,J_c}}{n^{dir}_{v_d,J_d}} = \frac{I^{col}_{v_c,J_c\to v_{lc},J_c\pm1}}{I^{dir}_{v_d,J_d\to v_{ld},J_d\pm1}}\left(\frac{I^{dir}_{v_d,J_d\to v_{ld},J_d\pm1}}{\sum\limits_{v''} I^{dir}_{v_d,J_d\to v'',J_d\pm1}}\right)\left(\frac{\sum\limits_{v''} I^{ref}_{v_c,J_{cr}\to v'',J_{cr}\pm1}}{I^{ref}_{v_c,J_{cr}\to v_{lc},J_{cr}\pm1}}\right) \\ \times\frac{\sum\limits_{v''}\nu_{v_d,J_d\to v'',J_d\pm1}\Gamma^{dir}_{v_d,J_d\to v'',J_d\pm1}}{\sum\limits_{v''}\nu_{v_c,J_{cr}\to v'',J_{cr}\pm1}\Gamma^{ref}_{v_c,J_{cr}\to v'',J_{cr}\pm1}}\frac{\nu^4_{v_c,J_{cr}\to v_{lc},J_{cr}\pm1}}{\nu^4_{v_c,J_c\to v_{lc},J_c\pm1}}\frac{S_{J_{cr},J_{cr}\pm1}}{S_{J_c,J_c\pm1}}\frac{(2J_c+1)}{(2J_{cr}+1)}. \quad (5.25)\end{aligned}$$

This is the final expression we need to analyze the vibration-changing collision data. $\frac{I^{col}_{v_c,J_c\rightarrow v_{lc},J_c\pm1}}{I^{dir}_{v_d,J_d\rightarrow v_{ld},J_d\pm1}}$ is the measured collisional to direct line intensity ratio. The terms in parentheses are the observed direct and collisional reference line branching ratios found in Tables 5.2, 5.3, 5.4 and 5.5. Frequencies are measured quantities and summed $\nu\Gamma$ factors are calculated (these ratios are very close to one). Hönl-London factors are given by $S^R_{J,J-1} = J$ and $S^P_{J,J+1} = J + 1$. Therefore, we have all the information we need to determine experimental values of the collisional level to direct level density ratios for each studied buffer gas and potassium density. These density ratios are related to the desired rate coefficients through Eq. 5.5. It should be noted that for collisional transfer within the same vibrational state (pure J-changing collisions), the reference transitions are the same as the direct level transitions and Eq. 5.25 reduces to Eq. 5.11.

5.3 Uncertainties

To fit the data recorded in this experiment accurately, we need to assign uncertainties to each measurement made in the laboratory. The measured collisional to direct line intensity ratios are given by

$$R_F = \frac{I^{col}}{I^{dir}}. \tag{5.26}$$

These ratios have an uncertainty given by

$$\begin{aligned}\delta R_F &= \left|\frac{\partial R_F}{\partial I^{col}}\right| \delta I^{col} + \left|\frac{\partial R_F}{\partial I^{dir}}\right| \delta I^{dir} \\ &= \frac{\delta I^{col}}{I^{dir}} + \frac{I^{col}}{(I^{dir})^2}\delta I^{dir} \\ &= \frac{\delta I}{I^{dir}}(1 + R_F) \end{aligned} \tag{5.27}$$

where δI is the uncertainty of the intensity measurements. This uncertainty is determined by the noise in the baseline for each individual scan and is the same for the collisional and direct lines. However, each scan must be considered individually because of differences in scan time, signal-to-noise, laser power and laser stability throughout the scan.

The most significant source of error in the present work stems from the determination of vapor densities. The determination of the alkali atom vapor density is based on white light absorption in the blue wing of the potassium D2 transition, and the results contain uncertainties due to the baseline uncertainties, imprecise knowledge of line broadening rates, approximations used in modeling the lineshape, imperfect spectral resolution, and non-uniformities in the heat pipe oven vapor column. When hot, the heat pipe system is not in thermal equilibrium, but rather is actually a dynamic system. Due to alkali metal migration away from the central region, temperature gradients, and partial separation of the sodium and potassium vapors, the alkali density is not uniform within the central region. However the absorption measurement can only determine an average density (column density divided by the length of the hot zone, $\int_0^L n(x)\mathrm{d}x/L$). Following Jabbour *et al.* [60]

and Wolfe *et al.* [31] we assign a conservative uncertainty of 30% for the measured alkali densities or pressures; i.e.,

$$\delta n_{alk} = 0.3 n_{alk} \tag{5.28}$$

and

$$\delta P_{alk} = 0.3 P_{alk}. \tag{5.29}$$

The buffer gas pressure is regulated by a valve (C in Fig. 4.1) allowing gas to flow into the system, and a second valve (B) connected to a vacuum pump allowing the pressure to be reduced. The pressure gauge used in the Lyon experiment has a precision of 0.5 Torr, while the gauge used in the Lehigh experiment has a precision of 0.01 Torr. Since typical buffer gas pressures were 1-10 Torr, the uncertainty in the total gas pressure ranges from 5 to 50% in Lyon. Note that the total gas pressure under operating conditions was $P_{total} = P_{fill}\frac{T_{hot}}{T_{cold}}$ for data recorded in 2013 (when the oven was filled at room temperature and sealed). However, in 2014, when the oven was brought to operating pressure while hot, $P_{total} = P_{fill}$. Because the alkali vapor displaces some of the buffer gas in the hot zone, the gauge reading P_{gauge} is

$$P_{gauge} = P_{total} = P_{BG} + P_{alk} \tag{5.30}$$

and therefore

$$\begin{aligned} \delta P_{BG} &= \left|\frac{\partial P_{BG}}{\partial P_{gauge}}\right| \delta P_{gauge} + \left|\frac{\partial P_{BG}}{\partial P_{alk}}\right| \delta P_{alk} \\ &= \delta P_{gauge} + \delta P_{alk} = \delta P_{gauge} + 0.3 P_{alk}. \end{aligned} \tag{5.31}$$

We obtain the buffer gas and alkali vapor densities from the ideal gas law:

$$n_{BG}(\mathrm{cm}^{-3}) = \frac{9.66 \times 10^{18} P_{BG}(Torr)}{T(K)} \tag{5.32}$$

and

$$n_{alk}(\mathrm{cm}^{-3}) = \frac{9.66 \times 10^{18} P_{alk}(Torr)}{T(K)}. \tag{5.33}$$

Thus

$$\begin{aligned} \delta n_{BG} &= \frac{n_{BG}}{P_{BG}} \delta P_{BG} = \frac{9.66 \times 10^{18}}{T} \delta P_{BG} \\ &= \frac{9.66 \times 10^{18} \cdot \delta P_{gauge}}{T(K)} + 0.3 n_{alk}. \end{aligned} \tag{5.34}$$

In general we record the intensity ratios as functions of the independent variables n_{BG} and n_{alk}. For fitting purposes, we choose to roll all of the uncertainties of measuring the intensity ratios and determining the buffer gas and alkali densities into the error for the dependent variable. The contributions from δn_{BG} and δn_{alk} can be added to Eq. 5.27 as follows:

$$\delta R_F = \left| \frac{\partial R_F}{\partial n_{BG}} \right| \delta n_{BG} + \left| \frac{\partial R_F}{\partial n_{alk}} \right| \delta n_{alk} + \frac{\delta I}{I^{dir}} (1 + R_F). \tag{5.35}$$

However, from a practical standpoint, we found it more convenient to fit the collisional to direct line *density* ratio to the fitting function given in Eq. 5.5. Since in each instance

$$R_F = \frac{I^{col}}{I^{dir}} = A \frac{n_c}{n_d} \equiv A n_F, \tag{5.36}$$

and therefore $\delta n_F = \frac{\delta R_F}{A}$, where A is the constant reflecting the various factors in

Eq. 5.25:

$$A = \frac{R_F}{n_F} = \left(\frac{\sum_{v''} I^{dir}_{v_d,J_d \to v'',J_d \pm 1}}{I^{dir}_{v_d,J_d \to v_{ld},J_d \pm 1}} \right) \left(\frac{I^{ref}_{v_c,J_{cr} \to v_{lc},J_{cr} \pm 1}}{\sum_{v''} I^{ref}_{v_c,J_{cr} \to v'',J_{cr} \pm 1}} \right)$$
$$\times \frac{\sum_{v''} \nu_{v_c,J_{cr} \to v'',J_{cr} \pm 1} \Gamma^{ref}_{v_c,J_{cr} \to v'',J_{cr} \pm 1}}{\sum_{v''} \nu_{v_d,J_d \to v'',J_d \pm 1} \Gamma^{dir}_{v_d,J_d \to v'',J_d \pm 1}} \frac{\nu^4_{v_c,J_c \to v_{lc},J_c \pm 1}}{\nu^4_{v_c,J_{cr} \to v_{lc},J_{cr} \pm 1}} \frac{S_{J_c,J_c \pm 1}}{S_{J_{cr},J_{cr} \pm 1}} \frac{(2J_{cr}+1)}{(2J_c+1)}. \quad (5.37)$$

For pure J-changing collisions, where the reference line is the direct line, most of these terms drop out and we find

$$A = \frac{R_F}{n_F} = \frac{\nu^4_{v_c,J_c \to v_{lc},J_c \pm 1}}{\nu^4_{v_d,J_d \to v_{ld},J_d \pm 1}} \frac{S_{J_c,J_c \pm 1}}{S_{J_d,J_d \pm 1}} \frac{(2J_d+1)}{(2J_c+1)}. \quad (5.38)$$

Thus with either of these expressions, A is constant, and we can assign uncertainties to the collisional to direct level density ratios (n_F) that are derived from the experimental data:

$$\frac{\delta R_F}{R_F} = \frac{\delta n_F}{n_F} = \left| \frac{\partial n_F}{\partial n_{BG}} \right| \frac{\delta n_{BG}}{n_F} + \left| \frac{\partial n_F}{\partial n_{alk}} \right| \frac{\delta n_{alk}}{n_F} + \frac{\delta I}{I^{dir}} \left(\frac{1}{R_F} + 1 \right). \quad (5.39)$$

For collisions which only change J, we use Eq. 5.5

$$n_F \equiv \frac{n_c}{n_d} = \frac{\frac{k^{\Delta}_{BG}}{\Gamma} n_{BG} + \frac{k^{\Delta}_{K}}{\Gamma} n_K}{1 + \frac{k^{Q,c}_{BG}}{\Gamma} n_{BG} + \frac{k^{Q,c}_{K}}{\Gamma} n_K} \quad (5.40)$$

and find

$$\frac{\delta n_F}{n_F} = \left| \frac{\frac{k_{BG}^{\Delta}}{\Gamma}}{\frac{k_{BG}^{\Delta}}{\Gamma} n_{BG} + \frac{k_K^{\Delta}}{\Gamma} n_K} - \frac{\frac{k_{BG}^{Q,c}}{\Gamma}}{1 + \frac{k_{BG}^{Q,c}}{\Gamma} n_{BG} + \frac{k_K^{Q,c}}{\Gamma} n_K} \right| \delta n_{BG} + \left| \frac{\frac{k_K^{\Delta}}{\Gamma}}{\frac{k_{BG}^{\Delta}}{\Gamma} n_{BG} + \frac{k_K^{\Delta}}{\Gamma} n_K} - \frac{\frac{k_K^{Q,c}}{\Gamma}}{1 + \frac{k_{BG}^{Q,c}}{\Gamma} n_{BG} + \frac{k_K^{Q,c}}{\Gamma} n_K} \right| \delta n_K + \frac{\delta I}{I^{dir}} \left(\frac{1}{R_F} + 1 \right). \quad (5.41)$$

Finally, multiplying through by n_F, we obtain

$$\delta n_F = \left| \frac{\frac{k_{BG}^{\Delta}}{\Gamma}}{\frac{k_{BG}^{\Delta}}{\Gamma} n_{BG} + \frac{k_K^{\Delta}}{\Gamma} n_K} - \frac{\frac{k_{BG}^{Q,c}}{\Gamma}}{1 + \frac{k_{BG}^{Q,c}}{\Gamma} n_{BG} + \frac{k_K^{Q,c}}{\Gamma} n_K} \right| n_F \delta n_{BG} + \left| \frac{\frac{k_K^{\Delta}}{\Gamma}}{\frac{k_{BG}^{\Delta}}{\Gamma} n_{BG} + \frac{k_K^{\Delta}}{\Gamma} n_K} - \frac{\frac{k_K^{Q,c}}{\Gamma}}{1 + \frac{k_{BG}^{Q,c}}{\Gamma} n_{BG} + \frac{k_K^{Q,c}}{\Gamma} n_K} \right| n_F \delta n_K + \frac{\delta I}{I^{dir}} (1 + R_F) \frac{n_F}{R_F}. \quad (5.42)$$

Equation 5.42 represents the total uncertainty in each n_F value when we carry out a global fit of n_F vs. n_{BG} and n_K where all parameters are varied. In practice, since the uncertainties depend on the rate coefficients that are being fitted, we update the uncertainties after each fit has converged to a set of values. This process is iterated until there are no further changes in the fitted rate coefficients. However, as I discuss in Chapter 6, there are cases where we choose to fix the quenching rate coefficients at values determined in other fits. In these cases, there is an additional uncertainty due to the statistical uncertainties in the fixed values of $k_{BG}^{Q,c}$ and $k_{alk}^{Q,c}$. In such cases, Eq. 5.39 (multiplied by n_F) must be expanded to include these terms:

$$\delta n_F = \left|\frac{\partial n_F}{\partial n_{BG}}\right| \delta n_{BG} + \left|\frac{\partial n_F}{\partial n_{alk}}\right| \delta n_{alk} + \frac{\delta I}{I^{dir}}\left(\frac{1}{R_F}+1\right) n_F + \left|\frac{\partial n_F}{\partial\left(\frac{k_{BG}^{Q,c}}{\Gamma}\right)}\right| \delta\left(\frac{k_{BG}^{Q,c}}{\Gamma}\right) + \left|\frac{\partial n_F}{\partial\left(\frac{k_{alk}^{Q,c}}{\Gamma}\right)}\right| \delta\left(\frac{k_{alk}^{Q,c}}{\Gamma}\right) \quad (5.43)$$

where the first row of terms is identical to Eq. 5.39 and the added terms appear in the second row. Acknowledging that the only alkali term we are taking into account at this point is the potassium term, the new terms here are evaluated as

$$\left|\frac{\partial n_F}{\partial\left(\frac{k_{BG}^{Q,c}}{\Gamma}\right)}\right| \delta\left(\frac{k_{BG}^{Q,c}}{\Gamma}\right) = \left|\frac{\frac{k_{BG}^{\Delta}}{\Gamma} n_{BG} + \frac{k_K^{\Delta}}{\Gamma} n_K}{\left(1+\frac{k_{BG}^{Q,c}}{\Gamma} n_{BG} + \frac{k_K^{Q,c}}{\Gamma} n_K\right)^2} n_{BG}\right| \delta\left(\frac{k_{BG}^{Q,c}}{\Gamma}\right)$$
$$= \left|\frac{1}{1+\frac{k_{BG}^{Q,c}}{\Gamma} n_{BG} + \frac{k_K^{Q,c}}{\Gamma} n_K}\right| n_{BG} n_F \delta\left(\frac{k_{BG}^{Q,c}}{\Gamma}\right) \quad (5.44a)$$

and

$$\left|\frac{\partial n_F}{\partial\left(\frac{k_{alk}^{Q,c}}{\Gamma}\right)}\right| \delta\left(\frac{k_{alk}^{Q,c}}{\Gamma}\right) = \left|\frac{\frac{k_{BG}^{\Delta}}{\Gamma} n_{BG} + \frac{k_K^{\Delta}}{\Gamma} n_K}{\left(1+\frac{k_{BG}^{Q,c}}{\Gamma} n_{BG} + \frac{k_K^{Q,c}}{\Gamma} n_K\right)^2} n_K\right| \delta\left(\frac{k_K^{Q,c}}{\Gamma}\right)$$
$$= \left|\frac{1}{1+\frac{k_{BG}^{Q,c}}{\Gamma} n_{BG} + \frac{k_K^{Q,c}}{\Gamma} n_K}\right| n_K n_F \delta\left(\frac{k_K^{Q,c}}{\Gamma}\right). \quad (5.44b)$$

The final form for the uncertainties in cases where the quenching rate coefficients

are fixed is given by

$$\begin{aligned}
\delta n_F = & \left| \frac{\frac{k_{BG}^{\Delta}}{\Gamma}}{\frac{k_{BG}^{\Delta}}{\Gamma} n_{BG} + \frac{k_K^{\Delta}}{\Gamma} n_K} - \frac{\frac{k_{BG}^{Q,c}}{\Gamma}}{1 + \frac{k_{BG}^{Q,c}}{\Gamma} n_{BG} + \frac{k_K^{Q,c}}{\Gamma} n_K} \right| n_F \delta n_{BG} \\
& + \left| \frac{\frac{k_K^{\Delta}}{\Gamma}}{\frac{k_{BG}^{\Delta}}{\Gamma} n_{BG} + \frac{k_K^{\Delta}}{\Gamma} n_K} - \frac{\frac{k_K^{Q,c}}{\Gamma}}{1 + \frac{k_{BG}^{Q,c}}{\Gamma} n_{BG} + \frac{k_K^{Q,c}}{\Gamma} n_K} \right| n_F \delta n_K \\
& + \frac{\delta I}{I^{dir}} \left(1 + R_F\right) \frac{n_F}{R_F} + \left| \frac{1}{1 + \frac{k_{BG}^{Q,c}}{\Gamma} n_{BG} + \frac{k_K^{Q,c}}{\Gamma} n_K} \right| n_{BG} n_F \delta \left(\frac{k_{BG}^{Q,c}}{\Gamma} \right) \\
& + \left| \frac{1}{1 + \frac{k_{BG}^{Q,c}}{\Gamma} n_{BG} + \frac{k_K^{Q,c}}{\Gamma} n_K} \right| n_K n_F \delta \left(\frac{k_K^{Q,c}}{\Gamma} \right). \qquad (5.45)
\end{aligned}$$

Chapter 6

Analysis and Results

6.1 Overview

In this chapter, I describe the data set we have obtained for the rotationally and vibrationally inelastic collisions of NaK molecules with argon, helium, and potassium atoms, as well as how the data are analyzed to determine population transfer in these collisions. In Section 6.2, I discuss the analysis of the spectra recorded with the Bomem FTS. Then in Section 6.3, I discuss the methods used for fitting small $|\Delta J|$ ($|\Delta J| \leq 4$) J-changing collisional data to determine quenching rate coefficients, which are then used in the fits of large $|\Delta J|$ ($|\Delta J| > 4$)J-changing collisions and all v-changing collisional data. The results from these fits are also reported in Section 6.3. A discussion of the assumptions used in our analysis and how these affect our final results is included in Section 6.4. Finally, A comparison of experimental rate coefficients obtained in our work with theoretical calculations carried out by Price, Malenda and Hickman is included in Section 6.5.

6.2 Analysis of Spectra

An important aspect of recording useful data for this work is that the collision environment must be controlled. We would like the perturber density to be sufficiently low that the single-collision approximation is valid. However, low perturber densities (both alkali and buffer gas) lead to low signal-to-noise ratios. A sufficiently high alkali atom density is required to create enough molecules to produce usable signal. There must also be enough buffer gas (or alkali atoms) present in the system to produce collisional lines that are discernible from the noise.

Spectra recorded using the Fourier transform spectrometer (FTS) contain multiple transitions that can be used to monitor a particular upper state (v', J') population, specifically the P $(J'' = J' + 1)$ and R $(J'' = J' - 1)$ transitions of each $2(A)^1\Sigma^+ (v') \rightarrow 1(X)^1\Sigma^+ (v'')$ vibrational band. Each peak within a spectrum (direct or collisional) has the same line width, which is limited by the resolution of the Bomem FTS. Therefore, a particular collisional line to a direct line intensity ratio is just the ratio of peak heights. Occasionally we observe a peak with significantly larger width. Such lines are most likely contaminated by another transition and should not be used in the analysis.

I assigned approximately 600 $2(A)^1\Sigma^+ (v', J') \rightarrow 1(X)^1\Sigma^+ (v'', J'')$ transition frequencies using the $2(A)^1\Sigma^+$ state database of T. Bergemann *et al.* [11] , which is based on experimental transition frequencies determined by A. J. Ross, and others, and $1(X)^1\Sigma^+$ ground state energies determined by Gerdes *et al.* [10]. To expedite the collection of all line intensities, a peak finding function of the Thermo Galactic

GRAMS computer program was utilized. This peak finder allows a minimum intensity to be set, and any peak with an intensity greater than this minimum is cataloged in a table by it's frequency and peak height. The minimum intensity value for each scan was set to be somewhat larger than the background noise level for that scan. The peak finder output table for a given scan was then input to a Fortran program I wrote to compare each peak frequency to a reference file of assigned $2(A)^1\Sigma^+ (v', J')$ $\rightarrow 1(X)^1\Sigma^+ (v'', J'')$ transition frequencies. If the observed peak frequency matched an assigned $A \rightarrow X$ line frequency within a set tolerance (usually 0.035 cm^{-1}) the peak was recorded in an output file along with the line intensity and frequency from the spectrum. The recorded information also included line assignment information, including whether the given line represented a P or R transition. The program allows for an absolute shift of the input frequency list, as the 2013 data needed to be corrected in frequency by $\Delta\nu = 0.025$ cm^{-1} to agree with the reference file which was assigned based on 2014 lines. The main reason for the difference in frequencies between the two years was that the Bomem interferometer was not evacuated in 2013 but was in 2014.

6.3 Fitting Methods and Results

In this section we present our results for population transfer between rotational and vibrational levels of the NaK $2(A)^1\Sigma^+$ state (v = 0, 1, 2) due to collisions of these molecules with argon, helium and potassium perturbers. I first present the global fit used to determine quenching rate coefficients as well as rate coefficients for $|\Delta J| \leq 4$ J-changing collisions within a single vibrational level. I then discuss the simpler, individual fits used to obtain rate coefficients for the larger $|\Delta J|$ J-changing

collisions and for the v-changing collisions using the quenching rates obtained in the global fit.

6.3.1 Global Fit and Results

In our first fitting attempts, we separately fit the $|\Delta J| \leq 4$ data for each of the four directly pumped levels $2(A)^1\Sigma^+$ (0, 14), $2(A)^1\Sigma^+$ (0, 30), $2(A)^1\Sigma^+$ (1, 26) and $2(A)^1\Sigma^+$ (2, 44). Within a given fit, the potassium quenching term ($k_K^{Q,c}$) is common to all data (see below), while the buffer gas quenching terms ($k_{Ar}^{Q,c}$, $k_{He}^{Q,c}$) are only relevant to the data recorded with that buffer gas. Individual J-changing rate coefficients $k_K^{\Delta J}, k_{Ar}^{\Delta J}$ and $k_{He}^{\Delta J}$ depend on the data for specific ΔJ values (and on the buffer gas). In the majority of the fits, all $k^{\Delta J}$ values and the buffer gas quenching terms were allowed to vary. The rate coefficients obtained from the separate fits for each pump transition varied greatly, and it was determined that a more robust fitting method was required.

The theoretical calculations by T. Price [61] show that the total inelastic cross section for $v = 0$ (obtained by summing the individual calculated cross sections for J-changing collisions) does not vary much over the range $J = 0$ - 50 for argon-NaK collisions (Fig. 6.1) and for helium-NaK collisions (Fig. 6.2). Since this total inelastic cross section is a good approximation to the total quenching cross section, one can conclude that $k_{Ar}^{Q,c}$ and $k_{He}^{Q,c}$ are independent of the particular collisional level c under consideration (hence justifying our use of global rate coefficients $k_{Ar,He}^{Q,c} \approx k_{Ar,He}^{Q}$ in the fits described above for each pump transition). The fact that the separate fitted buffer gas quenching rate coefficients for $v = 0$, 1, and 2 are not too different from each other, or from the fitted quenching rate coefficients for $v = 16$ obtained by

Wolfe *et al.* [31], indicates that it is reasonable to assume common quenching rate coefficients for all data sets obtained with different pump transitions.

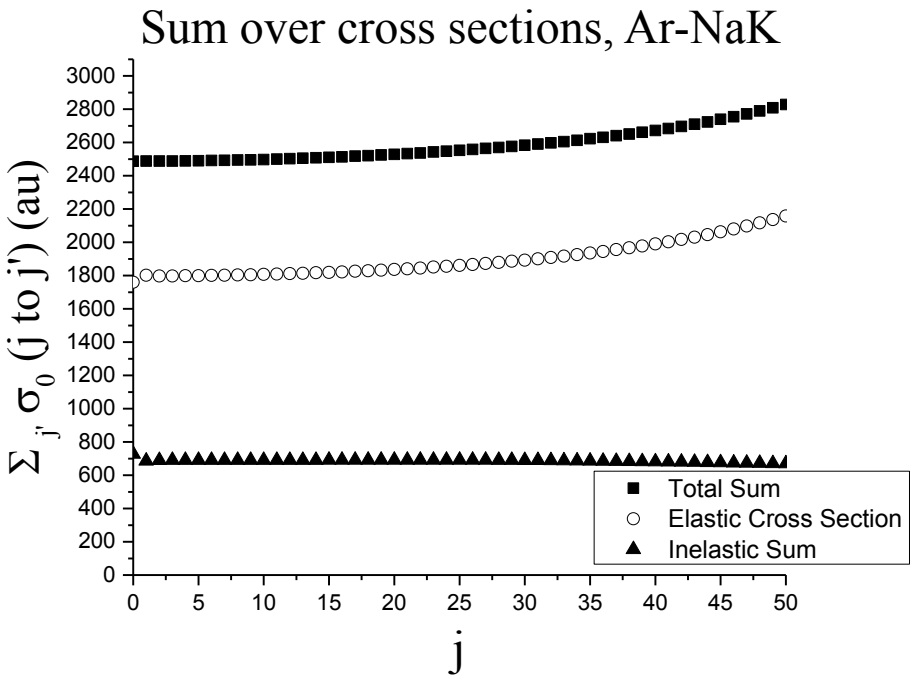

Figure 6.1: Total, elastic, and inelastic cross sections plotted versus initial J for collisions between argon and NaK molecules. Based on calculations of cross sections by T. Price [61].

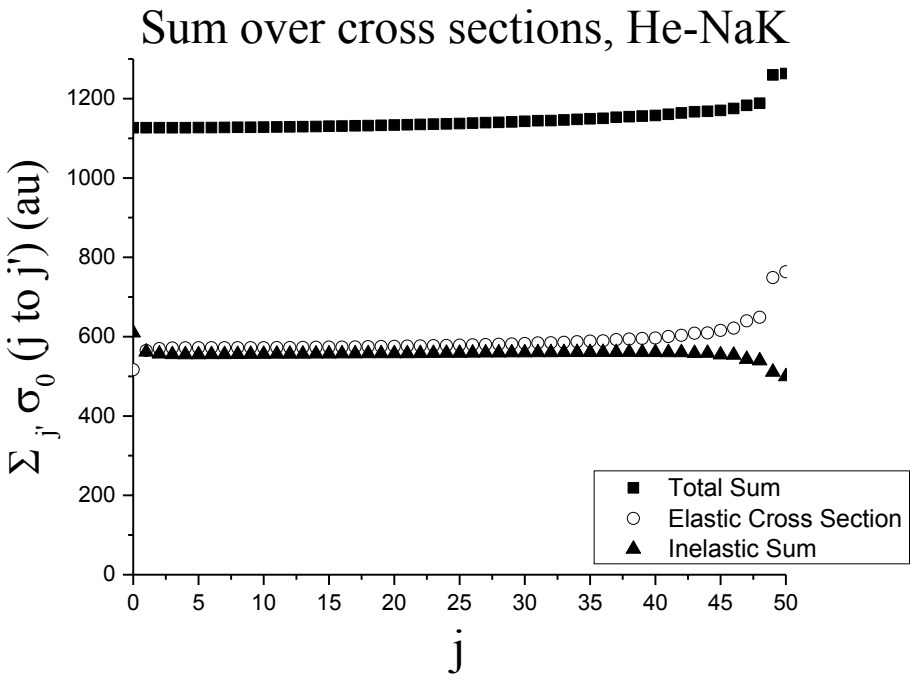

Figure 6.2: Total, elastic, and inelastic cross sections plotted versus initial J for collisions between helium and NaK molecules. Based on calculations of cross sections by T. Price [61].

Since we can assume common quenching rate coefficients for all pump transitions and all collisional levels, we gain the advantage that the total data set is much more robust than the data sets associated with the individual pump transitions. For example, we note that the data obtained with different pump transitions had different argon, helium, and potassium density ranges since data could not always be recorded for all four transitions on a given day. This was most apparent within the $2(A)^1\Sigma^+$ (0, 30) data set, which only includes two helium densities, meaning we could not effectively fit the helium rate coefficient for the (0, 30) pump in the separate pump transition fits.

In the global fit method we simultaneously fit all data for the four pump transitions, including data recorded with various densities of both argon and helium as the buffer gas. We then assumed all data shared the same k_{Ar}^{Q}, k_{He}^{Q}, and k_{K}^{Q} parameters. The individual $k_{P}^{\Delta J}$ rate coefficients for $\Delta J = \pm 1, \pm 2, \pm 3, \pm 4$ were considered to be independent of each other and different for each pump transition. This meant that the $k_{P}^{\Delta J,(0,14)}$, $k_{P}^{\Delta J,(0,30)}$, $k_{P}^{\Delta J,(1,26)}$, and $k_{P}^{\Delta J,(2,44)}$ rate coefficients all were separate fitting parameters, creating a 99-parameter fit. (This included 8 different ΔJ values for each of the 3 different perturber gases, and 4 different pump transitions, as well as 3 quenching rate coefficients.)

To test these ideas, several variations of the fit were carried out, in which the quenching rate coefficients were either allowed to vary, or were set to specific values. The reason for this was to see, specifically, how changing the potassium quenching rate coefficients affected the other fitted rate coefficients. In one fit, all terms (including k_{K}^{Q}) were allowed to vary, while in other fits, k_{K}^{Q} was set at a given value and not allowed to vary. In one fit the three quenching rate coefficients were set to the values obtained by Wolfe *et al.* [31] for the $2(A)^{1}\Sigma^{+}\,(v = 16,\ J = 30)$ pump transition; $\frac{k_{Ar}^{Q}}{\Gamma} = 2.81 \times 10^{-17}$ cm^3, $\frac{k_{He}^{Q}}{\Gamma} = 4.15 \times 10^{-17}$ cm^3, and $\frac{k_{K}^{Q}}{\Gamma} = 2.69 \times 10^{-16}$ cm^3. The reason k_{K}^{Q} was sometimes fixed is due to the fact that the potassium densities have large uncertainties and the fitted k_{K}^{Q} values sometimes converged to unphysical values. In all cases, the fits were iterated until convergence. $\frac{k_{Ar}^{\Delta J}}{\Gamma}$ and $\frac{k_{He}^{\Delta J}}{\Gamma}$ values obtained from these fits are shown in Figs. 6.3 and 6.4, respectively, for $1 \leq |\Delta J| \leq 4$.

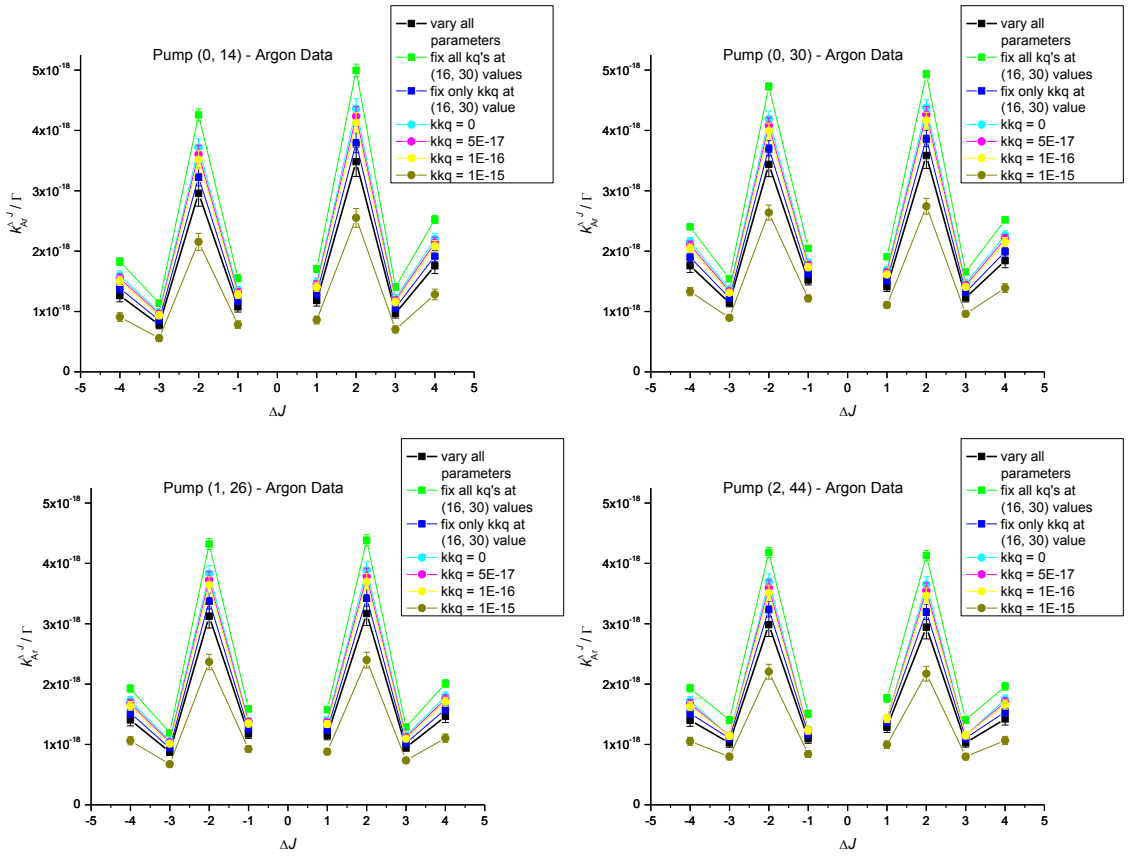

Figure 6.3: Various fits for directly pumped levels (0, 14), (0, 30), (1, 26) and (2, 44) with argon as the buffer gas. In one fit, all parameters ($\frac{k_{BG}^{\Delta J}}{\Gamma}$ and $\frac{k_K^{\Delta J}}{\Gamma}$ for $1 \leq |\Delta J| \leq 4$, and all quenching terms) were allowed to vary. One fit allowed all ΔJ terms to vary but fixed the quenching rates at the (16, 30) values. In other fits only the value of $\frac{k_K^Q}{\Gamma}$ was fixed, either at the (16, 30) value (2.69×10^{-16} cm^3) that was obtained by Wolfe *et al.* [31], or at one of several specific values (0, 5×10^{-17} cm^3, 1×10^{-16} cm^3, 1×10^{-15} cm^3).

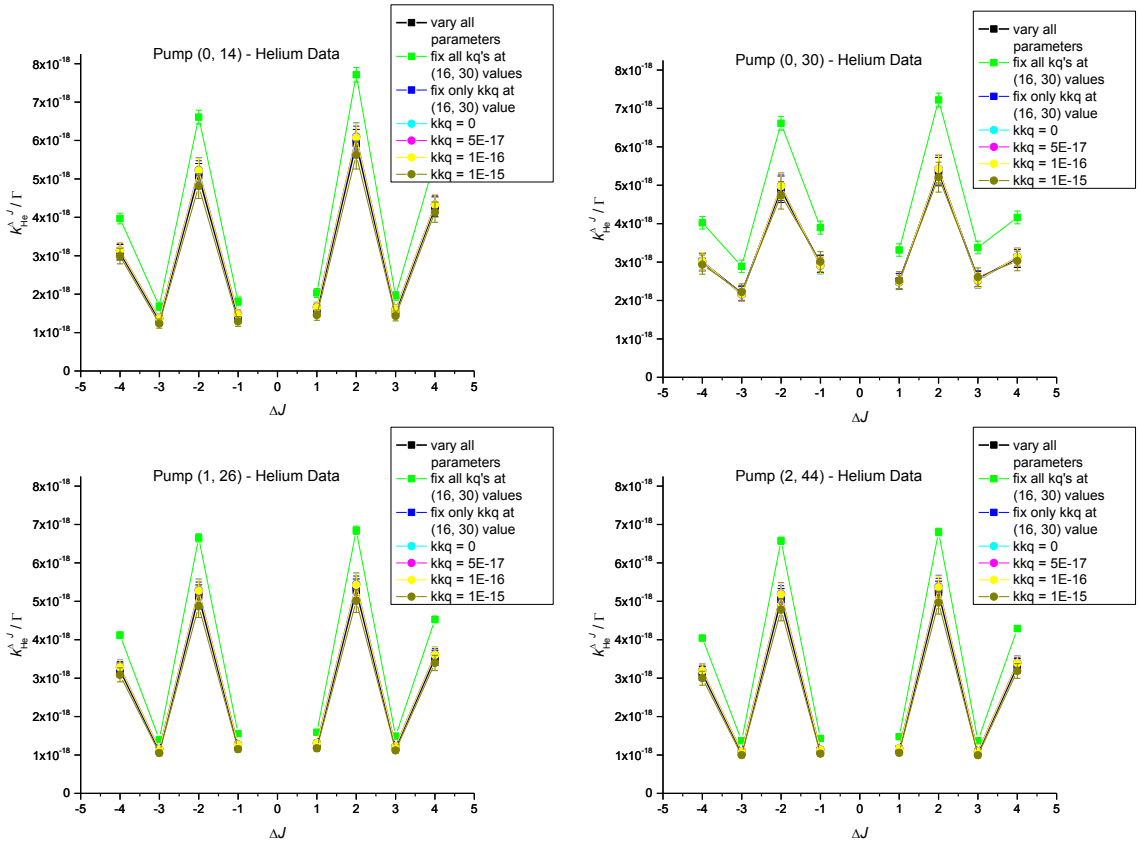

Figure 6.4: Various fits for directly pumped levels (0, 14), (0, 30), (1, 26) and (2, 44) with helium as the buffer gas. In one fit, all parameters ($\frac{k_{BG}^{\Delta J}}{\Gamma}$ and $\frac{k_K^{\Delta J}}{\Gamma}$ for $1 \leq |\Delta J| \leq 4$, and all quenching terms) were allowed to vary. One fit allowed all ΔJ terms to vary but fixed the quenching rates at the (16, 30) values. In other fits only the value of $\frac{k_K^Q}{\Gamma}$ was fixed, either at the (16, 30) value (2.69×10^{-16} cm^3) that was obtained by Wolfe *et al.* [31], or at one of several specific values (0, 5×10^{-17} cm^3, 1×10^{-16} cm^3, 1×10^{-15} cm^3).

From the figures it can be seen that the $k_{Ar,He}^{\Delta J}$ values are relatively insensitive to the value of k_K^Q. The argon and helium rate coefficients which resulted from these fits are given in Table 6.1 for the directly pumped level (0, 14), Table 6.2 for (0, 30), Table 6.3 for directly pumped level (1, 26), and Table 6.4 for the directly pumped

level (2, 44). Quenching rate coefficients obtained in these various fits for all pump transitions are also listed in these tables. There it can be seen that the argon and helium quenching rate coefficients are also relatively insensitive to the value of k_K^Q.

Rate Coefficients for $2(A)^1\Sigma^+$ (0, 14)						
Buffer Gas	ΔJ	Vary all	Fix all $\frac{k_P^Q}{\Gamma}$ at (16, 30)	Fix $\frac{k_K^Q}{\Gamma}$ at 5×10^{-17}	Fix $\frac{k_K^Q}{\Gamma}$ at 1×10^{-16}	Fix $\frac{k_K^Q}{\Gamma}$ at 1×10^{-15}
		(10^{-18} cm^3)	(10^{-18} cm^3)	(10^{-18} cm^3)	(10^{-18} cm^3)	(10^{-18} cm^3)
(Ar)	-4	1.26	1.83	1.55	1.51	0.91
	-3	0.78	1.14	0.96	0.94	0.56
	-2	2.96	4.26	3.60	3.51	2.15
	-1	1.08	1.55	1.31	1.28	0.78
	1	1.18	1.70	1.44	1.40	0.86
	2	3.48	5.00	4.23	4.13	2.55
	3	0.97	1.40	1.19	1.16	0.70
	4	1.76	2.53	2.14	2.09	1.28
(He)	-4	3.09	3.97	3.14	3.14	2.99
	-3	1.32	1.68	1.36	1.36	1.23
	-2	5.08	6.61	5.23	5.21	4.81
	-1	1.41	1.81	1.47	1.47	1.29
	1	1.58	2.03	1.66	1.65	1.45
	2	5.93	7.71	6.09	6.08	5.62
	3	1.53	1.96	1.59	1.58	1.43
	4	4.27	5.48	4.33	4.33	4.13
k_{Ar}^Q		1.75×10^{-17}	2.81×10^{-17}	2.28×10^{-17}	2.21×10^{-17}	1.11×10^{-17}
k_{He}^Q		2.96×10^{-17}	4.15×10^{-17}	3.08×10^{-17}	3.07×10^{-17}	2.74×10^{-17}
k_K^Q		4.30×10^{-16}	2.69×10^{-16}	5.0×10^{-1}	$1.0 \times x10^{-16}$	$1.0 \times x10^{-15}$

Table 6.1: The rate coefficients for argon and helium for the initial fits of the J-changing collisional rate coefficients following direct pumping of the $2(A)^1\Sigma^+$ (0, 14) level, with different limits or values used for the quenching coefficients. The last three rows represent the quenching rate coefficients; either fit or assigned.

Rate Coefficients for $2(A)^1\Sigma^+$ (0, 30)						
Buffer Gas	ΔJ	Vary all	Fix all $\frac{k_P^Q}{\Gamma}$ at (16, 30)	Fix $\frac{k_K^Q}{\Gamma}$ at 5×10^{-17}	Fix $\frac{k_K^Q}{\Gamma}$ at 1×10^{-16}	Fix $\frac{k_K^Q}{\Gamma}$ at 1×10^{-15}
		(10^{-18} cm^3)	(10^{-18} cm^3)	(10^{-18} cm^3)	(10^{-18} cm^3)	(10^{-18} cm^3)
(Ar)	-4	1.76	2.40	2.10	2.05	1.33
	-3	1.14	1.54	1.34	1.31	0.90
	-2	3.44	4.73	4.08	3.99	2.64
	-1	1.52	2.05	1.77	1.73	1.22
	1	1.41	1.91	1.65	1.61	1.11
	2	3.58	4.93	4.26	4.17	2.74
	3	1.23	1.66	1.44	1.41	0.96
	4	1.84	2.52	2.20	2.15	1.39
(He)	-4	3.00	4.02	3.02	3.02	2.93
	-3	2.19	2.89	2.16	2.17	2.22
	-2	4.90	6.61	4.98	4.98	4.74
	-1	2.95	3.90	2.91	2.92	3.01
	1	2.50	3.31	2.48	2.48	2.52
	2	5.36	7.22	5.43	5.42	5.21
	3	2.56	3.38	2.52	2.53	2.61
	4	3.10	4.16	3.13	3.13	3.03
k_{Ar}^Q		1.75×10^{-17}	2.81×10^{-17}	2.28×10^{-17}	2.21×10^{-17}	1.11×10^{-17}
k_{He}^Q		2.96×10^{-17}	4.15×10^{-17}	3.08×10^{-17}	3.07×10^{-17}	2.74×10^{-17}
k_K^Q		4.30×10^{-16}	2.69×10^{-16}	5×10^{-1}	1×10^{-16}	1×10^{-15}

Table 6.2: The rate coefficients for argon and helium for the initial fits of the J-changing collisional rate coefficients following direct pumping of the $2(A)^1\Sigma^+$ (0, 30) level, with different limits or values used for the quenching coefficients. The last three rows represent the quenching rate coefficients; either fit or assigned.

Rate Coefficients for $2(A)^1\Sigma^+$ (1, 26)						
Buffer Gas	ΔJ	Vary all	Fix all $\frac{k_P^Q}{\Gamma}$ at (16, 30)	Fix $\frac{k_K^Q}{\Gamma}$ at 5×10^{-17}	Fix $\frac{k_K^Q}{\Gamma}$ at 1×10^{-16}	Fix $\frac{k_K^Q}{\Gamma}$ at 1×10^{-15}
		(10^{-18} cm^3)	(10^{-18} cm^3)	(10^{-18} cm^3)	(10^{-18} cm^3)	(10^{-18} cm^3)
(Ar)	-4	1.41	1.93	1.68	1.64	1.06
	-3	0.88	1.19	1.04	1.01	0.67
	-2	3.12	4.32	3.73	3.64	2.37
	-1	1.17	1.59	1.37	1.35	0.92
	1	1.15	1.58	1.37	1.34	0.88
	2	3.17	4.38	3.78	3.70	2.40
	3	0.95	1.29	1.12	1.10	0.74
	4	1.46	2.01	1.75	1.71	1.10
(He)	-4	3.21	4.12	3.29	3.28	3.09
	-3	1.12	1.40	1.15	1.15	1.05
	-2	5.14	6.65	5.29	5.27	4.87
	-1	1.23	1.55	1.28	1.27	1.15
	1	1.26	1.59	1.31	1.30	1.17
	2	5.28	6.85	5.44	5.42	5.01
	3	1.19	1.49	1.23	1.22	1.12
	4	3.53	4.53	3.61	3.60	3.40
k_{Ar}^Q		1.75×10^{-17}	2.81×10^{-17}	2.28×10^{-17}	2.21×10^{-17}	1.11×10^{-17}
k_{He}^Q		2.96×10^{-17}	4.15×10^{-17}	3.08×10^{-17}	3.07×10^{-17}	2.74×10^{-17}
k_K^Q		4.30×10^{-16}	2.69×10^{-16}	5×10^{-1}	1×10^{-16}	1×10^{-15}

Table 6.3: The rate coefficients for argon and helium for the initial fits of the J-changing collisional rate coefficients following direct pumping of the $2(A)^1\Sigma^+$ (1, 26) level, with different limits or values used for the quenching coefficients. The last three rows represent the quenching rate coefficients; either fit or assigned.

Rate Coefficients for $2(A)^1\Sigma^+$ (2, 44)						
Buffer Gas	ΔJ	Vary all	Fix all $\frac{k_P^Q}{\Gamma}$ at (16, 30)	Fix $\frac{k_K^Q}{\Gamma}$ at 5×10^{-17}	Fix $\frac{k_K^Q}{\Gamma}$ at 1×10^{-16}	Fix $\frac{k_K^Q}{\Gamma}$ at 1×10^{-15}
		(10^{-18} cm^3)	(10^{-18} cm^3)	(10^{-18} cm^3)	(10^{-18} cm^3)	(10^{-18} cm^3)
(Ar)	-4	1.40	1.93	1.67	1.63	1.05
	-3	1.03	1.40	1.14	1.15	0.80
	-2	2.98	4.18	3.60	3.51	2.21
	-1	1.10	1.51	1.24	1.23	0.84
	1	1.29	1.76	1.43	1.43	1.00
	2	2.94	4.13	3.55	3.46	2.17
	3	1.03	1.41	1.15	1.15	0.80
(He)	-4	3.13	4.04	3.20	3.19	3.00
	-3	1.06	1.37	1.09	1.09	1.00
	-2	5.04	6.58	5.20	5.18	4.78
	-1	1.11	1.43	1.14	1.14	1.03
	1	1.14	1.48	1.17	1.17	1.06
	2	5.23	6.81	5.38	5.36	4.97
	3	1.06	1.37	1.09	1.09	0.99
	4	3.32	4.29	3.39	3.39	3.19
k_{Ar}^Q		1.75×10^{-17}	2.81×10^{-17}	2.28×10^{-17}	2.21×10^{-17}	1.11×10^{-17}
k_{He}^Q		2.96×10^{-17}	4.15×10^{-17}	3.08×10^{-17}	3.07×10^{-17}	2.74×10^{-17}
k_K^Q		4.30×10^{-16}	2.69×10^{-16}	5×10^{-1}	1×10^{-16}	1×10^{-15}

Table 6.4: The rate coefficients for argon and helium for the initial fits of the J-changing collisional rate coefficients following direct pumping of the $2(A)^1\Sigma^+$ (2, 44) level, with different limits or values used for the quenching coefficients. The last three rows represent the quenching rate coefficients; either fit or assigned.

It was decided that the "best" fit was the one in which all parameters were allowed to vary. The quenching rate coefficients obtained from this global fit (the first column in Tables 6.1 through 6.4) were then used to fit the individual $k_P^{|\Delta J|>4)}$ and $k_P^{\Delta v,J)}$ values for the four pump transitions. These results will be discussed in the next subsections, (6.3.2 and 6.3.3).

6.3.2 Individual Fits and Results: *J*-changing collisions

This section discusses the results of the individual fits for J-changing collisions and our four different directly pumped initial (v, J) levels. All fits have been carried out using the quenching rate coefficients determined in the global fit and presented in the previous section. In each case, $\frac{k_P^{\Delta J}}{\Gamma}$ values obtained in the fits have been multiplied by the appropriate gamma for that direct level, so that rate coefficients $k_P^{\Delta J}$ can be presented. These Γ values were obtained from the program LEVEL [59], using the previously mentioned experimentally determined $2(A)^1\Sigma^+$ and $1(X)^1\Sigma^+$ electronic state potentials of [9] and [10], respectively. Calculated Einstein A coefficients for transitions from each of the initially pumped levels down to $1(X)^1\Sigma^+$ ground state vibrational levels v_X in the range 0 to 20, and rotational levels obeying the selection rules for P and R transitions were summed to obtain the total radiative rate Γ. Figures 6.5, 6.6 and 6.7 show the results for $2(A)^1\Sigma^+$ (0, 14) argon, helium, and potassium rate coefficients, respectively, which are all included in Table 6.5. Figures 6.8, 6.9 and 6.10 show the results for $2(A)^1\Sigma^+$ (0, 30) argon, helium, and potassium rates, respectively, which are all included in Table 6.6. Figures 6.11, 6.12 and 6.13 give the results for $2(A)^1\Sigma^+$ (1, 26), which are included in Table 6.7. Table 6.8 includes the results for $2(A)^1\Sigma^+$ (2, 44), which are plotted in Figs. 6.14, 6.15 and 6.16.

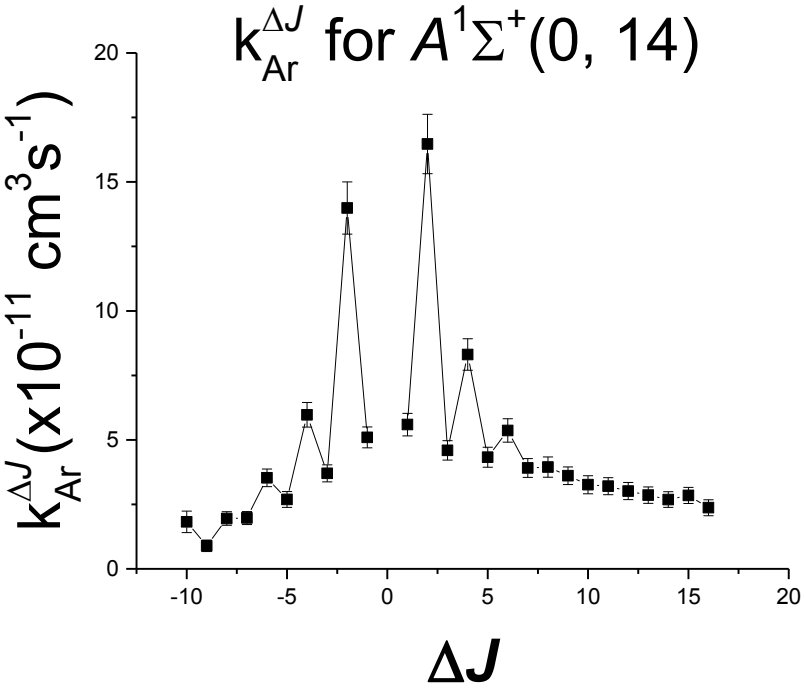

Figure 6.5: Results of the individual fits for J-changing collisions following direct pumping of the NaK $2(A)^1\Sigma^+$ (0, 14) level. Here, results for the argon rate coefficients for $\Delta J = -10$ to $\Delta J = 16$ have been plotted. It can be seen that the $\Delta J =$ even propensity continues past the previously fit $|\Delta J| \leq 4$ range.

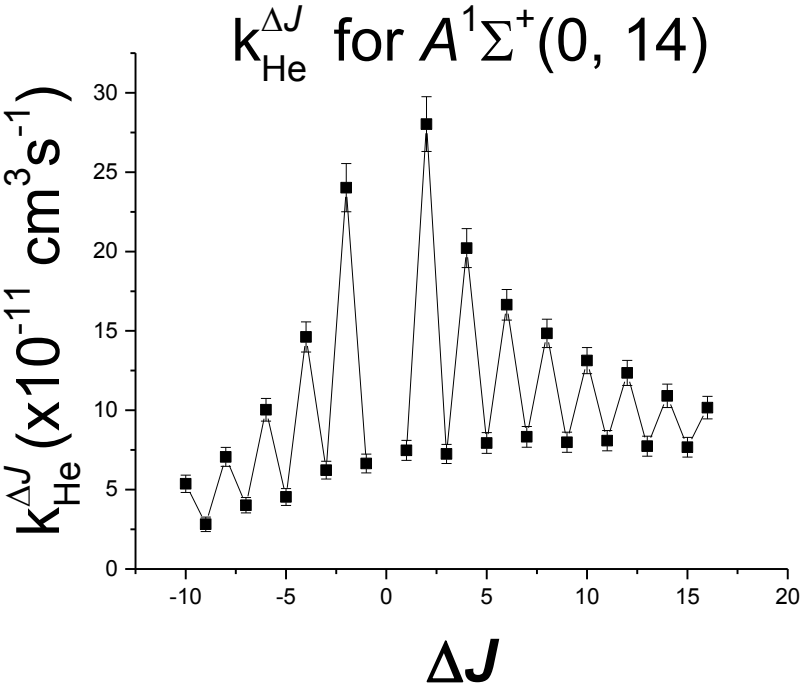

Figure 6.6: Results of the individual fits for J-changing collisions following direct pumping of the NaK $2(A)^1\Sigma^+$ (0, 14) level. Here, results for the helium rate coefficients for $\Delta J = -10$ to $\Delta J = 16$ have been plotted. It can be seen that the $\Delta J =$ even propensity continues past the previously fit $|\Delta J| \leq 4$ range.

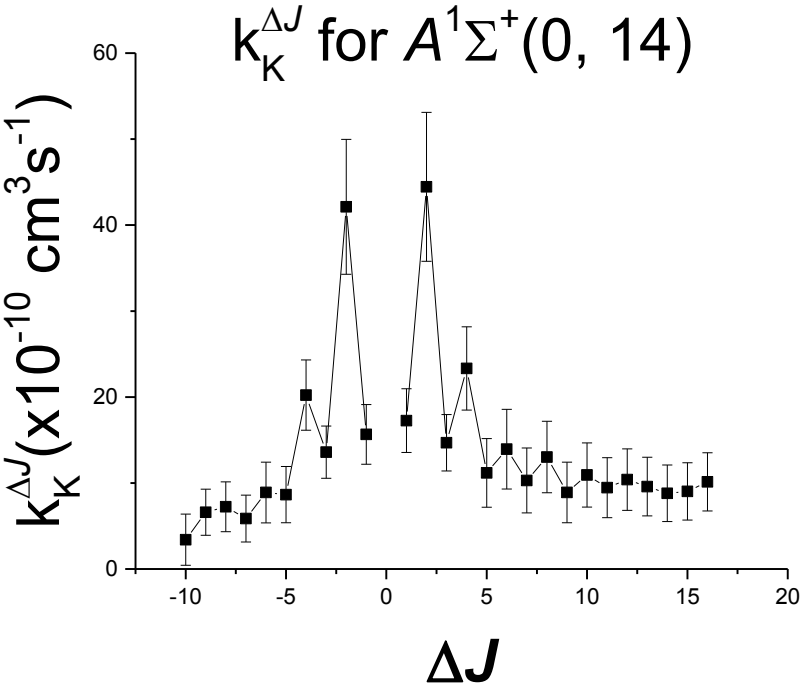

Figure 6.7: Results of the individual fits for J-changing collisions following direct pumping of the NaK $2(A)^1\Sigma^+$ (0, 14) level. Here, results for the potassium rate coefficients for $\Delta J = -10$ to $\Delta J = 16$ have been plotted. It can be see that the $\Delta J =$ even propensity continues past the previously fit $|\Delta J| \leq 4$ range, but is in contrast to the results of Wolfe *et al.* [31] and Jones [34] for $2(A)^1\Sigma^+$ (16, 30).

ΔJ	$k_{Ar}^{\Delta J}$ $(10^{-11} cm^3 s^{-1})$	$k_{He}^{\Delta J}$ $(10^{-11} cm^3 s^{-1})$	$k_{K}^{\Delta J}$ $(10^{-10} cm^3 s^{-1})$
-10	1.82 ± 0.42	5.37 ± 0.55	3.41 ± 2.98
-9	0.89 ± 0.22	2.82 ± 0.46	6.60 ± 2.69
-8	1.95 ± 0.27	7.06 ± 0.60	7.24 ± 2.90
-7	1.97 ± 0.25	4.02 ± 0.49	5.87 ± 2.72
-6	3.53 ± 0.34	10.03 ± 0.71	8.90 ± 3.53
-5	2.69 ± 0.31	4.54 ± 0.53	8.65 ± 3.27
-4	5.97 ± 0.48	14.62 ± 0.95	20.23 ± 4.08
-3	3.70 ± 0.33	6.23 ± 0.56	13.59 ± 3.04
-2	13.98 9 ± 1.01	24.02 ± 1.52	42.12 ± 7.84
-1	5.10 ± 0.41	6.65 ± 0.59	15.66 ± 3.47
1	5.59 ± 0.44	7.47 ± 0.63	17.26 ± 3.70
2	16.47 0 ± 1.15	28.03 ± 1.73	44.45 ± 8.66
3	4.60 ± 0.38	7.25 ± 0.60	14.69 ± 3.28
4	8.31 ± 0.61	20.22 ± 1.23	23.33 ± 4.84
5	4.33 ± 0.39	7.94 ± 0.66	11.18 ± 3.99
6	5.37 ± 0.45	16.65 ± 0.96	13.94 ± 4.64
7	3.91 ± 0.37	8.33 ± 0.66	10.30 ± 3.77
8	3.95 ± 0.39	14.85 ± 0.89	13.03 ± 4.15
9	3.61 ± 0.34	7.98 ± 0.63	8.90 ± 3.52
10	3.26 ± 0.35	13.13 ± 0.83	10.94 ± 3.73
11	3.20 ± 0.33	8.08 ± 0.64	9.46 ± 3.49
12	3.02 ± 0.33	12.35 ± 0.79	10.39 ± 3.58
13	2.86 ± 0.32	7.74 ± 0.63	9.59 ± 3.42
14	2.69 ± 0.31	10.91 ± 0.74	8.81 ± 3.29
15	2.85 ± 0.31	7.67 ± 0.62	9.03 ± 3.34
16	2.37 ± 0.31	10.17 ± 0.71	10.14 ± 3.38

Table 6.5: Results for $2(A)^1\Sigma^+$ (0, 14) individual fits of J-changing collisions with perturbers argon, helium and potassium. Rate coefficients $k_P^{\Delta J}$ are presented as the fit parameters ($\frac{k_P^{\Delta J}}{\Gamma}$) multiplied by $\Gamma_{(0,14)} = 4.73 \times 10^7$ s^{-1}.

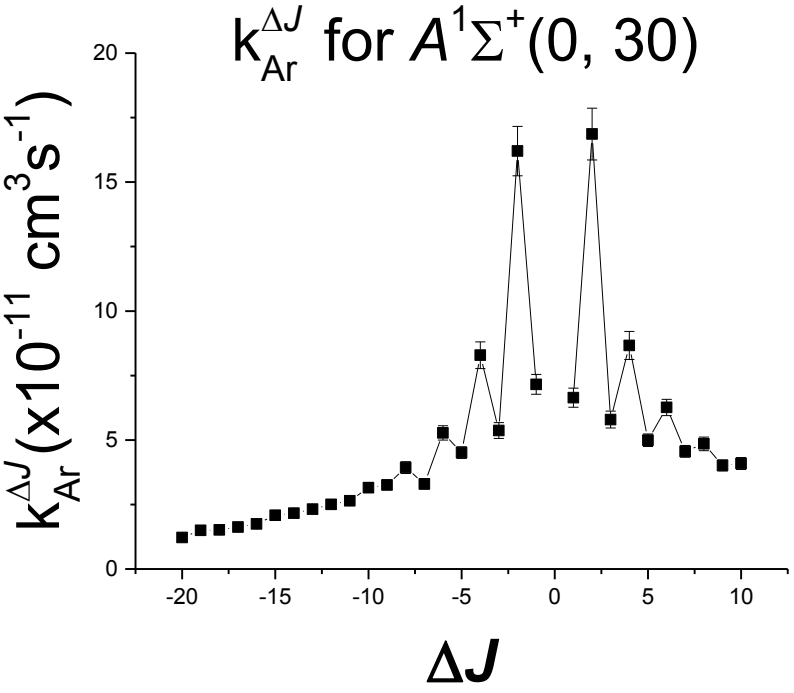

Figure 6.8: Results of the individual fits for $2(A)^1\Sigma^+$ (0, 30). Here, results for the argon rate coefficients for $\Delta J = -20$ to $\Delta J = 10$ have been plotted. The ΔJ = even propensity can be seen continuing past the previously fit $|\Delta J| \leq 4$ range.

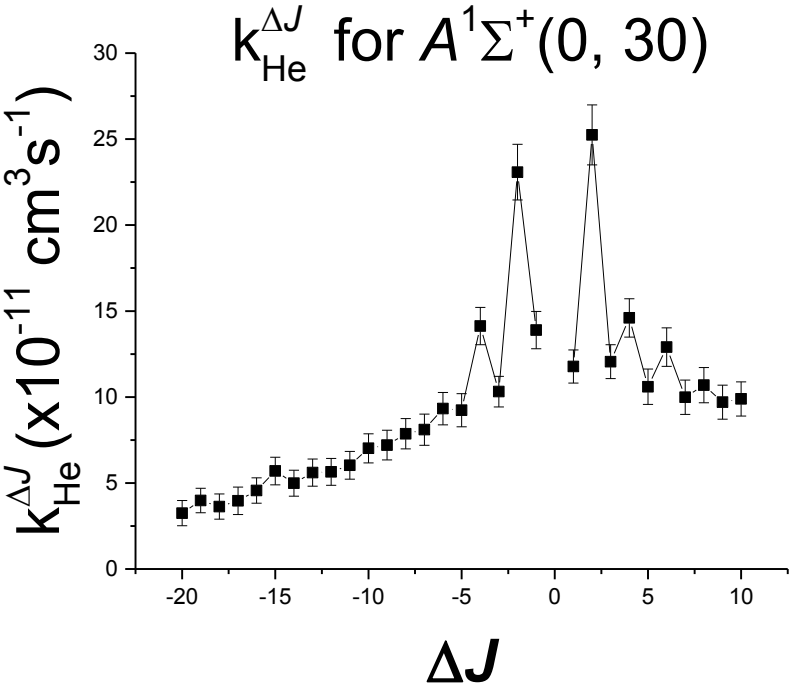

Figure 6.9: Results of the individual fits for $2(A)^1\Sigma^+$ (0, 30). Here, results for the helium rate coefficients for $\Delta J = -20$ to $\Delta J = 10$ have been plotted. The $\Delta J =$ even propensity can be seen continuing past the previously fit $|\Delta J| \leq 4$ range.

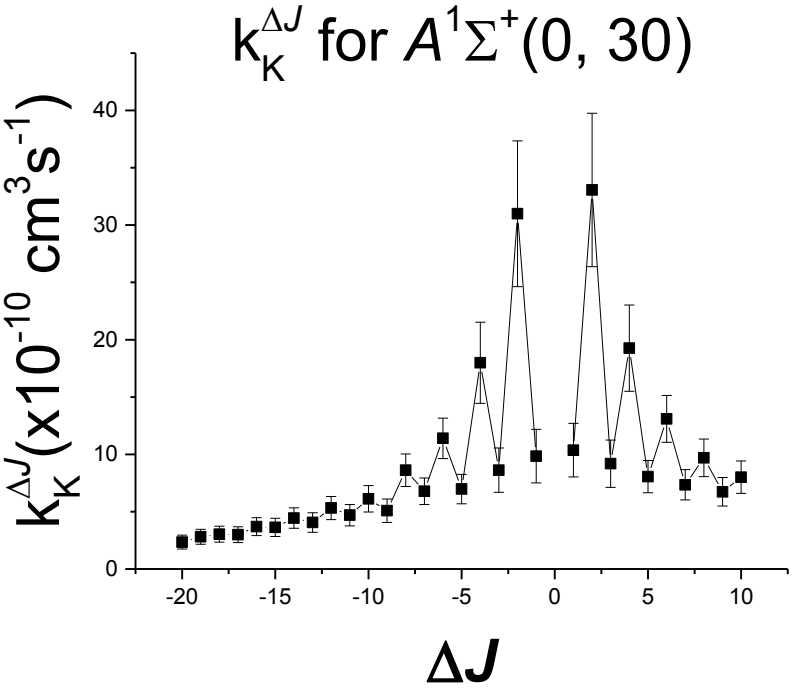

Figure 6.10: Results of the individual fits for $2(A)^1\Sigma^+(0,\ 30)$. Here, results for the potassium rate coefficients for $\Delta J = -20$ to $\Delta J = 10$ have been plotted. The $\Delta J =$ even propensity can be seen continuing past the previously fit $|\Delta J| \leq 4$ range, but is in contrast to the results of Wolfe *et al.* [31] and Jones [34] for $2(A)^1\Sigma^+(16,\ 30)$.

ΔJ	$k_{Ar}^{\Delta J}$ $(10^{-11} cm^3 s^{-1})$	$k_{He}^{\Delta J}$ $(10^{-11} cm^3 s^{-1})$	$k_{K}^{\Delta J}$ $(10^{-10} cm^3 s^{-1})$
-20	1.22 ± 0.12	3.25 ± 0.73	2.35 ± 0.61
-19	1.50 ± 0.12	3.98 ± 0.71	2.81 ± 0.66
-18	1.52 ± 0.13	3.63 ± 0.74	3.04 ± 0.69
-17	1.63 ± 0.13	3.97 ± 0.80	2.99 ± 0.69
-16	1.75 ± 0.14	4.56 ± 0.74	3.69 ± 0.78
-15	2.08 ± 0.15	5.70 ± 0.80	3.63 ± 0.79
-14	2.17 ± 0.16	4.99 ± 0.75	4.44 ± 0.89
-13	2.32 ± 0.15	5.61 ± 0.79	4.06 ± 0.85
-12	2.51 ± 0.17	5.65 ± 0.78	5.32 ± 1.01
-11	2.64 ± 0.17	6.03 ± 0.81	4.70 ± 0.93
-10	3.16 ± 0.19	7.02 ± 0.85	6.12 ± 1.15
-9	3.26 ± 0.18	7.21 ± 0.87	5.09 ± 1.02
-8	3.93 ± 0.23	7.87 ± 0.88	8.62 ± 1.42
-7	3.30 ± 0.20	8.10 ± 0.90	6.78 ± 1.16
-6	5.28 ± 0.28	9.33 ± 0.94	11.40 ± 1.76
-5	4.51 ± 0.23	9.23 ± 0.96	6.97 ± 1.28
-4	8.29 ± 0.52	14.13 ± 1.08	17.99 ± 3.54
-3	5.37 ± 0.31	10.32 ± 0.89	8.62 ± 1.93
-2	16.20 ± 0.96	23.08 ± 1.62	30.99 ± 6.36
-1	7.16 ± 0.38	13.90 ± 1.08	9.84 ± 2.34
1	6.64 ± 0.37	11.78 ± 0.96	10.36 ± 2.34
2	16.86 ± 1.00	25.25 ± 1.74	33.06 ± 6.69
3	5.79 ± 0.33	12.06 ± 0.98	9.19 ± 2.07
4	8.67 ± 0.55	14.60 ± 1.11	19.26 ± 3.76
5	4.99 ± 0.24	10.60 ± 1.03	8.05 ± 1.41
6	6.26 ± 0.32	12.91 ± 1.12	13.09 ± 2.04
7	4.56 ± 0.23	9.99 ± 1.00	7.35 ± 1.32
8	4.85 ± 0.26	10.69 ± 1.02	9.70 ± 1.64
9	4.01 ± 0.21	9.70 ± 0.99	6.74 ± 1.24
10	4.09 ± 0.23	9.89 ± 0.99	8.01 ± 1.41

Table 6.6: Results for $2(A)^1\Sigma^+$ (0, 30) individual fits of J-changing collisions with perturbers argon, helium and potassium. Rate coefficients $k_P^{\Delta J}$ are presented as the fit parameters ($\frac{k_P^{\Delta J}}{\Gamma}$) multiplied by $\Gamma_{(0,30)} = 4.71 \times 10^7$ s^{-1}.

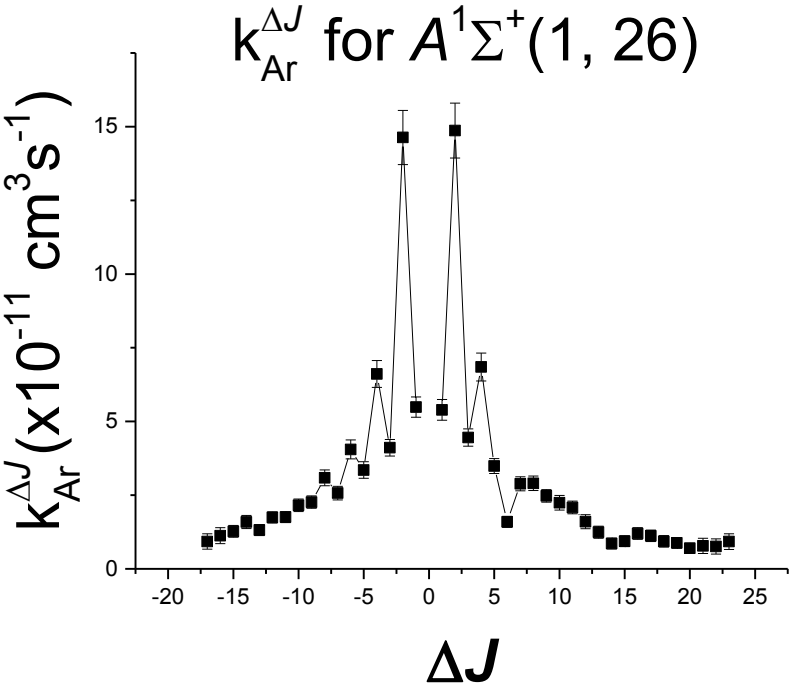

Figure 6.11: Results of the individual fits for $2(A)^1\Sigma^+$ (1, 26). Here, results for the argon rate coefficients for $\Delta J = -17$ to $\Delta J = 23$ have been plotted. The ΔJ = even propensity can be seen continuing past the previously fit $|\Delta J| \leq 4$ range. Effects of perturbations can be observed at $\Delta J = 6$ and $\Delta J =$ 12-19.

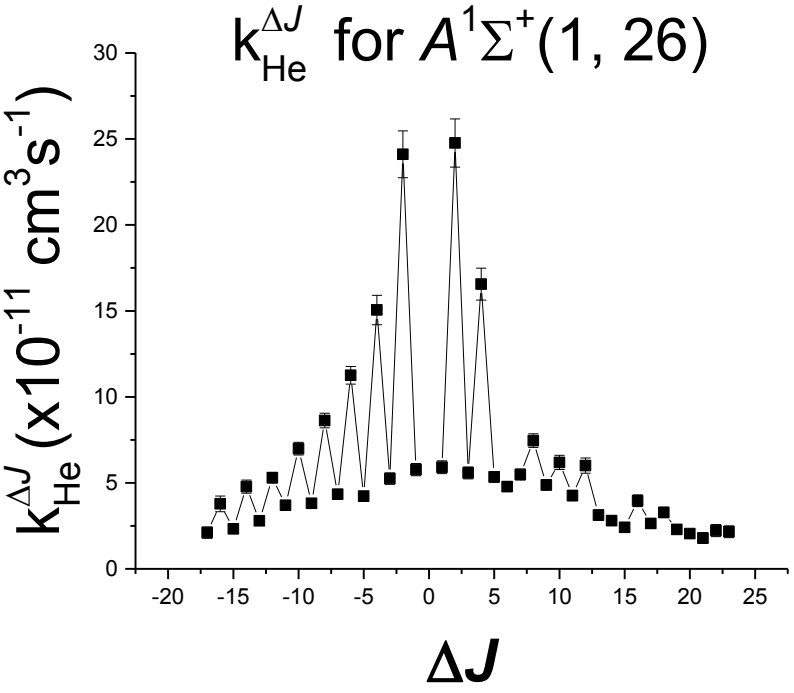

Figure 6.12: Results of the individual fits for $2(A)^1\Sigma^+(1,\ 26)$. Here, results for the helium rate coefficients for $\Delta J = -17$ to $\Delta J = 23$ have been plotted. The $\Delta J =$ even propensity can be seen continuing past the previously fit $|\Delta J| \leq 4$ range. Effects of perturbations can be observed at $\Delta J = 6$ and $\Delta J =$ 12-19.

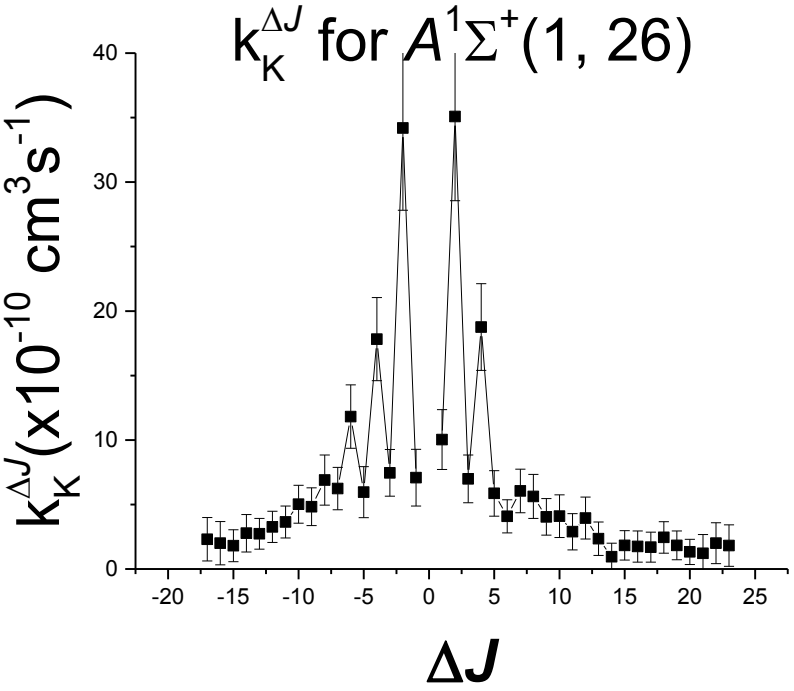

Figure 6.13: Results of the individual fits for $2(A)^1\Sigma^+(1,\ 26)$. Here, results for the potassium rate coefficients for $\Delta J = -17$ to $\Delta J = 23$ have been plotted. The $\Delta J =$ even propensity can be seen continuing past the previously fit $|\Delta J| \leq 4$ range, but is in contrast to the results of Wolfe *et al.* [31] and Jones [34] for $2(A)^1\Sigma^+(16,\ 30)$.

ΔJ	$k_{Ar}^{\Delta J}$ $(10^{-11} cm^3 s^{-1})$	$k_{He}^{\Delta J}$ $(10^{-11} cm^3 s^{-1})$	$k_{K}^{\Delta J}$ $(10^{-10} cm^3 s^{-1})$
-17	0.93 ± 0.26	2.11 ± 0.33	2.31 ± 1.68
-16	1.13 ± 0.27	3.78 ± 0.46	2.00 ± 1.68
-15	1.27 ± 0.20	2.32 ± 0.25	1.81 ± 1.24
-14	1.59 ± 0.23	4.78 ± 0.38	2.77 ± 1.45
-13	1.32 ± 0.19	2.80 ± 0.24	2.73 ± 1.20
-12	1.75 ± 0.19	5.30 ± 0.31	3.26 ± 1.21
-11	1.75 ± 0.19	3.70 ± 0.25	3.65 ± 1.24
-10	2.16 ± 0.21	6.99 ± 0.37	5.02 ± 1.47
-9	2.27 ± 0.21	3.81 ± 0.28	4.83 ± 1.46
-8	3.09 ± 0.27	8.63 ± 0.43	6.89 ± 1.94
-7	2.57 ± 0.23	4.34 ± 0.28	6.24 ± 1.64
-6	4.05 ± 0.32	11.26 ± 0.51	11.82 ± 2.46
-5	3.35 ± 0.28	4.23 ± 0.28	5.96 ± 1.98
-4	6.61 ± 0.46	15.06 ± 0.85	17.82 ± 3.22
-3	4.11 ± 0.28	5.25 ± 0.33	7.46 ± 1.81
-2	14.63 ± 0.92	24.11 ± 1.37	34.19 ± 6.38
-1	5.49 ± 0.34	5.77 ± 0.36	7.08 ± 2.20
1	5.39 ± 0.35	5.91 ± 0.37	10.04 ± 2.32
2	14.87 ± 0.93	24.76 ± 1.40	35.08 ± 6.52
3	4.46 ± 0.29	5.58 ± 0.35	6.99 ± 1.85
4	6.85 ± 0.47	16.56 ± 0.93	18.76 ± 3.36
5	3.49 ± 0.25	5.35 ± 0.31	5.86 ± 1.77
6	1.60 ± 0.19	4.78 ± 0.29	4.09 ± 1.29
7	2.88 ± 0.24	5.49 ± 0.32	6.05 ± 1.69
8	2.90 ± 0.24	7.46 ± 0.40	5.63 ± 1.70
9	2.48 ± 0.21	4.88 ± 0.29	4.04 ± 1.42
10	2.24 ± 0.25	6.19 ± 0.41	4.09 ± 1.66
11	2.08 ± 0.22	4.26 ± 0.30	2.89 ± 1.41
12	1.60 ± 0.24	6.00 ± 0.44	3.95 ± 1.63
13	1.24 ± 0.21	3.12 ± 0.29	2.35 ± 1.29
14	0.86 ± 0.18	2.80 ± 0.28	0.95 ± 1.06
15	0.94 ± 0.19	2.41 ± 0.26	1.83 ± 1.14
16	1.20 ± 0.20	3.96 ± 0.34	1.75 ± 1.21
17	1.12 ± 0.19	2.64 ± 0.27	1.69 ± 1.16
18	0.93 ± 0.19	3.28 ± 0.30	2.45 ± 1.22
19	0.88 ± 0.18	2.29 ± 0.25	1.83 ± 1.12
20	0.70 ± 0.17	2.05 ± 0.24	1.33 ± 0.98
21	0.78 ± 0.26	1.79 ± 0.32	1.22 ± 1.45
22	0.76 ± 0.26	2.23 ± 0.35	2.00 ± 1.59
23	0.92 ± 0.26	2.16 ± 0.35	1.82 ± 1.61

Table 6.7: Results for $2(A)^1\Sigma^+$ (1, 26) individual fits of J-changing collisions with perturbers argon, helium and potassium. Rate coefficients $k_P^{\Delta J}$ are presented as the fit parameters ($\frac{k_P^{\Delta J}}{\Gamma}$) multiplied by $\Gamma_{(1,26)} = 4.69 \times 10^7$ s^{-1}.

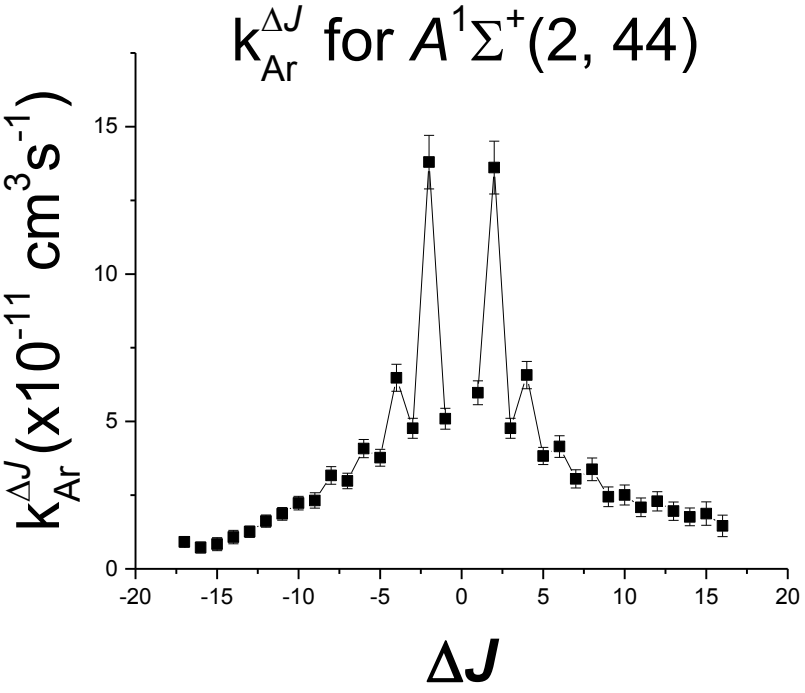

Figure 6.14: Results of the individual fits for $2(A)^1\Sigma^+$ (2, 44). Here, results for the argon rate coefficients for $\Delta J = -17$ to $\Delta J = 16$ have been plotted. The ΔJ = even propensity can be seen continuing past the previously fit $|\Delta J| \leq 4$ range.

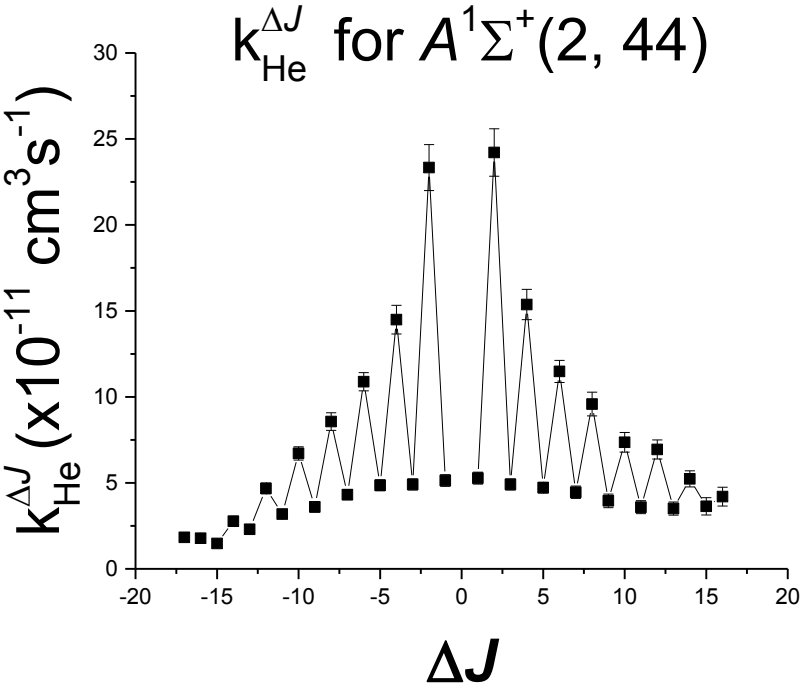

Figure 6.15: Results of the individual fits for $2(A)^1\Sigma^+(2,\ 44)$. Here, results for the helium rate coefficients for $\Delta J = -17$ to $\Delta J = 16$ have been plotted. The $\Delta J =$ even propensity can be seen continuing past the previously fit $|\Delta J| \leq 4$ range.

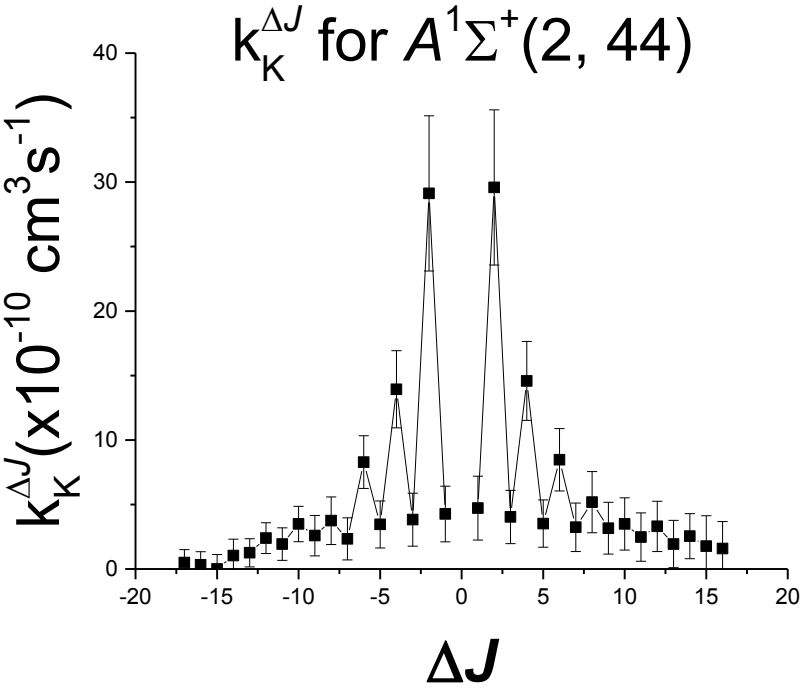

Figure 6.16: Results of the individual fits for $2(A)^1\Sigma^+(2,\ 44)$. Here, results for the potassium rate coefficients for $\Delta J = -17$ to $\Delta J = 16$ have been plotted. The $\Delta J =$ even propensity can be seen continuing past the previously fit $|\Delta J| \leq 4$ range, but is in contrast to the results of Wolfe *et al.* [31] and Jones [34] for $2(A)^1\Sigma^+(16,\ 30)$.

ΔJ	$k_{Ar}^{\Delta J}$ $(10^{-11} cm^3 s^{-1})$	$k_{He}^{\Delta J}$ $(10^{-11} cm^3 s^{-1})$	$k_{K}^{\Delta J}$ $(10^{-10} cm^3 s^{-1})$
-17	0.92 ± 0.18	1.83 ± 0.21	0.50 ± 1.01
-16	0.72 ± 0.19	1.78 ± 0.21	0.33 ± 1.02
-15	0.84 ± 0.22	1.48 ± 0.20	0.00 ± 1.12
-14	1.08 ± 0.23	2.76 ± 0.29	1.04 ± 1.27
-13	1.26 ± 0.19	2.30 ± 0.23	1.26 ± 1.09
-12	1.62 ± 0.21	4.68 ± 0.31	2.40 ± 1.19
-11	1.87 ± 0.22	3.18 ± 0.26	1.94 ± 1.26
-10	2.23 ± 0.23	6.71 ± 0.38	3.49 ± 1.37
-9	2.32 ± 0.26	3.60 ± 0.31	2.59 ± 1.57
-8	3.17 ± 0.30	8.57 ± 0.51	3.75 ± 1.84
-7	2.98 ± 0.26	4.32 ± 0.30	2.33 ± 1.63
-6	4.08 ± 0.31	10.88 ± 0.53	8.29 ± 2.04
-5	3.77 ± 0.29	4.86 ± 0.32	3.45 ± 1.82
-4	6.48 ± 0.46	14.49 ± 0.83	13.94 ± 3.00
-3	4.77 ± 0.34	4.91 ± 0.33	3.82 ± 2.06
-2	13.80 ± 0.91	23.34 ± 1.34	29.12 ± 6.02
-1	5.09 ± 0.36	5.14 ± 0.34	4.26 ± 2.16
1	5.97 ± 0.40	5.28 ± 0.35	4.72 ± 2.47
2	13.61 ± 0.90	24.22 ± 1.38	29.59 ± 6.02
3	4.77 ± 0.34	4.91 ± 0.33	4.03 ± 2.06
4	6.58 ± 0.46	15.37 ± 0.88	14.59 ± 3.07
5	3.83 ± 0.29	4.72 ± 0.31	3.52 ± 1.83
6	4.15 ± 0.37	11.48 ± 0.64	8.47 ± 2.42
7	3.05 ± 0.31	4.45 ± 0.36	3.24 ± 1.88
8	3.38 ± 0.39	9.58 ± 0.69	5.19 ± 2.38
9	2.45 ± 0.34	3.95 ± 0.40	3.16 ± 2.01
10	2.51 ± 0.34	7.36 ± 0.57	3.50 ± 2.03
11	2.09 ± 0.32	3.59 ± 0.38	2.47 ± 1.88
12	2.29 ± 0.33	6.95 ± 0.56	3.31 ± 1.95
13	1.96 ± 0.31	3.51 ± 0.38	1.94 ± 1.83
14	1.76 ± 0.30	5.23 ± 0.47	2.55 ± 1.75
15	1.88 ± 0.40	3.64 ± 0.51	1.77 ± 2.36
16	1.46 ± 0.36	4.20 ± 0.55	1.58 ± 2.10

Table 6.8: Results for $2(A)^1\Sigma^+$ (2, 44) individual fits of J-changing collisions with perturbers argon, helium and potassium. Rate coefficients $k_P^{\Delta J}$ are presented as the fit parameters ($\frac{k_P^{\Delta J}}{\Gamma}$) multiplied by $\Gamma_{(1,26)} = 4.63 \times 10^7$ s^{-1}.

J	ΔJ from (1,26)	$2(A)^1\Sigma^+$ (v=1)%	total $b^3\Pi$ (v= 5)%
30	4	96.96	3.04
31	5	96.16	3.84
32	6	76.77	23.23
33	7	94.55	5.45
34	8	95.18	4.82
35	9	94.55	5.45
36	10	93.35	6.65
37	11	91.24	8.76
38	12	87.09	12.91
39	13	77.38	22.63
40	14	54.46	45.54
41	15	64.82	35.18
42	16	76.79	23.21
43	17	78.71	21.29
44	18	75.81	24.19
45	19	69.36	30.64

Table 6.9: Percentages of $2(A)^1\Sigma^+$ and $b^3\Pi$ character in mixed rotational levels of nominal $2(A)^1\Sigma^+$ character. When rotational levels of the same J from two neighboring electronic levels have total energies that are approximately equal, the two levels can interact, creating mixed states, assuming some coupling mechanism exists for those two states. In the present case, the $2(A)^1\Sigma^+$ and $1(b)^3\Pi$ states are coupled by spin-orbit interaction. In our work, these mixed levels produce anomalously low intensities in the collisional spectrum because only the singlet amplitude contributes significantly to the collisional transfer and to the subsequent fluorescence emission.

An interesting feature can be seen in the $+\Delta J$ branch of $2(A)^1\Sigma^+$ (1, 26) data. Here, we notice a substantial dip in the sequence of rate coefficients, at $\Delta J = 6$, which appears to go against the normal ΔJ =even propensity. This deviation from the expected population ratio, is caused by a local perturbation of $2(A)^1\Sigma^+$ (1, 32) with the $1(b)^3\Pi_{\Omega=0,1,2}$(5, 32) level, which is a result of the spin-orbit interaction between the two levels. Table 6.9 shows percentages of $2(A)^1\Sigma^+$ and $b^3\Pi$ state character for levels that are nominally $2(A)^1\Sigma^+$ ($v = 1$) levels (i.e. have predominantly

$2(A)^1\Sigma^+$ character) [11]. Note that $2(A)^1\Sigma^+$ ($v = 1$) state levels with $J = 12$ - 19 are also highly mixed, so those measured rate coefficients are also suppressed relative to what they would be in the absence of perturbation.

6.3.3 Individual Fits and Results: *v, J*-changing collisions

In addition to our studies of NaK $2(A)^1\Sigma^+$ J-changing collisions with argon, helium, and potassium, we have also obtained a significant amount of data on collisions in which both v and J change. The present section describes our analysis of these data, and presents our results. These individual fits for collisions in which both v and J change were carried out with the same procedure as for the J-changing collision data, as outlined in the previous section 6.3.2.

Here I present the results of the individual fits carried out for collisions in which population was transferred from $2(A)^1\Sigma^+$ vibrational level $v = 2$ to level $v = 1$ ($\Delta v = -1$ transfer) and to $v = 0$ ($\Delta v = -2$), and for collisions in which population was transferred from $2(A)^1\Sigma^+$ vibrational level $v = 1$ to $v = 0$ ($\Delta v = -1$). The fits have been carried out using the quenching rate coefficients determined in the global fit of the $\Delta v = 0, |\Delta J| \leq 4$ data. Again, in each case, $\frac{k_P^\Delta}{\Gamma}$ values obtained in the fits have been multiplied by the appropriate gamma, so that values for rate coefficients k_P^Δ are presented.

Figures 6.17, 6.18 and 6.19 show the rate coefficient results for $\Delta v = -1$ collisions of NaK $2(A)^1\Sigma^+$ (2, 44) molecules with argon, helium, and potassium, respectively, and these are also listed in Table 6.10. Figures 6.20, 6.21 and 6.22 show the results for argon, helium, and potassium rate coefficients, respectively, for $\Delta v = -2$

collisions of NaK $2(A)^1\Sigma^+$ (2, 44) molecules. These values are listed in Table 6.11. Figures 6.23, 6.24 and 6.25 give the results for $2(A)^1\Sigma^+$ (1, 26) Δv = -1 collisions, which are listed in Table 6.12.

We see that the rate coefficients for v-changing collisions are about an order of magnitude smaller than those for J-changing collisions for small ΔJ ($|\Delta J| \leq 5$) and comparable to those for large ΔJ ($|\Delta J| \geq 15$). We also see that the $v = 1 \rightarrow v = 0$ rate coefficients are larger than the $v = 2 \rightarrow v = 1$ rate coefficients and the $v = 2 \rightarrow v = 1$ rate coefficients are larger than the $v = 2 \rightarrow v = 0$ rate coefficients, although these differences are not great. The fitted potassium rate coefficients are often equal to zero within error bars. The v-changing rate coefficients are also fairly independent of ΔJ. However it is possible that larger variations with ΔJ do occur, but are partially washed out due to multiple collision effects. We note the results reported in Figs. 6.17-6.25 and Tables 6.10 to 6.12 have not been corrected for multiple collision effects. We address this issue in more detail in Sec. 6.4.

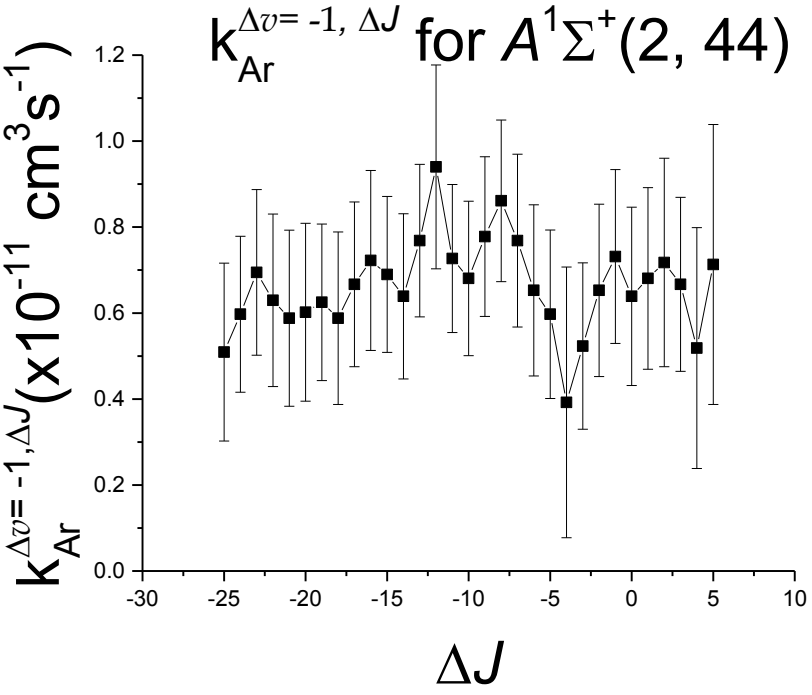

Figure 6.17: Results of the individual fits for NaK $2(A)^1\Sigma^+(2,\ 44)$ v- and J- changing collisions. Here, results for the argon rate coefficients for $\Delta v = -1$, $\Delta J = -25$ to $\Delta J = 5$ have been plotted. The ΔJ = -4 rate coefficient (which corresponds to the ro-vibrational level (1, 40)) is suppressed due to a perturbation as described in the previous section.

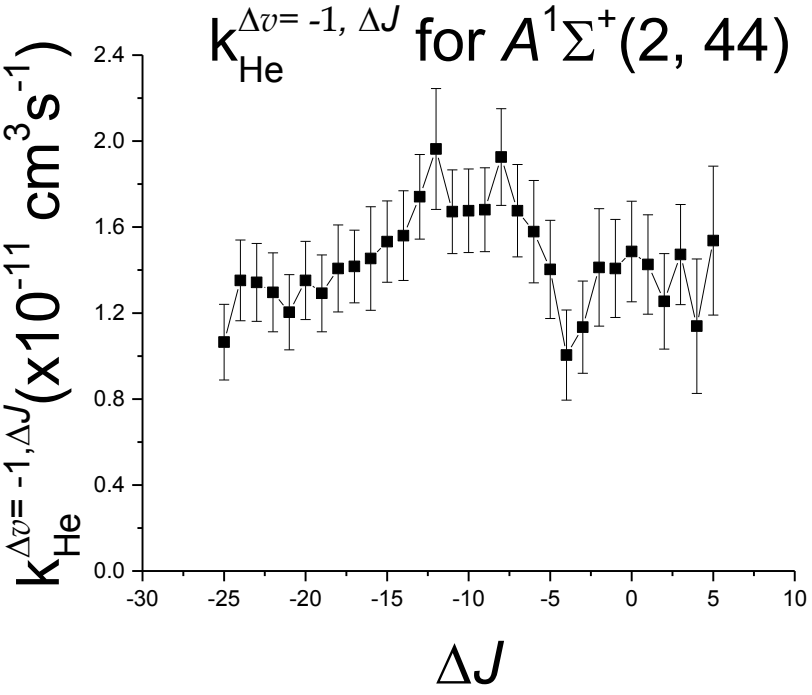

Figure 6.18: Results of the individual fits for NaK $2(A)^1\Sigma^+(2,\ 44)$ v- and J- changing collisions. Here, results for the helium rate coefficients for $\Delta v = -1$, $\Delta J = -25$ to $\Delta J = 5$ have been plotted. The ΔJ = -4 rate coefficient (which corresponds to the ro-vibrational level (1, 40)) is suppressed due to a perturbation as described in the previous section.

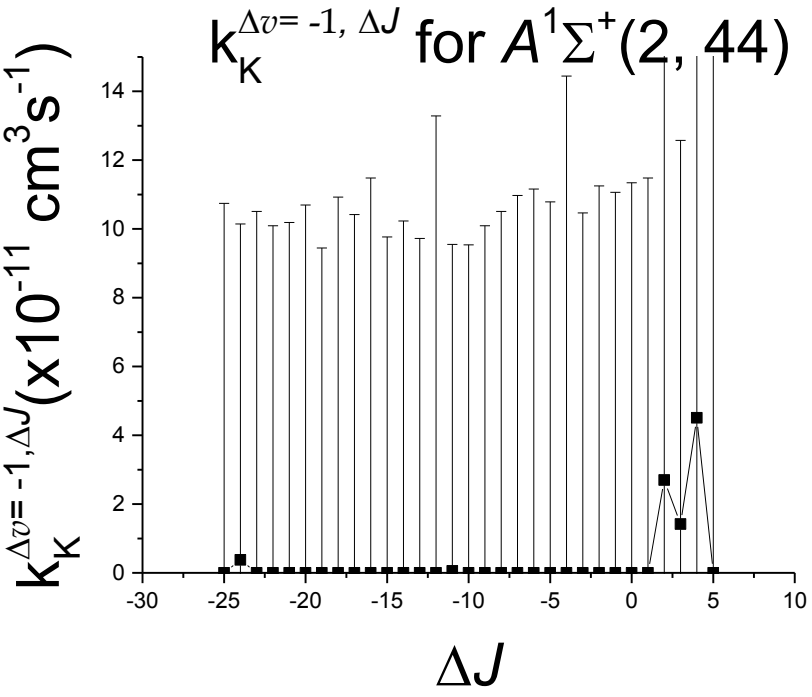

Figure 6.19: Results of the individual fits for NaK $2(A)^1\Sigma^+$ (2, 44) v- and J- changing collisions. Here, results for the potassium rate coefficients for $\Delta v = -1$, $\Delta J = -25$ to $\Delta J = 5$ have been plotted.

Rate coefficients for $2(A)^1\Sigma^+$ (2, 44), Δv = -1			
ΔJ	$k_{Ar}^{\Delta J}$ $(10^{-11} cm^3 s^{-1})$	$k_{He}^{\Delta J}$ $(10^{-11} cm^3 s^{-1})$	$k_{K}^{\Delta J}$ $(10^{-11} cm^3 s^{-1})$
-25	0.51 ± 0.21	1.06 ± 0.18	0.00 ± 10.74
-24	0.60 ± 0.18	1.35 ± 0.19	0.38 ± 9.77
-23	0.69 ± 0.19	1.34 ± 0.18	0.00 ± 10.51
-22	0.63 ± 0.20	1.30 ± 0.18	0.00 ± 10.09
-21	0.59 ± 0.20	1.20 ± 0.18	0.00 ± 10.19
-20	0.60 ± 0.21	1.35 ± 0.18	0.00 ± 10.70
-19	0.63 ± 0.18	1.29 ± 0.18	0.00 ± 9.45
-18	0.59 ± 0.20	1.41 ± 0.20	0.00 ± 10.93
-17	0.67 ± 0.19	1.42 ± 0.17	0.00 ± 10.42
-16	0.72 ± 0.21	1.45 ± 0.24	0.00 ± 11.48
-15	0.69 ± 0.18	1.53 ± 0.19	0.00 ± 9.77
-14	0.64 ± 0.19	1.56 ± 0.21	0.00 ± 10.23
-13	0.77 ± 0.18	1.74 ± 0.20	0.00 ± 9.72
-12	0.94 ± 0.24	1.96 ± 0.28	0.00 ± 13.29
-11	0.73 ± 0.17	1.67 ± 0.19	0.06 ± 9.49
-10	0.68 ± 0.18	1.68 ± 0.19	0.00 ± 9.54
-9	0.78 ± 0.19	1.68 ± 0.19	0.00 ± 10.09
-8	0.86 ± 0.19	1.93 ± 0.23	0.00 ± 10.51
-7	0.77 ± 0.20	1.68 ± 0.21	0.00 ± 10.97
-6	0.65 ± 0.20	1.58 ± 0.24	0.00 ± 11.16
-5	0.60 ± 0.20	1.40 ± 0.23	0.00 ± 10.79
-4	0.39 ± 0.31	1.00 ± 0.21	0.00 ± 14.45
-3	0.52 ± 0.19	1.13 ± 0.21	0.00 ± 10.46
-2	0.65 ± 0.20	1.41 ± 0.27	0.00 ± 11.25
-1	0.73 ± 0.20	1.41 ± 0.23	0.00 ± 11.07
0	0.64 ± 0.21	1.49 ± 0.23	0.00 ± 11.34
1	0.68 ± 0.21	1.43 ± 0.23	0.00 ± 11.48
2	0.72 ± 0.24	1.25 ± 0.22	2.70 ± 13.33
3	0.67 ± 0.20	1.47 ± 0.23	1.42 ± 11.16
4	0.52 ± 0.28	1.14 ± 0.31	4.51 ± 14.91
5	0.71 ± 0.33	1.54 ± 0.35	0.00 ± 17.36

Table 6.10: Results for individual fits of NaK $2(A)^1\Sigma^+$ (2, 44) v-, J-changing collision data with perturbers argon, helium and potassium. Rate coefficients $k_P^{\Delta J}$ are presented as the fit parameters ($\frac{k_P^{\Delta J}}{\Gamma}$) multiplied by $\Gamma_{(2,44)} = 4.63 \times 10^7$ s^{-1}.

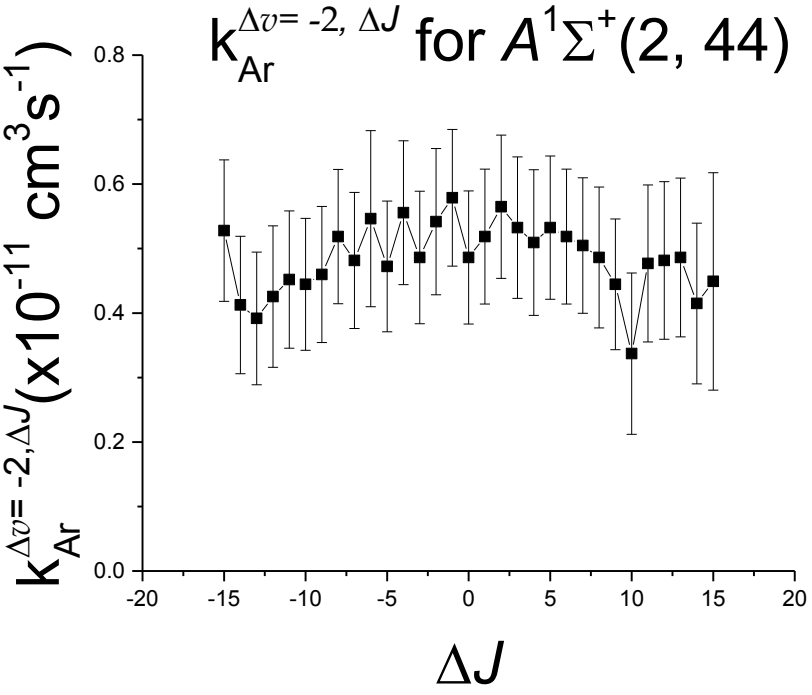

Figure 6.20: Results of the individual fits for NaK $2(A)^1\Sigma^+\,(2,\,44)$ v- and J- changing collisions. Here, results for the argon rate coefficients for $\Delta v = -2$, $\Delta J = -15$ to $\Delta J = 15$ have been plotted. The $\Delta J = 10$ rate coefficient (which corresponds to the ro-vibrational level (0, 54)) is suppressed due to a perturbation as described in the previous section.

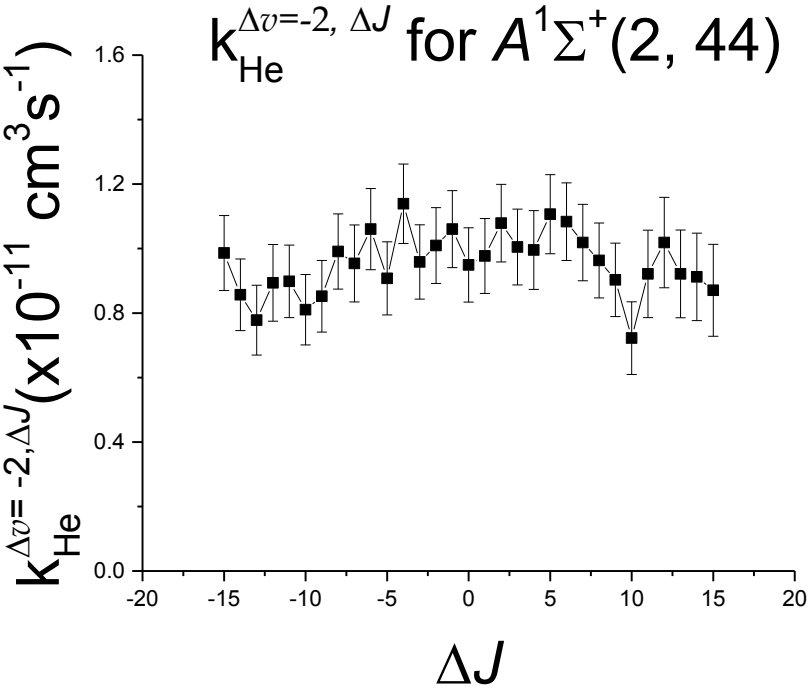

Figure 6.21: Results of the individual fits for NaK $2(A)^1\Sigma^+\,(2,\,44)$ v- and J- changing collisions. Here, results for the helium rate coefficients for $\Delta v = -2$, $\Delta J = -15$ to $\Delta J = 15$ have been plotted. The $\Delta J = 10$ rate coefficient (which corresponds to the ro-vibrational level (0, 54)) is suppressed due to a perturbation as described in the previous section.

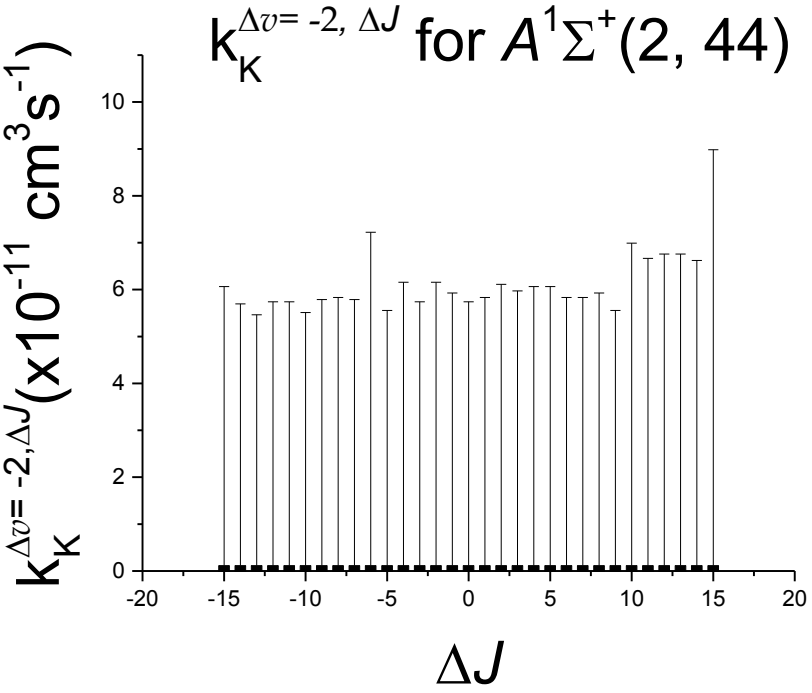

Figure 6.22: Results of the individual fits for NaK $2(A)^1\Sigma^+$ (2, 44) v- and J- changing collisions. Here, results for the potassium rate coefficients for $\Delta v = -2$, $\Delta J = -15$ to $\Delta J = 15$ have been plotted.

Rate coefficients for $2(A)^1\Sigma^+$ (2, 44), Δv = -2			
ΔJ	$k_{Ar}^{\Delta J}$ $(10^{-11} cm^3 s^{-1})$	$k_{He}^{\Delta J}$ $(10^{-11} cm^3 s^{-1})$	$k_{K}^{\Delta J}$ $(10^{-11} cm^3 s^{-1})$
-15	0.53 ± 0.11	0.99 ± 0.12	0.00 ± 6.07
-14	0.41 ± 0.11	0.86 ± 0.11	0.00 ± 5.69
-13	0.39 ± 0.10	0.78 ± 0.11	0.00 ± 5.46
-12	0.43 ± 0.11	0.89 ± 0.12	0.00 ± 5.74
-11	0.45 ± 0.11	0.90 ± 0.11	0.00 ± 5.74
-10	0.44 ± 0.10	0.81 ± 0.11	0.00 ± 5.51
-9	0.46 ± 0.11	0.85 ± 0.11	0.00 ± 5.79
-8	0.52 ± 0.10	0.99 ± 0.12	0.00 ± 5.83
-7	0.48 ± 0.11	0.95 ± 0.12	0.00 ± 5.79
-6	0.55 ± 0.14	1.06 ± 0.13	0.00 ± 7.22
-5	0.47 ± 0.10	0.91 ± 0.11	0.00 ± 5.56
-4	0.56± 0.11	1.14 ± 0.12	0.00 ± 6.16
-3	0.49 ± 0.10	0.96 ± 0.12	0.00 ± 5.74
-2	0.54 ± 0.11	1.01 ± 0.12	0.00 ± 6.16
-1	0.58 ± 0.11	1.06 ± 0.12	0.00 ± 5.93
0	0.49 ± 0.10	0.95 ± 0.12	0.00 ± 5.74
1	0.52 ± 0.10	0.98 ± 0.12	0.00 ± 5.83
2	0.56 ± 0.11	1.08 ± 0.12	0.00 ± 6.11
3	0.53 ± 0.11	1.00 ± 0.12	0.00 ± 5.97
4	0.51 ± 0.11	1.00 ± 0.12	0.00 ± 6.07
5	0.53 ± 0.11	1.11 ± 0.12	0.00 ± 6.07
6	0.52 ± 0.10	1.08 ± 0.12	0.00 ± 5.83
7	0.50 ± 0.11	1.02 ± 0.12	0.00 ± 5.83
8	0.49 ± 0.11	0.96 ± 0.12	0.00 ± 5.93
9	0.44 ± 0.10	0.90 ± 0.11	0.00 ± 5.56
10	0.34 ± 0.13	0.72 ± 0.11	0.00 ± 6.99
11	0.48 ± 0.12	0.92 ± 0.14	0.00 ± 6.67
12	0.48 ± 0.12	1.02 ± 0.14	0.00 ± 6.76
13	0.49 ± 0.12	0.92 ± 0.14	0.00 ± 6.76
14	0.41 ± 0.12	0.91 ± 0.14	0.00 ± 6.62
15	0.45 ± 0.17	0.87 ± 0.14	0.00 ± 8.98

Table 6.11: Results for individual fits of NaK $2(A)^1\Sigma^+$ (2, 44) v-, J-changing collision data with perturbers argon, helium and potassium. Rate coefficients $k_P^{\Delta J}$, Δv = -2 are presented as the fit parameters ($\frac{k_P^{\Delta J}}{\Gamma}$) multiplied by $\Gamma_{(2,44)} = 4.63 \times 10^7 \mathrm{s}^{-1}$.

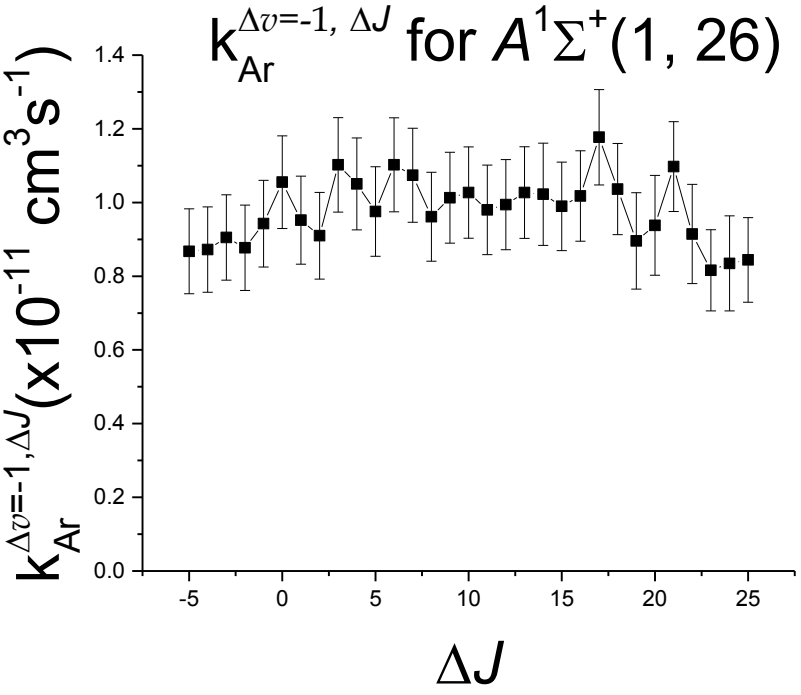

Figure 6.23: Results of the individual fits for NaK $2(A)^1\Sigma^+\,(1,\,26)$ v- and J- changing collisions. Here, results for the argon rate coefficients for $\Delta v = -1$, $\Delta J = -5$ to $\Delta J = 25$ have been plotted.

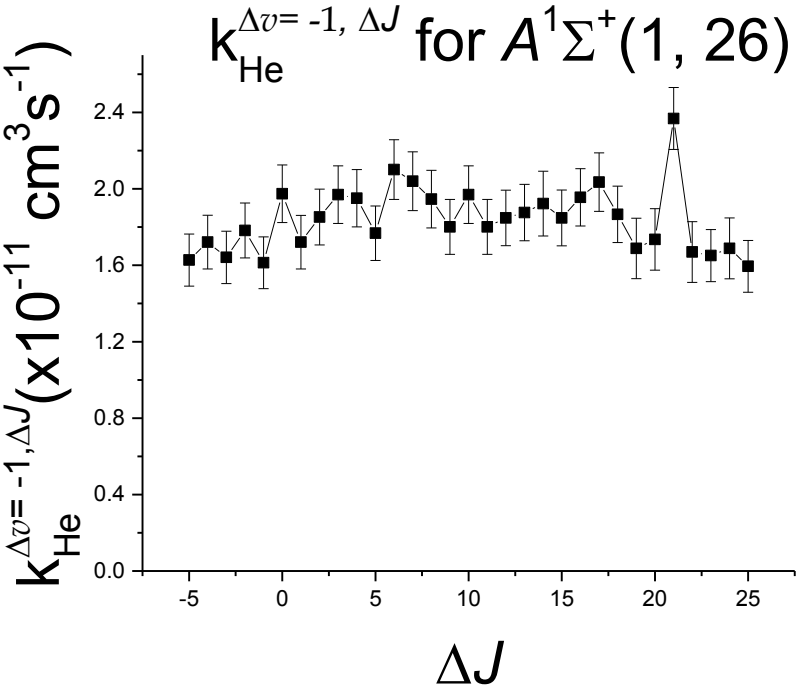

Figure 6.24: Results of the individual fits for NaK $2(A)^1\Sigma^+$ (1, 26) v- and J- changing collisions. Here, results for the helium rate coefficients for $\Delta v = -1$, $\Delta J = -5$ to $\Delta J = 25$ have been plotted.

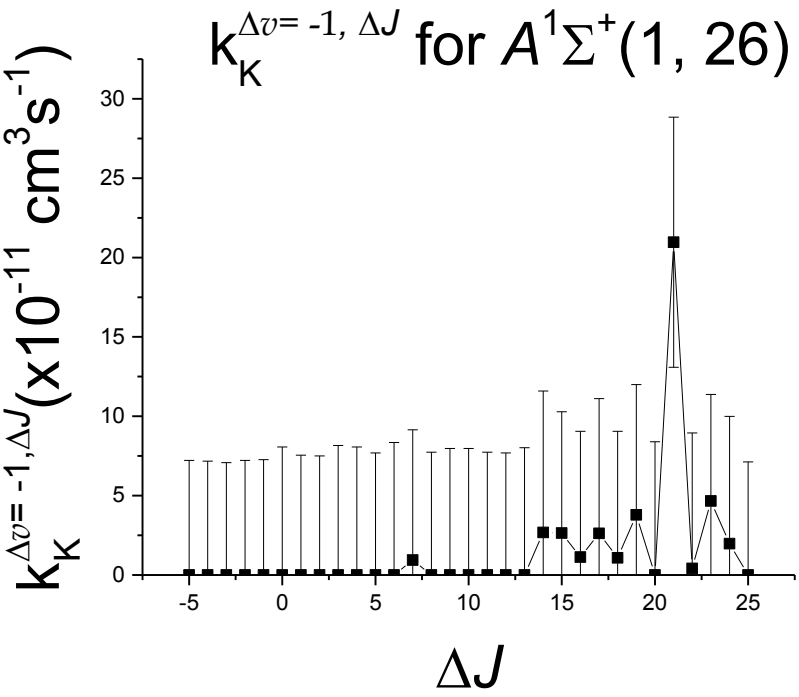

Figure 6.25: Results of the individual fits for NaK $2(A)^1\Sigma^+(1, 26)$ v- and J- changing collisions. Here, results for the potassium rate coefficients for $\Delta v = -1$, $\Delta J = -5$ to $\Delta J = 25$ have been plotted.

Rate coefficients for $2(A)^1\Sigma^+$ (1, 26), Δv = -1			
ΔJ	$k_{Ar}^{\Delta J}$ $(10^{-11} cm^3 s^{-1})$	$k_{He}^{\Delta J}$ $(10^{-11} cm^3 s^{-1})$	$k_{K}^{\Delta J}$ $(10^{-11} cm^3 s^{-1})$
-5	0.87 ± 0.12	1.63 ± 0.14	0.00 ± 7.22
-4	0.87 ± 0.12	1.72 ± 0.14	0.00 ± 7.18
-3	0.91 ± 0.12	1.64 ± 0.14	0.00 ± 7.08
-2	0.88 ± 0.12	1.78 ± 0.14	0.00 ± 7.22
-1	0.94 ± 0.12	1.61 ± 0.14	0.00 ± 7.27
0	1.06 ± 0.13	1.97 ± 0.15	0.00 ± 8.07
1	0.95 ± 0.12	1.72 ± 0.14	0.00 ± 7.55
2	0.91 ± 0.12	1.85 ± 0.15	0.00 ± 7.50
3	1.10 ± 0.13	1.97 ± 0.15	0.00 ± 8.16
4	1.05 ± 0.12	1.95 ± 0.15	0.00 ± 8.07
5	0.98 ± 0.12	1.77 ± 0.14	0.00 ± 7.69
6	1.10 ± 0.13	2.10 ± 0.16	0.00 ± 8.35
7	1.07 ± 0.13	2.04 ± 0.15	0.94 ± 8.21
8	0.96 ± 0.12	1.95 ± 0.15	0.00 ± 7.74
9	1.01 ± 0.12	1.80 ± 0.14	0.00 ± 7.97
10	1.03 ± 0.12	1.97 ± 0.15	0.00 ± 7.97
11	0.98 ± 0.12	1.80 ± 0.14	0.00 ± 7.74
12	0.99 ± 0.12	1.85 ± 0.15	0.00 ± 7.69
13	1.03 ± 0.12	1.88 ± 0.15	0.00 ± 8.02
14	1.02 ± 0.14	1.92 ± 0.17	2.68 ± 8.91
15	0.99 ± 0.12	1.85 ± 0.15	2.64 ± 7.64
16	1.02 ± 0.12	1.96 ± 0.15	1.13 ± 7.93
17	1.18 ± 0.13	2.04 ± 0.15	2.63 ± 8.49
18	1.04 ± 0.12	1.87 ± 0.15	1.08 ± 7.97
19	0.90 ± 0.13	1.69 ± 0.16	3.78 ± 8.21
20	0.94 ± 0.14	1.74 ± 0.16	0.00 ± 8.40
21	1.10 ± 0.12	2.37 ± 0.16	20.96 ± 7.88
22	0.91 ± 0.13	1.67 ± 0.16	0.41 ± 8.54
23	0.82 ± 0.11	1.65 ± 0.14	4.67 ± 6.71
24	0.83 ± 0.13	1.69 ± 0.16	1.97 ± 8.02
25	0.84 ± 0.11	1.59± 0.14	0.00 ± 7.13

Table 6.12: Results for individual fits of NaK $2(A)^1\Sigma^+$ (1, 26) v-, J-changing collisions with perturbers argon, helium and potassium. Rate coefficients $k_P^{\Delta J}$ are presented as the fit parameters ($\frac{k_P^{\Delta J}}{\Gamma}$) multiplied by $\Gamma_{(1,26)} = 4.69 \times 10^7 \mathrm{s}^{-1}$.

6.4 Approximations and Assumptions Used in This Work

In the derivation of the final expressions used in this work (Eqs. 5.14a, 5.14b and 5.25) for intensity ratios observed in J-changing and v-changing collisions, respectively, we have made several assumptions that should be discussed.

6.4.1 The Anisotropy Factor F

The first assumption, which was made just after Eq. 5.7, stated that the anisotropy factors F cancel in the ratio of collisional fluorescence to direct fluorescence. This argument is based on the fact that we only compare P collisional lines to P direct lines (or R lines to R lines). However the anisotropy factor is related to polarization, and we know that v and J changing collisions reduce the orientation and hence tend to depolarize the light. Therefore the anisotropy factor for a collisional line is different than that for a direct line.

To estimate the difference in the collisional and direct level anisotropy factors, we begin by introducing f as the percentage of the direct line emitted light that is collected by our detector. We follow an argument similar to that given in Chen *et al.* [62]. We define a coordinate system such that the laser propagates along the $\hat{x}$-direction, and is polarized in the $\hat{z}$-direction. We assume the fluorescence is observed at an angle θ with respect to the polarization axis $\hat{z}$. In the current experiment, we observe in the backwards $\hat{x}$-direction, so that the angle $\theta = 90°$, as shown in Fig. 6.26.

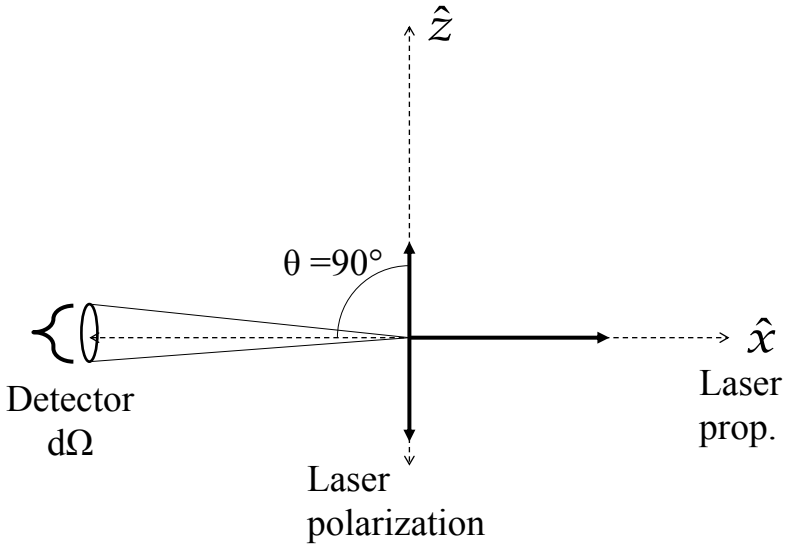

Figure 6.26: Diagram of laser propogation, polarization, and detector angle for our experiment. The fluorescence can be decomposed into two polarization components, one component perpendicular to $\hat{z}$ ($\perp$), and one component in the plane containing the $\hat{z}$ axis ($\parallel$).

For an excited state level $2(A)^1\Sigma^+ (v_e, J_e, M_e)$ directly populated from the ground state level $1(X)^1\Sigma^+ (v_g, J_g, M_g)$, (where $M_{e,g}$ are the individual magnetic sublevels for the two states), we can represent the populations in these individual sublevels as

$$n_{v_e,J_e,M_e} \propto \frac{n_{v_g,J_g}}{2J_g+1} \sum_{M_g} |\langle \alpha_g, v_g, J_g, M_g | \hat{e_1} \cdot \vec{\mu} | \alpha_e, v_e, J_e, M_e \rangle|^2 , \tag{6.1}$$

where $\alpha_{g,e}$ represents all other quantum numbers needed to represent the state, $\vec{\mu} = e\vec{r}$ is the electric dipole moment operator of the optically active electron. $\hat{e_1}$ is the unit vector describing the laser polarization ($\hat{z}$ in our case, which means $\hat{e_1} \cdot \vec{\mu} = \mu_z$).

If we observe fluorescence corresponding to a transition from an anisotropically populated level of the excited state to a final ro-vibrational level (f) of the ground state, the intensity of the component of this fluorescence polarized along the direction $\hat{e_2}$ is given by

$$I_{\hat{e_2}} \propto \sum_{M_f} \sum_{M_e} n_{v_e,J_e,M_e} \left|\langle \alpha_e, v_e, J_e, M_e | \hat{e_2} \cdot \vec{\mu} | \alpha_f, v_f, J_f, M_f \rangle\right|^2 . \tag{6.2}$$

If we combine Eqs. 6.1 and 6.2, we can obtain expressions for $I_\perp$ using $\hat{e_2} = \hat{e_\perp} = \hat{y}$,

$$I_\perp \propto \frac{n_{v_g,J_g}}{2J_g+1} \sum_{M_f} \sum_{M_e} \sum_{M_g} \left|\langle \alpha_g, v_g, J_g, M_g | \mu_z | \alpha_e, v_e, J_e, M_e \rangle\right|^2 \left|\langle \alpha_e, v_e, J_e, M_e | \mu_y | \alpha_f, v_f, J_f, M_f \rangle\right|^2 \tag{6.3}$$

and for $I_\parallel$ using $\hat{e_2} = \hat{e_\parallel} = \sin\theta\hat{z} - \cos\theta\hat{x} = \hat{z}$,

$$I_\parallel \propto \frac{n_{v_g,J_g}}{2J_g+1} \sum_{M_f} \sum_{M_e} \sum_{M_g} \left|\langle \alpha_g, v_g, J_g, M_g | \mu_z | \alpha_e, v_e, J_e, M_e \rangle\right|^2 \left|\langle \alpha_e, v_e, J_e, M_e | \sin\theta\mu_z - \cos\theta\mu_x | \alpha_f, v_f, J_f, M_f \rangle\right|^2 . \tag{6.4}$$

The dipole moment operator components can be used to construct a spherical tensor operator μ_q^k of rank $k = 1$ with $\mu_1^1 = -(2)^{-\frac{1}{2}} e(x+iy)$, $\mu_0^1 = ez$, $\mu_{-1}^1 = (2)^{-\frac{1}{2}} e(x-iy)$. Then, following the Wigner-Eckart theorem [63], we find

$$\langle \alpha, v, J, M | \mu_q^1 | \alpha', v', J', M' \rangle = (-1)^{1+J'-J} \langle J', M'1q | JM \rangle \langle \alpha, v, J \| \vec{\mu} \| \alpha', v', J' \rangle. \tag{6.5}$$

Here $\langle J', M'1q | JM \rangle$ is the Clebsch-Gordon coefficient, and the square of the reduced matrix element $|\langle \alpha, v, J \| \vec{\mu} \| \alpha', v', J' \rangle|^2$ is proportional to the Hönl-London factor

$S(J, J')$ [64]. The Clebsch-Gordon coefficients vanish unless $q + M' = M$, which reduces the triple summations in Eqs. 6.3 and 6.4 to single sums over $M = M_g$. Thus,

$$I_\perp \propto S(J_g, J_e)S(J_e, J_f)A_\perp, \tag{6.6}$$

and

$$I_\parallel \propto S(J_g, J_e)S(J_e, J_f)\left[A_\parallel \sin^2\theta + A_\perp \cos^2\theta\right] \tag{6.7}$$

where $A_\perp$ and $A_\parallel$ contain the Clebsch-Gordon coefficients,

$$A_\perp = \frac{1}{2J_g+1}\sum_M \frac{1}{2}\left\{|\langle J_f M-1, 11|J_e M\rangle|^2 + |\langle J_f M+1, 1-1|J_e M\rangle|^2\right\}|\langle J_e M, 10|J_g M\rangle|^2 \tag{6.8}$$

and

$$A_\parallel = \frac{1}{2J_g+1}\sum_M |\langle J_f M, 10|J_e M\rangle|^2 |\langle J_e M, 10|J_g M\rangle|^2. \tag{6.9}$$

These can be related to the particular rotational levels J and sublevels M as discussed in Zare, pg. 57 [63].

In our case we only collect a small portion of the light intensity in solid angle $d\Omega$, around detection angle θ, ϕ, which compares to the total intensity emitted at all angles as

$$f = \frac{I(\theta,\phi)d\Omega}{I_{tot}} = \frac{I(\theta,\phi)d\Omega}{\int_0^{2\pi}\int_{-1}^{1} I(\theta,\phi)d(\cos\theta)d\phi}. \tag{6.10}$$

The total fluorescence intensity has two components: $I_\perp$ and $I_\parallel$, where

$$I(\theta,\phi) = I_\perp(\theta,\phi) + I_\parallel(\theta,\phi), \tag{6.11}$$

and inserting this and Eqs. 6.6 and 6.7 into Eq. 6.10 yields

$$\begin{aligned}\frac{I(\theta,\phi)d\Omega}{I_{tot}} &= \frac{[I_\perp(\theta,\phi) + I_\parallel(\theta,\phi)]d\Omega}{\int_0^{2\pi} d\phi \int_{-1}^{1}[I_\perp(\theta,\phi) + I_\parallel(\theta,\phi)]d(\cos\theta)} \\ &= \frac{[A_\perp(1+\cos^2\theta) + A_\parallel \sin^2\theta]d\Omega}{\int_{-1}^{1} d\phi \int_0^{\pi}[A_\perp(1+\cos^2\theta) + A_\parallel \sin^2\theta]d(\cos\theta)} \\ &= \frac{[A_\perp(1+\cos^2\theta) + A_\parallel \sin^2\theta]d\Omega}{(2\pi)(\frac{8}{3}A_\perp + \frac{4}{3}A_\parallel)}.\end{aligned} \tag{6.12}$$

This can be further simplified by considering our specific experiment where $\theta = 90°$, such that

$$\frac{I(\theta,\phi)d\Omega}{I_{tot}} = \frac{[A_\perp + A_\parallel]d\Omega}{(2\pi)(\frac{8}{3}A_\perp + \frac{4}{3}A_\parallel)} = \frac{3(A_\perp + A_\parallel)}{4A_\perp + 2A_\parallel}\frac{d\Omega}{4\pi}. \tag{6.13}$$

The exact value of this is dependent on the specific Clebsch-Gordon coefficients, which depend on J_g, J_e, and J_f. We consider four possible combinations: pump from the ground state $1(X)^1\Sigma^+$ to the $2(A)^1\Sigma^+$ state on a P-transition ($J_e = J_g - 1$), and observe either P ($J_f = J_e + 1$) or R ($J_f = J_e - 1$) fluorescence, or pump an R-transition ($J_e = J_g + 1$) and look at P or R fluorescence. The expressions for $A_\parallel$ and $A_\perp$ pertaining to these four possibilities can then be determined from Eqs. 6.8 and 6.9 and the Clebsch-Gordon coefficients as given by Zare [63]. Calculating these values for various J_e values, we find that as J_e increases, the fractions $\frac{I(\theta,\phi)d\Omega}{I_{tot}}$ converge for the four combinations. Some of these values, for a range of J are listed in

Table 6.13.

$\frac{I(\theta,\phi)d\Omega}{I_{tot}}$ (units of $\frac{d\Omega}{4\pi}$)				
J_e	Pump P Observe P	Pump P Observe R	Pump R Observe P	Pump R Observe R
1	1.0049	1.050	1.050	1.500
10	1.038	1.050	1.050	1.067
14	1.041	1.050	1.050	1.062
26	1.045	1.050	1.050	1.056
30	1.045	1.050	1.050	1.055
44	1.047	1.049	1.050	1.053
100	1.049	1.050	1.050	1.052

Table 6.13: Values for $\frac{I(\theta,\phi)d\Omega}{I_{tot}}$, calculated at several J_e values. Note that at very small values of J the value of $\frac{I(\theta,\phi)d\Omega}{I_{tot}}$ is significantly greater than 1 for the pump R / observe R case, but this difference is less than 7% even at $J = 10$.

The fraction of direct line emission that reaches the detector, $f = \frac{I(\theta,\phi)d\Omega}{I_{tot}}$, is related to the anisotropy factor F by

$$F_{dir} = \frac{f_{dir}}{\frac{d\Omega}{4\pi}}. \tag{6.14}$$

During a collision, the orientation is partially destroyed, and consequently the polarization is reduced. In the "worst case" scenario, we can estimate that all polarization is destroyed, so that the collisional line fluorescence is completely isotropic (F=1). For J=14 (our smallest J_{dir} value), this is reflected in the ratio of collisional-to-direct anisotropy terms for an R-pumped, R-fluorescence direct line as

$$\frac{F_{col}}{F_{dir}} = \frac{1}{1.062} = 0.942. \tag{6.15}$$

Thus in the very worst case, the ratio of anisotropy factors differs from 1 by 6%. Since much of our data was recorded at higher J, and since the orientation is not completely destroyed in J-changing collisions, the actual correction is something less than this. Because other errors are much larger than this, we did not attempt to correct the results for the error associated with neglect of the anisotropy factor.

6.4.2 Sodium Contributions

The second significant approximation was made in expanding the sum over perturbers in the rate equation given by Eq. 5.4. There we approximated

$$\frac{n_c}{n_d} = \frac{\sum_P \frac{k_P^\Delta}{\Gamma} n_P}{1 + \sum_P \frac{k_P^Q}{\Gamma} n_P} \approx \frac{\frac{k_{BG}^\Delta}{\Gamma} n_{BG} + \frac{k_K^\Delta}{\Gamma} n_K}{1 + \frac{k_{BG}^Q}{\Gamma} n_{BG} + \frac{k_K^Q}{\Gamma} n_K}. \tag{6.16}$$

In this approximation, we neglect other possible perturbers such as sodium atoms, K_2, NaK and Na_2 molecules, and various impurities. We don't know much about possible impurities that may be present. However we use argon and helium buffer gas of 99.99% purity and sodium and potassium metals that are purified to better than 99.9%. Ratios of Na, K_2 and Na_2 densities relative to K atom densities can be estimated with the Nesmeyanov vapor pressure formulas at various temperatures in the range used in this experiment, and these values are listed in Table 6.14. Note that in general the NaK density lies between those of K_2 and Na_2, but cannot be obtained from the Nesmeyanov formula. So the density of NaK must be calculated

from the equilibrium constant,

$$\frac{1}{K_{eq}} \equiv \frac{n_{Na}n_K}{n_{NaK}} = \frac{\sigma}{kT}\frac{g_{Na}g_K}{g_{NaK}}\sqrt[3]{\frac{2\pi\mu kT}{h^2}}\frac{h^2}{8\pi^2 I}\left[1-\exp\left(-\frac{hc\omega_e}{kT}\right)\right]\exp\left(-\frac{D_0}{kT}\right) \tag{6.17}$$

(see Ref. [50]). Here g_{Na} and g_K are the degeneracies of the atomic ground states ($g_{Na} = g_K = 2$), $g_{NaK} = 1$ for the molecular ground state, μ is the reduced mass of the molecule, D_0 is the dissociation energy of the molecule in vibrational level $v = 0$, ω_e is the vibrational constant, and $\mathrm{I} = \mu R_{eq}^2$ is the moment of inertia of the molecule. $\sigma = 1$ for a heteronuclear molecule (or 2 for a homonuclear molecule). From Table 6.14 , it can be seen that all molecular densities are less than 2% of the potassium density. Therefore, even if the molecule-molecule collisional rate coefficients are 10 times larger than the potassium-molecule rate coefficients, these contributions add no more than 20% error to our reported potassium rates and much less to the noble gas rates.

Also as can be seen from Table 6.14, the sodium density is approximately an order of magnitude smaller than the potassium density and the collisional rates are probably comparable. However, the effects of Na collisions can be taken into account approximately as described below.

To include sodium collisions in Eq. 6.16 we should ideally add a term $(\frac{k_{Na}^{\Delta}}{\Gamma}n_{Na})$ for population transfer due to sodium collisions in the numerator and a quenching term $(\frac{k_{Na}^{Q}}{\Gamma}n_{Na})$ in the denominator,

$$\frac{n_c}{n_d} = \frac{\frac{k_{BG}^{\Delta}}{\Gamma}n_{BG} + \frac{k_K^{\Delta}}{\Gamma}n_K + \frac{k_{Na}^{\Delta}}{\Gamma}n_{Na}}{1 + \frac{k_{BG}^{Q}}{\Gamma}n_{BG} + \frac{k_K^{Q}}{\Gamma}n_K + \frac{k_{Na}^{Q}}{\Gamma}n_{Na}} \tag{6.18}$$

T(K)	n_K	$\frac{n_{Na}}{n_K}$	$\frac{n_{K_2}}{n_K}$	$\frac{n_{Na_2}}{n_K}$	$\frac{n_{NaK}}{n_K}$
563.2	$3.53124\times10^{+15}$	0.0510	0.0032	0.0004	0.0030
583.2	$6.3385\times10^{+15}$	0.0581	0.0040	0.0006	0.0039
603.2	$1.09162\times10^{+16}$	0.0657	0.0050	0.0008	0.0051
623.2	$1.81121\times10^{+16}$	0.0738	0.0061	0.0011	0.0064
643.2	$2.90557\times10^{+16}$	0.0822	0.0074	0.0014	0.0079
663.2	$4.52089\times10^{+16}$	0.0910	0.0088	0.0018	0.0097
683.2	$6.84153\times10^{+16}$	0.1002	0.0104	0.0023	0.0118
703.2	$1.00944\times10^{+17}$	0.1097	0.0121	0.0029	0.0141
723.2	$1.45531\times10^{+17}$	0.1195	0.0140	0.0036	0.0166

Table 6.14: Potassium densities calculated using the Nesmeyanov vapor pressure formula for the range of temperatures used in this experiment. The densities of Na, K_2 and Na_2 were also calculated using the Nesmeyanov formulas, and are reported as ratios to the potassium density at that temperature. The NaK density was calculated using Eq. 6.17, and taken as a ratio to the potassium density. Across the range of temperatures used in this work, the fraction of sodium-to-potassium densities does not exceed 12%.

which we can rewrite as

$$\frac{n_c}{n_d} = \frac{\frac{k_{BG}^{\Delta}}{\Gamma} n_{BG} + \frac{k_K^{\Delta}}{\Gamma}(1 + \frac{k_{Na}^{\Delta}}{k_K^{\Delta}} \frac{n_{Na}}{n_K}) n_K}{1 + \frac{k_{BG}^{Q,c}}{\Gamma} n_{BG} + \frac{k_K^{Q}}{\Gamma}(1 + \frac{k_{Na}^{Q}}{k_K^{Q}} \frac{n_{Na}}{n_K}) n_K}. \tag{6.19}$$

Since the potassium and sodium densities essentially scale together with temperature, it's difficult to separate the effects that the two alkalis have on NaK molecules in collisions. Since sodium and potassium are both alkalis with similar electronic structure, it's reasonable to assume that $\frac{k_{Na}^{\Delta}}{k_K^{\Delta}} \sim 1$ and $\frac{k_{Na}^{Q}}{k_K^{Q}} \sim 1$. Thus, we see that the alkali terms can be written as

$$\frac{k_K^{\Delta}}{\Gamma}\left(1 + \frac{k_{Na}^{\Delta}}{k_K^{\Delta}} \frac{n_{Na}}{n_K}\right) n_K \sim \frac{k_K^{\Delta}}{\Gamma}\left(1 + \frac{n_{Na}}{n_K}\right) n_K \tag{6.20}$$

and

$$\frac{k_K^Q}{\Gamma}\left(1+\frac{k_{Na}^Q}{k_K^Q}\frac{n_{Na}}{n_K}\right)n_K \sim \frac{k_K^Q}{\Gamma}\left(1+\frac{n_{Na}}{n_K}\right)n_K. \tag{6.21}$$

Therefore, the previously fitted potassium terms should be corrected as

$$\left(\frac{k_K^\Delta}{\Gamma}\right)_{\text{fitted}} n_K = \left(\frac{k_K^\Delta}{\Gamma}\right)_{\text{actual}}\left(1+\frac{n_{Na}}{n_K}\right)n_K = \left(\frac{k_K^\Delta}{\Gamma}\right)_{\text{actual}} n_{alk} \tag{6.22}$$

and

$$\left(\frac{k_K^Q}{\Gamma}\right)_{\text{fitted}} n_K = \left(\frac{k_K^Q}{\Gamma}\right)_{\text{actual}}\left(1+\frac{n_{Na}}{n_K}\right)n_K = \left(\frac{k_K^Q}{\Gamma}\right)_{\text{actual}} n_{alk} \tag{6.23}$$

where $n_{alk} = \left(1+\frac{n_{Na}}{n_K}\right)n_K$. Thus the actual alkali collisional rate coefficients can be obtained to a good approximation from our fitted potassium rate coefficients by the substitution

$$k_{alk} = \frac{k_K}{1+\frac{n_{Na}}{n_K}}. \tag{6.24}$$

The average of the fraction $\frac{n_{Na}}{n_K} = 0.083 \pm 0.037$ (see Table 6.14) over the range of temperatures used in the experiment, so that even without the correction of Eq. 6.24, the error in the potassium rates due to neglect of Na collisions is less than 10%. With this correction, which takes the sodium collisions into account to first order, we believe residual errors due to sodium collisions are probably reduced to below 5% (based on $k_{Na}^\Delta \sim k_K^\Delta$ and $k_{Na}^Q \sim k_K^Q$ being valid to within 30%). Whether or not this correction is made, the effect of neglect of Na collisions on all noble gas rate coefficients is negligible. Potassium rate coefficients presented earlier in this chapter have not been corrected in this manner, but could easily be corrected by dividing each reported value by 1.08.

6.4.3 Multiple Collision Regime

A third assumption that was made in deriving the collisional to direct line intensity ratios from our simplified rate equations (Eqs. 5.3 and 5.4) in Chapter 5 was the neglect of multiple collisions. In the ideal situation, the perturber densities are low enough that only one collision is likely to occur within the lifetime of the excited molecule. In reality, utilizing such low alkali densities results in very low NaK molecule densities (hence smaller direct line intensities since there are fewer molecules to absorb laser photons). In addition, if the noble gas density is also small, the collisional line intensities are an even smaller fraction of the direct line intensities, leading to very low signal-to-noise ratios. Therefore, as in many experiments of this nature, we must find a compromise between the desire for low densities and the problem of low signal. Unfortunately, the perturber densities required for acceptable signal-to-noise may in fact put us into the multiple collision regime, for at least some of our data. Consequently, we now try to estimate the impact this effect has on our measured rate coefficients.

If we return to Eq. 5.3 in Chapter 5,

$$\frac{n_c}{n_d} = \frac{\sum_P n_P \left[k_P^{d\rightarrow c} + \sum_{i\neq d} k_P^{i\rightarrow c} \frac{n_i}{n_d} \right]}{\left[\Gamma + \sum_P k_P^{Q,c} n_P \right]}, \tag{6.25}$$

we see that the first term in the numerator represents collisions that transfer population from the directly populated level (d) to the designated collisional level (c) in one step, and the second term (the sum over $i \neq d$) represents collisions populating level c from other levels $i \neq d$ that were populated from level d, either directly or

indirectly, in previous collisions. Figure 6.27 shows the level diagram corresponding to the rate equation that leads to Eq. 6.25.

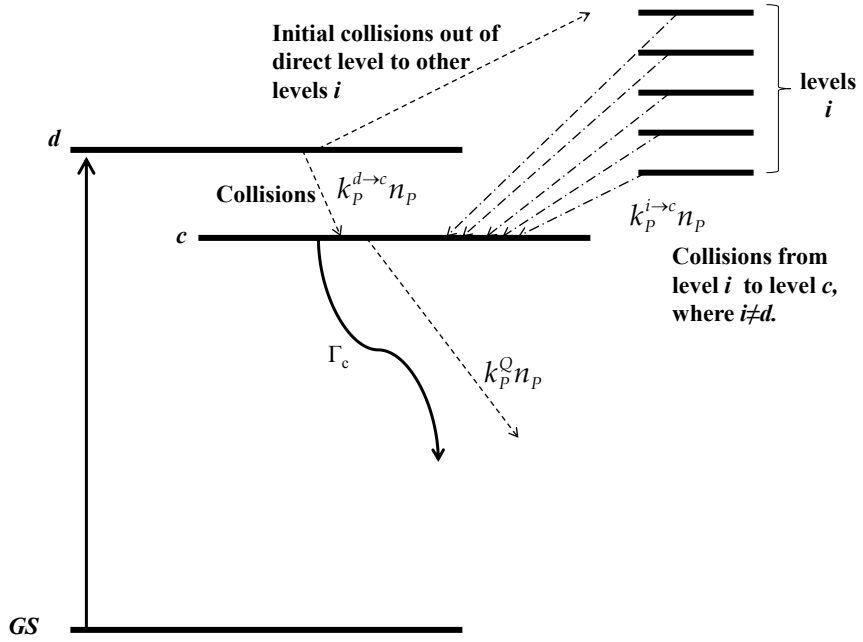

Figure 6.27: Level diagram outlining the collisional processes in Eq. 6.25. A directly populated level d undergoes collisions with a perturber P to transfer population either to the collisional level in which we are interested (c) or to other collisional levels i. Secondary collisions can then transfer population from the levels i to level c.

In our analysis up to now we have assumed the multiple collision term is negligible. One check on the validity of this assumption is to compare the sum of all available fitted J-changing rate coefficients for a particular perturber with the fitted quenching rate coefficient for that perturber k_P^Q. (Note: in principle the v-changing rate coefficients should also be included. However, these only contribute approximately 33% to the total and are therefore neglected here, but will be discussed later in this section.) Table 6.15 shows this comparison where we see that the quenching

rate coefficients are, in the worst cases, only ≈50% of the sums of individual ΔJ rate coefficients.

Direct level	$\sum_J k_{Ar}^{\Delta J,(0)}$ ($\mathrm{cm}^3 s^{-1}$)	$\sum_J k_{He}^{\Delta J,(0)}$ ($\mathrm{cm}^3 s^{-1}$)	$\sum_J k_{K}^{\Delta J,(0)}$ ($\mathrm{cm}^3 s^{-1}$)
$2(A)^1\Sigma^+$ (0, 14)	1.17×10^{-9}	2.72×10^{-9}	3.55×10^{-8}
$2(A)^1\Sigma^+$ (0, 30)	1.46×10^{-9}	2.84×10^{-9}	2.74×10^{-8}
$2(A)^1\Sigma^+$ (1, 26)	1.19×10^{-9}	2.41×10^{-9}	2.53×10^{-8}
$2(A)^1\Sigma^+$ (2, 44)	1.21×10^{-9}	2.27×10^{-9}	1.79×10^{-8}
k^Q ($\mathrm{cm}^3 s^{-1}$)	8.27×10^{-10}	1.39×10^{-9}	2.02×10^{-8}

Table 6.15: Comparison of fitted quenching rate coefficients with the sums of the $k^{\Delta J}$ values for a given initial level. These values were obtained using the global fit results for the quenching rate coefficients and zeroth order $k_P^{d\to c(0)}$ rate coefficients for argon, helium and potassium.

Since the total quenching rate should represent the sum of all collisional rates out of a given level, the fact that the sum of the J-changing rates is larger than the fitted quenching rates implies that we have over estimated the individual J-changing rates (by neglecting the multiple collision effects). In principle all data consisting of all measured $\frac{n_c}{n_d}$ and $\frac{n_i}{n_d}$ ratios for all levels c should be fit simultaneously as functions of the various perturber densities by using Eq. 6.25. But this procedure would couple all the rate coefficients together, and the fitting would become impractical, as even the fits of the $|\Delta J| \leq 4$ data already involve 99 fitted parameters without inclusion of multiple collision considerations. On the other hand, correcting the rate coefficients for multiple collision effects after the fact also doesn't work since the magnitude of the effect depends on the perturber densities. However, we can calculate an upper limit for the magnitude of the error in the various rate coefficients due to neglect of multiple collisions.

We start by noting that the previously determined $k_P^{i\to c}$ values are approximately equal for the same ΔJ but different initial J. This means we can, for example, approximate $k_P^{J=28\to J=25}$ by $k_P^{J=30\to J=27}$. The rate coefficients obtained in our original fit, which we now designate as the zeroth order rate coefficients $k_P^{\Delta J(0)}$, in fact represent the sum of the actual rate coefficient for one-step collisional transfer from the directly excited level ($k_P^{d\to c(\mathrm{act})}$) and the actual multiple collision terms that populate level c from all other levels i, i.e., $k_P^{i\to c(\mathrm{act})}\frac{n_i}{n_d}$. Thus for a given perturber, we have

$$k_P^{\Delta J(0)} = \left[k_P^{d\to c(\mathrm{act})} + \sum_{i\neq d} k_P^{i\to c(\mathrm{act})}\frac{n_i}{n_d}\right] \tag{6.26}$$

or

$$k_P^{\Delta J(\mathrm{act})} = \left[k_P^{d\to c(0)} - \sum_{i\neq d} k_P^{i\to c(\mathrm{act})}\frac{n_i}{n_d}\right]. \tag{6.27}$$

One way to proceed from here is to use the zeroth order $k_P^{\Delta J(0)}$ values as estimates of the $k_P^{i\to c(\mathrm{act})}$ values, with $\Delta J = c - i$. If the corrections were sufficiently small, we could obtain a first order estimate for each $k_P^{\Delta J(\mathrm{act})}$:

$$k_P^{\Delta J(1)} = k_P^{d\to c(0)} - \sum_{i\neq d} k_P^{\Delta J=c-i(0)}\frac{n_i}{n_d} \tag{6.28}$$

using known values for $\frac{n_i}{n_d}$. This process could be iterated, such that

$$k_P^{\Delta J(m)} = k_P^{d\to c(0)} - \sum_{i\neq d} k_P^{\Delta J=c-i(m-1)}\frac{n_i}{n_d}. \tag{6.29}$$

Unfortunately, when we tried this, we found that for high perturber densities some (or all) values of $k_P^{\Delta J=c-d(1)}$ turned out to be negative, which implies that multiple collisions are much more than a small correction at these densities. This causes

the iteration process to fail because the zeroth order rate coefficients are not a sufficiently good first estimate for the actual rate coefficients. In other words, estimating the multiple collision terms using the zeroth order rate coefficients grossly over compensates for these effects. Therefore another method of estimating the first order rate coefficients is needed. If we return to Eq. 6.26, we can write

$$\frac{k_P^{d\to c(\mathrm{act})}}{k_P^{d\to c(0)}} = \frac{k_P^{d\to c(\mathrm{act})}}{k_P^{d\to c(\mathrm{act})} + \sum_{i\neq d} k_P^{i\to c(\mathrm{act})} \frac{n_i}{n_d}} \tag{6.30}$$

which is exact. Now, it is not unreasonable to assume, as a first approximation, that each ΔJ collision is affected equally by multiple collisions; i.e. that $\frac{k_P^{d\to c(\mathrm{act})}}{k_P^{d\to c(0)}} \approx$ constant. Thus we can form an alternative first approximation to the actual rate coefficients as

$$\frac{k_P^{d\to c(1)}}{k_P^{d\to c(0)}} = \frac{k_P^{d\to c(0)}}{k_P^{d\to c(0)} + \sum_{i\neq d} k_P^{i\to c(0)} \frac{n_i}{n_d}} \tag{6.31}$$

or

$$k_P^{d\to c(1)} = \frac{(k_P^{d\to c(0)})^2}{k_P^{d\to c(0)} + \sum_{i\neq d} k_P^{i\to c(0)} \frac{n_i}{n_d}}. \tag{6.32}$$

These first order estimates can be substituted into the multiple collision term in Eq. 6.29 to give a second order estimate of the $k_P^{d\to c(\mathrm{act})}$ values. This process can then be iterated.

We carry out this process with the recognition that it is far from exact since, as we previously noted, these corrections depend on density through the terms $\frac{n_i}{n_d}$. In fact, because the zeroth order rate coefficients were fit to the density ratios, we can

accurately replace $\frac{n_i}{n_d}$ in the above equations with

$$\frac{n_i}{n_d} = \frac{\sum_P \frac{k_P^{d\to i(0)}}{\Gamma} n_P}{1 + \sum_P \frac{k_P^Q}{\Gamma} n_P}. \tag{6.33}$$

Thus the corrected (iterated) rate coefficients would only represent the actual rate coefficients if the perturber densities were the values used in Eq. 6.33 for all recorded data. But by using the highest perturber densities in Eq. 6.33 and then carrying out the calculations outlined above, we get a good estimate of an upper limit for the errors in our measured rate coefficients due to neglect of multiple collision effects. Initial rate coefficients values, as well as calculations for the first through sixth, 99th and 100th iterations are, for $2(A)^1\Sigma^+$ (0, 14), given in Tables 6.16, 6.17, and 6.18 for argon, helium, and potassium perturbers, respectively. Similar values for initial levels $2(A)^1\Sigma^+$ (0, 30), $2(A)^1\Sigma^+$ (1, 26) and $2(A)^1\Sigma^+$ (2, 44) are provided in Tables 6.19-6.21, 6.22-6.24, and 6.25-6.27, respectively. Note that in the case of the helium values for $2(A)^1\Sigma^+$ (2, 44), the iterative process didn't converge by 100 iterations, but did by 1000 iterations. Therefore, Table 6.26 includes results for the 999th and 1000th iterations, rather than for the 99th and 100th iterations.

$2(A)^1\Sigma^+$ (0, 14) Original and Corrected $k_{Ar}^{d\to c}$ values (in units of 10^{-11} cm^{3}s^{-1})									
		$k_{Ar}^{d\to c(n)}$ for iteration n							
ΔJ	$k_{Ar}^{d\to c(0)}$	n = 1	n = 2	n = 3	n = 4	n = 5	n = 6	n = 99	n = 100
-10	1.82	1.05	1.08	1.21	1.15	1.20	1.16	1.18	1.18
-9	0.89	0.32	0.03	0.14	0.06	0.13	0.07	0.10	0.10
-8	1.95	0.86	0.46	0.55	0.46	0.53	0.46	0.49	0.49
-7	1.97	0.89	0.66	0.84	0.72	0.82	0.74	0.78	0.78
-6	3.53	1.77	1.43	1.57	1.46	1.57	1.47	1.51	1.51
-5	2.69	1.20	0.81	0.99	0.85	0.97	0.86	0.91	0.91
-4	5.96	3.33	2.95	3.01	2.85	2.98	2.86	2.92	2.92
-3	3.70	1.74	1.31	1.51	1.32	1.49	1.34	1.41	1.41
-2	14.00	10.74	11.59	11.78	11.64	11.78	11.64	11.73	11.73
-1	5.11	2.62	2.34	2.58	2.36	2.56	2.38	2.46	2.46
1	5.58	2.87	2.62	2.93	2.66	2.90	2.69	2.79	2.79
2	16.46	12.53	13.62	13.91	13.67	13.91	13.72	13.81	13.81
3	4.60	2.03	1.37	1.70	1.38	1.66	1.40	1.53	1.53
4	8.32	4.54	4.09	4.30	3.97	4.26	3.99	4.12	4.12
5	4.32	1.85	1.25	1.68	1.31	1.65	1.35	1.49	1.49
6	5.34	2.42	1.70	2.09	1.71	2.06	1.75	1.90	1.90
7	3.91	1.61	1.00	1.48	1.08	1.44	1.11	1.27	1.27
8	3.94	1.58	0.84	1.31	0.92	1.29	0.95	1.11	1.11
9	3.61	1.46	0.88	1.37	0.95	1.32	0.98	1.14	1.14
10	3.26	1.24	0.52	1.00	0.59	0.96	0.62	0.79	0.79
11	3.20	1.26	0.69	1.14	0.73	1.11	0.77	0.93	0.93
12	3.02	1.17	0.61	1.08	0.67	1.05	0.70	0.87	0.87
13	2.86	1.12	0.61	0.98	0.59	0.94	0.62	0.77	0.77
14	2.69	1.05	0.59	0.96	0.58	0.92	0.61	0.75	0.75
15	2.85	1.30	1.23	1.60	1.28	1.58	1.31	1.44	1.44
16	2.37	1.02	0.87	1.22	0.91	1.20	0.94	1.06	1.06

Table 6.16: J-changing rate coefficients for argon, corrected for multiple collision effects (with $n_{Ar} = 2.13 \times 10^{17}$ cm^{-3} and $n_K = 2.12 \times 10^{15}$ cm^{-3}) obtained using quenching rate coefficients from the global fit results and zeroth order $k_{Ar}^{d\to c(0)}$ rate coefficients from the original global and individual fits. The zeroth, first through sixth, 99th and 100th order (corrected) argon rate coefficients for excitation of $2(A)^1\Sigma^+$ (0, 14) are presented here.

$2(A)^1\Sigma^+$ (0, 14) Original and Corrected $k_{He}^{d\to c}$ values (in units of 10^{-11} cm^{3}s^{-1})									
		$k_{He}^{d\to c(n)}$ for iteration n							
ΔJ	$k_{He}^{d\to c(0)}$	n = 1	n = 2	n = 3	n = 4	n = 5	n = 6	n = 99	n = 100
-10	5.39	2.84	2.85	2.98	2.89	3.06	2.84	3.80	2.12
-9	2.81	1.14	0.85	1.12	0.89	1.15	0.85	1.93	0.03
-8	7.05	3.44	3.01	3.04	2.86	3.12	2.78	4.20	1.72
-7	4.02	1.64	1.21	1.58	1.23	1.62	1.16	2.65	0.00
-6	10.03	5.06	4.61	4.63	4.37	4.73	4.27	6.20	2.84
-5	4.54	1.67	0.78	1.20	0.71	1.24	0.61	2.73	0.00
-4	14.62	7.99	7.99	7.99	7.62	8.14	7.47	9.93	5.68
-3	6.24	2.51	1.87	2.54	1.91	2.62	1.79	4.20	0.00
-2	24.03	15.85	17.64	17.97	17.55	18.16	17.36	20.29	15.23
-1	6.67	2.49	1.44	2.22	1.39	2.30	1.24	4.31	0.00
1	7.47	2.79	1.72	2.75	1.75	2.88	1.57	5.06	0.00
2	28.05	17.78	20.06	20.72	19.96	21.00	19.72	23.98	16.56
3	7.24	2.44	0.77	1.93	0.72	2.08	0.50	4.66	0.00
4	20.20	10.22	10.07	10.64	9.60	10.88	9.37	14.43	5.49
5	7.95	2.69	1.03	2.41	1.00	2.58	0.75	5.34	0.00
6	16.65	7.33	6.15	6.91	5.72	7.24	5.39	11.21	1.01
7	8.32	2.83	1.24	2.77	1.23	2.98	0.96	5.87	0.00
8	14.85	6.15	4.82	5.87	4.56	6.20	4.23	10.31	0.00
9	7.99	2.62	0.84	2.33	0.70	2.54	0.41	5.58	0.00
10	13.15	5.16	3.54	4.64	3.24	4.97	2.89	9.22	0.00
11	8.09	2.73	1.25	2.75	1.11	2.97	0.81	5.87	0.00
12	12.35	4.87	3.53	4.68	3.25	5.01	2.90	9.03	0.00
13	7.76	2.65	1.38	2.72	1.10	2.90	0.80	5.82	0.00
14	10.93	4.20	2.98	4.03	2.62	4.29	2.28	8.14	0.00
15	7.66	2.91	2.54	3.94	2.51	4.14	2.25	6.53	0.00
16	10.17	4.24	4.03	5.20	3.96	5.49	3.68	8.56	0.00

Table 6.17: J-changing rate coefficients for helium, corrected for multiple collision effects (with $n_{He} = 2.95 \times 10^{17}$ cm^{-3} and $n_K = 3.02 \times 10^{15}$ cm^{-3}) for excitation of $2(A)^1\Sigma^+$ (0, 14) are presented here.

$2(A)^1\Sigma^+$ (0, 14) Original and Corrected $k_K^{d\to c}$ values (in units of 10^{-11} cm^{3}s^{-1})									
		$k_K^{d\to c(n)}$ for iteration n							
ΔJ	$k_K^{d\to c(0)}$	n = 1	n = 2	n = 3	n = 4	n = 5	n = 6	n = 99	n = 100
-10	3.41	1.46	0.88	1.14	0.97	1.11	0.99	1.05	1.05
-9	6.62	3.80	3.99	4.39	4.20	4.38	4.22	4.29	4.29
-8	7.24	3.59	2.98	3.39	3.15	3.36	3.18	3.26	3.26
-7	5.87	2.49	1.35	1.69	1.38	1.63	1.40	1.51	1.51
-6	8.89	3.96	2.17	2.41	2.08	2.37	2.11	2.24	2.24
-5	8.66	3.89	2.63	3.09	2.69	3.04	2.73	2.88	2.88
-4	20.24	11.97	11.35	11.59	11.16	11.54	11.21	11.35	11.35
-3	13.58	7.00	6.34	6.95	6.43	6.91	6.48	6.67	6.67
-2	42.14	32.31	34.81	35.38	34.95	35.38	35.00	35.19	35.19
-1	15.66	8.04	7.14	7.76	7.14	7.71	7.19	7.43	7.43
1	17.26	8.99	8.37	9.22	8.47	9.13	8.56	8.85	8.85
2	44.46	32.97	35.85	36.70	36.00	36.70	36.09	36.37	36.37
3	14.71	6.81	5.34	6.34	5.44	6.24	5.53	5.87	5.87
4	23.32	12.58	11.40	12.11	11.16	12.01	11.26	11.59	11.59
5	11.16	4.42	2.08	3.32	2.26	3.20	2.36	2.76	2.76
6	13.95	5.82	3.18	4.19	3.12	4.09	3.21	3.62	3.62
7	10.31	3.97	1.81	3.27	2.13	3.15	2.23	2.67	2.67
8	13.01	5.63	4.03	5.49	4.36	5.39	4.46	4.92	4.92
9	8.89	3.22	0.89	2.31	1.12	2.19	1.23	1.68	1.68
10	10.93	4.43	2.71	4.03	2.86	3.92	2.95	3.41	3.41
11	9.46	3.70	2.03	3.34	2.17	3.24	2.28	2.73	2.73
12	10.41	4.33	3.02	4.23	3.10	4.14	3.20	3.65	3.65
13	9.60	4.03	2.91	3.99	2.88	3.87	2.97	3.40	3.40
14	8.80	3.57	2.21	3.10	2.04	2.99	2.12	2.54	2.54
15	9.03	4.23	4.13	5.16	4.24	5.11	4.32	4.69	4.69
16	10.12	5.25	5.68	6.67	5.82	6.62	5.91	6.24	6.24

Table 6.18: J-changing rate coefficients for potassium, corrected for multiple collision effects (with $n_{Ar} = 2.13 \times 10^{17}$ cm^{-3} and $n_K = 2.12 \times 10^{15}$ cm^{-3}) for excitation of $2(A)^1\Sigma^+$ (0, 14) are presented here.

$2(A)^1\Sigma^+$ (0, 30) Original and Corrected $k_{Ar}^{d\to c}$ values (in units of 10^{-11} cm^{3}s^{-1})									
		$k_{Ar}^{d\to c(n)}$ for iteration n							
ΔJ	$k_{Ar}^{d\to c(0)}$	n = 1	n = 2	n = 3	n = 4	n = 5	n = 6	n = 99	n = 100
-20	1.22	0.45	0.35	0.61	0.31	0.65	0.27	0.96	0.00
-19	1.50	0.58	0.53	0.83	0.50	0.87	0.46	1.20	0.00
-18	1.52	0.53	0.28	0.59	0.21	0.63	0.16	1.04	0.00
-17	1.62	0.55	0.22	0.54	0.12	0.57	0.07	1.06	0.00
-16	1.75	0.58	0.19	0.57	0.12	0.62	0.06	1.11	0.00
-15	2.08	0.74	0.41	0.83	0.37	0.89	0.31	1.40	0.00
-14	2.17	0.74	0.31	0.77	0.28	0.83	0.22	1.39	0.00
-13	2.32	0.79	0.32	0.80	0.28	0.86	0.22	1.48	0.00
-12	2.51	0.85	0.28	0.78	0.25	0.84	0.18	1.53	0.00
-11	2.64	0.89	0.31	0.84	0.28	0.89	0.21	1.62	0.00
-10	3.16	1.13	0.53	1.06	0.50	1.12	0.43	1.91	0.00
-9	3.26	1.19	0.66	1.25	0.69	1.31	0.62	2.06	0.00
-8	3.93	1.50	0.87	1.38	0.84	1.45	0.78	2.30	0.00
-7	3.30	1.12	0.28	0.79	0.24	0.84	0.17	1.79	0.00
-6	5.28	2.22	1.59	2.00	1.49	2.07	1.42	2.99	0.39
-5	4.51	1.79	1.21	1.73	1.22	1.79	1.16	2.69	0.09
-4	8.29	4.22	3.96	4.22	3.74	4.27	3.68	5.23	2.67
-3	5.37	2.26	1.62	2.01	1.53	2.05	1.47	3.04	0.43
-2	16.20	11.35	12.67	13.05	12.67	13.14	12.62	14.04	11.68
-1	7.16	3.53	3.42	3.83	3.42	3.88	3.37	4.90	2.36
1	6.64	3.11	2.70	3.00	2.64	3.04	2.59	4.01	1.64
2	16.86	12.01	13.33	13.61	13.38	13.71	13.33	14.55	12.53
3	5.79	2.58	2.01	2.29	1.99	2.33	1.95	3.24	1.07
4	8.67	4.50	4.04	4.08	3.82	4.11	3.78	4.95	2.99
5	4.99	2.14	1.50	1.73	1.48	1.76	1.45	2.57	0.67
6	6.26	2.98	2.44	2.58	2.38	2.62	2.36	3.34	1.65
7	4.56	2.04	1.59	1.79	1.59	1.80	1.56	2.47	0.91
8	4.85	2.24	1.74	1.86	1.69	1.87	1.66	2.45	1.08
9	4.01	1.98	1.91	2.12	1.98	2.14	1.96	2.64	1.47
10	4.09	2.11	2.09	2.28	2.18	2.30	2.16	2.74	1.73

Table 6.19: J-changing rate coefficients for argon, corrected for multiple collision effects (with $n_{Ar} = 2.13 \times 10^{17}$ cm^{-3} and $n_K = 2.12 \times 10^{15}$ cm^{-3}) for excitation of $2(A)^1\Sigma^+$ (0, 30) are presented here.

$2(A)^1\Sigma^+$ (0, 30) Original and Corrected $k_{He}^{d\to c}$ values (in units of 10^{-11} cm^{3}s^{-1})									
		$k_{He}^{d\to c(n)}$ for iteration n							
ΔJ	$k_{He}^{d\to c(0)}$	n = 1	n = 2	n = 3	n = 4	n = 5	n = 6	n = 99	n = 100
-20	3.25	1.12	0.97	1.65	0.77	1.92	0.39	3.04	0.00
-19	3.98	1.46	1.46	2.23	1.30	2.54	0.89	3.75	0.00
-18	3.63	1.12	0.50	1.23	0.17	1.56	0.00	3.13	0.00
-17	3.97	1.21	0.39	1.09	0.00	1.41	0.00	3.35	0.00
-16	4.56	1.46	0.81	1.71	0.51	2.09	0.00	4.01	0.00
-15	5.70	2.03	1.69	2.69	1.46	3.10	0.91	5.09	0.00
-14	4.99	1.53	0.53	1.54	0.24	1.97	0.00	4.33	0.00
-13	5.60	1.77	0.76	1.79	0.43	2.21	0.00	4.85	0.00
-12	5.65	1.71	0.48	1.58	0.20	2.04	0.00	4.90	0.00
-11	6.03	1.84	0.48	1.60	0.18	2.06	0.00	5.18	0.00
-10	7.02	2.29	1.13	2.30	0.86	2.77	0.18	6.08	0.00
-9	7.21	2.35	1.12	2.29	0.88	2.76	0.20	6.22	0.00
-8	7.87	2.64	1.39	2.51	1.14	2.99	0.47	6.74	0.00
-7	8.10	2.75	1.54	2.68	1.34	3.15	0.68	6.97	0.00
-6	9.33	3.33	2.04	2.89	1.59	3.32	0.94	7.82	0.00
-5	9.23	3.31	2.16	3.13	1.88	3.56	1.25	7.96	0.00
-4	14.13	6.41	6.45	7.21	6.08	7.63	5.46	11.96	0.00
-3	10.31	3.87	2.72	3.47	2.35	3.86	1.76	8.76	0.00
-2	23.08	13.66	16.06	16.81	15.87	17.24	15.35	21.90	9.23
-1	13.89	6.31	6.55	7.35	6.45	7.77	5.93	12.34	0.00
1	11.78	4.80	3.79	4.15	3.36	4.47	2.88	9.94	0.00
2	25.25	15.73	18.37	18.84	18.27	19.22	17.85	24.26	12.10
3	12.06	5.13	4.57	4.99	4.42	5.32	4.01	10.46	0.00
4	14.60	6.78	6.22	6.12	5.60	6.41	5.23	11.73	0.00
5	10.60	4.33	3.31	3.47	3.02	3.74	2.67	8.95	0.00
6	12.91	5.98	5.56	5.60	5.28	5.89	4.95	10.93	0.00
7	9.99	4.27	3.56	3.68	3.37	3.90	3.08	8.43	0.00
8	10.69	4.80	4.19	4.10	3.85	4.28	3.58	8.81	0.00
9	9.70	4.71	4.85	5.09	4.90	5.28	4.69	8.81	0.77
10	9.89	5.09	5.42	5.65	5.51	5.84	5.32	9.04	1.79

Table 6.20: J-changing rate coefficients for helium, corrected for multiple collision effecs (with $n_{He} = 2.95 \times 10^{17}$ cm^{-3} and $n_K = 3.02 \times 10^{15}$ cm^{-3}) for excitation of $2(A)^1\Sigma^+$ (0, 30) are presented here.

$2(A)^1\Sigma^+$ (0, 30) Original and Corrected $k_K^{d\to c}$ values (in units of 10^{-10} cm^{3}s^{-1})									
		$k_K^{d\to c(n)}$ for iteration n							
ΔJ	$k_K^{d\to c(0)}$	n = 1	n = 2	n = 3	n = 4	n = 5	n = 6	n = 99	n = 100
-20	2.35	0.87	0.66	1.16	0.57	1.25	0.49	1.81	0.00
-19	2.81	1.10	0.99	1.59	0.94	1.68	0.84	2.22	0.02
-18	3.04	1.09	0.65	1.25	0.49	1.36	0.38	2.10	0.00
-17	2.99	1.00	0.35	1.00	0.18	1.10	0.06	1.90	0.00
-16	3.69	1.30	0.68	1.41	0.53	1.53	0.40	2.43	0.00
-15	3.63	1.23	0.49	1.32	0.38	1.45	0.25	2.29	0.00
-14	4.44	1.58	0.85	1.71	0.73	1.85	0.59	2.87	0.00
-13	4.06	1.32	0.31	1.28	0.22	1.39	0.08	2.39	0.00
-12	5.32	1.93	1.03	2.01	0.94	2.15	0.79	3.33	0.00
-11	4.70	1.55	0.37	1.46	0.33	1.58	0.18	2.69	0.00
-10	6.12	2.19	0.97	1.95	0.81	2.09	0.65	3.50	0.00
-9	5.09	1.64	0.17	1.29	0.12	1.40	0.00	2.74	0.00
-8	8.62	3.56	2.66	3.65	2.56	3.82	2.41	5.23	0.71
-7	6.78	2.51	1.31	2.50	1.36	2.62	1.22	3.90	0.00
-6	11.40	5.13	4.20	4.99	3.91	5.13	3.77	6.69	2.08
-5	6.97	2.49	0.86	1.92	0.82	2.02	0.69	3.59	0.00
-4	17.99	9.80	9.75	10.31	9.33	10.46	9.18	12.01	7.54
-3	8.62	3.39	1.94	2.91	1.89	2.99	1.77	4.49	0.08
-2	30.99	21.67	24.12	24.87	24.02	24.96	23.93	26.47	22.42
-1	9.84	4.17	3.01	3.91	3.00	3.99	2.90	5.56	1.30
1	10.36	4.51	3.35	4.15	3.34	4.21	3.25	5.75	1.73
2	33.06	23.69	26.19	26.75	26.14	26.89	26.09	28.26	24.77
3	9.18	3.80	2.36	3.06	2.36	3.11	2.29	4.56	0.89
4	19.26	10.83	10.50	10.69	10.13	10.74	10.03	12.06	8.76
5	8.05	3.25	1.77	2.38	1.80	2.43	1.74	3.70	0.49
6	13.09	6.50	5.65	5.93	5.46	5.98	5.42	7.16	4.29
7	7.35	3.09	2.01	2.52	2.04	2.53	1.99	3.61	0.96
8	9.70	4.61	3.72	3.98	3.59	4.00	3.55	4.95	2.62
9	6.74	3.21	2.95	3.46	3.12	3.48	3.09	4.28	2.30
10	8.01	4.18	4.11	4.48	4.23	4.53	4.21	5.23	3.52

Table 6.21: J-changing rate coefficients for potassium, corrected for multiple collision effects (with $n_{Ar} = 2.13 \times 10^{17}$ cm^{-3} and $n_K = 2.12 \times 10^{15}$ cm^{-3}) for excitation of $2(A)^1\Sigma^+$ (0, 30) are presented here.

$2(A)^1\Sigma^+$ (1, 26) Original and Corrected $k_{Ar}^{d\to c}$ values (in units of 10^{-11} cm^{3}s^{-1})									
		$k_{Ar}^{d\to c(n)}$ for iteration n							
ΔJ	$k_{Ar}^{d\to c(0)}$	n = 1	n = 2	n = 3	n = 4	n = 5	n = 6	n = 99	n = 100
-17	0.93	0.41	0.34	0.45	0.37	0.44	0.38	0.41	0.41
-16	1.13	0.50	0.41	0.53	0.44	0.52	0.45	0.48	0.48
-15	1.27	0.55	0.42	0.56	0.45	0.54	0.46	0.50	0.50
-14	1.59	0.72	0.59	0.75	0.62	0.73	0.64	0.68	0.68
-13	1.32	0.50	0.19	0.35	0.21	0.33	0.23	0.28	0.28
-12	1.74	0.72	0.43	0.61	0.46	0.58	0.48	0.53	0.53
-11	1.75	0.72	0.43	0.64	0.48	0.61	0.50	0.55	0.55
-10	2.16	0.91	0.55	0.75	0.59	0.72	0.61	0.66	0.66
-9	2.27	0.98	0.70	0.93	0.76	0.90	0.78	0.84	0.84
-8	3.09	1.45	1.13	1.36	1.20	1.34	1.21	1.27	1.27
-7	2.57	1.09	0.67	0.89	0.71	0.85	0.73	0.79	0.79
-6	4.05	1.97	1.52	1.70	1.53	1.68	1.56	1.61	1.61
-5	3.35	1.55	1.17	1.39	1.22	1.37	1.24	1.30	1.30
-4	6.61	3.76	3.41	3.50	3.33	3.48	3.35	3.40	3.40
-3	4.11	1.99	1.60	1.79	1.61	1.76	1.63	1.69	1.69
-2	14.63	11.44	12.29	12.48	12.33	12.48	12.33	12.43	12.43
-1	5.49	3.03	2.91	3.10	2.93	3.08	2.95	3.01	3.01
1	5.39	2.94	2.78	2.95	2.78	2.94	2.80	2.86	2.86
2	14.87	11.73	12.57	12.76	12.57	12.71	12.62	12.66	12.66
3	4.46	2.25	1.93	2.11	1.93	2.09	1.95	2.02	2.02
4	6.85	4.12	4.01	4.12	3.97	4.10	3.99	4.04	4.04
5	3.49	1.63	1.26	1.47	1.29	1.45	1.31	1.37	1.37
6	1.59	0.42	0.00	0.00	0.00	0.00	0.00	0.00	0.00
7	2.88	1.31	0.98	1.20	1.02	1.18	1.04	1.10	1.10
8	2.90	1.42	1.31	1.54	1.39	1.52	1.41	1.46	1.46
9	2.48	1.11	0.84	1.06	0.87	1.02	0.90	0.95	0.95
10	2.24	1.00	0.78	0.98	0.82	0.95	0.83	0.89	0.89
11	2.08	0.93	0.74	0.96	0.79	0.94	0.81	0.87	0.87
12	1.60	0.64	0.35	0.54	0.39	0.52	0.41	0.46	0.46
13	1.24	0.44	0.08	0.28	0.12	0.25	0.14	0.19	0.19
14	0.86	0.25	0.00	0.00	0.00	0.00	0.00	0.00	0.00
15	0.94	0.31	0.00	0.15	0.00	0.12	0.02	0.07	0.07
16	1.20	0.50	0.39	0.57	0.45	0.55	0.47	0.51	0.51
17	1.12	0.47	0.35	0.53	0.40	0.51	0.41	0.46	0.46
18	0.93	0.36	0.20	0.34	0.22	0.32	0.24	0.27	0.27
19	0.88	0.34	0.17	0.29	0.18	0.27	0.19	0.23	0.23
20	0.70	0.25	0.04	0.14	0.03	0.12	0.04	0.08	0.08
21	0.78	0.31	0.16	0.24	0.14	0.23	0.16	0.19	0.19
22	0.76	0.35	0.34	0.44	0.36	0.43	0.38	0.40	0.40
23	0.92	0.50	0.54	0.64	0.57	0.63	0.58	0.61	0.61

Table 6.22: J-changing rate coefficients for argon, corrected for multiple collision effects (with $n_{Ar} = 1.50 \times 10^{17}$ cm^{-3} and $n_K = 1.48 \times 10^{15}$ cm^{-3}) for excitation of $2(A)^1\Sigma^+$ (1, 26) are presented here.

$2(A)^1\Sigma^+$ (1, 26) Original and Corrected $k_{He}^{d\to c}$ values (in units of 10^{-11} cm^{3}s^{-1})									
		$k_{He}^{d\to c(n)}$ for iteration n							
ΔJ	$k_{He}^{d\to c(0)}$	n = 1	n = 2	n = 3	n = 4	n = 5	n = 6	n = 99	n = 100
-17	2.11	0.87	0.71	1.01	0.77	1.01	0.77	1.31	0.47
-16	3.78	1.78	1.65	1.92	1.71	1.94	1.70	2.26	1.38
-15	2.32	0.85	0.38	0.71	0.40	0.70	0.40	1.08	0.01
-14	4.78	2.19	1.84	2.13	1.87	2.15	1.85	2.55	1.45
-13	2.80	1.02	0.41	0.78	0.41	0.76	0.41	1.22	0.00
-12	5.30	2.26	1.48	1.74	1.43	1.76	1.41	2.22	0.94
-11	3.70	1.50	1.09	1.57	1.17	1.57	1.17	2.07	0.66
-10	6.99	3.26	2.68	3.01	2.69	3.05	2.67	3.56	2.17
-9	3.81	1.45	0.77	1.25	0.80	1.24	0.79	1.80	0.23
-8	8.63	4.19	3.58	3.87	3.52	3.92	3.50	4.46	2.96
-7	4.34	1.70	1.05	1.58	1.10	1.58	1.10	2.19	0.48
-6	11.26	5.91	5.49	5.72	5.35	5.77	5.35	6.33	4.74
-5	4.23	1.53	0.55	1.07	0.55	1.07	0.54	1.73	0.00
-4	15.05	8.72	8.68	8.82	8.40	8.86	8.40	9.43	7.79
-3	5.25	2.13	1.47	2.05	1.51	2.05	1.51	2.72	0.83
-2	24.11	17.17	18.71	19.04	18.67	19.09	18.62	19.65	18.06
-1	5.77	2.42	1.83	2.41	1.86	2.42	1.85	3.10	1.15
1	5.91	2.48	1.85	2.42	1.84	2.42	1.83	3.12	1.12
2	24.76	17.87	19.56	19.84	19.42	19.89	19.42	20.45	18.85
3	5.58	2.26	1.52	2.10	1.51	2.11	1.51	2.80	0.80
4	16.56	10.36	11.12	11.49	11.07	11.54	11.07	12.10	10.51
5	5.35	2.13	1.38	1.95	1.36	1.96	1.36	2.64	0.65
6	4.78	1.44	0.00	0.00	0.00	0.00	0.00	0.00	0.00
7	5.49	2.29	1.79	2.39	1.81	2.40	1.81	3.05	1.12
8	7.46	3.48	3.12	3.63	3.18	3.64	3.18	4.18	2.61
9	4.88	1.97	1.38	1.94	1.37	1.94	1.36	2.55	0.71
10	6.19	2.73	2.26	2.73	2.27	2.73	2.27	3.25	1.71
11	4.26	1.67	1.11	1.68	1.14	1.67	1.13	2.22	0.52
12	6.00	2.77	2.54	3.01	2.56	3.01	2.56	3.49	2.02
13	3.12	1.06	0.29	0.82	0.32	0.82	0.32	1.32	0.00
14	2.80	0.82	0.00	0.00	0.00	0.00	0.00	0.27	0.00
15	2.41	0.74	0.00	0.37	0.00	0.36	0.00	0.85	0.00
16	3.96	1.68	1.39	1.82	1.45	1.82	1.45	2.19	1.00
17	2.64	0.96	0.53	1.00	0.58	1.00	0.59	1.37	0.12
18	3.28	1.37	1.13	1.54	1.19	1.53	1.19	1.85	0.79
19	2.29	0.82	0.40	0.79	0.41	0.78	0.41	1.12	0.00
20	2.04	0.67	0.02	0.27	0.00	0.24	0.00	0.60	0.00
21	1.79	0.60	0.12	0.41	0.07	0.39	0.07	0.73	0.00
22	2.23	0.96	0.91	1.23	0.97	1.22	0.97	1.44	0.68
23	2.16	0.98	1.03	1.34	1.08	1.34	1.08	1.56	0.80

Table 6.23: J-changing rate coefficients for helium, corrected for multiple collision effects (with $n_{He} = 1.13 \times 10^{17}$ cm^{-3} and $n_K = 2.92 \times 10^{15}$ cm^{-3}) for excitation of $2(A)^1\Sigma^+$ (1, 26) are presented here.

$2(A)^1\Sigma^+$ (1, 26) Original and Corrected $k_K^{d\to c}$ values (in units of 10^{-10} cm^{3}s^{-1})									
		$k_K^{d\to c(n)}$ for iteration n							
ΔJ	$k_K^{d\to c(0)}$	n = 1	n = 2	n = 3	n = 4	n = 5	n = 6	n = 99	n = 100
-17	2.31	1.13	1.12	1.44	1.22	1.41	1.25	1.33	1.33
-16	2.00	0.81	0.50	0.83	0.57	0.79	0.61	0.69	0.69
-15	1.81	0.61	0.00	0.27	0.00	0.21	0.00	0.09	0.09
-14	2.77	1.12	0.61	1.05	0.71	0.99	0.76	0.86	0.86
-13	2.73	1.02	0.31	0.77	0.40	0.71	0.45	0.57	0.57
-12	3.26	1.23	0.33	0.80	0.40	0.73	0.45	0.58	0.58
-11	3.65	1.47	0.76	1.31	0.90	1.24	0.95	1.09	1.09
-10	5.02	2.18	1.38	1.93	1.51	1.87	1.56	1.70	1.70
-9	4.83	2.08	1.37	1.95	1.48	1.87	1.54	1.69	1.69
-8	6.89	3.18	2.22	2.72	2.27	2.66	2.33	2.49	2.49
-7	6.24	2.87	2.19	2.83	2.35	2.76	2.41	2.57	2.57
-6	11.82	6.52	5.96	6.47	6.00	6.43	6.05	6.24	6.24
-5	5.96	2.48	1.23	1.83	1.32	1.74	1.38	1.55	1.55
-4	17.82	10.88	10.46	10.74	10.22	10.65	10.32	10.46	10.46
-3	7.46	3.40	2.34	3.00	2.50	2.93	2.56	2.73	2.73
-2	34.19	26.92	28.70	29.17	28.75	29.12	28.80	28.94	28.94
-1	7.08	3.04	1.56	2.11	1.59	2.02	1.65	1.82	1.82
1	10.04	5.30	4.83	5.53	5.02	5.49	5.11	5.25	5.25
2	35.08	28.09	29.83	30.30	29.88	30.25	29.92	30.06	30.06
3	6.99	3.05	1.70	2.27	1.74	2.19	1.81	1.98	1.98
4	18.76	12.33	12.52	12.94	12.48	12.85	12.57	12.71	12.71
5	5.86	2.44	1.16	1.75	1.23	1.66	1.29	1.46	1.46
6	4.08	1.19	0.00	0.00	0.00	0.00	0.00	0.00	0.00
7	6.05	2.82	2.24	2.94	2.44	2.87	2.51	2.68	2.68
8	5.63	2.62	2.16	2.78	2.35	2.72	2.42	2.55	2.55
9	4.04	1.59	0.66	1.24	0.74	1.15	0.80	0.96	0.96
10	4.09	1.72	1.05	1.57	1.13	1.48	1.18	1.32	1.32
11	2.89	1.02	0.11	0.67	0.21	0.60	0.27	0.42	0.42
12	3.95	1.79	1.44	1.93	1.53	1.87	1.59	1.72	1.72
13	2.35	0.81	0.03	0.56	0.15	0.51	0.21	0.35	0.35
14	0.95	0.17	0.00	0.00	0.00	0.00	0.00	0.00	0.00
15	1.83	0.60	0.00	0.37	0.00	0.30	0.03	0.15	0.15
16	1.74	0.59	0.03	0.38	0.07	0.33	0.11	0.21	0.21
17	1.69	0.59	0.08	0.48	0.15	0.43	0.20	0.31	0.31
18	2.45	1.13	1.03	1.41	1.13	1.37	1.17	1.27	1.27
19	1.83	0.73	0.41	0.75	0.47	0.70	0.51	0.61	0.61
20	1.33	0.44	0.00	0.14	0.00	0.09	0.00	0.00	0.00
21	1.21	0.41	0.00	0.15	0.00	0.11	0.00	0.02	0.02
22	2.00	1.07	1.17	1.42	1.23	1.39	1.26	1.33	1.33
23	1.82	0.98	1.05	1.26	1.10	1.24	1.12	1.18	1.18

Table 6.24: J-changing rate coefficients for potassium, corrected for multiple collision effects (with $n_{Ar} = 1.50 \times 10^{17}$ cm^{-3} and $n_K = 1.48 \times 10^{15}$ cm^{-3}) for excitation of $2(A)^1\Sigma^+$ (1, 26) are presented here.

$2(A)^1\Sigma^+$ (2, 44) Original and Corrected $k_{Ar}^{d\to c}$ values (in units of 10^{-11} cm^{3}s^{-1})									
		$k_{Ar}^{d\to c(n)}$ for iteration n							
ΔJ	$k_{Ar}^{d\to c(0)}$	n = 1	n = 2	n = 3	n = 4	n = 5	n = 6	n = 99	n = 100
-17	0.92	0.43	0.43	0.56	0.48	0.54	0.49	0.51	0.51
-16	0.72	0.26	0.11	0.23	0.14	0.21	0.15	0.18	0.18
-15	0.84	0.29	0.03	0.15	0.04	0.13	0.06	0.09	0.09
-14	1.08	0.41	0.17	0.32	0.21	0.30	0.22	0.26	0.26
-13	1.26	0.48	0.22	0.38	0.25	0.36	0.27	0.31	0.31
-12	1.62	0.67	0.42	0.60	0.46	0.58	0.48	0.52	0.52
-11	1.87	0.80	0.56	0.75	0.61	0.73	0.63	0.68	0.68
-10	2.23	0.97	0.68	0.85	0.70	0.83	0.72	0.77	0.77
-9	2.32	1.00	0.68	0.87	0.71	0.85	0.73	0.78	0.78
-8	3.17	1.50	1.25	1.44	1.29	1.43	1.31	1.37	1.37
-7	2.98	1.34	1.01	1.20	1.04	1.19	1.06	1.12	1.12
-6	4.08	1.99	1.62	1.77	1.61	1.75	1.62	1.69	1.69
-5	3.77	1.79	1.46	1.64	1.47	1.63	1.49	1.55	1.55
-4	6.48	3.66	3.43	3.51	3.34	3.50	3.36	3.42	3.42
-3	4.77	2.44	2.22	2.42	2.25	2.41	2.26	2.33	2.33
-2	13.80	10.56	11.44	11.62	11.48	11.62	11.48	11.58	11.58
-1	5.09	2.58	2.25	2.39	2.21	2.38	2.23	2.30	2.30
1	5.97	3.32	3.30	3.50	3.33	3.50	3.34	3.42	3.42
2	13.61	10.28	11.20	11.39	11.20	11.39	11.25	11.30	11.30
3	4.77	2.38	2.06	2.24	2.06	2.22	2.07	2.14	2.14
4	6.57	3.68	3.46	3.57	3.39	3.55	3.41	3.47	3.47
5	3.83	1.78	1.40	1.61	1.43	1.59	1.44	1.51	1.51
6	4.15	1.97	1.54	1.70	1.54	1.69	1.55	1.62	1.62
7	3.05	1.33	0.93	1.15	0.98	1.13	1.00	1.06	1.06
8	3.38	1.57	1.27	1.49	1.33	1.48	1.34	1.40	1.40
9	2.44	1.01	0.60	0.81	0.65	0.79	0.67	0.73	0.73
10	2.50	1.06	0.67	0.86	0.70	0.83	0.71	0.77	0.77
11	2.09	0.85	0.50	0.69	0.54	0.67	0.55	0.61	0.61
12	2.29	1.03	0.81	0.99	0.85	0.97	0.87	0.92	0.92
13	1.96	0.86	0.63	0.78	0.64	0.75	0.66	0.70	0.70
14	1.76	0.76	0.53	0.67	0.55	0.65	0.56	0.60	0.60
15	1.88	0.95	0.96	1.10	1.00	1.09	1.01	1.05	1.05
16	1.46	0.68	0.61	0.74	0.64	0.72	0.65	0.69	0.69

Table 6.25: J-changing rate coefficients for argon, corrected for multiple collision effects (with $n_{Ar} = 1.69 \times 10^{17}$ cm^{-3} and $n_K = 1.65 \times 10^{15}$ cm^{-3}) for excitation of $2(A)^1\Sigma^+$ (2, 44) are presented here.

$2(A)^1\Sigma^+$ (2, 44) Original and Corrected $k_{He}^{d\to c}$ values (in units of 10^{-11} cm^{3}s^{-1})									
		$k_{He}^{d\to c(n)}$ for iteration n							
ΔJ	$k_{He}^{d\to c(0)}$	n = 1	n = 2	n = 3	n = 4	n = 5	n = 6	n = 999	n = 1000
-17	1.83	0.81	0.78	1.03	0.87	1.02	0.88	0.95	0.95
-16	1.78	0.62	0.13	0.37	0.20	0.36	0.20	0.28	0.28
-15	1.48	0.45	0.00	0.10	0.00	0.07	0.00	0.00	0.00
-14	2.76	1.04	0.38	0.63	0.42	0.63	0.42	0.52	0.52
-13	2.30	0.84	0.36	0.67	0.41	0.65	0.42	0.54	0.54
-12	4.68	2.09	1.63	1.90	1.66	1.90	1.66	1.78	1.78
-11	3.18	1.28	0.89	1.26	0.95	1.24	0.96	1.10	1.10
-10	6.71	3.28	2.92	3.19	2.92	3.19	2.92	3.06	3.06
-9	3.60	1.42	0.88	1.26	0.91	1.24	0.92	1.07	1.07
-8	8.57	4.34	3.93	4.16	3.88	4.18	3.87	4.02	4.02
-7	4.32	1.78	1.28	1.72	1.33	1.69	1.34	1.52	1.52
-6	10.88	5.79	5.46	5.65	5.32	5.65	5.32	5.51	5.51
-5	4.86	2.05	1.56	2.03	1.61	2.00	1.62	1.81	1.81
-4	14.49	8.38	8.33	8.47	8.15	8.47	8.15	8.29	8.29
-3	4.91	1.99	1.33	1.82	1.37	1.80	1.38	1.59	1.59
-2	23.34	16.44	17.96	18.24	17.96	18.29	17.96	18.10	18.10
-1	5.14	2.08	1.42	1.95	1.47	1.92	1.49	1.70	1.70
1	5.28	2.17	1.55	2.11	1.63	2.08	1.64	1.86	1.86
2	24.21	17.08	18.66	18.98	18.66	19.03	18.66	18.84	18.84
3	4.91	1.93	1.16	1.69	1.20	1.66	1.21	1.44	1.44
4	15.37	8.80	8.75	8.89	8.57	8.94	8.52	8.70	8.70
5	4.72	1.85	1.11	1.63	1.17	1.61	1.18	1.39	1.39
6	11.48	5.88	5.32	5.51	5.19	5.56	5.19	5.37	5.37
7	4.45	1.75	1.06	1.56	1.13	1.54	1.13	1.34	1.34
8	9.58	4.72	4.20	4.49	4.18	4.52	4.17	4.35	4.35
9	3.95	1.50	0.79	1.25	0.84	1.23	0.85	1.04	1.04
10	7.36	3.33	2.50	2.75	2.44	2.76	2.44	2.60	2.60
11	3.59	1.37	0.73	1.13	0.75	1.10	0.77	0.94	0.94
12	6.95	3.35	2.98	3.29	3.02	3.31	3.02	3.17	3.17
13	3.50	1.44	1.03	1.37	1.04	1.34	1.05	1.19	1.19
14	5.23	2.36	1.85	2.08	1.83	2.08	1.83	1.95	1.95
15	3.63	1.76	1.81	2.15	1.89	2.13	1.90	2.01	2.01
16	4.20	1.95	1.73	2.00	1.80	2.00	1.80	1.90	1.90

Table 6.26: J-changing rate coefficients for helium, corrected for multiple collision effects (with $n_{He} = 1.13 \times 10^{17}$ cm^{-3} and $n_K = 2.92 \times 10^{15}$ cm^{-3}) for excitation of $2(A)^1\Sigma^+$ (2, 44). The zeroth, first through sixth, 999th and 1000th order helium rate coefficients are presented here.

$2(A)^1\Sigma^+$ (2, 44) Original and Corrected $k_K^{d\to c}$ values (in units of 10^{-10} cm^{3}s^{-1})									
		$k_K^{d\to c(n)}$ for iteration n							
ΔJ	$k_K^{d\to c(0)}$	n = 1	n = 2	n = 3	n = 4	n = 5	n = 6	n = 99	n = 100
-17	0.50	0.14	0.00	0.07	0.00	0.04	0.00	0.01	0.01
-16	0.33	0.05	0.00	0.00	0.00	0.00	0.00	0.00	0.00
-15	0.00	0.00	0.00	0.00	0.00	0.00	0.00	0.00	0.00
-14	1.04	0.31	0.00	0.04	0.00	0.00	0.00	0.00	0.00
-13	1.26	0.41	0.00	0.16	0.00	0.10	0.00	0.02	0.02
-12	2.40	1.02	0.60	1.00	0.73	0.94	0.78	0.86	0.86
-11	1.94	0.70	0.06	0.51	0.21	0.44	0.26	0.35	0.35
-10	3.49	1.58	1.07	1.56	1.23	1.50	1.28	1.38	1.38
-9	2.59	0.98	0.21	0.75	0.40	0.67	0.46	0.56	0.56
-8	3.75	1.50	0.42	0.89	0.49	0.80	0.55	0.66	0.66
-7	2.33	0.73	0.00	0.03	0.00	0.00	0.00	0.00	0.00
-6	8.29	4.54	4.03	4.56	4.13	4.49	4.19	4.33	4.33
-5	3.45	1.28	0.01	0.67	0.23	0.59	0.30	0.43	0.43
-4	13.94	8.70	8.38	8.80	8.29	8.70	8.38	8.52	8.52
-3	3.82	1.41	0.00	0.68	0.16	0.58	0.24	0.39	0.39
-2	29.12	23.66	25.09	25.70	25.23	25.65	25.33	25.47	25.47
-1	4.26	1.60	0.00	0.68	0.12	0.57	0.20	0.37	0.37
1	4.72	1.92	0.61	1.39	0.83	1.31	0.92	1.09	1.09
2	29.59	23.94	25.42	26.07	25.56	25.97	25.60	25.79	25.79
3	4.03	1.48	0.00	0.63	0.04	0.53	0.12	0.31	0.31
4	14.58	9.12	8.89	9.35	8.80	9.26	8.84	9.03	9.03
5	3.52	1.24	0.00	0.56	0.00	0.47	0.05	0.24	0.24
6	8.47	4.47	3.82	4.40	3.86	4.33	3.93	4.12	4.12
7	3.24	1.16	0.00	0.71	0.17	0.64	0.24	0.43	0.43
8	5.19	2.35	1.56	2.18	1.66	2.11	1.72	1.90	1.90
9	3.16	1.22	0.38	1.06	0.54	0.98	0.60	0.78	0.78
10	3.50	1.38	0.45	1.00	0.50	0.93	0.56	0.73	0.73
11	2.47	0.89	0.08	0.67	0.19	0.60	0.25	0.41	0.41
12	3.31	1.44	0.95	1.48	1.04	1.43	1.10	1.25	1.25
13	1.94	0.68	0.00	0.44	0.02	0.37	0.07	0.21	0.21
14	2.55	1.08	0.65	1.06	0.69	1.01	0.73	0.86	0.86
15	1.77	0.73	0.47	0.88	0.56	0.84	0.61	0.71	0.71
16	1.58	0.63	0.31	0.64	0.36	0.61	0.39	0.49	0.49

Table 6.27: J-changing rate coefficients for potassium, corrected for multiple collision effects (with $n_{Ar} = 1.69 \times 10^{17}$ cm^{-3} and $n_K = 1.65 \times 10^{15}$ cm^{-3}) for excitation of $2(A)^1\Sigma^+$ (2, 44) are presented here.

We note that in this iteration procedure the first order rate coefficients are smaller than the zeroth order values. The second order coefficients are larger than the first order coefficients, and further iterations tend to oscillate between the second and third corrected values, converging to a consistent set of values. However, in some cases, the iterations give fairly consistent results for the first few iterations, but then begin to diverge. We discuss how we deal with these cases below. But, in general these iterated rate coefficients, which are based on calculations for the highest perturber densities used in our experiments, give a reasonable estimate of how much our measured rate coefficients may be affected by multiple collisions in the worst cases. We can see that our zeroth order fitted values of the largest rate coefficients, representing $\Delta J = \pm 2$, might overestimate the actual rate coefficients by 20-25%, due to multiple collisions, whereas the zeroth order rate coefficients for larger ΔJ values ($|\Delta J| \approx 10$) could be as much as, or even more than, a factor of 3 too large. At lower perturber densities, these effects are less, so the above estimates are indeed strictly an upper limit. Nevertheless, because the $\frac{n_i}{n_d}$ ratios saturate at relatively low densities, we believe this "multiple collision correction", based on the highest densities used in the experiment, is probably a pretty good representation for the required correction at most densities.

Thus, in cases where this multiple collision correction process converges to a consistent set of values, we take the values obtained in the final iteration as the "best" measured rate coefficients determined in our work. [In the case where the multiple collision correction iterations failed to converge, we report the average of the fifth and sixth iterations as our final rate coefficients. These average values are actually not too different than the average of the 99th and 100th iteration values, although

the differences between the fifth and sixth iteration values are much smaller than the differences between the 99th and 100th iteration values.]

Figures 6.28 – 6.30 show a comparison of the zeroth order fitted rate coefficients and the final rate coefficients corrected for multiple collision effects for initial level $2(A)^1\Sigma^+$ (0, 14). Similar figures for initial levels $2(A)^1\Sigma^+$ (0, 30), $2(A)^1\Sigma^+$ (1, 26), and $2(A)^1\Sigma^+$ (2, 44) are presented in Figs. 6.31 – 6.33, 6.34 – 6.36, and 6.37 – 6.39, respectively. The true values should lie between the two sets of results in each plot, but are likely to be closer to the corrected (lower) values. In any event, it is important to note that although multiple collision effects have a strong effect on absolute rate coefficients, they have a relatively small effect on the *relative* values of rate coefficients for different ΔJ's. I also present a comparison of the quenching rate coefficients to the sums of the *final* rate coefficients in Table 6.28, in a similar fashion to the comparison of the quenching rate coefficients to the sums of the zeroth order values given in Table 6.15.

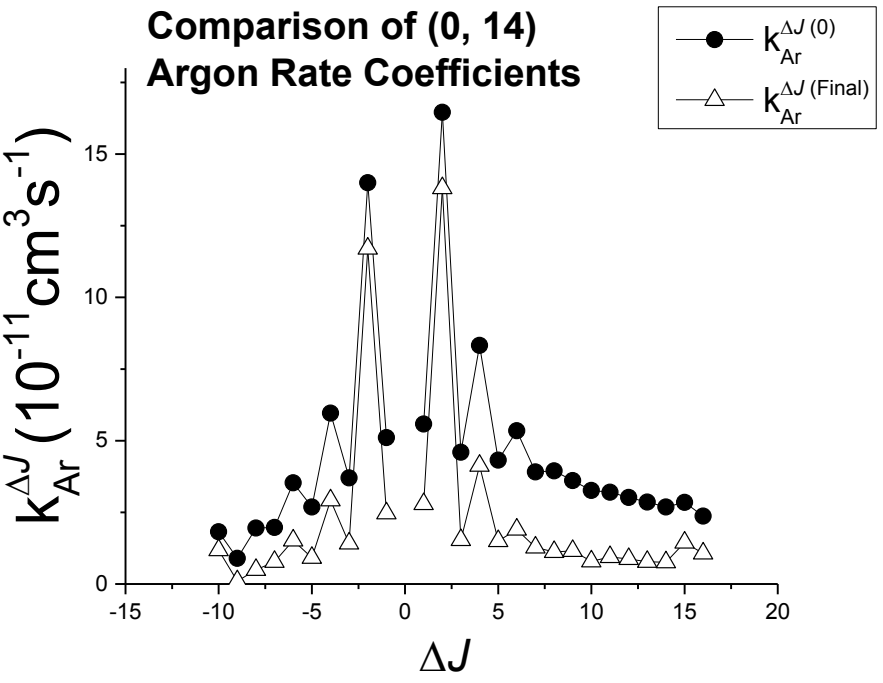

Figure 6.28: Comparison of the zeroth order (original fit) and final argon rate coefficients which include multiple collision effects, for initial level $2(A)^1\Sigma^+$ (0, 14). Values are presented in Table 6.16.

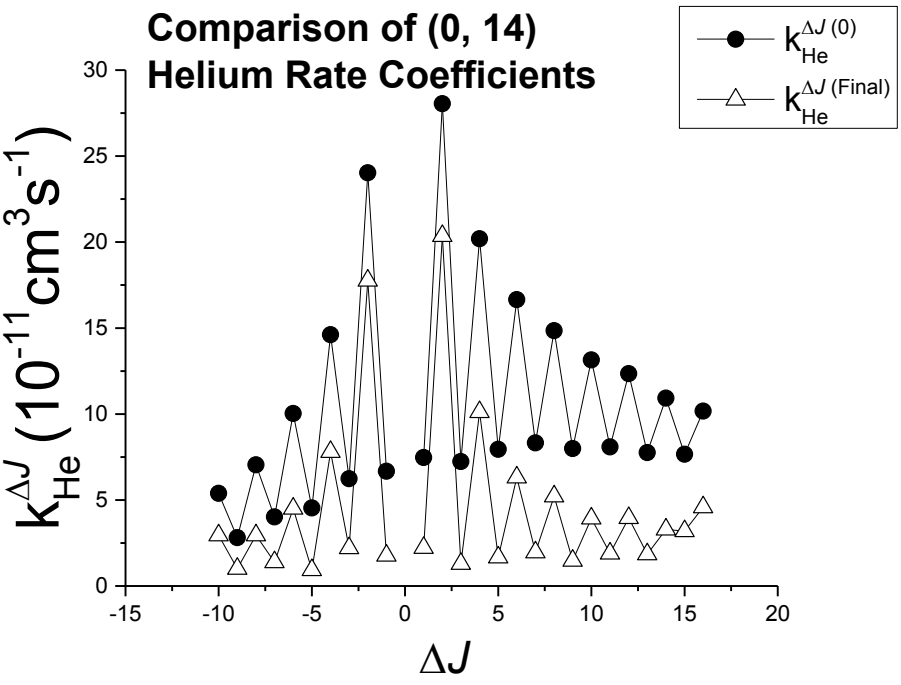

Figure 6.29: Comparison of the zeroth order (original fit) and final helium rate coefficients which include multiple collision effects, for initial level $2(A)^1\Sigma^+$ (0, 14). Values are presented in Table 6.17.

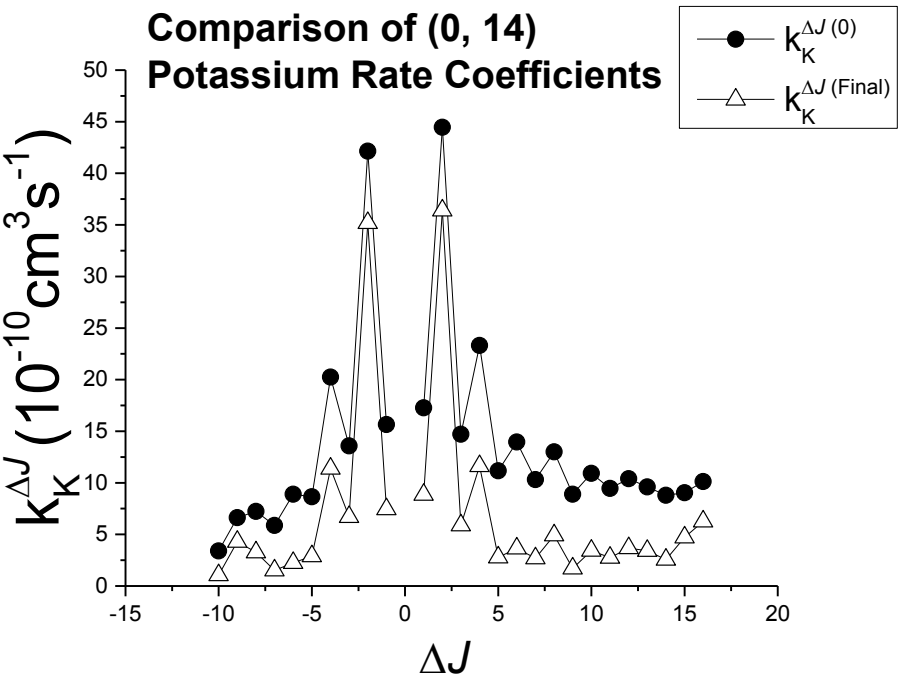

Figure 6.30: Comparison of the zeroth order (original fit) and final potassium rate coefficients which include multiple collision effects, for initial level $2(A)^1\Sigma^+$ (0, 14). Values are presented in Table 6.18.

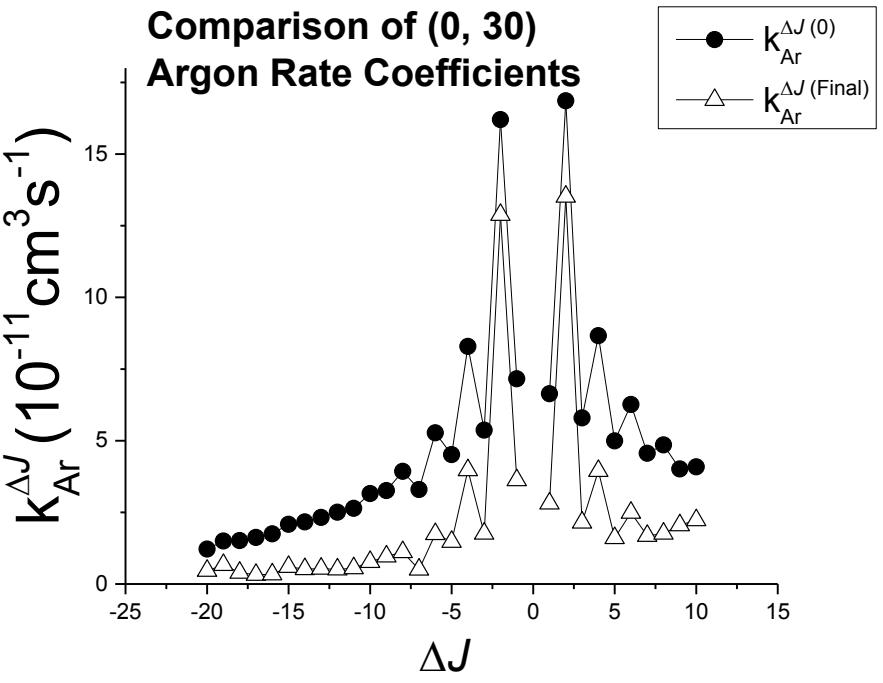

Figure 6.31: Comparison of the zeroth order (original fit) and final argon rate coefficients which include multiple collision effects, for initial level $2(A)^1\Sigma^+$ (0, 30). Values are presented in Table 6.19.

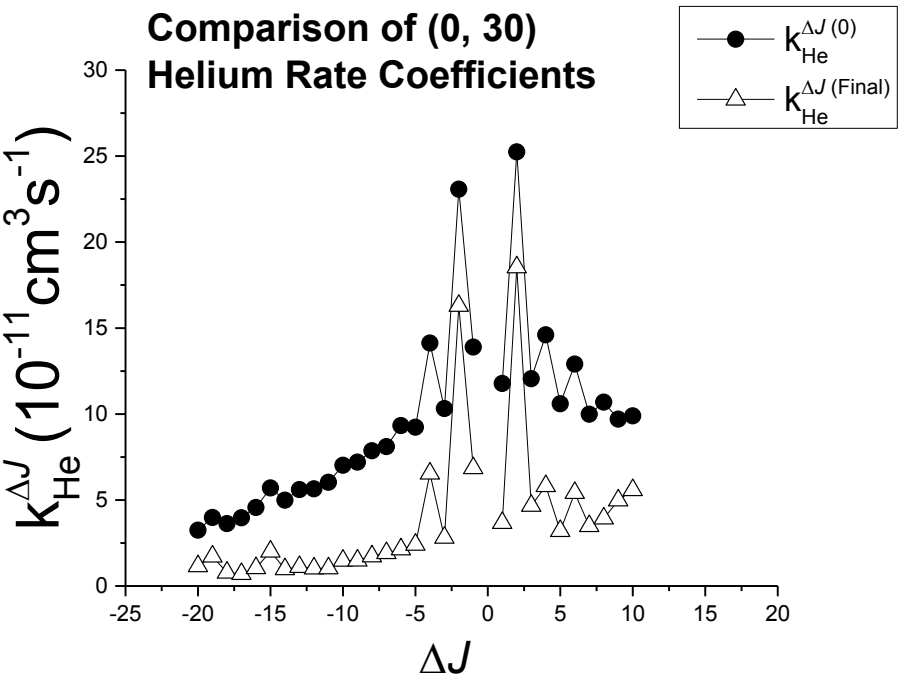

Figure 6.32: Comparison of the zeroth order (original fit) and final helium rate coefficients which include multiple collision effects, for initial level $2(A)^1\Sigma^+$ (0, 30). Values are presented in Table 6.20.

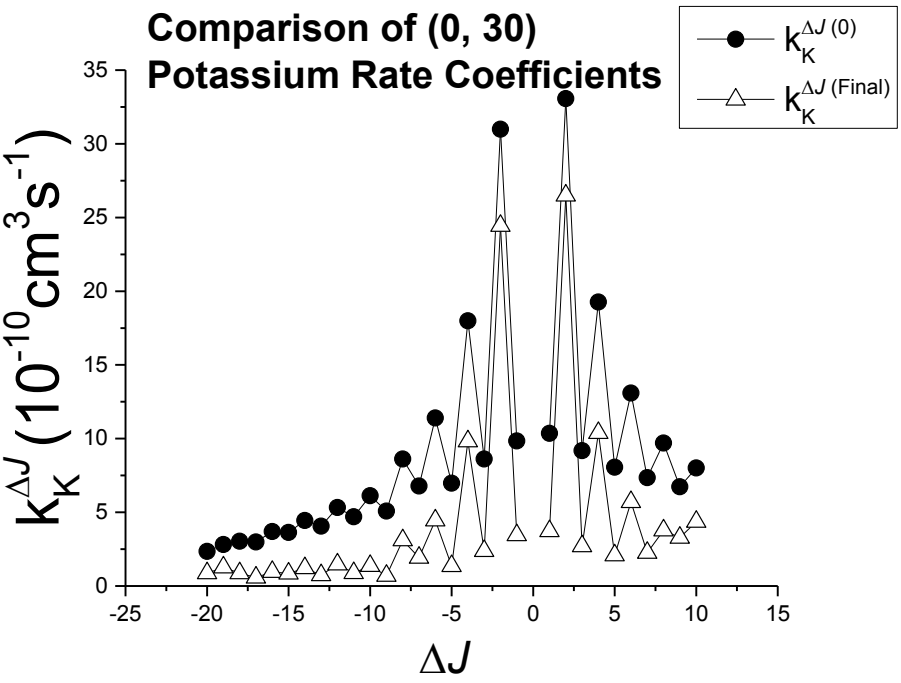

Figure 6.33: Comparison of the zeroth order (original fit) and final potassium rate coefficients which include multiple collision effects, for initial level $2(A)^1\Sigma^+$ (0, 30). Values are presented in Table 6.21.

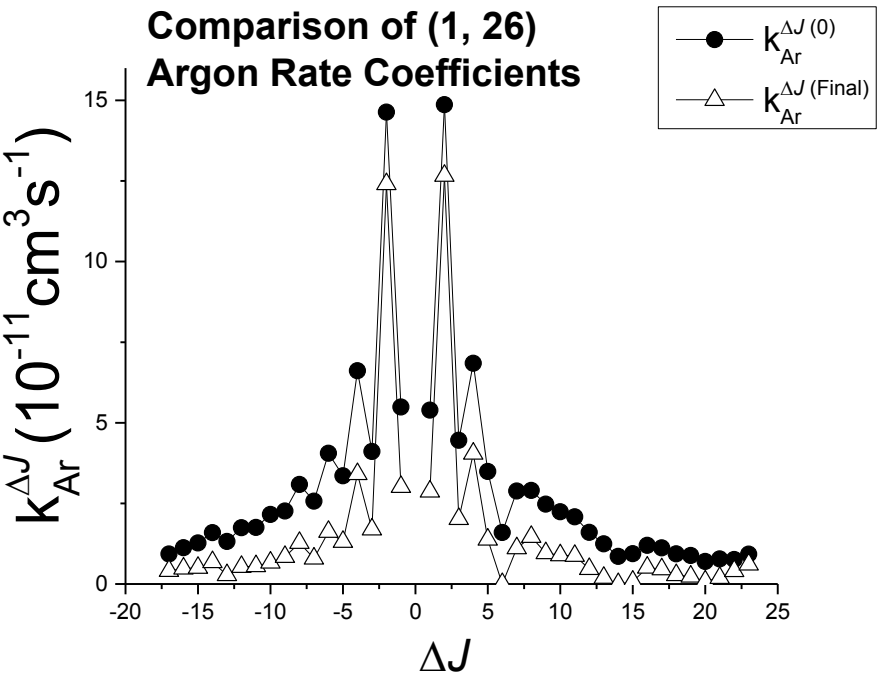

Figure 6.34: Comparison of the zeroth order (original fit) and final argon rate coefficients which include multiple collision effects, for initial level $2(A)^1\Sigma^+$ (1, 26). Values are presented in Table 6.22.

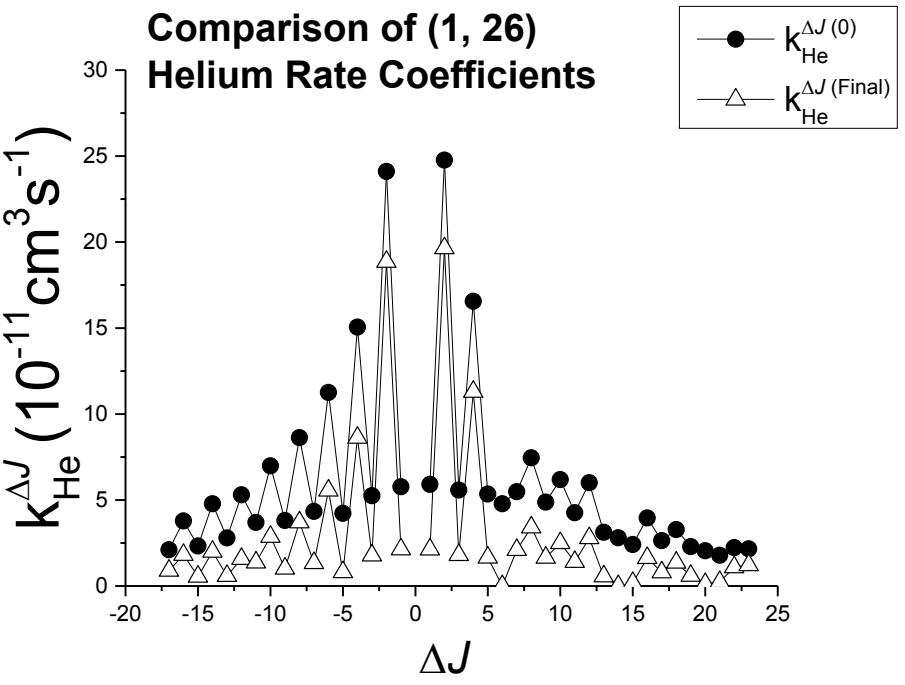

Figure 6.35: Comparison of the zeroth order (original fit) and final helium rate coefficients which include multiple collision effects, for initial level $2(A)^1\Sigma^+$ (1, 26). Values are presented in Table 6.23.

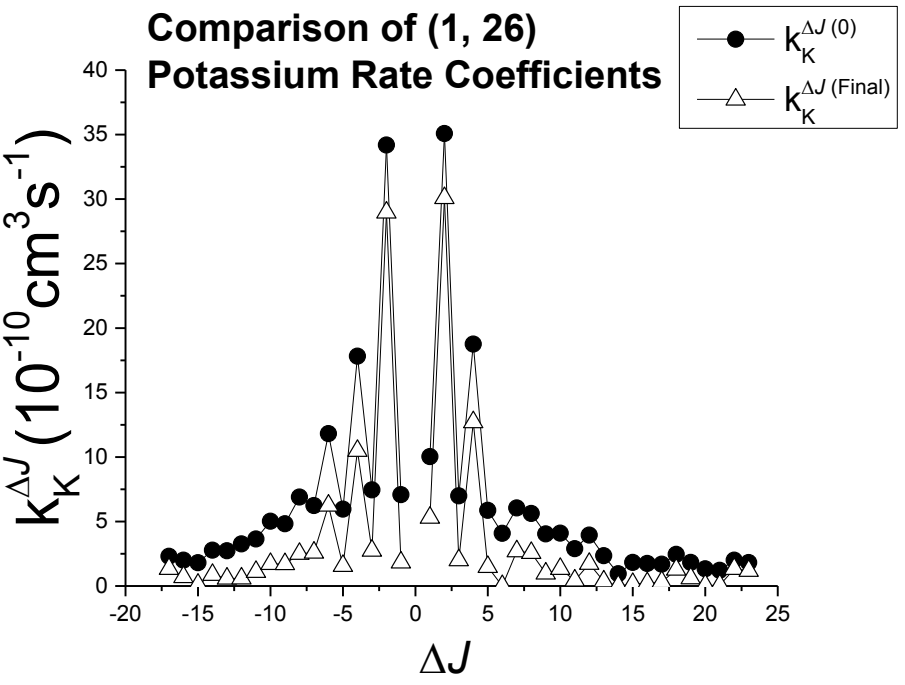

Figure 6.36: Comparison of the zeroth order (original fit) and final potassium rate coefficients which include multiple collision effects, for initial level $2(A)^1\Sigma^+$ (1, 26). Values are presented in Table 6.24.

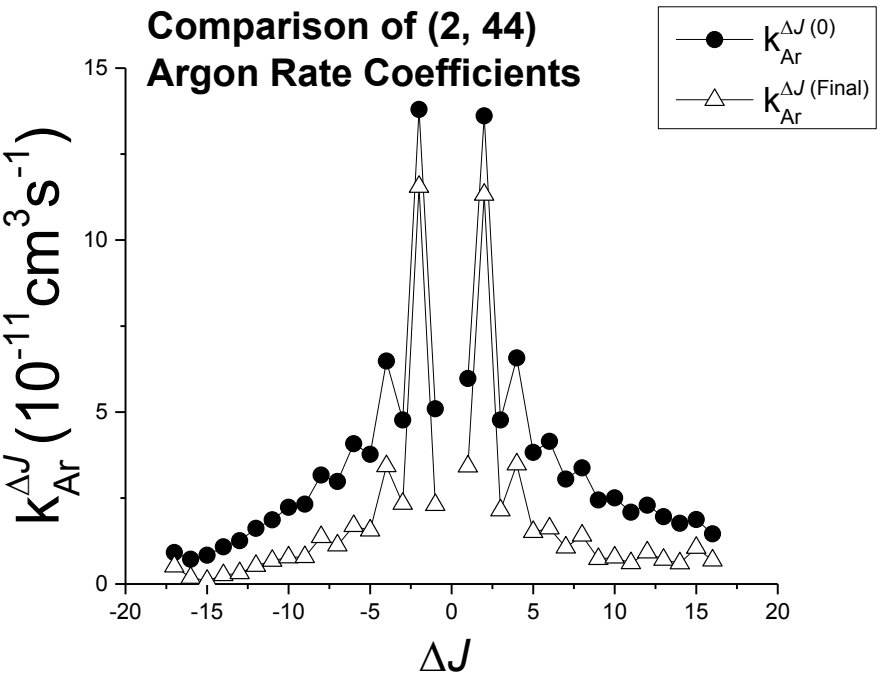

Figure 6.37: Comparison of the zeroth order (original fit) and final argon rate coefficients which include multiple collision effects, for initial level $2(A)^1\Sigma^+$ (2, 44). Values are presented in Table 6.25.

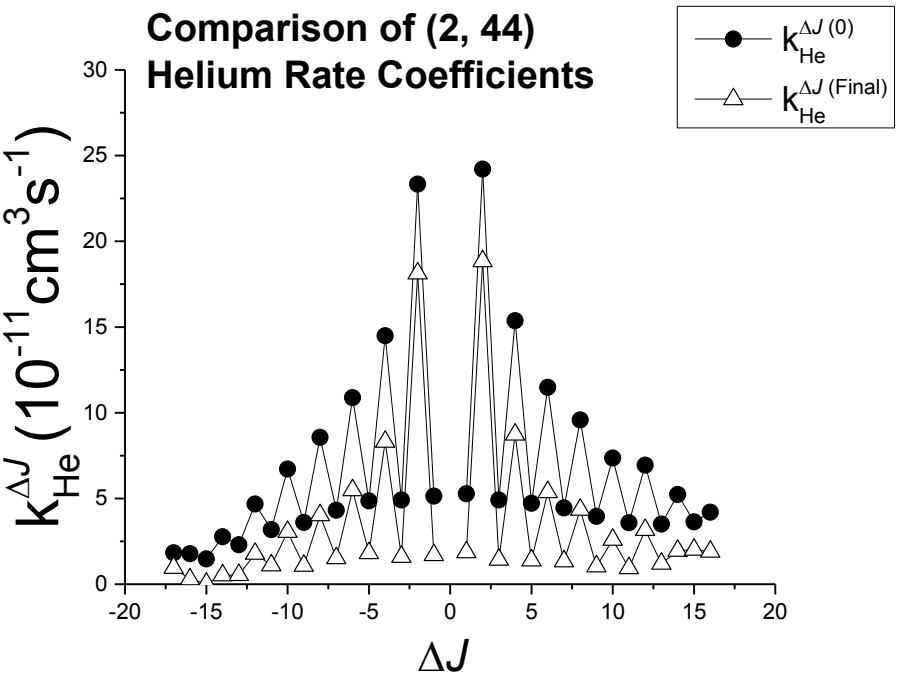

Figure 6.38: Comparison of the zeroth order (original fit) and final helium rate coefficients which include multiple collision effects, for initial level $2(A)^1\Sigma^+$ (2, 44). Values are presented in Table 6.26.

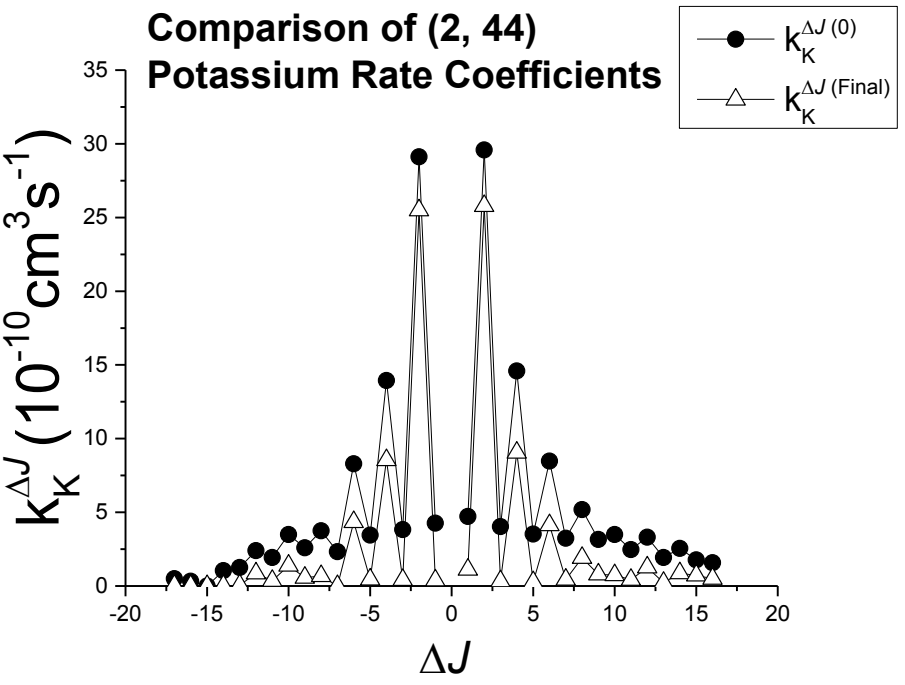

Figure 6.39: Comparison of the zeroth order (original fit) and final potassium rate coefficients which include multiple collision effects, for initial level $2(A)^1\Sigma^+$ (2, 44). Values are presented in Table 6.27.

Direct level	$\sum_J k_{Ar}^{\Delta J,\mathrm{Final}}$ ($\mathrm{cm}^3 s^{-1}$)	$\sum_J k_{He}^{\Delta J\mathrm{Final}}$ ($\mathrm{cm}^3 s^{-1}$)	$\sum_J k_{K}^{\Delta J\mathrm{Final}}$ ($\mathrm{cm}^3 s^{-1}$)
astate	argon sum	helium sum	K sum
$2(A)^1\Sigma^+$ (0, 14)	5.94×10^{-10}	1.17×10^{-9}	1.81×10^{-8}
$2(A)^1\Sigma^+$ (0, 30)	6.80×10^{-10}	1.15×10^{-9}	1.27×10^{-8}
$2(A)^1\Sigma^+$ (1, 26)	6.22×10^{-10}	1.14×10^{-9}	1.32×10^{-8}
$2(A)^1\Sigma^+$ (2, 44)	6.15×10^{-10}	9.21×10^{-10}	1.10×10^{-8}
k^Q ($\mathrm{cm}^3 s^{-1}$)	8.27×10^{-10}	1.39×10^{-9}	2.02×10^{-8}

Table 6.28: Comparison of fitted quenching rate coefficients with the sums of the $k^{\Delta J}$ values for a given initial level. These values were obtained using the "final" value from the multiple collision analysis, which is the average of the $k_P^{d\to c(99)}$ and $k_P^{d\to c(100)}$(or in some cases the $k_P^{d\to c(5)}$ and $k_P^{d\to c(6)}$) rate coefficients, for argon, helium and potassium.

After the correction of the individual rate coefficients, we see that the summation of the final terms for each directly populated level, over all individual $k^{\Delta J}$, has been reduced to less than the quenching rate. These reduced values are presented in Table 6.28.

We also note that our measured rate coefficients should, of course, obey the principle of detailed balance. The only place we can actually test this is by comparing the values of $k_P^{\Delta J=16}$ for $2(A)^1\Sigma^+$ (0, 14) with $k_P^{\Delta J=-16}$ for $2(A)^1\Sigma^+$ (0, 30), Unfortunately, both of these values have large uncertainties due to the large values of $|\Delta J|$, and large multiple collision corrections involved. In addition, relative values of these rate coefficients are no better than the absolute values since they were obtained from entirely separate scans (relative values of rate coefficients for the same initial level but different ΔJ's are determined very accurately). Nevertheless, detailed balance predicts that $k_{0,14}^{\Delta J=16} \approx 2k_{0,30}^{\Delta J=-16}$. We find that our final (0, 14) coefficients are indeed larger than those for (0, 30), but by larger factors than predicted (3.1 for argon and 4.4 for helium).

We have described our calculation of the impact of multiple collisions on our collisional rate coefficients for vibrationally elastic collisions. However, we can also expand this type of analysis to the v-changing collisions. We estimate that the effect of multiple collisions on v and J changing collisions is similar to that of large ΔJ vibrationally elastic collisions: the corrected rate coefficients turn out to be approximately half of the original fitted values.

To study this more quantitatively, we expand the summation of states i in Eq. 6.27 to include vibration, as well as rotation changing transitions as

$$k_P^{i\to c}\frac{n_i}{n_d} = k_P^{(v_i,J_i)\to(v_c,J_c)}\frac{n_{(v_i,J_i)}}{n_{(v_d,J_d)}}, \tag{6.34}$$

where now v_i does not necessarily have to equal either v_c or v_d. However, it is clear that there are two likely "paths" that can be taken from the directly populated level d to the (final) collisionally populated level c. In the first case, a collision transfers population from d to i, where rotational level i is in the same vibrational level as level d, and then a second collision transfers population from i to c. Therefore $v_d = v_i \neq v_c$ [or, $v_d, J_d \to v_{i=d}, J_i \to v_c, J_c$]. In the second case, the first collision transfers population from d to i, where $v_i \neq v_d$, but $v_i = v_c$ [or, $v_d, J_d \to v_{i=c}, J_i \to v_c, J_c$]. While the initial and final ro-vibrational levels are identical in these two cases, the cases are distinguished by whether the vibrationally inelastic transition occurs on the first or second step.

An important note pertaining to the results of the multiple collision analysis for

vibration and rotation-changing collisions is related to the rate coefficients on the ends of the ΔJ ranges studied. Because only a finite number of ΔJ values were fit for each set of vibrationally inelastic collisions, the values on the ends of the ΔJ range are not properly corrected for transfer from neighboring states characterized by larger $|\Delta J|$. This is, of course, also true for the multiple collision corrections for vibrationally elastic collisions, but it is less of a problem in that case because the population falls off with $|\Delta J|$. For the vibrationally inelastic collisions, we see that original fitted values $k_P^{\Delta v, \Delta J(0)}$ do not vary much with ΔJ (see Sec. 6.3.3). Therefore we find that the rate coefficients at the ends of the ΔJ range are adjusted downward less than they should be and less than those near the center of the ΔJ range. This introduces an apparent increase in the vibrationally inelastic collision rate coefficients at both ends of the ΔJ range relative to those at the center of the range. This is not a real effect, and we believe all of the rate coefficients are comprable in magnitude to those near the center of the range, just as all of the originally fitted rate coefficients for the vibrationally inelastic collisions are comparable before the multiple collision corrections are applied.

For the vibration-changing collisional rate coefficients, the "final" values we report are those obtained from the average of the 99th and 100th iterations of the multiple collision calculations, with the caveat about the values on the ends of the ΔJ range mentioned above. In the multiple collision analysis of the helium rate coefficients for $v = 2 \rightarrow v = 0$ and $v = 1 \rightarrow v = 0$, we find that the iterations of multiple collision calculations never truly converge, but continued to oscillate between the values from iterations 99 and 100.

Initial v, J-changing rate coefficients values, as well as calculations for the first through sixth, 99th and 100th iterations are, for $2(A)^1\Sigma^+$ (2, 44) $\Delta v = -2$, given in Tables 6.29 and 6.30 for argon and helium perturbers, respectively. Similar values for $2(A)^1\Sigma^+$ (2, 44) $\Delta v = -1$ are provided in Tables 6.31 (argon) and 6.32 (helium), and for $2(A)^1\Sigma^+$ (1, 26) $\Delta v = -1$ in Tables 6.33(argon), and 6.34 (helium). Figures 6.40 and 6.41 show a comparison of the zeroth order fitted rate coefficients and the final rate coefficients corrected for multiple collision effects for initial level $2(A)^1\Sigma^+$ (2, 44), $\Delta v = -2$. Figures 6.42 and 6.43 present similar figures for $2(A)^1\Sigma^+$ (2, 44), $\Delta v = -1$, and Figures 6.44 and 6.45 present figures for $2(A)^1\Sigma^+$ (1, 26), $\Delta v = -1$. Similar to the J-changing multiple collision results, the true values should lie between the two sets of results in each plot (except near the ends of the ΔJ ranges where even the "corrected" values are probably too large). As stated previously, we believe that the actual values for all ΔJ's are likely to be closer to the corrected (lower) values near the center of the ΔJ range.

$2(A)^1\Sigma^+$ (2, 44), Δv = -2 Original and Corrected $k_{Ar}^{d\to c,\Delta v,\Delta J}$ values (in units of 10^{-12} cm^{3}s^{-1})									
		$k_{Ar}^{d\to c(n)}$ for iteration n							
ΔJ	$k_{Ar}^{d\to c(0)}$	n = 1	n = 2	n = 3	n = 4	n = 5	n = 6	n = 99	n = 100
-15	5.36	3.21	3.15	3.83	3.26	3.78	3.31	3.53	3.53
-14	4.19	2.10	1.58	2.29	1.65	2.24	1.71	1.96	1.96
-13	3.98	1.69	0.45	1.22	0.45	1.14	0.52	0.81	0.81
-12	4.32	1.89	0.80	1.71	0.87	1.63	0.94	1.27	1.27
-11	4.59	1.99	0.81	1.85	0.93	1.77	1.01	1.37	1.37
-10	4.51	1.87	0.47	1.56	0.56	1.47	0.64	1.03	1.03
-9	4.67	1.93	0.52	1.72	0.64	1.61	0.73	1.15	1.15
-8	5.26	2.27	0.94	2.22	1.08	2.11	1.18	1.62	1.62
-7	4.89	1.99	0.50	1.85	0.65	1.73	0.75	1.22	1.22
-6	5.55	2.36	0.91	2.30	1.04	2.18	1.15	1.64	1.64
-5	4.79	1.86	0.14	1.60	0.29	1.48	0.40	0.91	0.91
-4	5.64	2.36	0.81	2.31	0.96	2.18	1.08	1.60	1.60
-3	4.94	1.88	0.02	1.55	0.15	1.41	0.27	0.81	0.81
-2	5.50	2.23	0.55	2.12	0.71	1.99	0.84	1.39	1.39
-1	5.88	2.49	1.00	2.63	1.19	2.50	1.33	1.88	1.88
0	4.94	1.83	0.00	1.35	0.00	1.20	0.01	0.57	0.57
1	5.26	2.04	0.12	1.72	0.25	1.57	0.38	0.95	0.95
2	5.73	2.38	0.81	2.45	1.03	2.32	1.16	1.72	1.72
3	5.41	2.16	0.43	2.03	0.60	1.88	0.73	1.28	1.28
4	5.17	2.02	0.21	1.74	0.35	1.60	0.48	1.01	1.01
5	5.41	2.21	0.60	2.13	0.76	1.99	0.89	1.41	1.41
6	5.26	2.16	0.61	2.07	0.78	1.94	0.90	1.39	1.39
7	5.12	2.09	0.54	1.96	0.70	1.84	0.82	1.30	1.30
8	4.94	2.04	0.64	1.96	0.83	1.85	0.94	1.39	1.39
9	4.51	1.76	0.13	1.38	0.24	1.26	0.34	0.78	0.78
10	3.42	1.15	0.00	0.33	0.00	0.21	0.00	0.00	0.00
11	4.84	2.10	0.87	1.97	0.99	1.88	1.09	1.46	1.46
12	4.89	2.28	1.42	2.39	1.56	2.31	1.65	1.97	1.97
13	4.94	2.33	1.42	2.32	1.49	2.23	1.57	1.88	1.88
14	4.21	2.04	1.44	2.20	1.52	2.13	1.58	1.84	1.84
15	4.56	2.39	1.98	2.68	2.05	2.62	2.11	2.35	2.35

Table 6.29: *v, J*-changing rate coefficients for argon, corrected for multiple collision effects (with $n_{Ar} = 1.69 \times 10^{17}$ cm^{-3} and $n_K = 1.65 \times 10^{14}$ cm^{-3}) for excitation of $2(A)^1\Sigma^+$ (2, 44), Δv =-2 are presented here.

$2(A)^1\Sigma^+$ (2, 44), Δv = -2 Original and Corrected $k_{He}^{d\to c,\Delta v,\Delta J}$ values (in units of 10^{-12} cm^{3}s^{-1})									
		$k_{He}^{d\to c(n)}$ for iteration n							
ΔJ	$k_{He}^{d\to c(0)}$	n = 1	n = 2	n = 3	n = 4	n = 5	n = 6	n = 99	n = 100
-15	10.01	5.64	5.36	6.91	5.45	6.91	5.50	6.63	5.78
-14	8.70	4.37	3.52	5.12	3.57	5.12	3.60	4.79	3.89
-13	7.90	3.31	1.02	2.81	0.93	2.75	0.97	2.40	1.31
-12	9.07	4.07	2.25	4.26	2.27	4.22	2.32	3.84	2.68
-11	9.12	3.90	1.65	3.95	1.72	3.90	1.78	3.49	2.18
-10	8.23	3.15	0.10	2.43	0.06	2.36	0.12	1.92	0.55
-9	8.65	3.33	0.27	2.89	0.31	2.82	0.38	2.35	0.84
-8	10.06	4.15	1.38	4.17	1.49	4.11	1.57	3.62	2.05
-7	9.68	3.84	0.87	3.88	1.04	3.83	1.12	3.33	1.64
-6	10.76	4.39	1.32	4.39	1.43	4.31	1.51	3.77	2.05
-5	9.21	3.37	0.00	2.97	0.00	2.88	0.00	2.32	0.47
-4	11.56	4.79	1.76	5.12	1.97	5.08	2.06	4.50	2.64
-3	9.73	3.56	0.00	3.21	0.00	3.12	0.00	2.53	0.55
-2	10.25	3.78	0.00	3.28	0.00	3.17	0.03	2.60	0.65
-1	10.76	4.14	0.63	4.28	0.85	4.22	0.94	3.65	1.58
0	9.64	3.36	0.00	2.55	0.00	2.43	0.00	1.76	0.00
1	9.92	3.52	0.00	2.94	0.00	2.84	0.00	2.16	0.04
2	10.95	4.19	0.48	4.14	0.74	4.06	0.85	3.50	1.49
3	10.20	3.73	0.00	3.38	0.00	3.29	0.00	2.69	0.60
4	10.11	3.70	0.00	3.18	0.00	3.05	0.00	2.44	0.50
5	11.23	4.49	1.23	4.79	1.42	4.75	1.51	4.15	2.13
6	11.00	4.42	1.30	4.69	1.54	4.60	1.64	4.05	2.22
7	10.34	4.02	0.64	3.97	0.75	3.88	0.83	3.30	1.41
8	9.78	3.79	0.57	3.58	0.71	3.48	0.80	2.99	1.35
9	9.17	3.44	0.00	2.96	0.00	2.88	0.08	2.35	0.61
10	7.33	2.45	0.00	1.18	0.00	1.08	0.00	0.55	0.00
11	9.35	3.79	1.07	3.74	1.10	3.68	1.17	3.20	1.65
12	10.34	4.75	3.11	5.45	3.24	5.36	3.32	4.98	3.75
13	9.35	4.09	2.08	4.35	2.08	4.30	2.14	3.88	2.55
14	9.26	4.47	3.37	5.26	3.44	5.22	3.49	4.89	3.84
15	8.84	4.25	3.19	5.08	3.22	5.03	3.27	4.68	3.60

Table 6.30: *v, J*-changing rate coefficients for helium, corrected for multiple collision effects (with $n_{He} = 1.13 \times 10^{17}$ cm^{-3} and $n_K = 2.92 \times 10^{14}$ cm^{-3}) for excitation of $2(A)^1\Sigma^+$ (2, 44), Δv =-2 are presented here.

$2(A)^1\Sigma^+$ (2, 44), Δv = -1 Original and Corrected $k_{Ar}^{d\to c,\Delta v,\Delta J}$ values (in units of 10^{-12} cm^{3}s^{-1})									
		$k_{Ar}^{d\to c(n)}$ for iteration n							
ΔJ	$k_{Ar}^{d\to c(0)}$	n = 1	n = 2	n = 3	n = 4	n = 5	n = 6	n = 99	n = 100
-25	5.17	2.56	1.81	2.63	1.88	2.53	1.96	2.23	2.23
-24	6.06	3.13	2.51	3.47	2.63	3.36	2.73	3.02	3.02
-23	7.05	3.57	2.70	3.84	2.85	3.72	2.97	3.32	3.32
-22	6.39	2.94	1.60	2.82	1.73	2.68	1.86	2.24	2.24
-21	5.97	2.49	0.65	1.98	0.78	1.82	0.93	1.34	1.34
-20	6.11	2.54	0.71	2.18	0.91	2.02	1.06	1.51	1.51
-19	6.35	2.61	0.67	2.27	0.90	2.09	1.07	1.54	1.54
-18	5.97	2.31	0.04	1.69	0.25	1.49	0.42	0.92	0.92
-17	6.77	2.77	0.72	2.52	1.00	2.31	1.18	1.71	1.71
-16	7.33	3.12	1.24	3.13	1.59	2.93	1.79	2.33	2.33
-15	7.00	2.81	0.51	2.41	0.76	2.17	0.96	1.53	1.53
-14	6.49	2.40	0.00	1.46	0.00	1.20	0.00	0.54	0.54
-13	7.80	3.27	1.17	3.23	1.52	2.99	1.73	2.33	2.33
-12	9.54	4.48	2.98	5.08	3.43	4.89	3.66	4.25	4.25
-11	7.38	2.90	0.35	2.39	0.62	2.13	0.84	1.44	1.44
-10	6.91	2.55	0.00	1.49	0.00	1.20	0.00	0.51	0.51
-9	7.90	3.24	0.93	3.02	1.26	2.76	1.49	2.09	2.09
-8	8.74	3.89	2.09	4.18	2.53	3.95	2.75	3.33	3.33
-7	7.80	3.26	1.14	3.19	1.54	2.97	1.76	2.33	2.33
-6	6.63	2.55	0.16	2.03	0.52	1.80	0.71	1.22	1.22
-5	6.06	2.21	0.00	1.51	0.00	1.26	0.16	0.70	0.70
-4	3.98	1.10	0.00	0.00	0.00	0.00	0.00	0.00	0.00
-3	5.31	1.82	0.00	0.81	0.00	0.58	0.00	0.00	0.00
-2	6.63	2.76	0.97	2.62	1.36	2.43	1.53	1.96	1.96
-1	7.43	3.30	1.70	3.32	2.06	3.15	2.24	2.69	2.69
0	6.49	2.69	0.73	2.18	0.94	1.97	1.10	1.51	1.51
1	6.91	3.02	1.26	2.66	1.49	2.48	1.65	2.04	2.04
2	7.29	3.50	2.34	3.66	2.59	3.49	2.74	3.09	3.09
3	6.77	3.12	1.63	2.75	1.75	2.59	1.88	2.20	2.20
4	5.26	2.38	1.25	2.22	1.38	2.09	1.49	1.77	1.77
5	7.24	4.06	3.71	4.67	3.91	4.55	4.01	4.27	4.27

Table 6.31: *v, J*-changing rate coefficients for argon, corrected for multiple collision effects (with $n_{Ar} = 1.69 \times 10^{17}$ cm^{-3} and $n_K = 1.65 \times 10^{14}$ cm^{-3}) for excitation of $2(A)^1\Sigma^+$ (2, 44), Δv =-1 are presented here.

$2(A)^1\Sigma^+$ (2, 44), Δv = -1 Original and Corrected $k_{He}^{d\to c,\Delta v,\Delta J}$ values (in units of 10^{-12} cm^{3}s^{-1})									
		$k_{He}^{d\to c(n)}$ for iteration n							
ΔJ	$k_{He}^{d\to c(0)}$	n = 1	n = 2	n = 3	n = 4	n = 5	n = 6	n = 99	n = 100
-25	10.81	5.08	3.38	5.69	3.36	5.59	3.44	4.51	4.49
-24	13.72	7.05	5.97	8.55	6.06	8.51	6.16	7.29	7.29
-23	13.63	6.35	4.17	7.19	4.23	7.10	4.33	5.69	5.69
-22	13.16	5.69	2.53	5.64	2.46	5.50	2.58	4.02	4.00
-21	12.22	4.79	0.76	4.23	0.73	4.12	0.86	2.47	2.44
-20	13.72	5.59	1.61	5.36	1.67	5.22	1.82	3.50	3.47
-19	13.11	5.03	0.45	4.54	0.54	4.40	0.70	2.52	2.50
-18	14.29	5.59	0.89	5.17	1.03	5.03	1.20	3.09	3.06
-17	14.38	5.55	0.59	5.17	0.74	5.03	0.93	2.95	2.92
-16	14.76	5.59	0.21	4.94	0.40	4.75	0.59	2.65	2.62
-15	15.56	6.02	0.81	5.78	1.00	5.59	1.20	3.38	3.35
-14	15.84	6.02	0.28	5.31	0.46	5.08	0.68	2.85	2.82
-13	17.67	7.19	2.33	7.71	2.65	7.52	2.87	5.17	5.12
-12	19.93	8.55	4.13	9.64	4.57	9.40	4.79	7.10	7.05
-11	16.97	6.53	0.84	6.30	1.08	6.06	1.31	3.68	3.64
-10	17.01	6.39	0.02	5.36	0.15	5.08	0.39	2.69	2.66
-9	17.06	6.53	0.65	6.20	0.95	5.97	1.20	3.58	3.54
-8	19.55	8.18	3.40	8.98	3.91	8.70	4.15	6.39	6.35
-7	17.01	6.63	1.18	6.67	1.62	6.44	1.88	4.20	4.16
-6	16.03	6.06	0.41	5.55	0.87	5.26	1.10	3.16	3.14
-5	14.24	5.08	0.00	4.13	0.00	3.85	0.00	1.72	1.70
-4	10.20	2.89	0.00	0.00	0.00	0.00	0.00	0.00	0.00
-3	11.52	3.64	0.00	1.66	0.00	1.40	0.00	0.00	0.00
-2	14.34	5.55	0.79	5.22	1.25	4.98	1.45	3.19	3.16
-1	14.29	5.55	0.79	5.12	1.17	4.94	1.40	3.22	3.20
0	15.09	6.35	2.66	6.72	3.00	6.49	3.21	4.84	4.79
1	14.48	5.92	1.79	5.64	1.99	5.41	2.19	3.82	3.80
2	12.74	5.17	1.52	4.94	1.65	4.70	1.83	3.25	3.23
3	14.95	6.67	3.58	6.82	3.66	6.63	3.84	5.22	5.22
4	11.56	5.08	2.81	5.69	3.02	5.50	3.17	4.32	4.31
5	15.60	8.13	7.10	9.87	7.33	9.73	7.47	8.60	8.60

Table 6.32: *v, J*-changing rate coefficients for helium, corrected for multiple collision effects (with $n_{He} = 1.13 \times 10^{17}$ cm^{-3} and $n_K = 2.92 \times 10^{14}$ cm^{-3}) for excitation of $2(A)^1\Sigma^+$ (2, 44), Δv =-1 are presented here.

$2(A)^1\Sigma^+$ (1, 26), Δv = -1 Original and Corrected $k_{Ar}^{d\to c,\Delta v,\Delta J}$ values (in units of 10^{-12} cm^{3}s^{-1})									
		$k_{Ar}^{d\to c(n)}$ for iteration n							
ΔJ	$k_{Ar}^{d\to c(0)}$	n = 1	n = 2	n = 3	n = 4	n = 5	n = 6	n = 99	n = 100
-5	8.70	4.75	4.26	5.31	4.39	5.22	4.47	4.84	4.84
-4	8.74	4.60	3.92	5.12	4.07	5.03	4.17	4.57	4.57
-3	9.07	4.31	2.71	4.04	2.78	3.91	2.90	3.37	3.37
-2	8.79	3.94	1.95	3.37	2.00	3.22	2.12	2.64	2.64
-1	9.45	4.23	2.16	3.84	2.32	3.68	2.46	3.04	3.04
0	10.58	4.98	3.23	5.12	3.49	4.94	3.64	4.26	4.26
1	9.54	4.11	1.72	3.63	1.90	3.45	2.06	2.72	2.72
2	9.12	3.74	0.97	2.97	1.14	2.76	1.31	2.00	2.00
3	11.05	5.03	3.04	5.26	3.35	5.08	3.53	4.26	4.26
4	10.53	4.59	2.18	4.42	2.43	4.21	2.62	3.37	3.37
5	9.78	3.98	1.02	3.27	1.19	3.04	1.39	2.16	2.16
6	11.05	4.84	2.51	4.94	2.84	4.75	3.05	3.84	3.84
7	10.76	4.62	2.07	4.54	2.37	4.32	2.59	3.40	3.40
8	9.64	3.81	0.64	3.05	0.82	2.79	1.03	1.86	1.86
9	10.15	4.18	1.38	3.89	1.67	3.66	1.88	2.72	2.72
10	10.29	4.30	1.66	4.21	1.99	3.98	2.20	3.04	3.04
11	9.82	3.96	1.02	3.50	1.27	3.25	1.49	2.32	2.32
12	9.96	4.07	1.24	3.71	1.50	3.47	1.72	2.54	2.54
13	10.29	4.31	1.64	4.13	1.95	3.90	2.16	2.98	2.98
14	10.25	4.30	1.62	4.03	1.89	3.80	2.10	2.90	2.90
15	9.92	4.05	1.09	3.40	1.28	3.15	1.49	2.27	2.27
16	10.20	4.31	1.66	3.95	1.90	3.73	2.10	2.87	2.87
17	11.80	5.50	3.59	5.92	3.97	5.73	4.16	4.89	4.89
18	10.39	4.56	2.25	4.40	2.51	4.20	2.69	3.40	3.40
19	8.98	3.56	0.33	2.25	0.41	2.02	0.58	1.26	1.26
20	9.40	4.05	1.66	3.55	1.84	3.37	2.01	2.65	2.65
21	11.00	5.36	3.85	5.78	4.20	5.64	4.36	4.98	4.98
22	9.17	4.19	2.35	3.95	2.49	3.79	2.62	3.17	3.17
23	8.18	3.53	1.29	2.70	1.33	2.53	1.46	1.96	1.96
24	8.37	4.21	3.31	4.62	3.47	4.50	3.58	4.01	4.01
25	8.46	4.46	3.80	4.98	3.96	4.89	4.06	4.45	4.45

Table 6.33: *v, J*-changing rate coefficients for argon, corrected for multiple collision effects (with $n_{Ar} = 1.5 \times 10^{17}$ cm^{-3} and $n_K = 1.48 \times 10^{15}$ cm^{-3}) for excitation of $2(A)^1\Sigma^+$ (1, 26), Δv =-1 are presented here.

$2(A)^1\Sigma^+$ (1, 26), Δv = -1 Original and Corrected $k_{He}^{d\to c,\Delta v,\Delta J}$ values (in units of 10^{-12} cm^{3}s^{-1})									
		$k_{He}^{d\to c(n)}$ for iteration n							
ΔJ	$k_{He}^{d\to c(0)}$	n = 1	n = 2	n = 3	n = 4	n = 5	n = 6	n = 99	n = 100
-5	16.31	8.08	6.53	9.82	6.58	9.87	6.58	9.82	6.58
-4	17.25	8.41	6.49	10.01	6.49	10.06	6.49	10.01	6.49
-3	16.45	7.10	3.33	7.33	3.21	7.33	3.21	7.29	3.22
-2	17.86	7.71	3.55	7.80	3.37	7.80	3.37	7.80	3.38
-1	16.17	6.30	0.72	5.41	0.56	5.41	0.57	5.41	0.59
0	19.79	8.37	3.46	8.55	3.37	8.60	3.37	8.55	3.39
1	17.25	6.72	1.12	6.58	1.18	6.53	1.19	6.53	1.21
2	18.57	7.24	1.20	6.96	1.19	6.96	1.20	6.91	1.22
3	19.74	8.04	2.82	8.88	3.07	8.88	3.09	8.88	3.11
4	19.55	7.57	1.15	7.38	1.13	7.38	1.13	7.33	1.15
5	17.72	6.39	0.00	5.36	0.00	5.31	0.00	5.26	0.00
6	21.06	8.37	2.24	9.02	2.39	9.02	2.40	9.02	2.42
7	20.45	7.94	1.54	8.27	1.74	8.23	1.76	8.23	1.78
8	19.51	7.19	0.00	6.53	0.00	6.49	0.00	6.49	0.00
9	18.05	6.39	0.00	5.69	0.00	5.69	0.00	5.64	0.00
10	19.74	7.38	0.38	7.38	0.46	7.38	0.46	7.38	0.48
11	18.05	6.39	0.00	5.64	0.00	5.59	0.00	5.59	0.00
12	18.52	6.67	0.00	6.20	0.00	6.20	0.00	6.20	0.00
13	18.80	6.91	0.00	6.58	0.00	6.53	0.00	6.53	0.00
14	19.27	7.19	0.22	6.96	0.18	6.96	0.18	6.96	0.20
15	18.52	6.77	0.00	6.02	0.00	6.02	0.00	5.97	0.00
16	19.60	7.61	1.42	7.94	1.47	7.94	1.47	7.94	1.49
17	20.40	8.13	2.25	8.55	2.43	8.55	2.44	8.55	2.46
18	18.71	7.19	1.03	7.05	0.92	7.05	0.92	7.05	0.93
19	16.92	6.02	0.00	4.09	0.00	4.06	0.00	4.04	0.00
20	17.39	6.77	1.14	6.58	1.02	6.63	1.02	6.58	1.04
21	23.74	11.28	8.32	13.72	8.60	13.77	8.65	13.77	8.65
22	16.73	6.82	2.27	7.00	2.09	7.00	2.09	7.00	2.10
23	16.54	6.67	1.69	5.97	1.40	5.92	1.40	5.92	1.41
24	16.92	7.94	5.83	9.92	5.88	9.92	5.88	9.92	5.88
25	15.98	7.29	4.66	8.37	4.57	8.41	4.58	8.37	4.59

Table 6.34: *v, J*-changing rate coefficients for helium, corrected for multiple collision effects (with $n_{He} = 1.13 \times 10^{17}$ cm^{-3} and $n_K = 2.92 \times 10^{14}$ cm^{-3}) for excitation of $2(A)^1\Sigma^+$ (1, 26), Δv =-1 are presented here.

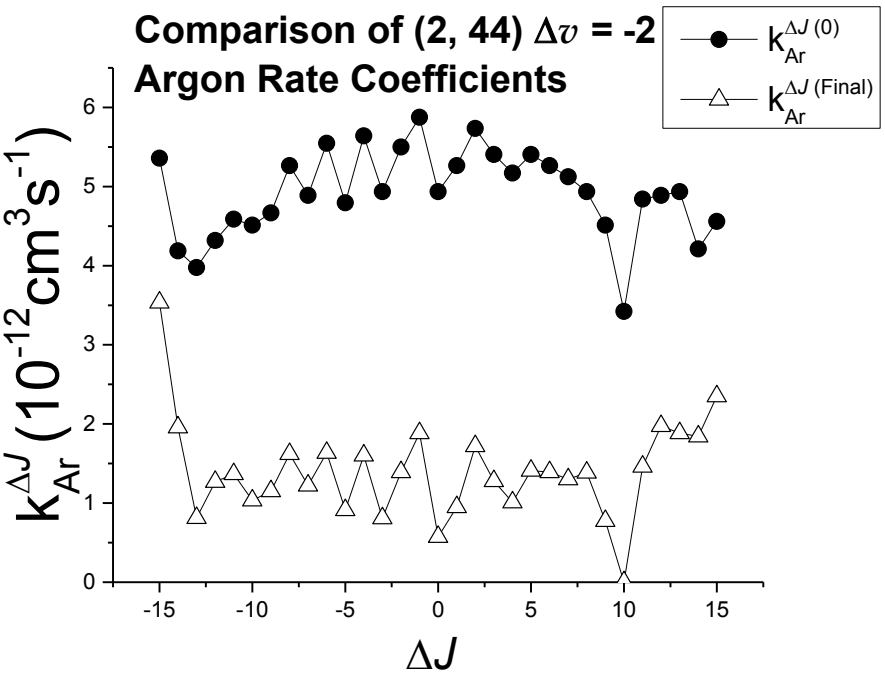

Figure 6.40: Comparison of the zeroth order (original fit) and final argon rate coefficients which include multiple collision effects, for initial level $2(A)^1\Sigma^+$ (2, 44), Δv = -2 . Values are presented in Table 6.29.

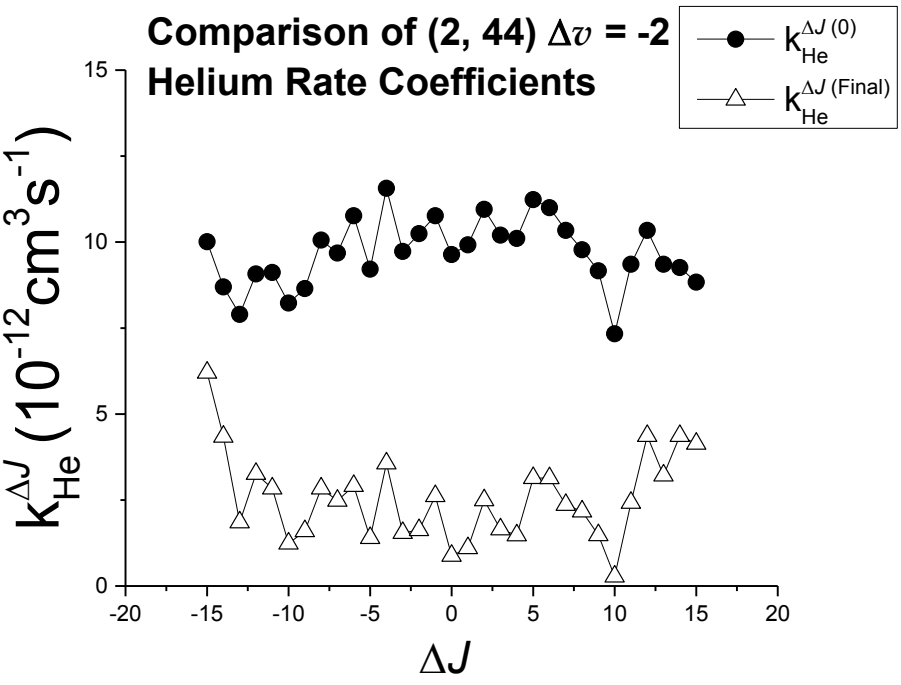

Figure 6.41: Comparison of the zeroth order (original fit) and final helium rate coefficients which include multiple collision effects, for initial level $2(A)^1\Sigma^+$ (2, 44), Δv = -2 . Values are presented in Table 6.30.

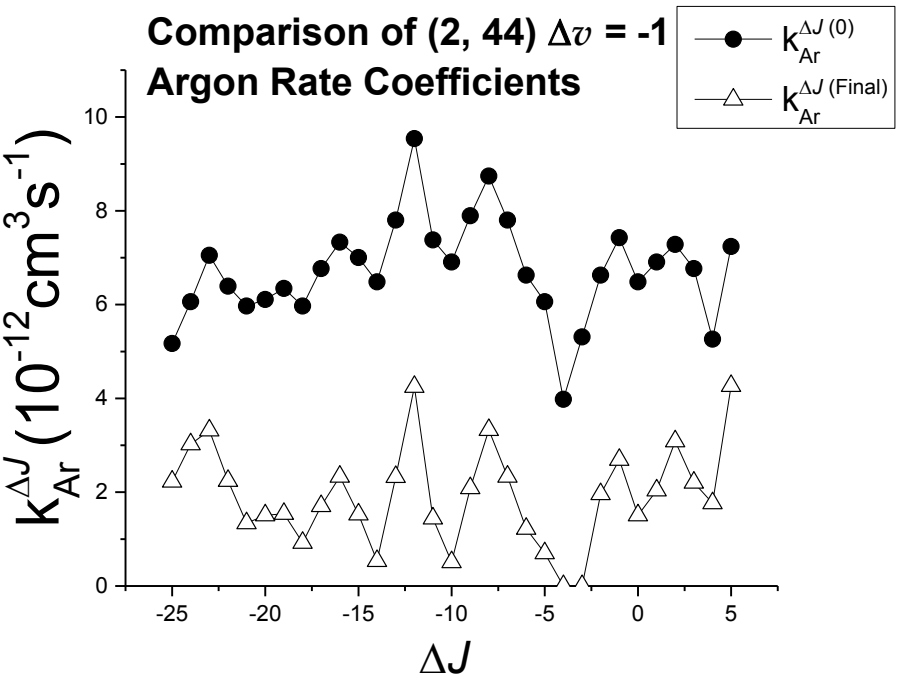

Figure 6.42: Comparison of the zeroth order (original fit) and final argon rate coefficients which include multiple collision effects, for initial level $2(A)^1\Sigma^+$ (2, 44), Δv = -1 . Values are presented in Table 6.31.

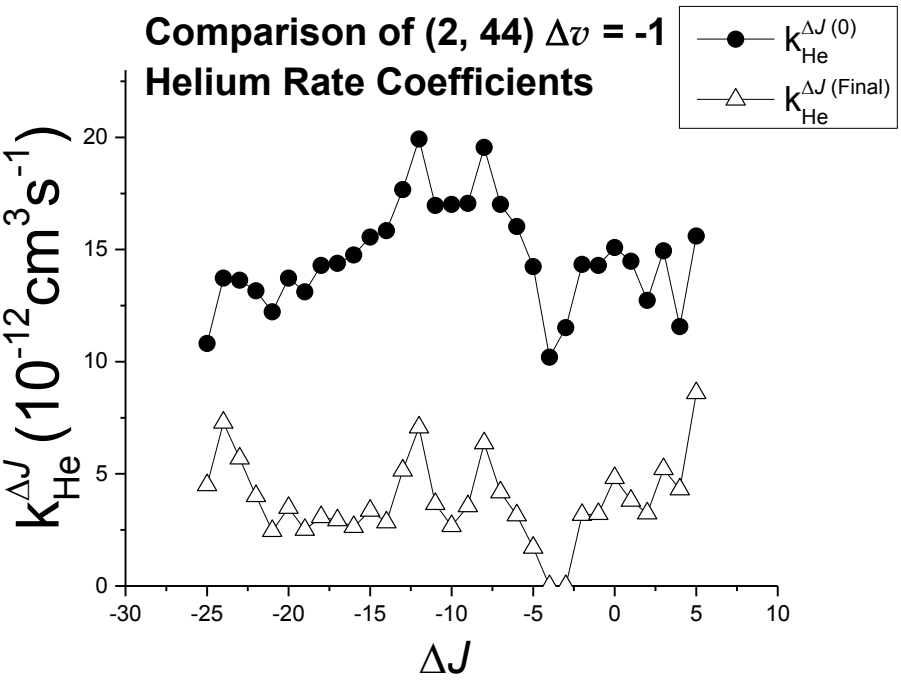

Figure 6.43: Comparison of the zeroth order (original fit) and final helium rate coefficients which include multiple collision effects, for initial level $2(A)^1\Sigma^+$ (2, 44), Δv = -1 . Values are presented in Table 6.32.

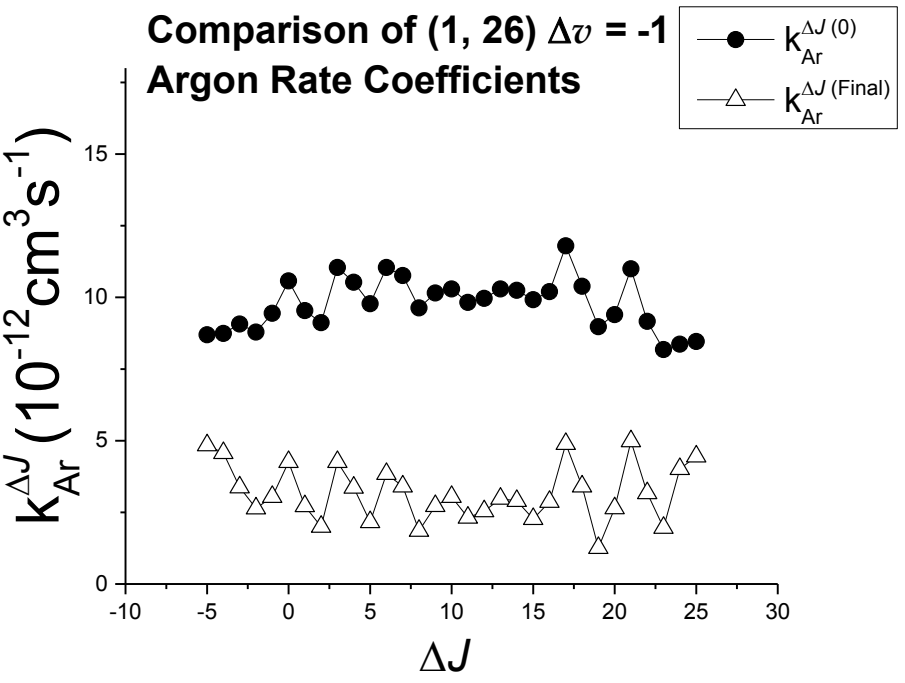

Figure 6.44: Comparison of the zeroth order (original fit) and final argon rate coefficients which include multiple collision effects, for initial level $2(A)^1\Sigma^+$ (1, 26), Δv = -1 . Values are presented in Table 6.33.

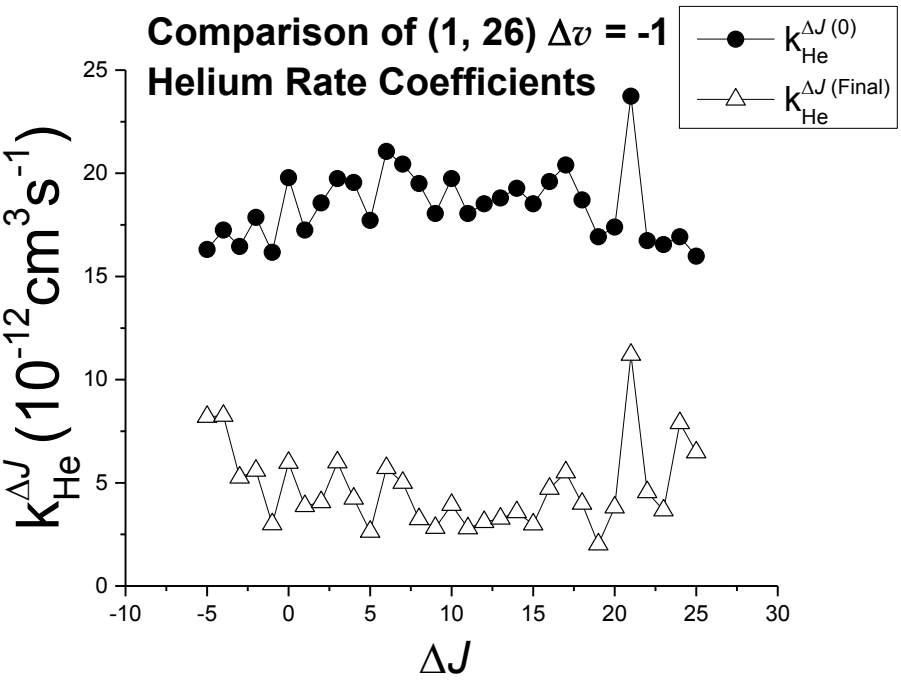

Figure 6.45: Comparison of the zeroth order (original fit) and final helium rate coefficients which include multiple collision effects, for initial level $2(A)^1\Sigma^+$ (1, 26), Δv = -1 . Values are presented in Table 6.34.

6.5 Comparison of Experiment and Theory

The first calculations of cross sections for rotationally inelastic collisions of NaK molecules with noble gas atoms carried out by the Hickman group at Lehigh involved molecules in the initial levels $2(A)^1\Sigma^+$ ($v = 0$, $J \leq 25$), with helium as the perturber [65]. These calculations did not show a ΔJ = even propensity, while experimental results for $2(A)^1\Sigma^+$ (16, 30) with argon perturbers did show a strong ΔJ = even propensity [31]. Direct comparison of the two sets of results was not completely valid, due to differences in perturbers (argon calculations would require substantially more computer resources) and initial $2(A)^1\Sigma^+$ levels ($v = 16$, $J = 30$ was used in the experiment, while the theoretical calculations were carried out for v=0).

Malenda *et al.* [33] used a better basis set than the earlier work, and produced results demonstrating a ΔJ = even propensity for collisions between $2(A)^1\Sigma^+$ NaK molecules and helium atoms, covering a larger range of J (0 to 40). In the mean time, experimental data with helium as the perturber were recorded with initial level $2(A)^1\Sigma^+$ ($v = 16$, $J = 30$), where again a ΔJ= even propensity was observed [34].

The current calculations by T. Price *et al.* [33, 35, 66] of population transfer for NaK $2(A)^1\Sigma^+$ (v=0, $J \leq 30$) in collisions with helium show a more dramatic ΔJ = even propensity for helium than for argon, which agrees with the experimental results. Calculations for collisions with argon have now also been completed, for v = 0, J = 0-60, but there are still advances being made in the quality of the calculated

potential surfaces being used. Work with Drs. P. Crozet and A. J. Ross at Université Lyon-1 (this dissertation) has also expanded the experimental data available for analysis. This work collected and analyzed collisional spectra with initial states $2(A)^1\Sigma^+$ (v=0, J=14, 30) and the same perturbers (helium and argon) that were used in the theoretical calculations, as well as for additional vibrational levels $v = 1$, 2. Data were also collected for $2(A)^1\Sigma^+$ (16, 14) to continue the comparison of how differing initial v, J combinations affect the collisional rate coefficients. Figures 6.46 through 6.49 show comparisons of experimental rate coefficient results (corrected for multiple collision effects described in the preceeding section) with theoretical calculations of cross sections (converted to rate coefficients using $k_P^\Delta = \sigma_P^\Delta \bar{v}$ with $\bar{v}$ being the thermally averaged relative speed) for J-changing collisions of $2(A)^1\Sigma^+$ (0, 14) and $2(A)^1\Sigma^+$ (0, 30) with both argon and helium perturbers.

It should be noted that the absolute magnitudes of the theoretical rate coefficients are in excellent agreement with the experimental values. This agreement is, in the argon cases, better once corrections for multiple collision effects have been applied to the experimental results (see Sec. 6.4.3), however the difference between experimental and theoretical results becomes larger for the helium rate coefficients. In addition, the most recent theoretical calculations also do a good job in determining the magnitude of the ΔJ = even propensity, although there is a slight discrepancy at large $|\Delta J|$ for the argon cross sections, where the calculations show a transition from a ΔJ = even propensity to a ΔJ = odd propensity that is not observed experimentally. This discrepency may be due to minor shortcomings of the basis set used in the theoretical calculations, and work is currently being done by Price *et al.* [35, 66] to clarify this.

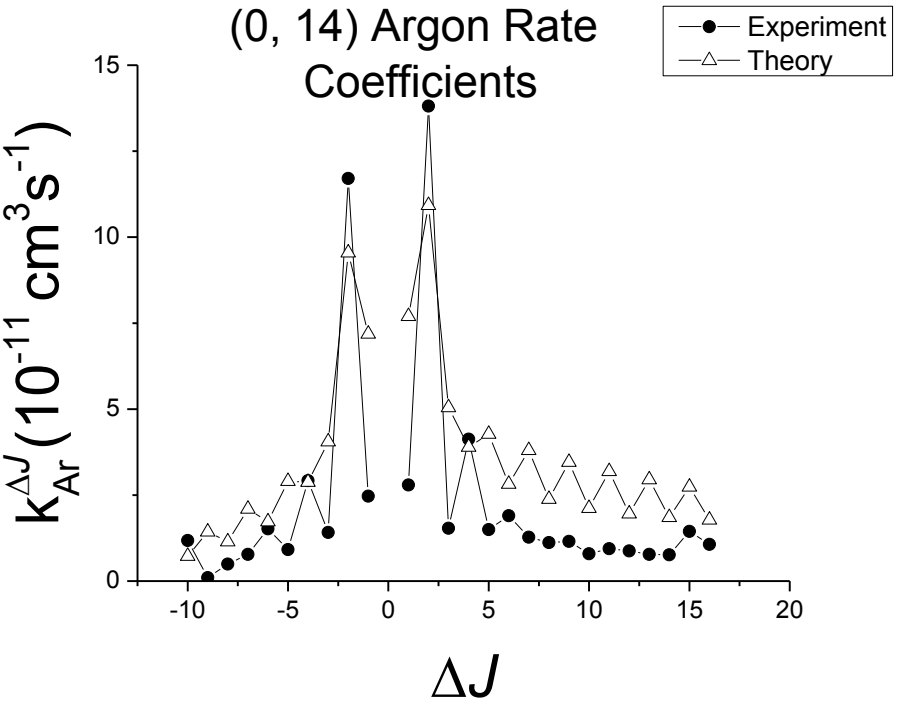

Figure 6.46: Comparison of theoretical and experimental rate coefficients for collisions of NaK $2(A)^1\Sigma^+$ (0, 14) molecules with argon perturbers. Theoretical cross sections are converted to rate coefficients by $k_P^{\Delta} = \sigma_P^{\Delta}\bar{v}$. The experimental rate coefficients presented are the "final" values presented in the previous section which approximately take into account the effects of multiple collisions.

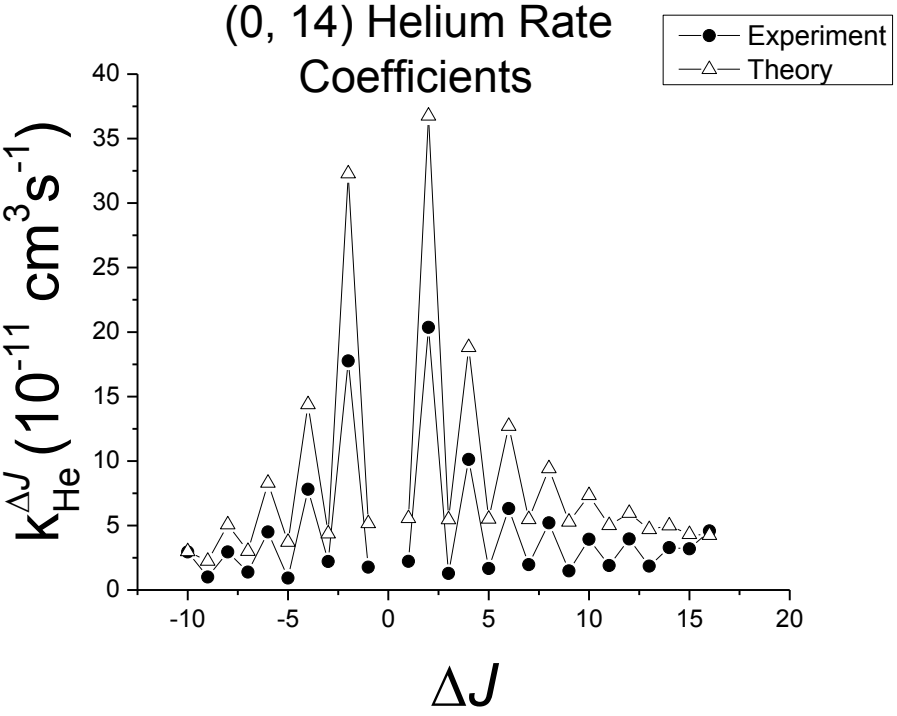

Figure 6.47: Comparison of theoretical and experimental rate coefficients for collisions of NaK $2(A)^1\Sigma^+$ (0, 14) molecules with helium perturbers. Theoretical cross sections are converted to rate coefficients by $k_P^{\Delta} = \sigma_P^{\Delta}\bar{v}$. The experimental rate coefficients presented are the "final" values presented in the previous section which approximately take into account the effects of multiple collisions.

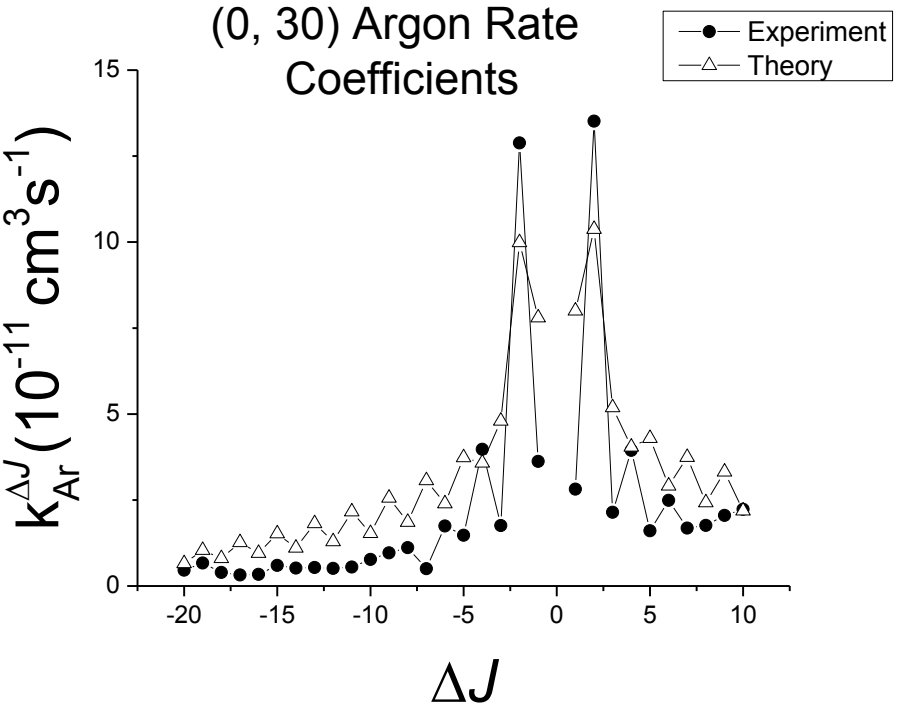

Figure 6.48: Comparison of theoretical and experimental rate coefficients for collisions of NaK $2(A)^1\Sigma^+$ (0, 30) molecules with argon perturbers. Theoretical cross sections are converted to rate coefficients by $k_P^\Delta = \sigma_P^\Delta \bar{v}$. The experimental rate coefficients presented are the "final" values presented in the previous section which approximately take into account the effects of multiple collisions.

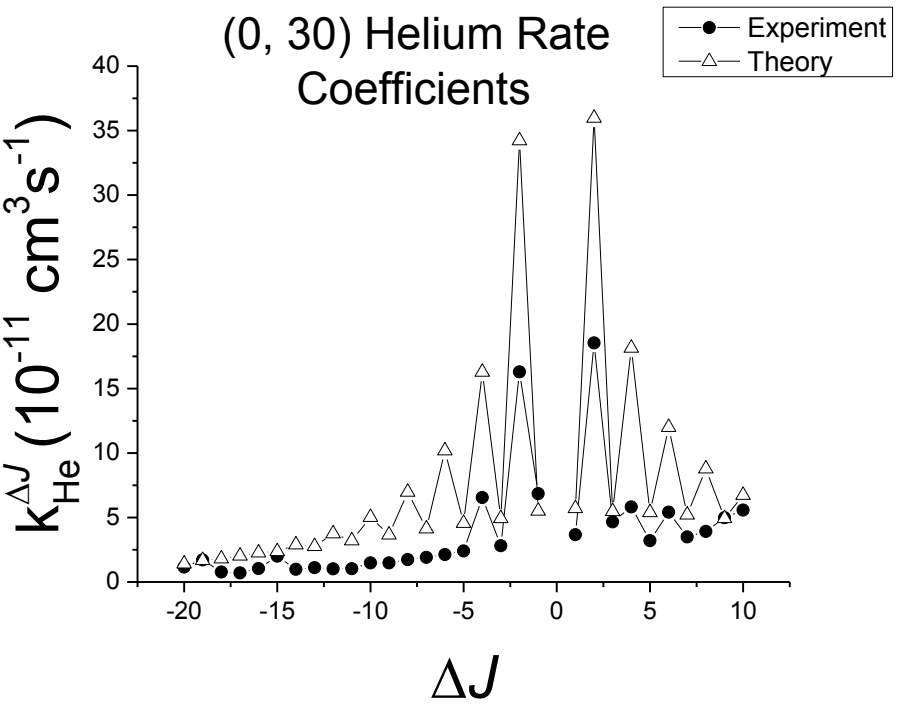

Figure 6.49: Comparison of theoretical and experimental rate coefficients for collisions of NaK $2(A)^1\Sigma^+$ (0, 30) molecules with helium perturbers. Theoretical cross sections are converted to rate coefficients by $k_P^{\Delta} = \sigma_P^{\Delta}\bar{v}$. The experimental rate coefficients presented are the "final" values presented in the previous section which approximately take into account the effects of multiple collisions.

Chapter 7

Conclusions and Future Work

7.1 Inelastic Collisions

This dissertation has discussed investigations of vibrationally and rotationally inelastic collisions of NaK with argon, helium and potassium as collision partners. Previous studies of inelastic collisions involving the NaK molecule in our group were completed at higher initial $2(A)^1\Sigma^+$ state levels ($v = 16$, $J = 30$), with argon [31, 34] and helium perturbers [34]. We have expanded upon this by looking at lower initial vibrational states ($v = 0$, 1, 2) and wider ranges of ΔJ, which much more closely align with the theoretical calculations of Malenda, Price, Hickman and coworkers [32, 33, 35, 66]. Vibrationally inelastic collisions have also been studied experimentally in the current work.

Previous work by Wolfe *et al.* [31] showed a strong propensity for ΔJ = even transitions in collisions of NaK $2(A)^1\Sigma^+$ (v =16, J = 30) molecules with argon. Jones' [34] use of helium as a collisional partner for the same initial state showed

that the ΔJ = even propensity was much more pronounced than in the argon collisions. No ΔJ = even propensity was seen in these previous studies for NaK-K collisions. However in the current experiment we did see a ΔJ = even propensity in the potassium rate coefficients. We originally thought, in the preliminary fitting stage, that this was an artifact due to the relatively low potassium densities and our inability to completely disentangle the potassium and noble gas collision rates. However this ΔJ = even propensity in NaK-K collisions seems to be present in all J-changing data analyzed in this work for $v = 0$, 1 and 2. This important question could be answered with a "pure" potassium experiment conducted with the heat pipe oven operating in "heat pipe mode". In this mode of operation, the noble gas is excluded from the interaction zone, only NaK+K collisions occur, and the presence or absence of a ΔJ = even propensity would be directly apparent from even a quick look at the data. Unfortunately, heat pipe mode was not used during the Lyon visits, and the NaK heat pipe oven at Lehigh has now been decommissioned. The probe laser required for the Lehigh pump/probe experiment is also no longer available.

We also presented experimentally determined rate coefficients for vibrationally inelastic collisions in this dissertation. In collisions of NaK with both argon and helium, no ΔJ = even propensity was observed for either perturber case (although such a propensity, if it existed, might have been masked by multiple collision effects). The experimentally fit rate coefficients for vibration-changing collisions ($k^{\Delta v,\Delta J}$) were, on average, an order of magnitude smaller than the J-changing collision rate coefficients for small values of $|\Delta J|$ ($k^{|\Delta J|\leq 5}$) and approximately on the same order of magnitude as rate coefficients for large values of $|\Delta J|$ ($k^{|\Delta J|\geq 15}$). The effects of

multiple collisions on our fitted collisional rate coefficients were also discussed, and estimates of correction factors were determined.

Dr. Hickman's group at Lehigh has carried out theoretical calculations of cross sections for rotationally inelastic collisions of NaK molecules in the $2(A)^1\Sigma^+$ v=0 level with argon and helium perturbers [33, 35]. Our measurements provide a direct test of these calculations for both NaK-He and NaK-Ar systems, in the same vibrational level used in these calculations, as well as for a wider range of ΔJ than studied in previous experiments (previous experimental work only covered the range $-4 \leq \Delta J \leq +4$). In their calculations, Hickman and coworkers have found that the quality of the interaction potential energy surfaces for NaK and the collisional partner are important, and that the predicted ΔJ = even propensity is sensitive to the degree to which the interaction potential deviates from inversion symmetry when you exchange the potassium and sodium atoms.

7.2 Future Work

During J. Jones' work at Lehigh University [34] and in our work in Lyon, additional v- and J-changing collisional data were collected using the NaK $2(A)^1\Sigma^+$ (v=16, J=14) initial level, with both argon and helium as the collisional partners. These data have not yet been analyzed due to time constraints. Therefore a useful future project would involve compilation and analysis of these data, which would allow comparison of rate coefficients for two initial vibrational levels (v = 0, 16), each with the same two initial rotational levels (J = 14, 30). This information can give a

more definitive understanding of the effect of initial v and J on the rates associated with rotationally inelastic collisions. In addition to this, an extension of the current work would be to collect v- and J-changing collision data with the same initial levels as in the present work, but with different inert gas perturbers. This would allow us to learn more about how population transfer is affected by the mass and polarizability of the collisional partner. The observed ΔJ = even propensity of NaK-Ar collisions is less pronounced than for NaK-He collisions, and it would be interesting to see if collisions of NaK with larger, more polarizable inert gases (such as xenon) continued the trend of reduced ΔJ = even propensity with increased perturber mass or increased perturber polarizability.

In addition, Malenda *et al.* [33] and Price *et al.* [35, 66] have carried out theoretical calculations for the transfer of population, orientation, and alignment in rotationally inelastic collisions of NaK-He and NaK-Ar. Wolfe *et al.* [31] and Jones [34] investigated the experimental transfer of both population and orientation in rotationally inelastic collisions of NaK with argon and with both helium and argon, respectively. Orientation for a level J is defined as [63]

$$\mathscr{O} = \langle \cos\theta \rangle = \left\langle \frac{M_J}{\sqrt{J(J+1)}} \right\rangle \tag{7.1}$$

and represents the first moment of the distribution of population over the magnetic sublevels M_J; i.e. positive orientation implies $M_J > 0$ levels are preferentially populated and vice versa for negative orientation. Alignment is defined as [63]

$$\mathscr{A} = \left\langle \frac{3M_J^2 - J(J+1)}{\sqrt{J(J+1)[J(J+1) - \frac{3}{4}}} \right\rangle, \tag{7.2}$$

and represents the second moment of the distribution of population over M_J; i.e. non-zero alignment implies that either the high $|M_J|$ or low $|M_J|$ levels are more likely to be populated. Wolfe *et al.* [31] and Jones [34] found expressions relating the orientation to experimental signals obtained using a circularly polarized pump beam and a linearly polarized probe beam in a polarization spectroscopy setup. The circularly polarized pump beam prepares an orientation in the magnetic sublevels of the intermediate level. If instead, a linearly polarized pump beam, polarized at 45° with respect to the vertical polarization of the probe beam is used, the intermediate state can be prepared with a non-zero alignment but no net orientation. Before I began the work presented in this dissertation, I derived an expression relating the $2(A)^1\Sigma^+$ (intermediate) state alignment to the experimental signal obtained with this 45° linearly polarized pump beam. A proposed future project for a student could be to perform an experimental alignment study using this relation, experimentally determining the transfer of alignment in collisions of NaK with helium or argon. This would provide another excellent test of the theoretical calculations of Hickman and coworkers.

Bibliography

[1] W. Demtroder, *Laser Spectroscopy Volume 1: Basic Principles; Fourth Edition* (Springer, Berlin, 2008).

[2] J. Kinsey, "Laser-induced fluorescence", Ann. Rev. Phys. Chem. **28**, 349 (1977).

[3] A. Delon and R. Jost, "Laser-induced dispersed fluorescence spectroscopy of 107 vibronic levels of NO_2 ranging from 12,000 to 17,600 cm^{-1}", J. Chem. Phys. **114**, 331 (2001).

[4] M. Clyne and I. McDermid, "Laser-induced fluorescence: electronically excited states of small molecules", Adv. Chem. Phys. **50**, 1 (1982).

[5] C. Amiot, "Laser-induced fluorescence of Rb_2", J. Chem. Phys. **93**, 8591 (1990).

[6] C. Amiot, W. Demtroder, and C. Vidal, "High resolution Fourier-spectroscopy and laser spectroscopy of Cs_2", J. Chem. Phys. **88**, 5265 (1988).

[7] A. Ross, C. Effantin, J. D'Incan, and R. Barrow, "Long-range potentials for the $X^1\Sigma^+$ and $a^3\Sigma^+$ states of the NaK Molecule", Mol. Phys. **56**, 903–912 (1985).

[8] I. Russier-Antoine, A. Ross, M. Aubert-Frécon, F. Martin, and P. Crozet, "An improved potential energy curve for the ground state of NaK", J. Phys. B **33**, 2753 (2000).

[9] A. Ross, R. Clements, and R. Barrow, "The $A(2)^1\Sigma^+$ state of NaK", J. Mol. Spectrosc. **127**, 546 – 548 (1988).

[10] A. Gerdes, M. Hobein, H. Knóckel, and E. Tiemann, "Ground state potentials of the NaK Molecule", Eur. Phys. J. D. **49**, 67 – 73 (2008).

[11] H. Harker, P. Crozet, A. J. Ross, K. Richter, J. Jones, C. Faust, J. Huennekens, A. V. Stolyarov, H. Salami, and T. Bergeman, "Experimental and theoretical studies of the coupled $2(A)^1\Sigma^+$ and $b^3\Pi$ states of NaK", Phys. Rev. A **92**, 012506 (2015).

[12] J. Woerdman, "Doppler-free two-photon transitions of the sodium molecule", Chem. Phys. Lett. **43**, 279–282 (1976).

[13] Li Li and R. W. Field, "Direct observation of high-lying $^3\Pi_g$ states of the sodium molecule by optical-optical double resonance", J. Phys. Chem. **87**, 3020–3022 (1983).

[14] E. Laub, I. Mazsa, S. Webb, J. L. Civita, I. Prodan, Z. Jabbour, R. Namiotka, and J. Huennekens, "Experimental Study of the NaK $3^1\Pi$ State", J. Mol. Spectrosc. **193**, 376–388 (1999), erratum: **221**, 142-144 (2003).

[15] L. Morgus, P. Burns, R. D. Miles, A. D. Wilkins, U. Ogba, A. P. Hickman, and J. Huennekens, "Experimental study of the NaK $3^3\Pi$ double minimum state", J. Chem. Phys. **122**, 144313 (2005).

[16] J. Huennekens, I. Prodan, A. Marks, L. Sibbach, E. Galle, T. Morgus, and Li Li, "Experimental studies of the NaK $1^3\Delta$ state", J. Chem. Phys. **113**, 7384–7397 (2000).

[17] A. D. Wilkins, L. Morgus, J. Hernandez-Guzman, J. Huennekens, and A. P. Hickman, "The NaK $1^{1,3}\Delta$ states: Theoretical and experimental studies of fine and hyperfine structure of rovibrational levels near the dissociation limit", J. Chem. Phys. **123**, 124306 (2005).

[18] R. D. Miles, L. Morgus, D. O. Kashinski, J. Huennekens, and A. P. Hickman, "Nonadiabatic coupling in the $3^3\Pi$ and $4^3\Pi$ states of NaK", J. Chem. Phys. **125**, 154304 (2006).

[19] P. Burns, L. Sibbach-Morgus, A. D. Wilkins, F. Halpern, L. Clarke, R. D. Miles, Li Li, A. P. Hickman, and J. Huennekens, "The $4^3\Sigma^+$ state of NaK: Potential energy curve and hyperfine structure", J. Chem. Phys. **119**, 4743–4754 (2003).

[20] S. Ashman, B. McGeehan, C. M. Wolfe, C. Faust, K. Richter, J. Jones, A. P. Hickman, and J. Huennekens, "Experimental Studies of the NaCs $5^3\Pi_0$ and $1(a)^3\Sigma^+$ Electronic States", J. Chem. Phys. **136**, 114313 (2012).

[21] C. Faust, Ph.D. thesis, Lehigh University, 2014.

[22] C. Ottinger, R. Velasco, and R. Zare, "Some Propensity Rules in Collision-Induced Rotational Quantum Jumps", J. Chem. Phys. **52**, 1636–1643 (1970).

[23] T. P. Scott, N. Smith, and D. E. Pritchard, "Application of fitting laws to rotationally inelastic rate constants: $Li^*_2(A^1\Sigma)$+Ne, Ar, Xe.", J. Chem. Phys. **80**, 4841–4850 (1984).

[24] P. D. Magill, B. Stewart, N. Smith, and D. Pritchard, "Dynamics of quasiresonant vibration−rotation transfer in atom-diatom scattering", Phys. Rev. Lett. **60**, 1943 (1988).

[25] B. Stewart, P. D. Magill, and D. E. Pritchard, "Quasi-Resonant Vibrational-Rotational Transfer in Inelastic Li_2^*-Ne Collisions", J. Phys. Chem. A **104**, 10565–10575 (2000).

[26] Y. Gao and B. Stewart, "Comparison of experimental and computed vibrationally inelastic rate constants for Li_2 $A^1\Sigma_u^+ -$Ne collisions", J. Chem. Phys. **103**, 860–863 (1995).

[27] Y. Gao, P. S. Gorgone, S. Davis, E. K. McCall, and B. Stewart, "Dependence of level-resolved energy transfer on initial vibrational level in Li_2 $(A)^1\Sigma_u^+$-Ne collisions", J. Chem. Phys. **104**, 1415–1426 (1996).

[28] K. Bergmann and W. Demtroder, "Inelastic cross sections of excited molecules. III. Absolute cross sections for rotational and vibrational transitions in the Na_2 $(B^1\Pi_u)$ state", J. Phys. B **5**, 2098 (1972).

[29] A. J. McCaffery, "Quasiresonant vibration-rotation transfer: A kinematic interpretation", J. Chem. Phys. **111**, 7697–7700 (1999).

[30] M. H. Alexander and H. Werner, "Rotationally inelastic collisions of $Li_2(A^1\Sigma_u^+)$ with Ne: Fully *ab initio* cross sections and comparison with experiment", J. Chem. Phys. **95**, 6524–6535 (1991).

[31] C. Wolfe, S. Ashman, J. Bai, B. Beser, E. H. Ahmed, A. M. Lyyra, and J. Huennekens, "Collisional Transfer of Population and Orientation in NaK", J. Chem. Phys. **134**, 174301 (2011).

[32] R. F. Malenda, Ph.D. thesis, Lehigh University, 2012.

[33] R. F. Malenda, T. J. Price, J. Stevens, L. Uppalapati, A. Fragale, P. Weiser, A. Kuczala, D. Talbi, and A. P. Hickman, "Theoretical Calculations of Rotationally Inelastic Collisions of He with NaK($A^1\Sigma^+$): Transfer of Population, Orientation, and Alignment", J. Chem. Phys. **142**, 224301 (12 pages) (2015).

[34] J. Jones, Ph.D. thesis, Lehigh University, 2015.

[35] T. J. Price, A. C. Towne, D. Talbi, and A. P. Hickman, "Semiclassical model for the distribution of final polar angles and m' states in rotationally inelastic collisions", Chem. Phys. Lett. **645**, 180–186 (2016).

[36] G. Herzberg, *Spectra of Diatomic Molecules* (Van Nostrand Reinhold, New York, 1950).

[37] J. L. Dunham, "The Energy Levels of a Rotating Vibrator", Phys. Rev. **41**, 721–731 (1932).

[38] P. F. Bernath, *Spectra of Atoms and Molecules* (Oxford University Press, New York, 1995).

[39] Li Li, A. Lazoudis, P. Yi, Y. Liu, J. Huennekens, R. W. Field, and A. M. Lyyra, "Hyperfine structure of the $1^3\Delta_g$, $2^3\Pi_g$, and $3^3\Sigma_g^+$ states of ^{6}Li^{7}Li", J. Chem. Phys. **116**, 10704–10712 (2002).

[40] Li Li, T. An, T. Whang, A. M. Lyyra, W. C. Stwalley, R. W. Field, and R. A. Bernheim, "Hyperfine splitting of the $1^3\Delta_g$ Rydberg state of $^7Li_2$", J. Chem. Phys. **96**, 3342–3343 (1992).

[41] P. Qi, G. Lazarov, A. M. Lyyra, Y. Liu, C. Cui, Li Li, and G.-H. Jeung, "The Na_2 $2^3\Pi_g$ state: New observations and hyperfine structure", J. Chem. Phys. **124**, 184304 (2006).

[42] Y. Liu, Li Li, G. Lazarov, A. Lazoudis, A. M. Lyyra, and R. W. Field, "Hyperfine structures of the $2^3\Sigma_g^+$, $3^3\Sigma_g^+$, and $4^3\Sigma_g^+$ states of Na_2", J. Chem. Phys. **121**, 5821–5827 (2004).

[43] Li Li and R. W. Field, "A spin-orbit $2^1\Pi_g \sim 2^3\Pi_g$ perturbation in Na_2: Hyperfine splittings, perturbation matrix elements, and electronic structure implications", J. Mol. Spectrosc. **123**, 237–246 (1987).

[44] D. Li, F. Xie, Li Li, V. B. Sovkov, V. S. Ivanov, E. Ahmed, A. M. Lyyra, J. Huennekens, and S. Magnier, "The $^{39}K_2$ $2^3\Sigma_g^+$ state: Observation and analysis", J. Chem. Phys. **126**, 194314 (2007).

[45] Y. Chu, F. Xie, D. Li, Li Li, V. B. Sovkov, V. S. Ivanov, and A. M. Lyyra, "Experimental study of the $^{39}K_2$ $2^3\Pi_g$ state by perturbation facilitated infrared-infrared double resonance and two-photon excitation spectroscopy", J. Chem. Phys. **122**, 074302 (2005).

[46] K. Ishikawa, T. Kumauchi, M. Baba, and H. Kato, "Hyperfine structure of the NaK $c^3\Sigma^+$ state and the effects of perturbation", J. Chem. Phys. **96**, 6423–6432 (1992).

[47] C. R. Vidal and J. Cooper, "Heat Pipe Oven: A New, Well-Defined Metal Vapor Device for Spectroscopic Measurements", J. Appl. Phys. **40**, 3370–3374 (1969).

[48] Bomem, Inc., Elegant Spectroscopy: Optical Configuration for the Bomem DA3 Series - Fourier Transform Spectrophotometer, Manual for Bomem FTS, 1986.

[49] C. Wolfe, Ph.D. thesis, Lehigh University, 2010.

[50] L. Morgus, Ph.D. thesis, Lehigh University, 2005.

[51] A. N. Nesmeyanov, *Vapor Pressure of the Chemical Elements* (Elsevier Publishing, New York, 1963).

[52] R. Chang, *General Chemistry* (McGraw-Hill Higher Education, New York, 2000).

[53] P. Perrot, *A to Z of Thermodynamics* (Oxford University Press, New York, 1998).

[54] E. Lewis, "Collisional relaxation of atomic excited states, line broadening and interatomic interactions", Physics Reports **58**, 1 – 71 (1980).

[55] J. Huennekens and A. Gallagher, "Self-broadening of the Sodium Resonance Lines and Excitation Transfer Between the $3P_{\frac{3}{2}}$ and $3P_{\frac{1}{2}}$ Levels", Phys. Rev. A **27**, 1851–1864 (1983).

[56] N. Lwin, D. McCartan, and E. Lewis, "The Determination of Collision Damping Constants", The Astrophysical Journal **213**, 599–606 (1977).

[57] C. Carrington, D. Stacey, and J. Cooper, "Multipole relaxation and transfer rates in the impact approximation: application to the resonance interaction", J. Phys. B **6**, 417 (1973).

[58] N. Lwin and D. McCartan, "Collision broadening of the potassium resonance lines by noble gases", J. Phys. B **11**, 3841 (1978).

[59] R. Le Roy, LEVEL 8.0: A Computer Program for Solving the Radial Schrodinger Equation for Bound and Quasibound Levels, university of Waterloo. Chemical Physics Research Report CP-663, 2007, see http://leroy.uwaterloo.ca/programs/ .

[60] Z. Jabbour, J. Sagle, R. Namiotka, and J. Huennekens, "Measurement of the self-broadening rate coefficients of the cesium resonance lines", J. Quant. Spectrosc. Radiat. Transfer **54**, 767 – 778 (1995).

[61] T. Price, Private communications, 2016.

[62] H. Chen, L. Li, G. Lazarov, X. Wang, A. M. Lyyra, J. Huennekens, and R. W. Field, "Rotational Pattern Difference in Resolved Fluorescence Spectra with Different Detection Schemes", J. Mol. Spectrosc. **196**, 197–211 (1999).

[63] R. Zare, *Angular Momentum: Understanding Spatial Aspects in Chemistry and Physics* (Wiley, New York, 1988).

[64] I. Kovacs, *Rotational Structure in the Spectra of Diatomic Molecules* (Hilger, London, 1969).

[65] R. F. Malenda, J. Jones, C. Faust, K. Richter, C. M. Wolfe, A. P. Hickman, J. Huennekens, D. Talbi, and F. Gatti, "Rotationally inelastic collisions of He and Ar with NaK: Experiment and theory", Abstract D1.00047. 43rd Meeting of American Physical Society Division of Atomic, Molecular, and Optical Physics, Orange County, CA, June 4-8, 2012.

[66] T. Price, Ph.D. thesis, Lehigh University, (in preparation).

Vita

Kara grew up in western New York, where she started her college career at Rochester Institute of Technology as an Imaging Science major. Eventually, she changed her major to Physics with the hopes of teaching at either the high school or college level. She graduated from SUNY College at Brockport Magna Cum Laude with a B.S. in Physics in 2010. During her time at Brockport, Kara had the opportunity to attend Lehigh University's Physics Research Experience for Undergraduates (REU) program, where she was introduced to research in the field of molecular spectroscopy. After that, she decided that graduate school was the next step in her education and moved to Bethlehem, PA to return to Lehigh University to pursue a graduate degree in physics.

While in her first year at Lehigh, Kara met her (now) husband Ria, and they both enjoy spending their free time playing video games and being involved with flat track roller derby. Kara finished her M.S. in Physics in January of 2012, and continued her previous work in Professor John Huennekens' lab. She also was able to continue her undergraduate interest of science outreach to local elementary schools while at Lehigh. In the falls of 2013 and 2014, she had the wonderful opportunity to collaborate with Drs. Amanda Ross and Patrick Crozet in Lyon, France. Kara is excited to move to Middletown, CT for the next year to begin a Visiting Professor position at Wesleyan University.